2015

Neutrino and Antineutrino Induced Meson Production

Libo Jiang
University of South Carolina

Neutrino and Antineutrino Induced Meson Production

by

Libo Jiang

Bachelor of Science
Northeast Forest University 2006

Master of Science
Harbin Institute of Technology 2008

Submitted in Partial Fulfillment of the Requirements

for the Degree of Doctor of Philosophy in

Physics

College of Arts and Sciences

University of South Carolina

2015

Accepted by:

Roberto Petti, Major Professor

Vitaly Rassolov, Committee Member

Steffen Strauch, Committee Member

Jeffery Wilson, Committee Member

Lacy Ford, Vice Provost and Dean of Graduate Studies

Dedication

This dissertation is dedicated to my family.

Acknowledgments

First of all, great gratitude to Professor Roberto Petti and Professor Sanjib Mishra. They gave me indispensable guidance and assistance to my work during the past few years and let me know how beautiful the physics is. 5 years ago, they warmly brought me into neutrino physics area, and are very thoughtful and helpful in supervision of my research and schedule. They continued answering my queries endlessly.

Many thanks to my committee members, Dr. Vitaly Rassolov, Dr. Steffen Strauch, and Dr. Jeff Wilson. Their guidance and help are very important to my research.

Many thanks to my colleagues and friends at University of South Carolina: Xinch--un Tian, Chris Kullenberg, Brian Mecurio, Jae Jun Kim, Kevin Wilson, Hongyue Duyang, Andrew Svenson, Kevin Wood, Tyler Alion, and Bing Guo. During the past few years, they gave me a lot of help and I had the pleasure of working with them.

I would also like to say a few works to thank Dr. Huifeng Fu, and Dr. Tianhong Wang. They helped a lot in my theoretical calculations and understanding the electroweak theory.

Thank to the excellent work of the collaborators from ELBNF/DUNE, NOMAD collaborations.

At the end, thank to everyone I mentioned and those I forgot, thank you very much.

Abstract

Coherent meson production measurement is very important in physics research. First, the coherent pion production is a potential background to ν oscillation in next generation of Long Base Line Experiment(ELBNF/DUNE); second, coherent pion and coherent ρ production provide a detailed test of CVC and PCAC hypothesis; third, coherent meson production can be used to monitor the neutrino and anti-neutrino fluxes in the experiment. This dissertation focuses on two parts: coherent π^- production in NOMAD, and coherent ρ simulation using LBNF fluxes. With the NOMAD data, the ratio between cross-sections of coherent π^- and $\bar{\nu}_\mu$ charged current interactions was measured and compared with the measurements of coherent π^+. The experience of coherent π analysis may be used to evaluate the sensitivity of ELBNF/DUNE project to coherent processes. With the ELBNF process, I wrote a new C++ simulation package and generated 100k coherent ρ^+ events. It is known that for the neutrino-induced process, the incoming neutrino fluxes could not be measured directly, and the Q^2 and other variables related to it are unknown in the neutrino-induced neutral current interactions. The photon-induced coherent ρ^0 provides a way to get additional information to constrain the incoming neutrino fluxes. I calculated the ratios between the cross-sections of neutrino-induced coherent $\rho^\pm$, ρ^0 and photon-induced coherent ρ^0. With these ratios, some kinematic variable distributions are reweighted with this ratio in this thesis.

Table of Contents

List of Tables

List of Figures

Chapter 1

Electroweak Theory and Neutrino Interaction

1.1 Weak Interaction and Electroweak Theory

Theoretically, all the interactions between particles can be classified into four fundamental interactions and listed in order of decreasing strength as: the strong interaction, electromagnetism, the weak interaction, and gravity. The weak interaction operates between all particles except photons and gravitons. It causes reactions which make particles ultimately decay into the stable leptons and hadrons, such as electrons, neutrinos, protons, and so on. These decays are the natural sources for us to study the weak interaction, however, only in a limited energy region. The advent of neutrino experiments in humans' laboratories ameliorated the situation by enabling us to explore weak interactions in a much wider energy region. The neutrino-hadron scattering is one such experiment.

The neutrino-hadron scattering can be classified with the help of a plane composed of Q^2 and ν [16], where Q^2 and ν are the square of the momentum transfer and the energy transfer between the initial and final leptons respectively (Q^2 and ν are defined in chapter 2). Figure 1.1 shows the weak interactions with respect to Q^2 and ν. In this figure, Region I with very small Q^2 and ν represents weak decays; Region II (diagonal line) represents (quasi-)elastic scattering; Region III is the resonance region, starting with the line $W = M + m_\pi$(W is the hadronic mass, M is the proton mass, m_π is the pion mass); Region IV with high values of Q^2 and ν is the domain of deep inelastic scattering; And region V with low Q^2 and high ν values is coherent

scattering, which is the focus of this thesis. In this Region, the interactions with very low Q^2 allow study two basic properties of the weak current: One is the conservation of the vector current (It is also called CVC hypothesis), which was introduced to explain the equality of the vector muon and nuclear beta decay. The other one is the partial conservation of the axial current (It is also called PCAC hypothesis) which can be used to explain the small ($\sim 20\%$) renormalization of the nuclear axial decay constant by the strong interactions [36]. When the Q^2 is very low, the nuclear stays intact in coherent process, then the nucleons inside can not be considered as free. In this case, the perturbative theory of strong interactions can not be used. To study the processes with very low Q^2, the Hadron Dominance Model has been brought up to describe the hadronic behavior in coherent process, which is going to be introduced in this chapter. Therefore, the study of coherent meson production can also provide a detailed test of Hadron Dominance Model.

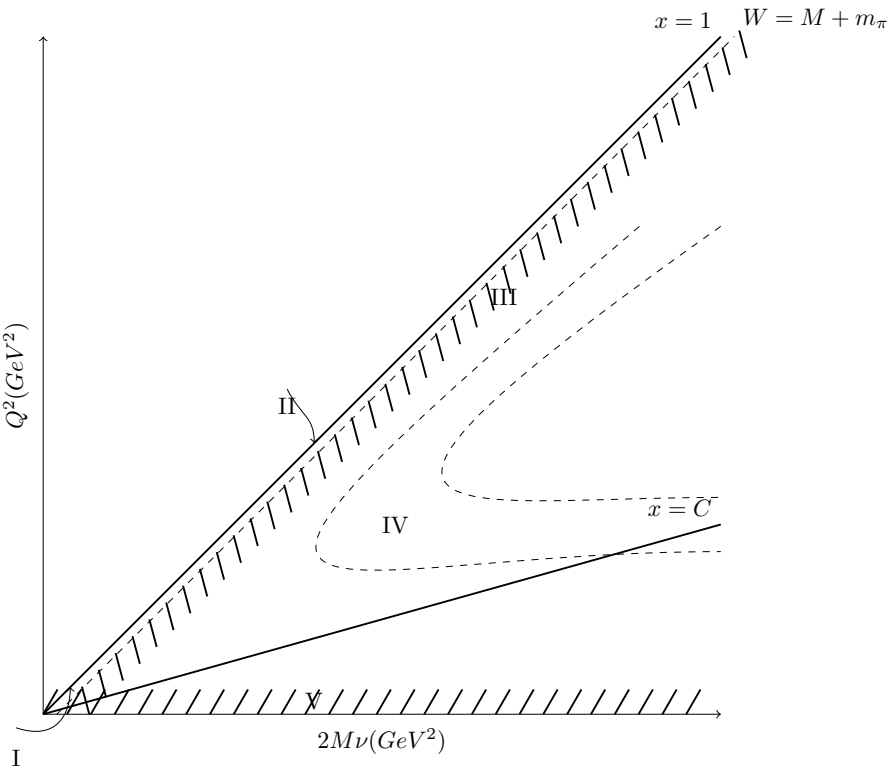

Figure 1.1: The (Q^2, ν) plane in neutrino interactions [36].

Space-Time Structure of the Weak Charged and Neutral Current

This subsection gives basics of electroweak theory (which can be found in many textbooks, such as [33] and [30]). For convenience, we give the convention for the Dirac matrices in this thesis as follows.

Let $\{\gamma_\mu, \mu = 0, 1, 2, 3\}$ be an orthonormal set of vectors in space-time. The signature of space-time is expressed by the equations:

$$\gamma_0^2 = 1, \gamma_1^2 = \gamma_2^2 = \gamma_3^2 = -1, \tag{1.1}$$

$$\gamma_\mu \quad = \quad g_{\mu\nu}\gamma^\nu, \tag{1.2}$$

and the matrices follow an anti-commutation relation:

$$\{\gamma_\mu, \gamma_\nu\}_+ = \frac{1}{2}(\gamma_\mu\gamma_\nu + \gamma_\nu\gamma_\mu) \quad = \quad g_{\mu\nu}. \tag{1.3}$$

As usual, a special multivector

$$i\gamma^0\gamma^1\gamma^2\gamma^3 \quad = \quad \gamma_5 \tag{1.4}$$

is introduced which can be used to construct peudoscalars. A multivetor is said to be even (odd) if it commutes (anti-commutes) with γ_5. A slashed 4-momentum (or other 4-vector) represents the product of the 4-momentum (or other 4-vector) with γ_μ.

In the Standard Model the electroweak interaction is described by a gauge field theory. The gauge group is the $SU(2)_L \times U(1)_Y$ group, where L indicates that this $SU(2)$ group only acts on the left-handed components of fermion fields. The subscript Y for $U(1)$ group is called hypercharge and specifies this $U(1)$ group.

The local $SU(2)_L \times U(1)_Y$ gauge invariance of the electroweak Lagrangian is guaranteed by introducing the covariant derivative D_μ,

$$D_\mu = \partial_\mu + igA_\mu^i\tau^i + ig'B_\mu\frac{Y}{2}, \tag{1.5}$$

where $\tau^i = \sigma^i/2$ $(i = 1, 2, 3)$ with σ^i being the Pauli matrix. A^i_μ and B_μ are gauge boson fields. For each generator of the group, there is a gauge field. The covariant derivative transforms as

$$D_\mu \to D'_\mu = U(\theta^i(x), \eta(x)) D_\mu U^{-1}(\theta^i(x), \eta(x)), \tag{1.6}$$

where

$$U(\theta^i(x), \eta(x)) = e^{i\theta^i(x)\tau^i + i\eta(x)Y/2}, \tag{1.7}$$

with $\theta^i(x)$ and $\eta(x)$ being the parameters of the transformation. Then the gauge boson fields transform as

$$A^i_\mu \tau^i \to A'^i_\mu \tau^i = U(\theta^j(x))[A^i_\mu \tau^i - \frac{i}{g}\partial_\mu] U^{-1}(\theta^i(x)), \tag{1.8}$$

$$B_\mu \to B'_\mu = B_\mu - \frac{1}{g'}\partial_\mu \eta(x). \tag{1.9}$$

The interaction part of the Lagrangian can be written as

$$\begin{aligned} \mathcal{L}_I &= -\frac{1}{2}\bar{L_L}(g\not{A}^i\sigma^i - g'\not{B})L_L - \frac{1}{2}\bar{Q_L}(g\not{A}^i\sigma^i + \frac{1}{3}g'\not{B})Q_L \\ &\quad + g'\bar{e_R}\not{B}e_R - \frac{2}{3}g'\bar{u_R}\not{B}u_R + \frac{1}{3}g'\bar{d_R}\not{B}d_R, \end{aligned} \tag{1.10}$$

where L_L and Q_L represent the left-handed lepton doublet and the left-handed quark doublet in the fundamental representation of $SU(2)_L$ group respectively. Specifically, for the first generation of the Standard Model,

$$L_L = \begin{pmatrix} \nu_{eL} \\ e_L \end{pmatrix}, \qquad Q_L = \begin{pmatrix} u_L \\ d_L \end{pmatrix}. \tag{1.11}$$

In order to see the interaction term for neutrinos explicitly, we take the explicit form of the Pauli matrices and obtain

$$\begin{aligned} \mathcal{L}_{I,L} &= -\frac{1}{2}\begin{pmatrix} \bar{\nu_{eL}} & e_L \end{pmatrix} \begin{pmatrix} g\not{A}_3 - g'\not{B} & g(\not{A}_1 - i\not{A}_2) \\ g(\not{A}_1 + i\not{A}_2) & -g\not{A}_3 - g'\not{B} \end{pmatrix} \begin{pmatrix} \nu_{eL} \\ e_L \end{pmatrix} \\ &\quad + g'\bar{e_R}\not{B}e_R, \end{aligned} \tag{1.12}$$

where we have omitted the quark part of the Lagrangian. This equation shows that the interactions are inter-mediated by the mixtures of the gauge fields. The off-diagonal terms of Equation (1.12) are conjugations of each other, so we can introduce a complex field W_μ by

$$W^\mu \equiv \frac{A_1^\mu - iA_2^\mu}{\sqrt{2}}. \tag{1.13}$$

Replacing A_1^μ and A_2^μ with W^μ, we have, for interactions between neutrinos and electrons,

$$\begin{aligned} \mathcal{L}^{(CC)} &= -\frac{g}{\sqrt{2}}\{\bar{\nu_{eL}}\not{W} e_L + \bar{e_L}\not{W}^\dagger \nu_{eL}\} \\ &= -\frac{g}{2\sqrt{2}}\bar{\nu_e}\gamma^\mu(1-\gamma^5)eW_\mu + H.c. \\ &= -\frac{g}{2\sqrt{2}} j_{W,L}^\mu W_\mu + H.c., \end{aligned} \tag{1.14}$$

where

$$j_{W,L}^\mu = \bar{\nu_e}\gamma^\mu(1-\gamma^5)e = 2\bar{\nu_e}\gamma^\mu e_L. \tag{1.15}$$

The complex gauge field W_μ carries a charge which should be the electrical charge to guarantee the conservation of electrical charge. So the current $j_{W,L}^\mu$ is called the (leptonic) charged current and the corresponding part of Lagrangian is indicated by CC (which represents charged current) as a superscript (see Equation (1.14)).

The diagonal terms of Equation (1.12) are mixtures of A_3^μ and B^μ, so we can introduce two fields Z^μ and A^μ as the linear combinations of A_3 and B^μ by

$$A^\mu = \sin\theta_W A_3^\mu + \cos\theta_W B^\mu, \tag{1.16}$$

$$Z^\mu = \cos\theta_W A_3^\mu - \sin\theta_W B^\mu, \tag{1.17}$$

where θ_W is a parameter to be determined and is usually called the weak mixing angle or Weinberg angle. Recalling that the electromagnetic interaction should come out of the electroweak theory, we require that A_μ is just the photon field. This requirement determines the Weinberg angle and the relation among the couplings g, g' and the electric coupling e.

To see how this happens, let us pick up the neutral current (NC) Lagrangian from Equation (1.12):

$$\mathcal{L}^{(NC)} = -\frac{1}{2}\{\bar{\nu_{eL}}(g\not{A}_3 - g'\not{B})\nu_{eL} - \bar{e_L}(g\not{A}_3 + g'\not{B})e_L - 2g'\bar{e_R}\not{B}e_R\}. \tag{1.18}$$

Substituting A_3^μ and B^μ with A^μ and Z^μ by using Equations (1.16) and (1.17), we obtain

$$\begin{aligned}\mathcal{L}^{(NC)} &= -\frac{1}{2}\{\bar{\nu_{eL}}[g\cos\theta_W + g'\sin\theta_W)\not{Z} + (g\sin\theta_W - g'\cos\theta_W)\not{A}]\nu_{eL} \\ &\quad -\bar{e_L}[g\cos\theta_W - g'\sin\theta_W)\not{Z} + (g\sin\theta_W + g'\cos\theta_W)\not{A}]e_L \\ &\quad -2g'\bar{e_R}[-\sin\theta_W\not{Z} + \cos\theta_W\not{A}]e_R\}. \end{aligned}\tag{1.19}$$

As neutral particles, neutrinos should not interact with the electromagnetic field, so we have

$$g\sin\theta_W = g'\cos\theta_W. \tag{1.20}$$

Now taking this relation back into Equation (1.19), we obtain

$$\begin{aligned}\mathcal{L}_{I,L}^{(NC)} &= -\frac{g}{2\cos\theta_W}\{\bar{\nu_{eL}}\not{Z}\nu_{eL} - (1-2\sin^2\theta_W)\bar{e_L}\not{Z}e_L + 2\sin^2\theta_W\bar{e_R}\not{Z}e_R\} \\ &\quad +g\sin\theta_W\bar{e}\not{A}e. \end{aligned}\tag{1.21}$$

The last term describes electrons interacting with photons, which is just what we need for electromagnetic interactions, so the coupling $g\sin\theta_W$ should be equal to the electrical coupling e:

$$g\sin\theta_W = e. \tag{1.22}$$

We have 4 parameters g, g', e and θ_W with 2 equations (1.20) and (1.22), so in principle, we can choose any two of them to describe the theory. From Equations (1.20) and (1.22), we can also deduce

$$\tan\theta_W = \frac{g'}{g}, \tag{1.23}$$

and

$$g^2 + g'^2 = e^2. \tag{1.24}$$

Experimentally, the value of $\sin^2\theta_W$ can be extracted from neutral current processes, and is different according to different renormalization prescriptions. In the on-shell scheme, it is

$$\sin^2\theta_W = 1 - \frac{M_W^2}{M_Z^2}, \tag{1.25}$$

where M_W and M_Z are the masses of W and Z respectively.

To sum up, the neutral current Lagrangian can be written as

$$\mathcal{L}^{(NC)} = \mathcal{L}^Z + \mathcal{L}^\gamma, \tag{1.26}$$

where $\mathcal{L}^\gamma$ is the electrodynamic (QED) Lagrangian (interaction part) and is given by

$$\mathcal{L}^\gamma = -e j^\mu_{\gamma,L} A_\mu \tag{1.27}$$

where the leptonic electromagnetic current $j^\mu_{\gamma,L}$ is

$$j^\mu_{\gamma,L} = -\bar{e}\gamma^\mu e. \tag{1.28}$$

The weak neutral current Lagrangian $\mathcal{L}^Z$ is given by

$$\mathcal{L}^Z = -\frac{g}{2\cos\theta_W} j^\mu_{Z,L} Z_\mu, \tag{1.29}$$

where the leptonic weak neutral current is

$$j^\mu_{Z,L} = 2g^\nu_L \bar{\nu_{eL}}\gamma^\mu \nu_{eL} + 2g_L \bar{e_L}\gamma^\mu e_L + 2g_R \bar{e_R}\gamma^\mu e_R. \tag{1.30}$$

The coefficients g^ν_L, g_L, and g_R can be read off from Equation (1.21). Finally, the leptonic weak neutral current can be written as

$$j^\mu_{Z,L} = \bar{\nu}_e\gamma^\mu(g^\nu_V - g^\nu_A\gamma^5)\nu_e + \bar{e}\gamma^\mu(g^l_V - g^l_A\gamma^5)e, \tag{1.31}$$

where

$$g^{\nu,l}_V = g^{\nu,l}_L + g^{\nu,l}_R, \tag{1.32}$$

$$g^{\nu,l}_A = g^{\nu,l}_L - g^{\nu,l}_R. \tag{1.33}$$

Following the same procedure, one can deduce the Lagrangian for quarks. The corresponding interaction Lagrangian is

$$\begin{aligned}\mathcal{L}_{I,Q} &= \mathcal{L}_Q^{(NC)} + \mathcal{L}_Q^{(CC)} \\ &= -ej^{\nu}_{\gamma,Q}A_\nu - \frac{g}{2\cos\theta_W}j^{\nu}_{Z,Q}Z_\nu - \frac{g}{2\sqrt{2}}j^{\nu}_{W,Q}W_\nu - \frac{g}{2\sqrt{2}}(j^{\nu}_{W,Q})^\dagger W^\dagger_\nu. \quad (1.34)\end{aligned}$$

The first two terms after the second equality sign constitute the neutral current Lagrangian while the last two terms constitute the charged current Lagrangian. The quark weak charged current $j^{\nu}_{W,Q}$, the quark weak neutral current $j^{\nu}_{Z,Q}$ and the quark electromagnetic current $j^{\nu}_{\gamma,Q}$ read, respectively,

$$j^{\nu}_{W,Q} = \bar{u}\gamma^\nu(1-\gamma_5)d, \quad (1.35)$$

$$j^{\nu}_{Z,Q} = \bar{u}\gamma^\nu(g^u_V - g^u_A)u + \bar{d}\gamma^\nu(g^d_V - g^d_A\gamma_5)d, \quad (1.36)$$

$$j^{\nu}_{\gamma,Q} = \frac{2}{3}\bar{u}\gamma^\nu u - \frac{1}{3}\bar{d}\gamma^\nu d. \quad (1.37)$$

For coefficients $g^{u,d}_V$ and $g^{u,d}_A$, we have, in general,

$$g^f_L = I^f_3 - q_f\sin^2\theta_W, \quad (1.38)$$

$$g^f_R = -q_f\sin^2\theta_W, \quad (1.39)$$

$$g^f_V = g^f_L + g^f_R = I^f_3 - 2q_f\sin^2\theta_W, \quad (1.40)$$

$$g^f_A = g^f_L - g^f_R = I^f_3. \quad (1.41)$$

where the superscript f denotes a specific fermion (lepton or quark) field. I_3 is the third component of the weak isospin and q_f is the electrical charge of the corresponding fermion.

We have shown that the electroweak interaction includes the weak interaction which is inter-mediated by charged gauge fields $W^\pm$ and neutral gauge fields Z (Feynman diagrams of these two interactions are shown in Figure 1.2), and the electromagnetic interaction which is inter-mediated by photon fields.

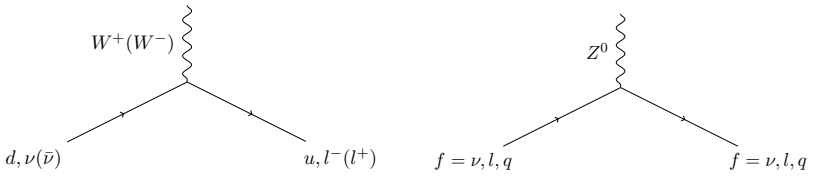

Figure 1.2: Diagrams of Weak Charged and Neutral Current

The weak interaction is a short range interaction, because the gauge bosons are massive. Roughly, we have R_{weak} (Range of Weak Interaction)

$$R_{weak} = \frac{\hbar c}{M_W c^2} \approx 2 \times 10^{-18} m = 0.002 fm \ll 0.1 fm. \tag{1.42}$$

Weak Current of Hadrons and the CVC and PCAC hypothesis

The previous subsection gives the weak currents for leptons and quarks. In the real world, quarks never show up as isolated particles, instead only hadrons which are composed with quarks (as well as gluons) appear in experiments. For the coherent pion and rho processes, we encounter weak current for nucleons.

In the quark model proton and neutron are the states of $|uud\rangle$ and $|udd\rangle$ respectively. The weak interaction of these nucleons has more complicated structures compared to that of leptons or bare quarks, because it suffers from other interactions (mainly the strong interaction). However, the weak current of nucleons still consists of a vector current V_α and an axial-vector current A_α according to Lorentz invariance of the theory. So we may write

$$[J^{weak}_{hadron}]_\alpha = V_\alpha - A_\alpha. \tag{1.43}$$

V_α and A_α can be expressed as suitable Dirac matrices sandwiched between spinors for nucleons. To specify, the vector current may consist of a γ_α term (corresponding to a vector form factor or point-like interaction), a $\sigma_{\alpha\beta} q^\beta$ term (called weak magnetism;

q^β is the four-momentum transferred and $\sigma_{\alpha\beta} = \frac{1}{2}[\gamma_\alpha\gamma_\beta - \gamma_\beta\gamma_\alpha])$, and a q^α term (corresponding to an induced scalar form factor). The axial current may consist of a $\gamma_\alpha\gamma_5$ term (corresponding to an axial-vector form factor or point-like interaction), a $\sigma_{\alpha\beta}q^\beta\gamma_5$ term (pseudotensor form factor), and a $q_\alpha\gamma_5$ term (induced pseudoscalar form factor). Form factors for each term are dependent on the type of hadrons involved and this is expressed as h_1 and h_2 indices.

$$\begin{aligned} V_\alpha &= \bar{\psi}_{h_1}[\gamma_\alpha f_1^{h_1h_2}(Q^2,\nu) - i\sigma_{\alpha\beta}q^\beta f_2^{h_1h_2}(Q^2,\nu) + q^\alpha f_3^{h_1h_2}(Q^2,\nu)]\psi_{h_2}, \\ A_\alpha &= \bar{\psi}_{h_1}[\gamma_\alpha g_1^{h_1h_2}(Q^2,\nu) - i\sigma_{\alpha\beta}q^\beta g_2^{h_1h_2}(Q^2,\nu) + q^\alpha g_3^{h_1h_2}(Q^2,\nu)]\gamma_5\psi_{h_2}, \end{aligned} \tag{1.44}$$

where $\psi_{h_1(h_2)}$ represents the spinor of nucleon $h_1(h_2)$ [51].

All the form factors f_i and g_i are real according to the time reversal invariance of the strong interaction [27]. Furthermore, in the exact isospin invariance, one finds

$$f_3(Q^2) = 0, \qquad g_2(Q^2) = 0. \tag{1.45}$$

As a consequence, the contraction of vector current V_α with q^α vanishes, i.e., $q^\alpha V_\alpha = 0$. The f_1 term vanishes due to the free Dirac equation for the nucleon spinors (remember that in the isospin symmetric-case, the proton and neutron have the same mass). The f_2 term vanishes due to the anti-symmetric property of $\sigma_{\alpha\beta}$. On the other hand, $q^\alpha V_\alpha = 0$ implies $\partial^\alpha V_\alpha = 0$ in the configuration space, i.e., the vector current is conserved in the case that the strong interaction is isospin invariant. This property was proposed in Ref. [25, 28] and is called the conserved vector current (CVC) hypothesis.

Originally, the CVC hypothesis was proposed to explain why the vector current is not renormalized by the strong interaction in the β decay experiment. In the experiment, the nucleons have very small momentum transfer ($Q^2 \approx 0$). In this region all the kinematic terms (those which include q_α) become negligible and the

weak current takes a form similar to that at the leptonic vertex

$$\begin{aligned}[J^{weak}_{hadron}]_\alpha(Q^2=0) &= V_\alpha - A_\alpha \\ &= \bar{\psi}_p\gamma_\alpha(f_1^{pn}(Q^2=0) - g_1^{pn}(Q^2=0)\gamma_5)\psi_n, \end{aligned} \tag{1.46}$$

and by definition

$$f_1(0) = g_V, \qquad g_1(0) = g_A. \tag{1.47}$$

Experiments tell us that $g_V \simeq 1$, which implies that the coupling of this hadronic current is consistent with that of the corresponding leptonic current. Analogously to the conservation of electrical current leading to the universality of electron/proton charge, this universality of weak vector charge implies a conservation of the weak vector current. It should be mentioned that the isospin is not an exact symmetry, but is violated by the electromagnetic interactions, responsible for the mass difference of u and d quarks (thus proton and neutron), so the vector current is not exactly conserved. However, the violation of isospin symmetry is very small, so the CVC hypothesis is a good approximation.

Now, we consider the axial current. Experiments tell us that $g_A \simeq 1.25$, which is different from unity. This implies that the axial-vector current is affected by strong interactions and is not conserved. (In fact, if the axial current were conserved, the commonly observed pion decay $\pi^\pm \to \mu^\pm\nu$ would be forbidden.) For this non-conserved axial current, there is another hypothesis, called partially conserved axial current (PCAC) hypothesis, that relates the derivative of the axial current to the pion field, which was first proposed in Ref. [26]. We will give more details about PCAC in the next chapter.

The Goldberger-Treiman Relation

The CVC is a consequence of isospin invariance of the underlying theory, which arises when the quarks' masses are equal. When the quarks masses are zero, another

symmetry arises, that is the chiral $SU(2)$ symmetry. This chiral symmetry would result in the conservation of the axial current, so that $q^\alpha A_\alpha = 0$. Now consider the axial current of neutron-proton transition. From Equation (1.44), we have, for the g_1 term:

$$\begin{aligned} q^\mu A_\mu^{g_1} &= g_1(q^2)\bar{p}(\not{p} - \not{p}')\gamma_5 n \\ &= -g_1(q^2)\bar{p}\not{p}'\gamma_5 n - g_1(q^2)\bar{p}\gamma_5 \not{p} n \\ &= -(m_p + m_n)g_1(q^2)\bar{p}\gamma_5 n, \end{aligned} \tag{1.48}$$

and for the g_3 term:

$$q^\mu A_\mu^{g_3} = \bar{p} q^2 g_3 \gamma_5 n. \tag{1.49}$$

The g_2 term vanishes automatically. Then we have

$$(m_p + m_n)g_1(q^2) = q^2 g_3(q^2). \tag{1.50}$$

From this equation, we see that, either g_1 goes to zero as $q^2 \to 0$ or $g_3(q^2)$ has a pole. From experiments, we have known that $g_1(0) = g_A \simeq 1.25$, so $g_3(q^2)$ should have a pole at $q^2 \to 0$. This pole is due to the interaction of pions with the weak current of hadrons, which gives a contribution

$$\frac{q^\mu}{q^2} f_\pi \sqrt{2} g_{\pi NN} \bar{p}\gamma_5 n \tag{1.51}$$

to the matrix element of the axial vector current.

Comparing Equation (1.50) and Equation (1.51), we obtain

$$m_N g_A = \frac{g_\pi g_{\pi NN}}{\sqrt{2}}, \tag{1.52}$$

where the proton mass and neutron mass are taken as the same and $m_N = m_p = m_n$. This is the Goldberger-Treiman relation [31].

Vector Meson Dominance Model(VMD) and Hadron Dominance Model(HDM)

The discussion of the previous subsection tells us that the axial vector current of hadrons receives contributions from interactions with pions, and sheds light on how to treat the hadron currents. For example, the electrical current of hadrons may be treated with the so called the Vector Meson Dominance Model (VMD) (details of this model can be found in Refs. [13, 32]) where the amplitude of a photon scattering off a hadron is obtained by summing over the amplitudes of dominant vector meson-hadron scatterings (multiplied by corresponding meson propagators). Specifically one has

$$\mathcal{M}(\gamma + \alpha \to \beta) = \sum_{V=\rho^0,\omega,\phi} \frac{e}{g_V} \frac{m_V^2}{Q^2 + m_V^2} \mathcal{M}(V + \alpha \to \beta), \tag{1.53}$$

where m_V is the mass of corresponding meson and $e\frac{m_V^2}{g_V}$ is the coupling constant of the vector meson to the photon. The foundation of this model is the observation that the photon-induced processes exhibit hadronic properties as shown in Figure 1.3. The total cross-sections of photon-induced processes and pion-nucleon scatterings have similar resonance structures at low energy, but become structureless at higher energy.

On the theoretical side, the VMD model assumes the photon state $|\gamma>$ is the superposition of a "bare" photon state($|\gamma_B>$) and a sum of hadronic states with the same quantum numbers as the photon ($J^{PC} = 1^{--}, Q = B = S = 0$). Then the state vector could be written as

$$|\gamma> \simeq \sqrt{Z_3}|\gamma_B> + \sqrt{\alpha_{em}}|h>, \tag{1.54}$$

where Z_3 is the renormalization constant of photon factor, and $\alpha_{em} = \frac{1}{137}$ is the fine structure constant. In the simplest case, one picks up the three lightest vector mesons and then obtains Equation (1.53).

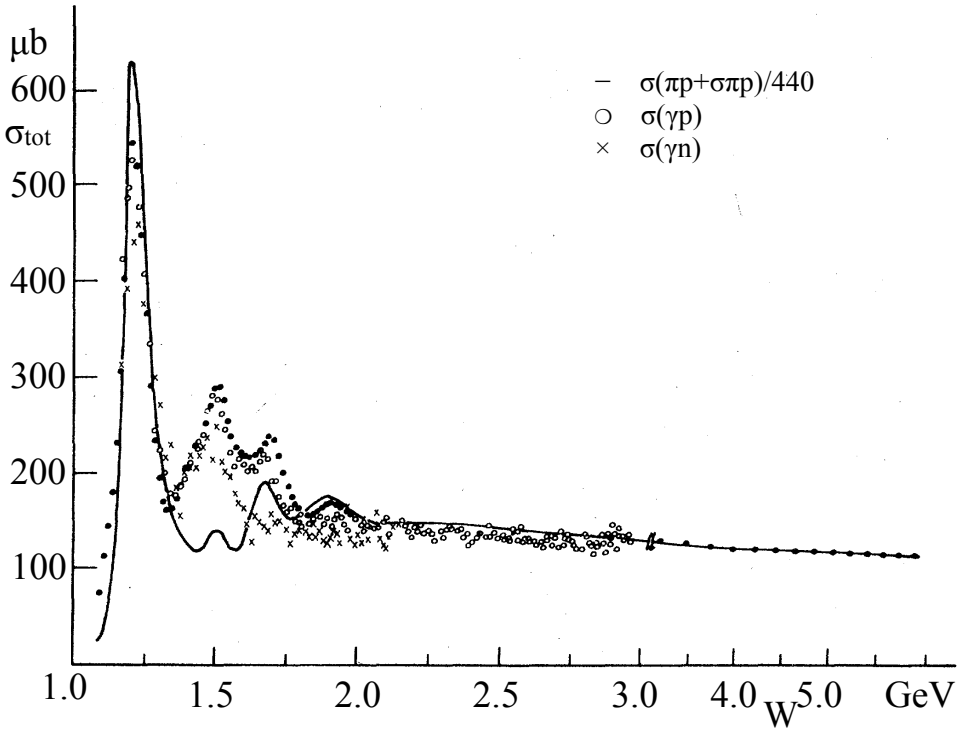

Figure 1.3: Total cross-section as a function of energy for interactions of photons and hadrons [50].

The idea of the Vector Meson Dominance Model can be generalized to the weak interacting processes, those via exchanging $W^{\pm}$. This leads to the Hadron Dominance Model(HDM) [42]. Unlike the VMD model, which only needs contributions from vector mesons, in this model, the vector meson (ρ) contributes to the hadronic vector current and the axial-vector meson (a_1) contributes to the hadronic axial current. In addition, there is a contribution described by PCAC hypothesis. To specify, we have [50]

$$\sigma(\nu_l + \alpha \to l + \beta) \quad \propto \quad \sum_{i=\rho,a_1,\pi} \sigma(i + \alpha \to \beta) + \text{interference} \quad \text{terms.} \tag{1.55}$$

Chapter 2

Challenges of Precision Oscillation Experiments

In the past, there have been many detectors designed for neutrino experiments. Neutrino beams are produced at particle accelerators which offer the greatest control over the neutrino being studied.

Short Baseline Neutrino Experiment:

Experiments at a short baseline (defined as $\lesssim 1$ km) look at neutrino beams with energy ranging from stopped Muon decay (< 53 MeV) to several hundred GeV.

For example, in the LSND experiment [49], the signal $\bar{\nu}_\mu \to \bar{\nu}_e$ was found [9, 11, 23] as well as $\nu_\mu \to \nu_e$ although weaker than the $\bar{\nu}_\mu \to \bar{\nu}_e$ [22, 10]. The MiniBooNE experiment [19, 14] is also a short baseline neutrino experiment is designed to check the result of LNSD signal.

Long Baseline Neutrino Experiment:

The Long Baseline Neutrino Experiment (LBNE), now called the Deep Underground Neutrino Experiment (DUNE), was designed for a high sensitivity measurement to many parameters [1]:

(1) First, it is the measurement of $\nu_\mu \to \nu_e$ and $\bar{\nu}_\mu \to \bar{\nu}_e$ oscillations with ν_e ($\bar{\nu}_e$) appearance and ν_μ ($\bar{\nu}_\mu$) disappearance, including a precision measurement of the third mixing angle θ_{13}, measurement of the CP violation phase δ_{CP}, and determination of the mass hierarchy (MH) (the sign of Δm^2_{13}).

The experimental sensitivity, quantified by $\Delta\chi^2$ parameters, is calculated by com-

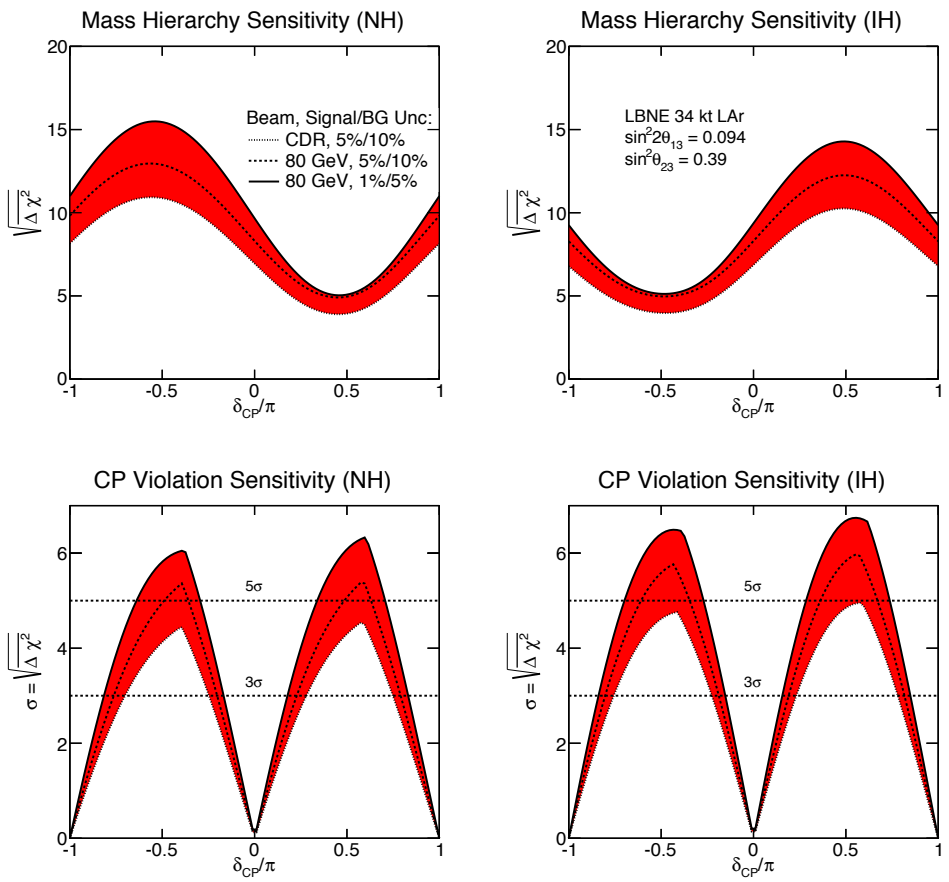

Figure 2.1: The significance with which the mass hierarchy (top) and CP violation ($\delta_{CP} \neq 0$ or π, bottom) can be determined by the LBNE experiment with 34-kt far detector as a function of the value of δ_{CP}. The plots on the left are for normal hierarchy and the plots on the right are for inverted hierarchy. The width of the red band shows the range of the sensitivity that is achieved by LBNE when varying the beam design and the signal and background uncertainties [1]

.

paring the predicted spectra for various scenarios. As the sensitivity, the definitions of $\Delta\chi^2$ for neutrino MH and CP-violation sensitivity are different [1]:

$$\Delta\chi^2_{MH} = |\chi^2_{MH^{test}=IH} - \chi^2_{MH^{test}=NH}|, \tag{2.1}$$

The sensitivity of the mass hierarchy is defined in Equation 2.1. Because the oscillation experiments can only probe the squared difference of the neutrino masses, whether or not m_2 is heavier than m_3 remains unknown. If m_2 is lighter than m_3, this scenario is called normal mass hierarchy. If m_2 is heavier than m_3, this scenario

is called inverted mass hierarchy. Normal and inverted mass hierarchy are shown in Figure 2.2.

Figure 2.1 shows the sensitivities for determining the mass hierarchy (MH) and CP violation as a function of the true value of δ_{CP} after six years of running in the LBNE 34 kt configuration. Let's consider the sensitivity of neutrino MH first. The sensitivities of normal hierarchy (NH) and inverted hierarchy (IH) are evaluated separately and shown at the top of this figure. The X axis in this figure is the phase factor δ/π. In the left top of this figure shows the sensitivity of normal hierarchy, There are three curves, the bottom one (solid line) is the result of prediction without near detector, the middle one is the result of prediction without the high resolution near detector but with beam improvement [1], the top one is the result of prediction with near detector and with beam improvement. We could see, with the beam design and high resolution near detector, the sensitivity is improved. The thicker the band is, the more the sensitivity improved.

The determination of the mass hierarchy (MH, or ordering) is very important in physics because neutrinos are fundamental particles, and knowing their properties is very critical [39]; The mass hierarchy could help people to know the nature of neutrinos: are they Majorana or Dirac particles? The question of CP violation could also be answered through the mass hierarchy, which is a very fundamental parameter of νSM (SM+3right-handed ν's), and study mass hierarchy may provide the answers to why there is more matter than anti-matter and the connections between the neutrinos and dark matter. Let's see the relationship between neutrino mass hierarchy and CP violation. The uncertainty of the CP violation reads [1]

$$\Delta\chi^2_{CPV} = min(\Delta\chi^2_{CP}(\delta^{test}_{CP} = 0), \Delta\chi^2_{CP}(\delta^{test}_{CP} = \pi)), \tag{2.2}$$

$$\Delta\chi^2_{CP} = \chi^2_{\delta^{test}_{CP}} - \chi^2_{\delta^{test}_{true}}. \tag{2.3}$$

Since the true value of δ_{CP} is unknown, a scan is performed over all possible values

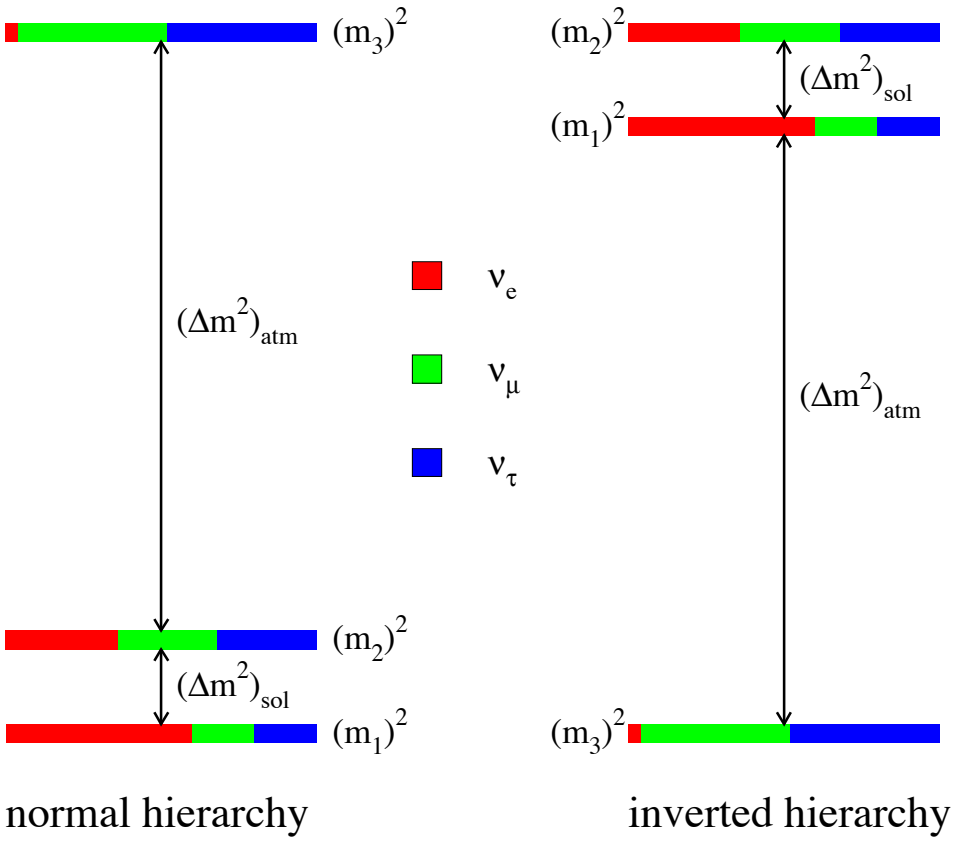

Figure 2.2: Normal and inverted mass hierarchy [35].

of δ_{CP}^{true}. The individual χ^2 values are calculated using [1]

$$\chi^2(\mathbf{n}^{true}, \mathbf{n}^{test}, f) = 2 \sum_{i}^{N_{reco}} (n_i^{true} \ln \frac{n_i^{true}}{n_i^{test}(f)} + n_i^{test}(f) - n_i^{true}) + f^2, \tag{2.4}$$

where $\mathbf{n}$ are event rate vectors in N_{reco} bins of reconstructed energy and f represents a nuisance parameter to be profiled. Nuisance parameters include the values of mixing angles, mass splittings and signal and background normalization. The nuisance parameters are constrained by Gaussian priors; in the case of the oscillation parameters, the Gaussian prior has standard deviation determined by taking 1/6 of the 3σ range allowed by the global fit [24]. The sensitivity of CP violation in the ELBNF/DUNE project is shown at the bottom of Figure 2.1, and is similar to the mass hierarchy sensitivity. The sensitivity to the CP violation is also improved using a high resolution near detector and with beam improvements. When δ is around -0.5π or 0.5π,

the sensitivity is increased from 3σ level to 5σ level. The inverted mass hierarchy scenario gives similar result as the normal mass hierarchy scenario but with higher sensitivity.

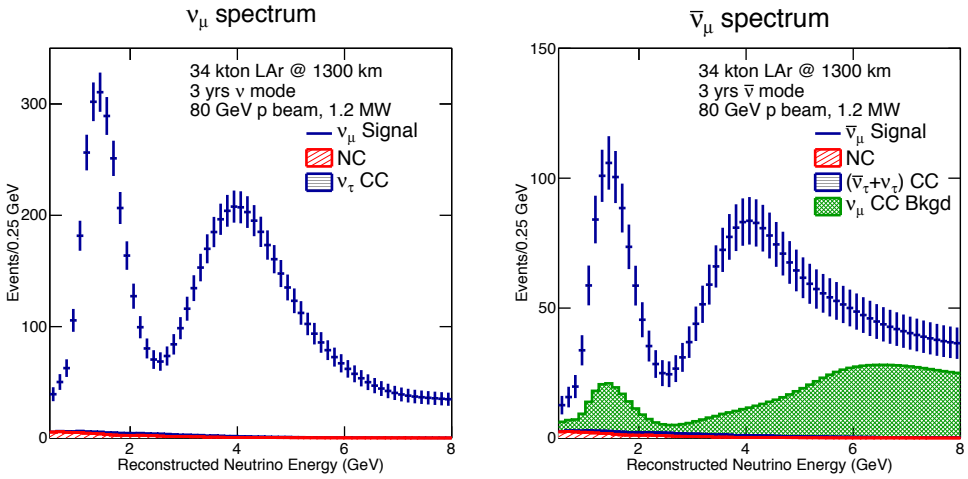

Figure 2.3: The expected reconstructed neutrino energy spectrum of ν_μ or $\bar{\nu}_\mu$ events in a 34-kt LArTPC for three years of neutrino(left) and anti-neutrino(right) running with a 1.2-MW beam [1].

(2) The ELBNF/DUNE is also designed for the precision measurement of $\sin^2\theta_{23}$ and $|\Delta m^2_{32}|$ in the $\nu_\mu/\bar{\nu}_\mu$ disappearance channel. Figure 2.3 and Figure 2.4 show the predicted spectrum of neutrino and anti-neutrino.

In Figure 2.5, the distributions of MH and CP-violation sensitivities as a function of exposure are shown. Similar to the Figure 2.1, there are also three set of lines are shown in these two figures. The top one is the result of 1%5% which is the goal of the ELBNF/DUNE scientific program, with no systematic; The middle line with the value 2%5% represents the results with beam improvement, but no near detector; The bottom line represents the results with no beam improvement and no near detector existence. From this figure, we can see an obvious improvement in sensitivity with beam improvements and a near detector. From this figure, it is obvious that the signal and background normalization uncertainties on the MH sensitivity is small, even at high exposures, given the large $\nu/\bar{\nu}$ asymmetry at 1,300 km compared to CP

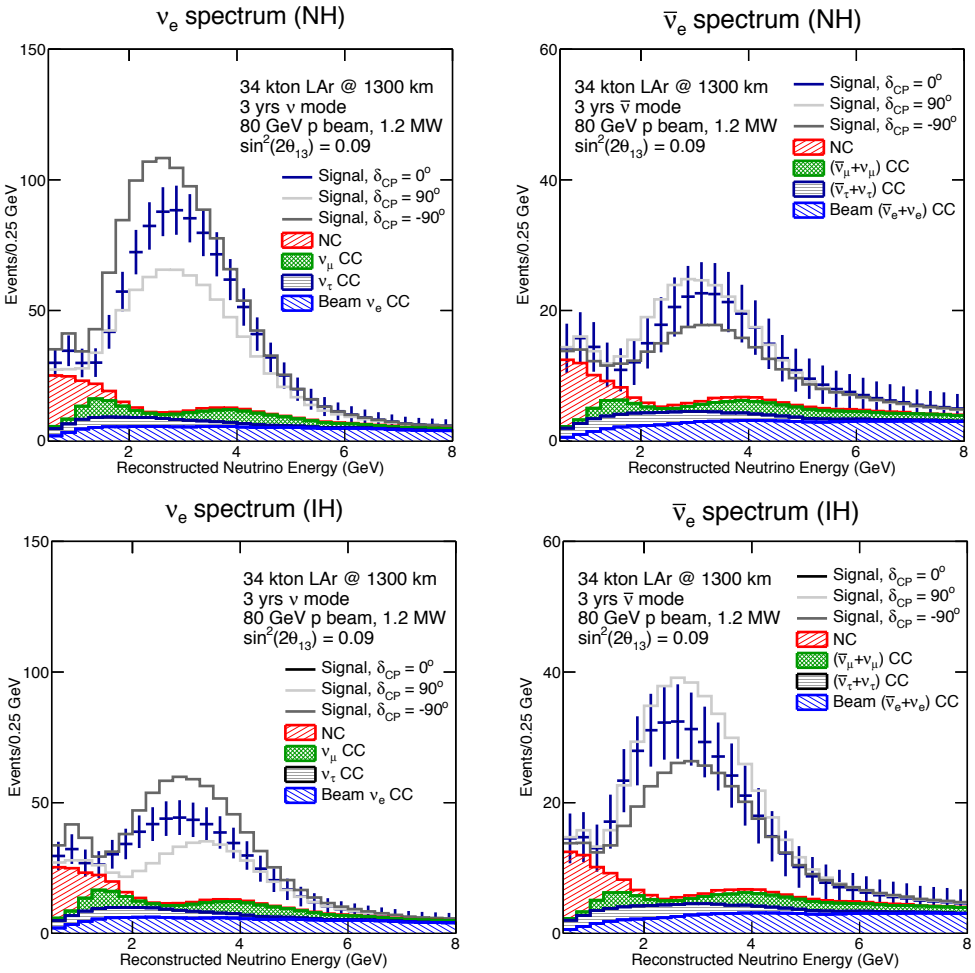

Figure 2.4: The expected reconstructed neutrino energy spectrum of ν_e or $\bar{\nu}_e$ oscillation events in a 34-kt LArTPC for three years of neutrino (left) and anti-neutrino (right) running with a 1.2-MW, 80-GeV beam assuming $\sin^2(2(2\theta_{13}) = 0.09$. The plots on the top are for normal hierarchy and the plots on the bottom are for inverted hierarchy [1].

violation which is even significant at high exposure.

(3) ELBNF/DUNE project is also designed to determine the θ_{23} octant using combined precision measurements of the $\nu_e/\bar{\nu}_e$ appearance and $\nu_\mu/\bar{\nu}_\mu$ disappearance channels.

(4) Another goal of ELBNF/DUNE project is to search for nonstandard physics, which could manifest itself as a difference in the high-precision measurement of ν_μ and $\bar{\nu}_\mu$ oscillations over long baselines.

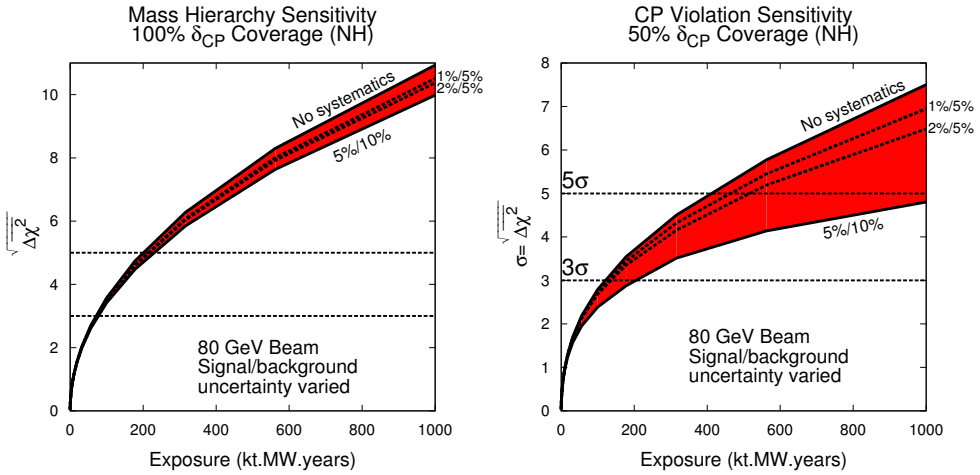

Figure 2.5: The mass hierarchy (left) and CP violation (right) sensitivities as a function of exposure in kt· year, for true normal hierarchy. The band represents the range of signal and background normalization errors [1].

The massive high-resolution far detector of ELBNF/DUNE project is a 34 kt liquid argon time-projection chamber (LArTPC) deep ground locates at Sanford Laboratory at a 4850 foot depth, 1300 km from Fermilab, and will enable LBNE to significantly expand the search for proton decay as predicted by Grand Unified Theories, as well as study the dynamics of core-collapse supernovae through observation of their neutrino bursts, should any occur in our galaxy during LBNE's operating lifetime [1].

Besides the far detector, a high resolution near neutrino detector is also proposed for high precision measurements of the neutrino mass matrix, neutrino interactions, structure of nucleons/nuclei, and so on. This high resolution detector will be introduced in chapter 3.

Absolute and Relative Flux Measurements

Relative Flux: Any neutrino experiment needs to predict or measure the neutrino and anti-neutrino flux. In the ELBNF/DUNE project, the primary interest is the relative flux determination [1].

The relative neutrino flux could be measured through the charged current neutrino

scattering process ($\nu_\mu + e^- \rightarrow \mu^- + \nu_e$) with low hadronic-energy deposition (ν) on the electron. The threshold of this process is $E_\nu > 10.8GeV$. Because of the existence of the neutrino in the final state, the incoming neutrino energy could not be fully reconstructed. The intranuclear effects tell us that not all the hadrons escape from the nucleus, which will also affect the measurement of the visible energy of hadronic system. To minimize the fraction of the total interaction energy carried by the hadronic system, low ν_0 is brought up, where ν_0 is a given value of visible hadronic energy in the interaction. Then the differential cross-section could be expressed with ν_0 [1]:

$$\mathcal{N}(\nu < \nu_0) \simeq C\Phi(E_\nu)\nu_0[\mathcal{A} + (\frac{\nu_0}{E_\nu})\mathcal{B} + (\frac{\nu_0}{E_\nu})^2\mathcal{C} + \mathcal{O}(\frac{\nu_0}{E_\nu})^3], \tag{2.5}$$

where the coefficients are $\mathcal{A} = \mathcal{F}_2$, $\mathcal{B} = (\mathcal{F}_2 \pm \mathcal{F}_3)/2$, $\mathcal{C} = (\mathcal{F}_2 + \mathcal{F}_3)/6$, and $\mathcal{F}_i = \int_0^2 \int_0^{\nu_0} F_i(x)dxd\nu$ is the integral of the structure function $F_i(x)$. The dynamics of neutrino-nucleon scattering implies that the number of events in a given energy bin with hadronic energy $E_{had} < \nu_0$ is proportional to the (anti) neutrino flux in that energy bin up to corrections $\mathcal{O}(\nu_0/E_\nu)$ and $\mathcal{O}(\nu_0/E_\nu)^0$. The number of $\mathcal{N}(\nu < \nu_0)$ is therefore proportional to the flux, up to correction factors of the order $\mathcal{O}(\nu_0/E_\nu)$ or smaller, which are not significant for small values of ν_0 at energies $\geq \nu_0$. The coefficients $\mathcal{A}$ and $\mathcal{B}$ and $\mathcal{C}$ are determined for each energy bin and neutrino flavor within the ND data.

Low Energy Absolute Flux: Neutrino-Electron-NC Scattering

The low energy absolute flux could be determined by the neutral current neutrino scattering on the electron ($\nu_\mu + e^- \rightarrow \nu_\mu + e^-$) [40].

$$\sigma(\nu_l e \rightarrow \nu_l e) = \frac{G_\mu^2 m_e E_\nu}{2\pi}[1 - 4\sin^2\theta_W + \frac{16}{3}\sin^4\theta_W], \tag{2.6}$$

$$\sigma(\bar{\nu}_l e \rightarrow \bar{\nu}_l e) = \frac{G_\mu^2 m_e E_\nu}{2\pi}[\frac{1}{3} - \frac{4}{3}\sin^2\theta_W + \frac{16}{3}\sin^4\theta_W], \tag{2.7}$$

From Equation 2.6 and Equation 2.7, we could see the cross-section only depends on the knowledge of $\sin^2\theta_W$.

High Energy Absolute Flux: Neutrino-Electron CC scattering

The ν_μ-e^- CC interaction (inverse Muon decay(IMD): $\nu_\mu + e^- \rightarrow \mu^- + \nu_e$) could be used to determine the high energy absolute flux. Considering the energy threshold for this process, IMD requires $E_\nu \geq 10.8GeV$. The high-resolution ND in the ELBNF neutrino beam will observe $\geq 2,000$ IMD events within three years. The reconstruction efficiency of the single, energetic forward μ^- will be $\geq 98\%$; the angular resolution of the IMD μ is ≤ 1 mrad [1]. The background, primarily originated from the ν_μ−QE interactions, can be precisely constrained using a control sample [1].

Low Energy Absolute Flux: QE in Water and Heavy-Water Targets

The quasi-elastic charged current (QE-CC) scattering ($\nu_\mu n(p) \rightarrow \mu^- p(n)$) on deuterium at low Q^2 could be used to extract the low energy absolute neutrino flux. Since $(m_\mu/M_n)^2$ at $Q^2 = 0$, could be neglected, the cross-section is independent of neutrino energy for $(2E_\nu M_n)^{1/2} > m_\mu$ [1]:

$$\frac{d\sigma}{dQ^2}|Q^2 = 0| = \frac{G_\mu^2 cos^2\theta_C}{2\pi}[F_1^2(0) + G_A^2(0)] = 2.08 \times 10^{-38} cm^2 GeV^{-2} \tag{2.8}$$

which is determined by neutron β decay and has a theoretical uncertainty$< 1\%$. The flux can be extracted experimentally by measuring low Q^2 QE interactions ($\leq$ 0.05GeV) and extrapolating the result to the limit of $Q^2 = 0$. The measurement requires a deuterium(or hydrogen for anti-neutrino) target to minimize the smearing due to Fermi motion and other nuclear effects. This requirement can only be achieved by using both H_2O and D_2O targets embedded in the fine-grained tracker and extracting the events produced in deuterium by statistical subtraction of larger oxygen component [1].

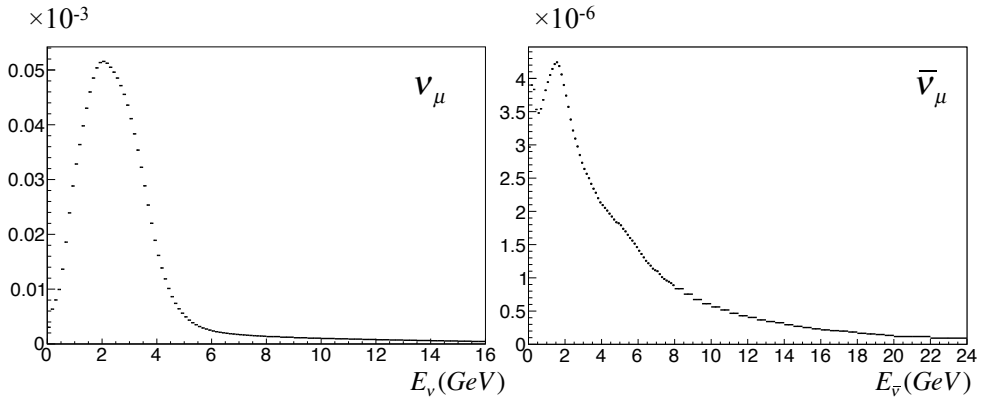

Figure 2.6: ν_μ and $\bar{\nu}_\mu$ flux distribution in ELBNF/DUNE project.

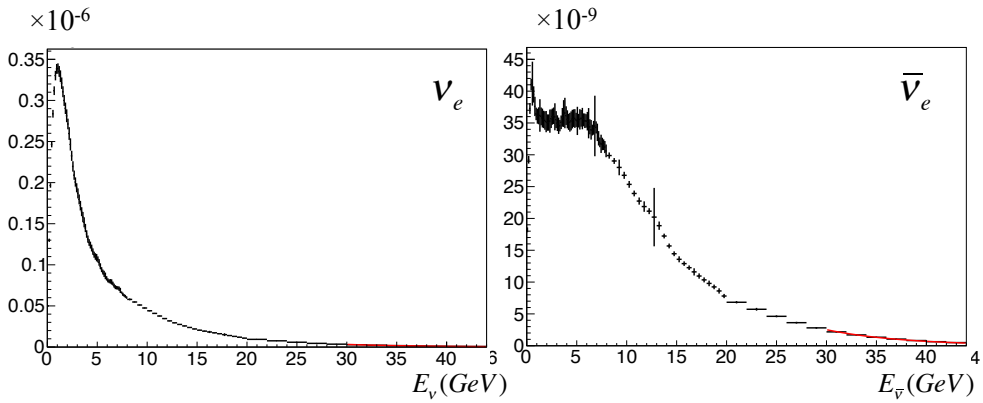

Figure 2.7: ν_e and $\bar{\nu}_e$flux distribution in ELBNF/DUNE project.

Measurement of $\nu/\bar{\nu}$ Flux Ratio

Figure 2.6 and Figure 2.7 show the distribution of neutrino fluxes at the near detector in predicted ELBNF/DUNE projects. In the ELBNF neutrino beam, there will have a $< 10\%$ contamination of neutrinos of the "wrong sign" in the oscillation energy region ($\bar{\nu}$'s in the ν beam and vice-versa) from the decay of wrong sign hadrons that propagate down the center of the focusing horns (where there is no magnetic field) into the decay volume. A $\leq 1\%$ contamination of ν_e and $\bar{\nu}_e$ in the ν_e appearance signal region is produced by the decays of tertiary Muons from Pion decays, and decays of Kaons [1].

The measurement of the neutrino fluxes is very important in the neutrino inter-

action analysis for the following reasons:

Similar to the NOMAD Beam, The LBNF fluxes also have two beam modes: neutrino beam mode and anti-neutrino beam mode. The neutrino beam mode is dominated by ν, and the anti-neutrino beam mode is dominated by $\bar{\nu}$. However, there are still a contamination in each beam mode. It is very important to constrain the contamination of each beam.

Second, measuring these fluxes is important to perform procedure measurement of cross sections and electroweak measurement, such weak mixing angle.

Third, since the coherent process is leaving the target nucleus largely unaffected, it is optimum to monitor the neutrino source.

Fourth, Since the ratio of coherent cross section for ν and $\bar{\nu}$ can be calculated precisely, it is possible to constrain the critical ratio of $\nu/\bar{\nu}$ fluxes.

Finally, the neutrino and anti-neutrino induced coherent Pion production have the same cross-section under PCAC theorem, so we can measure the neutrino vs anti-neutrino flux precisely which is very important for LBNF/DUNE oscillation measurements.

Determination of $\nu(\bar{\nu})$ energy scale

In ELBNF/DUNE, the determination of the oscillation parameters depends on the knowledge of the neutrino energy. Thus, reconstructing the neutrino energy becomes very critical in the experiment. It must be reconstructed on an event-by event basis because the neutrino beams are quite broad in energy due to their production in a secondary decay of primarily produced hadrons. The determination of neutrino energy could be measured from the kinematics of the outgoing particles, Since the coherent process is not as sensitive to nuclear effects as other kind of processes, then study of coherent processes is very important in determining the neutrino spectrum.

Chapter 3

Coherent Meson Production by Neutrino (Theory)

3.1 Kinematics of (Anti)Neutrino Scattering

Before we proceed let's define some notation used throughout this chapter (see Figure 3.1). (The derivation in the section was created in collaboration with C. T. Kullenberg)

E and **E'** : The incoming neutrino and outgoing lepton energies.

k and **k'** : The four-momenta of the incoming neutrino and outgoing lepton.

p and **p'** : The four-momenta of initial and final hadron states.

q : The four-momentum transfer.

$\boldsymbol{\nu}$: The energy transfer.

M : The mass of the target nucleon.

$\mathbf{Q^2}$: The negative of the square of the four-momentum transfer.

The mathematical expressions of $\boldsymbol{\nu}$, **q** and $\mathbf{Q^2}$ are shown in Equation (3.1),

$$\begin{aligned} \nu &= E - E' \\ q &= k - k' = \left(E - E', \vec{k} - \vec{k'}\right) = \left(\nu, \vec{q}\right) \\ Q^2 &= -q^2 = |\vec{q}|^2 - \nu^2 \end{aligned} \tag{3.1}$$

Looking more carefully at Q^2 we have:

$$Q^2 = 2(EE' - \vec{k} \cdot \vec{k'}) - m_\nu^2 - m_l^2 \tag{3.2}$$

W^2: Invariant hadronic mass $W^2 = (q+p)^2$.

If we assume that the lepton masses are negligible $(m_\nu, m_l \approx 0)$ then $\vec{k} \cdot \vec{k'} = |\vec{k}||\vec{k'}| \cos\theta \approx EE' \cos\theta$ and we have:

$$Q^2 \approx 2EE'(1 - \cos\theta) \qquad (m_l \to 0) \tag{3.3}$$

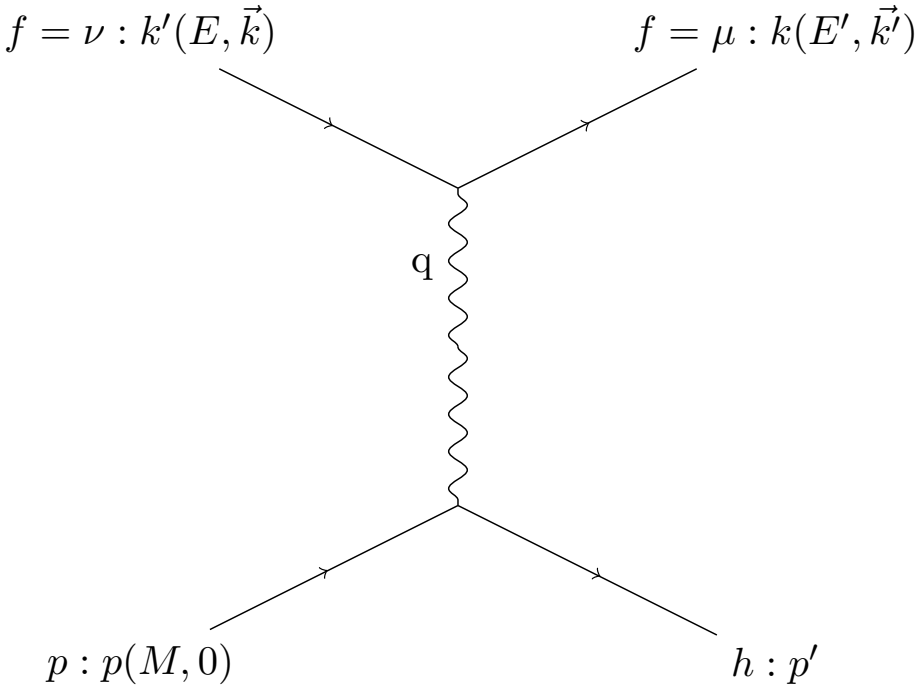

Figure 3.1: Kinematics of neutrino scattering.

3.2 Neutrino Induced Coherent Pion

According to the Feymann Rules, the amplitude of a neutrino induced hadronic interaction can be obtained from the weak current at the leptonic and hadronic vertexes:

$$\mathcal{M} = \frac{G_F}{\sqrt{2}} \left[J^{weak}_{lepton}\right]^\alpha \left[J^{weak}_{hadron}\right]_\alpha, \tag{3.4}$$

where

$$\frac{G_F}{\sqrt{2}} = \frac{g^2}{8M_W^2}. \tag{3.5}$$

The form of the weak current in purely leptonic interactions is known as:

$$\left[J^{weak}_{lepton}\right]_\alpha = \bar{\psi}_l \gamma_\alpha (1-\gamma_5)\psi_\nu. \tag{3.6}$$

The exact form of the weak current is known for free quark interactions; however, it is more complicated in the case of bound quarks in nucleons, which can be written as

$$\left[J^{weak}_{hadron}\right]_\alpha = V_\alpha - A_\alpha. \tag{3.7}$$

While V_α transforms like a vector under parity, A_α transforms like an axial vector. Combining the leptonic current and hadronic current, we have:

$$\mathcal{M} = \frac{G_F}{\sqrt{2}} \mathcal{L}^\alpha [V_\alpha - A_\alpha], \tag{3.8}$$

where

$$\mathcal{L}^\alpha = \bar{\psi}_l \gamma^\alpha (1-\gamma^5)\psi_\nu. \tag{3.9}$$

The scattering amplitude can be written as:

$$\mathcal{M}^2 = \frac{G_F^2}{2} \mathcal{L}^\alpha \mathcal{L}^{\beta *} [V_\alpha + A_\alpha][V^*_\beta + A^*_\beta], \tag{3.10}$$

and

$$A_{\alpha\beta} = [V_\alpha - A_\alpha][V^*_\beta - A^*_\beta]. \tag{3.11}$$

Besides the leptonic tensor and the hadronic tensor, in some conditions, the interference between the vector and axial vector terms is also considered. However, this term vanishes in the case of coherent interactions in the limit $Q^2 \to 0$. Here the leptonic tensor is defined as

$$\begin{aligned} \mathcal{L}^{\alpha\beta} &= \mathcal{L}^\alpha \mathcal{L}^{\beta *} \\ &= 8\{p^\alpha_\nu p^\beta_\mu + p^\beta_\nu p^\alpha_\mu - p_\nu \cdot p_\mu g^{\alpha\beta} + i\epsilon^{\alpha\beta\gamma\delta} p_{\nu_\gamma} p_{\mu_\delta}\}. \end{aligned} \tag{3.12}$$

Now let's show some details as follows. Using Equation (3.9), we have

$$\begin{aligned} \mathcal{L}^{\alpha\beta} &= \mathcal{L}^\alpha \mathcal{L}^{\beta *} \\ &= (\bar{\psi}_l \gamma^\alpha (1-\gamma_5)\psi_\nu)(\bar{\psi}_l \gamma^\beta (1-\gamma_5)\psi_\nu)^\dagger \\ &= \bar{\psi}_l \gamma^\alpha (1-\gamma_5)\psi_\nu \psi^\dagger_\nu (1-\gamma_5)\gamma^{\beta\dagger} \bar{\psi}_l{}^\dagger \end{aligned} \tag{3.13}$$

Using the anti-communicative relationship and the formula of the sum over the spin of Dirac field:

$$\{\gamma_5, \gamma_\mu\} = 0. \tag{3.14}$$

$$\sum_s \psi_l \bar{\psi}_l = \not{p}_l + m. \tag{3.15}$$

In the present analysis, the neutrino mass can be safely taken to be 0, so we have:

$$\sum_s \psi_\nu \bar{\psi}_\nu = \not{p}_\nu. \tag{3.16}$$

The leptonic tensor now becomes

$$\begin{aligned} \mathcal{L}^{\alpha\beta} &= Tr(\psi_l \bar{\psi}_l \gamma^\alpha (1-\gamma_5) \psi_\nu \bar{\psi}_\nu (1+\gamma_5)\gamma^\beta) \\ &= Tr((\not{p}_\mu + m)\gamma^\alpha (1-\gamma_5)\ \not{p}_\nu (1+\gamma_5)\gamma^\beta). \end{aligned} \tag{3.17}$$

The subscripts ν and μ indicate the neutrino and the muon, not the four vector index.

$$\begin{aligned} \mathcal{L}^{\alpha\beta} &= Tr(\psi_l \bar{\psi}_l \gamma^\alpha (1-\gamma_5) \psi_\nu \bar{\psi}_\nu (1+\gamma_5)\gamma^\beta) \\ &= Tr((\not{p}_\mu + m)\gamma^\alpha (1-\gamma_5)\ \not{p}_\nu (1+\gamma_5)\gamma^\beta) \\ &= Tr((\not{p}_\mu + m)\gamma^\alpha (\not{p}_\nu - \gamma_5\ \not{p}_\nu)(1+\gamma_5)\gamma^\beta) \\ &= 2Tr((\not{p}_\mu + m)\gamma^\alpha (\not{p}_\nu + \not{p}_\nu \gamma_5)\gamma^\beta). \end{aligned} \tag{3.18}$$

In the last equality, the anti-commutation relation has been used.

$$\begin{aligned} \mathcal{L}^{\alpha\beta} &= 2Tr[\not{p}_\mu \gamma^\alpha \not{p}_\nu \gamma^\beta + m\gamma^\alpha \not{p}_\nu \gamma^\beta + \not{p}_\mu \gamma^\alpha \not{p}_\nu \gamma_5 \gamma^\beta - m\gamma^\alpha \not{p}_\nu \gamma_5 \gamma^\beta] \\ &= 2Tr[\not{p}_\mu \gamma^\alpha \not{p}_\nu \gamma^\beta + \not{p}_\mu \gamma^\alpha \not{p}_\nu \gamma_5 \gamma^\beta]. \end{aligned} \tag{3.19}$$

Using the trace technology:

$$Tr[\not{p}_\mu \gamma^\alpha \not{p}_\nu \gamma^\beta] = 4p_\mu^\alpha p_\nu^\beta - 4p_\mu \cdot p_\nu g^{\alpha\beta} + 4p_\mu^\beta p_\nu^\alpha \tag{3.20}$$

$$Tr[\not{p}_\mu \gamma^\alpha \not{p}_\nu \gamma_5 \gamma^\beta] = -i\epsilon^{l\alpha m\beta}(p_\mu)_l (p_\nu)_m. \tag{3.21}$$

The indices $\alpha\beta\gamma\delta$ are four momentum indices and are summed over. For small lepton masses ($m_\mu \to 0$), it can be shown that $p_\nu \cdot p_\mu$ approaches $\frac{Q^2}{2}$.

Taking the limit $Q^2 \to 0$ then causes the term $p_\nu \cdot p_\mu$ to vanish. From the equality $p_\nu \cdot p_\mu = E_\nu E_\mu(1 - \cos\theta)$, again assuming negligible lepton masses, it is obvious that the limit $Q^2 \to 0$ refers to the case where the neutrino and muon direction are parallel. In this limit the four momenta can be written $p_\nu = |E_\nu/\nu|q$ and $p_\mu = |E_\mu/\nu|q$, and the lepton tensor becomes:

$$\mathcal{L}^{\alpha\beta} = 16\frac{E_\nu E_\mu}{\nu^2}q^\alpha q^\beta. \tag{3.22}$$

Using this tensor, the amplitude can be expressed in terms of the derivative of the hadronic weak currents. As the vector current is conserved (CVC), the derivative of the vector current $\partial^\alpha V_\alpha$ vanishes and only the derivative of the axial vector current remains. Hence the aforementioned conclusion that the axial vector current dominates at very low Q^2.

$$\mathcal{M}^2 = 8G^2\frac{E_\nu E_\mu}{\nu^2}|\partial^\alpha A_\alpha|^2. \tag{3.23}$$

In 1960 Goldberger and Treiman used the possibility of almost conserving the axial vector current (in the limit of massless pions), by introducing a pseudoscalar current, to predict the rate of pion decay. This result in an expression for the axial -vector form factor, commonly known as the Goldberger-Treiman relation.

$$(M_p + M_n)g_1(0) = \sqrt{2}f_\pi g_{\pi N}. \tag{3.24}$$

Here M_p and M_n are the masses of the proton and neutron, f_π is the pion decay constant, and $g_{\pi N}$ is the pion-nucleon coupling constant.

This leads to another statement of the PCAC (partially conserved axial current) hypothesis, first proposed by Gell-Mann and Levy in 1960:

$$\partial^\alpha A_\alpha = f_\pi M_\pi^2 \phi_\pi. \tag{3.25}$$

where ϕ_π is the pion field. Now let's go into some details of the PCAC hypothesis. First, we have

$$\begin{aligned} < 0|A^\mu(x)|\pi(p^\nu) > &= < 0|\exp(i\hat{P}\cdot x)A^\mu(0)\exp(-i\hat{P}\cdot x)|\pi(p^\nu) > \\ < 0|\partial_\mu A^\mu(x)|\pi(p^\nu) > &= \partial_\mu < 0|A^\mu(x)|\pi(p^\nu) > \\ &= \partial_\mu < 0|\exp(i\hat{P}\cdot x)A^\mu(0)\exp(-i\hat{P}\cdot x)|\pi(p^\nu) > \\ &= \partial_\mu < 0|A^\mu(0)|\pi(p^\nu) > \exp(-iP\cdot x) \\ &= -iP_\mu < 0|A^\mu(0)|\pi(p^\nu) > \exp(-iP\cdot x). \end{aligned} \tag{3.26}$$

Since $< 0|A^\mu(0)|\pi(p^\nu) >$ is an axial vector function of p_μ, it can be written as

$$< 0|A^\mu(0)|\pi(p^\nu) >= if_\pi p^\mu, \tag{3.27}$$

where f_π is the pion decay constant. So

$$\begin{aligned} < 0|\partial_\mu A^\mu(x)|\pi(p^\nu) > &= p_\mu \cdot p^\mu f_\pi \exp(-iP\cdot x) \\ &= m_\pi^2 f_\pi < 0|\phi_\pi(x)|\pi(p^\nu) > . \end{aligned} \tag{3.28}$$

This equation shows that PCAC is exact on the pion mass shell, while off the pion mass shell, it is assumed that the operator equation 3.25 still holds.

With CVC and PCAC, and neglecting the mass of the leading lepton (muon), now we can deal with the matrix element, which is $< \mathcal{B}|\partial_\alpha A^\alpha|\mathcal{A} >$, where $\mathcal{A}$ and $\mathcal{B}$ represent initial and final nucleon respectively.

Using Equation (3.25), we have

$$\begin{aligned} < \mathcal{B}|\partial_\mu A^\mu|\mathcal{A} > &= < \mathcal{B}|f_\pi m_\pi^2 \phi_\pi|\mathcal{A} > \\ &= f_\pi m_\pi^2 < \mathcal{B}|\phi_\pi|\mathcal{A} > . \end{aligned} \tag{3.29}$$

The transition matrix element $< \mathcal{B}|\phi_\pi|\mathcal{A} >$ has a pole at the $q^2 = m_\pi^2$ and its residue is just the amplitude of the scattering $< \mathcal{A} + \pi \to \mathcal{B} >$. So it is reasonable to assume

$$< \mathcal{B}|\partial_\mu A^\mu|\mathcal{A} > = f_\pi \frac{m_\pi^2}{Q^2 + m_\pi^2} < \mathcal{A} + \pi \to \mathcal{B} > \tag{3.30}$$

at the low energy region $0 \lesssim q^2 \lesssim m_\pi^2$. Precisely, there are also other pole contributions from other particles [16], and considering them leads to an extension of PCAC.

In the limit of $Q^2 \to 0$, the result given above leads us to (Note that $i\partial^\alpha \leftrightarrow q^\alpha$)

$$\begin{aligned} q_\alpha A^{\alpha\beta} q_\beta &= q_\alpha < A^\alpha >< A^\beta >^* q_\beta \\ &= f_\pi < \mathcal{B}|\mathcal{A} + \pi > f_\pi < \mathcal{B}|\mathcal{A} + \pi > \\ &= f_\pi^2 |\mathcal{M}(\mathcal{A} + \pi \to \mathcal{B})|^2. \end{aligned} \tag{3.31}$$

Inserting Equation (3.31) into Equation (3.23) gives:

$$|\mathcal{M}|^2 = 8G_F^2 \frac{E_\nu E_\mu}{\nu^2} f_\pi^2 |\mathcal{M}(\mathcal{A} + \pi \to \mathcal{B})|^2. \tag{3.32}$$

Then we have

$$\begin{aligned} d\sigma(\nu + \mathcal{A} \to \mu + \mathcal{B}) &= 8G_F^2 \frac{E_\nu E_\mu}{4E_\nu M_N \nu^2} f_\pi^2 | < \mathcal{M}(\mathcal{A} + \pi \to \mathcal{B} >)|^2 \\ &\quad \times (2\pi)^4 \delta^4(p_\nu + p_{Zi} - p_\mu - p_{Zf}) \\ &\quad \times \frac{1}{(2\pi)^3} \frac{d^3 p_\mu}{2E_\mu} \frac{1}{(2\pi)^3} \frac{d^3 p_{Zf}}{2E_{Zf}}. \end{aligned} \tag{3.33}$$

The integrating measure is

$$d^3 p_\mu = |\vec{p_\mu}|^2 dp_\mu d\Omega = |\vec{p_\mu}|^2 dp_\mu 2\pi d\cos\theta. \tag{3.34}$$

For the massless particle $|\vec{p_\mu}| = E_\mu$, $Q^2 = 2E_\nu E_\mu(1 - \cos\theta)$; $dE_\mu = -d\nu$; $dQ^2 = -2E_\nu E_\mu d\cos\theta$. So

$$\begin{aligned} d^3 p_\mu &= E_\mu^2 dE_\mu 2\pi \frac{1}{-2E_\nu E_\mu} dQ^2 \\ &= E_\mu^2 (-d\nu) 2\pi \frac{1}{-2E_\nu E_\mu} dQ^2 \\ &= E_\mu^2 2\pi \frac{1}{-2E_\nu E_\mu} dQ^2 d\nu \\ &= \frac{\pi E_\mu}{E_\nu} dQ^2 d\nu. \end{aligned} \tag{3.35}$$

Now, we can write the scattering amplitude of $|\mathcal{M}(\mathcal{A}+\pi\rightarrow\mathcal{B})|^2$ into the form of cross-sections,

$$\begin{aligned} d\sigma(\mathcal{A}+\pi\rightarrow\mathcal{B}) &= \frac{|\mathcal{M}(\mathcal{A}+\pi\rightarrow\mathcal{B})|^2}{4M_N\nu} \\ &\times(2\pi)^4\delta^4(p_\nu+p_{Zi}-p_\mu-p_{Zf})\frac{1}{(2\pi)^3}\frac{d^3p_{Zf}}{2E_{Zf}}. \end{aligned} \tag{3.36}$$

Then the differential cross-section becomes

$$d\sigma(\nu+\mathcal{A}\rightarrow\mu+\mathcal{B})|_{Q^2\rightarrow 0}=\frac{G_F^2f_\pi^2(1-y)}{2\pi^2\nu}\sigma(\pi+\mathcal{A}\rightarrow\mathcal{B})dQ^2d\nu. \tag{3.37}$$

This expression is known as Adler's theorem, it is valid for the limit $Q^2\rightarrow 0$; it relates the weak neutrino nucleus cross-section to that of the strong pion-nucleus cross-section. In the calculation above, the mass of the lepton muon is neglected. If the lepton mass is not neglected, the leptonic tensor becomes

$$\mathcal{L}_{\mu\nu}=8\{k_\mu k'_\nu+k_\nu k'_\mu+k\cdot k'g_{\mu\nu}\}. \tag{3.38}$$

Because the hadronic tensor is symmetric, the anti-symmetric tensor term in leptonic tensor has no contribution.

It is interesting that the cross-section is not dominated by exchanging the pion meson at $Q^2=0$ under PCAC. To show this, let's write the hadronic current into 2 parts, one of which represents the pionic contribution and the other one represents nonpionic contribution.

$$j^\mu=if_\pi\frac{q^\mu}{Q^2+m_\pi^2}\mathcal{M}(\alpha+\pi\rightarrow\beta)+j'^\mu. \tag{3.39}$$

$$j^{\nu*}=-if_\pi\frac{q^\nu}{Q^2+m_\pi^2}\mathcal{M}^*(\alpha+\pi\rightarrow\beta)+j'^{\nu*}. \tag{3.40}$$

The hadronic tensor becomes

$$\begin{aligned} W^{\mu\nu} &= j^\mu j^{\nu*} \\ &= j'^\mu j'^{\nu*}+j'^\mu\times(-if_\pi\frac{q^\nu}{Q^2+m_\pi^2}\mathcal{M}^*)+j'^{\nu*}\times if_\pi\frac{q^\mu}{Q^2+m_\pi^2}\mathcal{M} \\ &+f_\pi\frac{q^\mu}{Q^2+m_\pi^2}\mathcal{M}\times f_\pi\frac{q^\nu}{Q^2+m_\pi^2}\mathcal{M}^*. \end{aligned} \tag{3.41}$$

$$iq_\mu j^\mu = f_\pi \frac{Q^2}{Q^2 + m_\pi^2} \mathcal{M} + iq_\mu j'^\mu. \tag{3.42}$$

Using the result of PCAC,

$$iq_\mu j^\mu = f_\pi \mathcal{M}(\alpha + \pi \to \beta). \tag{3.43}$$

$$iq_\mu j'^\mu = f_\pi \frac{m_\pi^2}{Q^2 + m_\pi^2} \mathcal{M}. \tag{3.44}$$

Now let's calculate $\sum j'^\mu \mathcal{M}^*$. Assume

$$\sum j'^\mu \mathcal{M}^* = ap^\mu + bq^\mu, \tag{3.45}$$

where a and b are constants.

$$\begin{aligned} iq_\mu \sum j'^\mu \mathcal{M}^* &= iq_\mu (ap^\mu + bq^\mu) \\ &= iap \cdot q + ibq^2. \end{aligned} \tag{3.46}$$

When $Q^2 \approx 0$,

$$\begin{aligned} iq_\mu \sum j'^\mu \mathcal{M}^* &= iq_\mu (ap^\mu + bq^\mu) \\ &= iap \cdot q. \end{aligned} \tag{3.47}$$

Then, we have

$$a = \frac{f_\pi |\mathcal{M}|^2}{ip \cdot q}. \tag{3.48}$$

Combine with the leptonic tensor, and we get the cross-section:

$$\begin{aligned} \frac{d^2\sigma(\nu + A- > \mu + \pi + B)}{dQ^2 d\nu}|_{Q^2 \to 0} &= \frac{G^2 f_\pi^2 (1-y)}{2\pi^2 \nu} \sigma(\pi + \mathcal{A} \to \mathcal{B}) \\ &\times [1 - \frac{\nu}{E'} \frac{m_\mu^2}{Q^2 + m_\pi^2} + \frac{\nu^2}{4EE'} \frac{m_\mu^2 (Q^2 + m_\mu^2)}{(Q^2 + m_\pi^2)^2}]. \end{aligned} \tag{3.49}$$

For the coherent process $\bar{\nu}\mathcal{A} \to \mu^+ \pi^- \mathcal{B}$, the only change is the leptonic tensor:

$$\begin{aligned} \mathcal{L}^{\alpha\beta} &= \mathcal{L}^\alpha \mathcal{L}^{\beta *} \\ &= 8\{p_\nu^\alpha p_\mu^\beta + p_\nu^\beta p_\mu^\alpha - p_\nu \cdot p_\mu g^{\alpha\beta} - i\epsilon^{\alpha\beta\gamma\delta} p_{\nu\gamma} p_{\mu\delta}\}. \end{aligned} \tag{3.50}$$

However, under the assumption of the small Q^2 and leptonic mass ≈ 0, then the leptonic tensor $= 0$. Then we come to the conclusion that the cross-section of the process $\bar{\nu}\mathcal{A} \to \mu^+\pi^-\mathcal{B}$

$$d\sigma(\bar{\nu} + A- > \mu^+ + \pi^- + B)|_{Q^2\to 0} = d\sigma(\nu + A- > \mu^- + \pi^+ + B)|_{Q^2\to 0}. \tag{3.51}$$

For the neutral current (NC) interaction, we have

$$f_{\pi^0} = \frac{f_{\pi^\pm}}{\sqrt{2}}. \tag{3.52}$$

$$\begin{aligned} d\sigma(\nu + \mathcal{A} \to \nu' + \mathcal{A}' + \pi^0) &= G_F^2 \frac{EE'}{4EM\nu^2} 2f_\pi^2 |\mathcal{M}(\mathcal{A} + \pi \to \mathcal{A}'| \\ &\times (2\pi)^4 \delta^4(p + k - p' - k') \\ &\frac{1}{(2\pi)^3}\frac{d^3p'}{2E'}\frac{1}{(2\pi)^3}\frac{d^3k'}{2k'_0}. \end{aligned} \tag{3.53}$$

$$\begin{aligned} d\sigma(\mathcal{A} + \pi \to \mathcal{A}') &= \frac{|\mathcal{M}(\mathcal{A} + \pi \to \mathcal{A}')|^2}{4M_N\nu} \\ &\times (2\pi)^4 \delta^4(p_\nu + p_{Zi} - p_\mu - p_{Zf}) \frac{1}{(2\pi)^3}\frac{d^3p_{Zf}}{2E_{Zf}}. \end{aligned} \tag{3.54}$$

$$d\sigma(\nu + \mathcal{A} \to \nu' + \mathcal{A}' + \pi^0) = \frac{G_F^2 f_\pi^2}{4\pi^3\nu}\sigma(\mathcal{A} + \pi \to \mathcal{A}')d^3p'. \tag{3.55}$$

where $d^3p' = \pi\frac{E'}{E}dQ^2d\nu$. Making a variable change with

$$\begin{aligned} x &= \frac{Q^2}{2M\nu} \\ y &= \frac{\nu}{E}, \end{aligned} \tag{3.56}$$

we have

$$\begin{aligned} dQ^2d\nu &= \begin{vmatrix} \frac{\partial Q^2}{\partial x} & \frac{\partial Q^2}{\partial y} \\ \frac{\partial \nu}{\partial x} & \frac{\partial \nu}{\partial y} \end{vmatrix} \times dxdy \\ &= 2ME\nu dxdy \\ &= 2ME^2 y dxdy, \end{aligned} \tag{3.57}$$

and

$$\begin{aligned} d^3p' &= \pi\frac{E'}{E}2ME^2ydxdy \\ &= 2M\pi E'Eydxdy, \end{aligned} \tag{3.58}$$

so

$$\begin{aligned} d\sigma(\nu+\mathcal{A}\to\nu'+\mathcal{A}'+\pi^0) &= \frac{G_F^2 f_\pi^2}{4\pi^3\nu}d\sigma(\mathcal{A}+\pi\to\mathcal{A}') \qquad (3.59) \\ & \quad 2M\pi E'Eydxdy \\ &= \frac{G_F^2 f_\pi^2 ME}{2\pi^2}\frac{E'y}{\nu}d\sigma(\mathcal{A}+\pi\to\mathcal{A}')dxdy \\ &= \frac{G_F^2 ME}{\pi^2}\frac{1}{2}f_\pi^2(1-y)[d\sigma(\mathcal{A}+\pi\to\mathcal{A}') \\ & \quad \times dxdy]. \qquad (3.60) \end{aligned}$$

In the last equality, we used the formula that $y = \frac{\nu}{E}$, Then, we have:

$$\begin{aligned} [\frac{d\sigma(\nu+\mathcal{A}\to\nu'+\mathcal{A}'+\pi^0)}{dxdydt}]_{Q^2=0} &= \frac{G_F^2 ME}{\pi^2}\frac{1}{2}f_\pi^2(1-y) \\ & \quad \times[\frac{d\sigma(\mathcal{A}+\pi\to\mathcal{A}')}{dt}]. \end{aligned} \tag{3.61}$$

which is consistent with the result given by [37].

3.3 Neutrino Induced Coherent ρ

This section deals with high ν (energy transfer) and low Q^2 (negative of the square of the 4-momentum transfer) production of ρ mesons in neutrino interactions. In the regime of low Q^2 the distances probed are larger than in DIS (deep inelastic scattering). The target nucleon constituents, therefore, cannot be considered as free particles and the perturbative theoretical approach towards strong interactions cannot be applied. Here the theory of VMD (Vector Meson Dominance) applied to weak interactions is used to produce a cross-section for ρ production in the low Q^2 regime. The derivation of this section was created in collaboration with C.T.Kullenberg. We

will link cross-section of the production of coherent ρ mesons by neutrinos ($\nu + \mathcal{A} \rightarrow \mu + \rho + \mathcal{A}$) to the transverse and longitudinal cross-sections of coherent meson scattering ($\rho + \mathcal{A} \rightarrow \rho + \mathcal{A}$).

During this calculation we will assume that the target is at rest in the lab frame, and we will assume that the lepton masses can be ignored.

The square of the scattering amplitude is written as:

$$|\mathcal{M}|^2 = \frac{G_F^2}{2} \mathcal{L}_{\mu\nu} W^{\mu\nu}, \tag{3.62}$$

where $W^{\mu\nu}$ is the hadronic tensor. Experiments are generally blind to particle polarization, so one must average over the initial particle spins and sum over all final particle spin states and momenta. This must be done for both the hadronic and leptonic tensors. One might re-write the square of the amplitude as:

$$< |\mathcal{M}|^2 >= \frac{G_F^2}{2} < \mathcal{L}_{\mu\nu} >< W^{\mu\nu} >, \tag{3.63}$$

where the brackets indicate the initial and final state averaging and summing process. Often, however, the distinction is implied and one continues to use the form in Equation (3.62).

The Hadronic Tensor

Using the hadron dominance assumption we will consider only the contribution of the ρ meson to the hadronic vector current. The calculation of the hadronic tensor will proceed in the normal fashion, but we will ignore the axial vector contribution and we will impose $q_\mu W^{\mu\nu} = 0$ due to CVC (Conservation of Vector Current).

The most general symmetric form of the hadronic tensor is [20]

$$W^{\mu\nu} = W_1 g^{\mu\nu} + W_2 \frac{p^\mu p^\nu}{M^2} + W_4 \frac{q^\mu q^\nu}{M^2} + W_5 \frac{p^\mu q^\nu + q^\mu p^\nu}{M^2}, \tag{3.64}$$

where the coefficients W_i are functions of ν and q^2. We keep only symmetric terms as asymmetric terms arise from the interference of the vector and axial vector currents.

So, from CVC we have:

$$q_\mu W^{\mu\nu} = W_1 q^\nu + W_2 \frac{q\cdot p p^\nu}{M^2} + W_4 \frac{q^2 q^\nu}{M^2} + W_5 \frac{q\cdot p q^\nu + q^2 p^\nu}{M^2} = 0, \tag{3.65}$$

which implies that the factors W_4 and W_5 can be expressed in terms of W_1 and W_2. Looking at functions of p^ν and q^ν separately:

$$\begin{aligned} W_5 &= W_2 \frac{q\cdot p}{Q^2} \\ W_4 &= W_2 \frac{(q\cdot p)^2}{Q^4} + W_1 \frac{M^2}{Q^2}. \end{aligned} \tag{3.66}$$

The hadronic tensor can be written as:

$$W^{\mu\nu} = W_1 \left(g^{\mu\nu} + \frac{q^\mu q^\nu}{Q^2}\right) + \frac{W_2}{M^2}\left(p^\mu + \frac{p\cdot q}{Q^2} q^\mu\right)\left(p^\nu + \frac{p\cdot q}{Q^2} q^\nu\right). \tag{3.67}$$

The ρ dominance hypothesis is implemented by expressing the hadronic current as [42]

$$J^\mu = \frac{f_\rho}{Q^2 + m_\rho^2}\left[g^{\mu\nu} - \frac{q_\mu q^\nu}{m_\rho^2}\right]\mathcal{A}_\nu(\rho + \alpha \to \beta), \tag{3.68}$$

where f_ρ is the coupling constant of the ρ meson to the W boson and $\epsilon_\mu^{(i)} A^\mu$ represents the amplitude of a ρ meson with polarization $\epsilon^{(i)}$. We can write the hadronic tensor as a product of the J^μ currents.

$$\begin{aligned} W^{\mu\nu} &= J^\mu J^{\nu *} \\ &= \left(\frac{f_\rho}{Q^2 + m_\rho^2}\right)^2 \left(\left[g^{\mu\sigma} - \frac{q_\mu q^\sigma}{m_\rho^2}\right]\mathcal{A}_\sigma(\rho + \alpha \to \beta)\right) \\ &\qquad \times \left(\left[g^{\nu\omega} - \frac{q_\nu q^\omega}{m_\rho^2}\right]\mathcal{A}_\omega(\rho + \alpha \to \beta)\right)^*. \end{aligned} \tag{3.69}$$

By conservation of isospin current we have $q^\mu \mathcal{A}_\mu = 0$, so the q factors disappear giving us simply:

$$W^{\mu\nu} = C_\rho^2 M^{\mu\nu}, \tag{3.70}$$

where we have defined:

$$\begin{aligned} M^{\mu\nu} &= \mathcal{A}^\mu \mathcal{A}^{\nu *} \\ C_\rho &= \left(\frac{f_\rho}{Q^2 + m_\rho^2}\right). \end{aligned} \tag{3.71}$$

$M^{\mu\nu}$ must undergo the usual averaging and summing of states.

Linking W_1 and W_2 to σ_T and σ_L

We have written $W^{\mu\nu}$ in terms of the unknown coefficients W_1 and W_2, and we have also shown $W^{\mu\nu}$ to be proportional to $M^{\mu\nu}$. We would like to express $W^{\mu\nu}$ in terms of the transverse (σ_T) and longitudinal (σ_L) polarized cross-sections of the incident ρ meson. We can accomplish this if we use the following definitions from [20] and [50]:

$$\begin{aligned} \sigma_T &= \sigma_T(\rho + \alpha \to \beta) = \frac{1}{|\vec{q}|}\epsilon_\mu^{*T} M^{\mu\nu} \epsilon_\nu^T \\ \sigma_L &= \sigma_L(\rho + \alpha \to \beta) = \frac{1}{|\vec{q}|}\epsilon_\mu^{*L} M^{\mu\nu} \epsilon_\nu^L. \end{aligned} \tag{3.72}$$

It should be noted here that these definitions do not include integration over final momenta, which must be done eventually. We will also need the explicit form of the polarization vectors given here [20].

$$\epsilon^T = \mp\frac{1}{\sqrt{2}}\begin{pmatrix} 0 \\ 1 \\ \pm i \\ 0 \end{pmatrix} \qquad \epsilon^L = \frac{1}{\sqrt{Q^2}}\begin{pmatrix} |\vec{q}| \\ 0 \\ 0 \\ \nu \end{pmatrix}. \tag{3.73}$$

Massive vector bosons have three possible polarization vectors (two transverse and one longitudinal). In our calculations we will make use of $\epsilon_\mu^* \epsilon^\mu$, which has the same value for both transverse polarizations. It, therefore, doesn't matter which one we choose when we use ϵ^T.

Now from Equation (3.70) we see that $M^{\mu\nu} = \frac{1}{C_\rho^2} W^{\mu\nu}$, and looking at Equation (3.67) we can write it very simply:

$$M^{\mu\nu} = \frac{1}{C_\rho^2}\left[W_1 \mathcal{F}_1 + W_2 \mathcal{F}_2\right], \tag{3.74}$$

where, for economy of space, we have made functions $\mathcal{F}_1$ and $\mathcal{F}_2$:

$$\begin{aligned} \mathcal{F}_1 &= \left(g^{\mu\nu} + \frac{q^\mu q^\nu}{Q^2}\right) \\ \mathcal{F}_2 &= \frac{1}{M^2}\left(p^\mu + \frac{p\cdot q}{Q^2} q^\mu\right)\left(p^\nu + \frac{p\cdot q}{Q^2} q^\nu\right). \end{aligned} \tag{3.75}$$

Now putting our new form of $M^{\mu\nu}$ into σ_T and σ_L:

$$\begin{aligned}\sigma_T &= \frac{1}{C_\rho^2|\vec{q}|}\epsilon_\mu^{*T}(W_1\mathcal{F}_1 + W_2\mathcal{F}_2)\epsilon_\nu^T \\ \sigma_L &= \frac{1}{C_\rho^2|\vec{q}|}\epsilon_\mu^{*L}(W_1\mathcal{F}_1 + W_2\mathcal{F}_2)\epsilon_\nu^L. \end{aligned} \tag{3.76}$$

Or we might make a few simple definitions to clean it up a bit:

$$\begin{aligned}\sigma_T &= \frac{1}{C_\rho^2|\vec{q}|}(W_1A_T + W_2B_T) \\ \sigma_L &= \frac{1}{C_\rho^2|\vec{q}|}(W_1A_L + W_2B_L). \end{aligned} \tag{3.77}$$

At this point one need only calculate A_T, B_T, A_L and B_L, which are just contractions of the polarization vectors with the functions $\mathcal{F}_1$ and $\mathcal{F}_2$, in order to express W_1 and W_2 in terms of σ_T and σ_L.

By noting that $q^\nu\epsilon_\nu = 0$ (due to gauge invariance), $p = \Big(M, 0, 0, 0\Big)$ because the target is at rest and using the explicit form of the polarization vectors in Equation (3.73) it is easily shown that:

$$\begin{aligned} A_T = \epsilon_\mu^{*T}\mathcal{F}_1\epsilon_\nu^T &= -1 \\ B_T = \epsilon_\mu^{*T}\mathcal{F}_2\epsilon_\nu^T &= 0 \\ A_L = \epsilon_\mu^{*L}\mathcal{F}_1\epsilon_\nu^L &= 1 \\ B_L = \epsilon_\mu^{*L}\mathcal{F}_2\epsilon_\nu^L &= \frac{|\vec{q}|^2}{Q^2}. \end{aligned} \tag{3.78}$$

Putting these back into Equation (3.77) and solving for W_1 and W_2 gives us the relationships that we've been looking for.

$$\begin{aligned} W_1 &= -C_\rho^2|\vec{q}|\sigma_T \\ W_2 &= \frac{C_\rho^2Q^2}{|\vec{q}|}\left(\sigma_T + \sigma_L\right). \end{aligned} \tag{3.79}$$

We can put this form of W_1 and W_2 into our expression for the hadronic tensor $W^{\mu\nu}$

in Equation Equation (3.67).

$$W^{\mu\nu} = \left(\frac{f_\rho}{Q^2+m_\rho^2}\right)^2\Bigg[-|\vec{q}|\sigma_T\left(g^{\mu\nu}+\frac{q^\mu q^\nu}{Q^2}\right) + \frac{Q^2(\sigma_T+\sigma_L)}{|\vec{q}|M^2}\left(p^\mu+\frac{p\cdot q}{Q^2}q^\mu\right)\left(p^\nu+\frac{p\cdot q}{Q^2}q^\nu\right)\Bigg]. \tag{3.80}$$

Calculating $|\mathcal{M}|^2$

Now that we have the Hadronic and Leptonic tensors in a useable form we can put them into the equation for the square of the scattering amplitude Equation (3.62).

To simplify a bit we will rewrite Equation (3.80) using the definitions we made in Equation (3.71) and Equation (3.75).

$$W^{\mu\nu} = |\vec{q}|f_\rho^2\left[-\sigma_T\mathcal{F}_1+\frac{Q^2}{|\vec{q}|^2}(\sigma_T+\sigma_L)\mathcal{F}_2\right]. \tag{3.81}$$

Putting this into $|\mathcal{M}|^2$:

$$|\mathcal{M}|^2 = 4|\vec{q}|G_F^2C_\rho^2\Big[-\sigma_T(T_1+T_2-T_3) + \frac{Q^2}{|\vec{q}|^2}(\sigma_T+\sigma_L)(T_4+T_5-T_6)\Big]. \tag{3.82}$$

Were we need to calculate the six T_i terms:

$$T_1=\left(k'_\mu k_\nu\mathcal{F}_1\right)\quad T_2=\left(k_\mu k'_\nu\mathcal{F}_1\right)\quad T_3=\left(k\cdot k' g_{\mu\nu}\mathcal{F}_1\right)$$

$$T_4=\left(k'_\mu k_\nu\mathcal{F}_2\right)\quad T_5=\left(k_\mu k'_\nu\mathcal{F}_2\right)\quad T_6=\left(k\cdot k' g_{\mu\nu}\mathcal{F}_2\right) \tag{3.83}$$

To do this we will use:

$$k\cdot k'\approx\frac{Q^2}{2}\qquad (m_l\to 0) \tag{3.84}$$

which will give us the following for the first three terms:

$$T_1+T_2-T_3=\left(2\frac{(k\cdot q)(k'\cdot q)}{Q^2}-k\cdot k'\right)\approx -Q^2. \tag{3.85}$$

For the second set of three terms we will simplify with the following relations that are valid when the target is at rest:

$$p^2 = M^2 \qquad p \cdot q = M\nu$$
$$p \cdot k = ME \qquad p \cdot k' = ME'. \tag{3.86}$$

This will give us:

$$(T_4 + T_5 - T_6) = \frac{1}{2}\left(4EE' - Q^2\right). \tag{3.87}$$

Putting Equation (3.85) and Equation (3.87) into Equation (3.82) we can write the square of the scattering amplitude.

$$|\mathcal{M}|^2 = 4G_F^2|\vec{q}|f_\rho^2\frac{Q^2}{(Q^2+m_\rho^2)^2}\left[\sigma_T + \frac{(\sigma_T+\sigma_L)}{2|\vec{q}|^2}\left(4EE' - Q^2\right)\right]. \tag{3.88}$$

Calculating the Cross-Section

The differential cross-section is given by [41].

$$d\sigma = \frac{|\mathcal{M}|^2}{2E_A 2E_B \mathcal{U}_{AB}}\left(\prod_f \frac{d^3p_f}{(2\pi)^3}\frac{1}{2E_f}\right)(2\pi)^4\delta^4(p_A + p_B - \mathbf{\Sigma}p_f), \tag{3.89}$$

where A and B are the initial particles, p_f[s] are final state particle four-momenta, and $\mathcal{U}_{AB}$ is the relative velocity between A and B in the laboratory frame, which in this case is unity because the neutrino effectively moves at the speed of light and the target is at rest.

Here we are considering two final state "particles", the outgoing lepton and the final hadronic state. So the differential cross-section can be written as:

$$d\sigma = \frac{|\mathcal{M}|^2}{2E2M}\left(\frac{d^3k'}{(2\pi)^3}\frac{1}{2E'}\right)\left(\frac{d^3p'}{(2\pi)^3}\frac{1}{2p'_0}\right)(2\pi)^4\delta^4(k + p - k' - p'). \tag{3.90}$$

Integrating Over p' for σ_T and σ_L

At this point we need to expose some slightly ambiguous notation that we have been using for the ρ transverse and longitudinal cross-sections. We will deal here with σ_T, but these arguments apply equally well to σ_L .

We have so far defined the transverse cross-section as:

$$\sigma_T^0 = \frac{1}{|\vec{q}|}\epsilon_\mu^{*T} M^{\mu\nu} \epsilon_\nu^T = \frac{1}{|\vec{q}|}|\epsilon_\mu^T A^\mu|^2$$

We can think of this as the amplitude squared for the process $(\rho + \alpha \rightarrow \beta)$, normalized by the inverse of the ρ momentum. For now we have renamed the original definition as σ_T^0 . To transform it into an actual cross-section we must integrate over the final momenta.

We can use Equation (3.89) with the amplitude we have and note that the velocity of the ρ in the lab frame is $\frac{|\vec{q}|}{\nu}$ (in general $p = \gamma m v = Ev \Rightarrow v = \frac{p}{E}$), and because the target is at rest we have:

$$\mathcal{U}_{AB} = \frac{|\vec{q}|}{\nu}. \tag{3.91}$$

So we can write the true cross-section σ_T as:

$$\begin{aligned}
\sigma_T &= \int \frac{|\epsilon_\mu^T A^\mu|^2}{2\nu 2M(\frac{|\vec{q}|}{\nu})} \left(\frac{d^3p'}{(2\pi)^3}\frac{1}{2p_0'}\right)(2\pi)^4\ \delta^4(q+p-p') \\
&= \int \frac{|\epsilon_\mu^T A^\mu|^2}{2|\vec{q}|2M} \left(\frac{d^3p'}{2p_0'}\right)(2\pi)\ \delta(\nu + M - p_0')\ \delta^3(\vec{q}+\vec{p}-\vec{p}') \\
&= \left(\frac{|\epsilon_\mu^T A^\mu|^2}{|\vec{q}|}\right)\frac{\pi}{2p_0' 2M}\ \delta(\nu + M - p_0') \\
&= \left(\frac{\pi}{4Mp_0'}\ \delta(\nu + M - p_0')\right)\sigma_T^0.
\end{aligned} \tag{3.92}$$

We can see that if we multiply the original definition of σ_T^0 by the factor $(\frac{\pi}{4Mp_0'}\delta(\nu + m - p_0'))$ then we obtain the full cross-section σ_T, which has been integrated over the final momenta. This is identically true for the longitudinal ρ cross-section σ_L. And because $|\mathcal{M}|^2$ is linearly proportional to σ_T^0 and σ_L^0 we might modify $|\mathcal{M}|^2$ itself by this same factor, absorbing it and simply stating that we have performed the momentum integration for σ_T and σ_L . So we can write:

$$|\mathcal{M}|^2 \left(\frac{\pi}{4Mp_0'}\ \delta(\nu + M - p_0')\right) \xrightarrow[\sigma_L \text{ over } p']{\text{Integrate } \sigma_T \text{ and}} |\mathcal{M}|^2. \tag{3.93}$$

If we are presented with this factor then we will absorb it into $|\mathcal{M}|^2$ and make reference to this rule.

Integrating Over p' for $d\sigma$

We will now return, after our digression, to Equation Equation (3.90). We must integrate over the final momenta.

$$\begin{aligned} d\sigma &= \int_{p'} \frac{|\mathcal{M}|^2}{2E2M}\left(\frac{d^3k'}{(2\pi)^3}\frac{1}{2E'}\right)\left(\frac{d^3p'}{(2\pi)^3}\frac{1}{2p'_0}\right)(2\pi)^4\,\delta^4(k+p-k'-p') \\ &= \frac{|\mathcal{M}|^2}{2E2M}\left(\frac{d^3k'}{(2\pi)^3}\frac{1}{2E'}\right)\left(\frac{1}{(2\pi)^3}\frac{1}{2p'_0}\right)(2\pi)^4\,\delta(E+M-E'-p'_0) \\ &= |\mathcal{M}|^2\left(\frac{\pi}{4Mp'_0}\delta(\nu+M-p'_0)\right)\left(\frac{d^3k'}{(2\pi)^3}\frac{1}{2EE'}\right). \end{aligned} \tag{3.94}$$

Here we will invoke our rule Equation (3.93) and absorb the middle term into $|\mathcal{M}|^2$ giving us:

$$d\sigma = |\mathcal{M}|^2\left(\frac{d^3k'}{(2\pi)^3}\frac{1}{2EE'}\right). \tag{3.95}$$

$d\sigma$ in Terms of dQ^2 and $d\nu$

We would now like to express $d\sigma$ in terms of dQ^2 and $d\nu$ rather than d^3k'. Let's first look at dQ^2. When ignoring the lepton masses we have from Equation (3.3) $Q^2 \approx 2EE'(1-\cos\theta)$. For it's derivative we have:

$$dQ^2 = \left(\frac{\partial Q^2}{\partial\theta}\right)d\theta + \left(\frac{\partial Q^2}{\partial E'}\right)dE' + \left(\frac{\partial Q^2}{\partial E}\right)dE. \tag{3.96}$$

We will not integrate over the initial momentum (or energy for $m=0$), therefore $dE \to 0$ leaving us with:

$$dQ^2 = \left(\frac{\partial Q^2}{\partial\theta}\right)d\theta + \left(\frac{\partial Q^2}{\partial E'}\right)dE'. \tag{3.97}$$

Now for $d\nu$ we simply have $d\nu = d(E-E') = dE - dE' \to d\nu = -dE'$. The minus sign seems troublesome, but it is a simple matter of changing the integration limits.

$$\int_0^E dE' = -\int_E^0 d\nu = \int_0^E d\nu. \tag{3.98}$$

When the outgoing lepton has zero energy, the full energy E has been transferred to the hadronic system. We will absorb the minus sign into $d\nu$ and integrate from

zero momentum transfer to full energy transfer (which one might normally expect). So $dE' \to d\nu$, and if we multiply dQ^2 by this we have:

$$dQ^2 d\nu = \left(\frac{\partial Q^2}{\partial \theta}\right) d\theta dE' + \left(\frac{\partial Q^2}{\partial E'}\right) (dE')^2. \tag{3.99}$$

We will not integrate twice over the final momenta, so $(dE')^2 \to 0$ and we finally have:

$$\begin{aligned} dQ^2 d\nu &= \left(\frac{\partial Q^2}{\partial \theta}\right) d\theta dE' \\ &= (2EE' \sin\theta)\, d\theta dE'. \end{aligned} \tag{3.100}$$

For d^3k' we have:

$$\begin{aligned} d^3k' &= |\vec{k}'|^2 d|\vec{k}'| d\Omega \approx E'^2 dE' d\Omega \\ &= 2\pi E'^2 dE' \sin\theta d\theta. \end{aligned} \tag{3.101}$$

Putting the above two equations together we can relate d^3k' to $dQ^2 d\nu$.

$$d^3k' = \pi \frac{E'}{E} dQ^2 d\nu. \tag{3.102}$$

After inserting this into Equation (3.95) we have a new form for our cross-section.

$$d\sigma = |\mathcal{M}|^2 \left(\frac{dQ^2 d\nu}{16\pi^2 E^2}\right). \tag{3.103}$$

Final Cross-Section

Simply inserting our $|\mathcal{M}|^2$ from Equation (3.88) into Equation (3.103) gives us the following:

$$\begin{aligned} \frac{d^2\sigma(\nu\alpha \to \mu\beta)}{dQ^2 d\nu} &= \frac{G_F^2 |\vec{q}|}{4\pi^2 E^2} f_\rho^2 \frac{Q^2}{(Q^2 + m_\rho^2)^2} \\ &\times \left[\sigma_T + \frac{(\sigma_T + \sigma_L)}{2|\vec{q}|^2}\left(4EE' - Q^2\right)\right]. \end{aligned} \tag{3.104}$$

We are basically done here, but one might also make a couple of definitions to write this in another way.

$$\epsilon = \frac{4EE' - Q^2}{4EE' + Q^2 + 2\nu^2}. \tag{3.105}$$

$$R = \frac{d\sigma_L/dt}{d\sigma_T/dt}. \tag{3.106}$$

Then we can modify the term in brackets and write the cross-section in its final form.

$$\begin{aligned}\frac{d^3\sigma(\nu_\mu \mathcal{A} \to \mu^- \rho^+ \mathcal{A})}{dQ^2 d\nu dt} &= \frac{G_F^2}{4\pi^2} f_\rho^2 \frac{|\vec{q}|}{E^2} \left(\frac{Q}{Q^2 + m_\rho^2}\right)^2 \left(\frac{1+\epsilon R}{1-\epsilon}\right) \\ &\times \left[\frac{d\sigma_T(\rho^+ \mathcal{A} \to \rho^+ \mathcal{A})}{dt}\right].\end{aligned} \tag{3.107}$$

For the anti-neutrino process $\bar{\nu}\mathcal{A} \to \mu^+ \rho^- \mathcal{A}$ we have the same coupling constant between the ρ^- and the W boson.

$$f_\rho^+ = f_\rho^-. \tag{3.108}$$

For the anti-particle process the leptonic tensor is different only in the sign of the anti-symmetric term [50].

$$< L^{\mu\nu} >_{\bar{\nu}} = 8\Big(k^\mu k'^\nu + k^\nu k'^\mu - k \cdot k' g^{\mu\nu} - i\epsilon^{\mu\nu\sigma\lambda} k_\lambda k'_\sigma\Big). \tag{3.109}$$

Because the leptonic tensor contracts with the hadronic tensor, and the hadronic tensor is symmetric, the anti-symmetric term must vanish. Therefore the leptonic tensor is the same, the hadronic tensor is unchanged, and we might then conclude that the cross-sections of the neutrino and anti-neutrino processes are equal.

$$\sigma(\bar{\nu}\mathcal{A} \to \mu^+ \rho^- \mathcal{A}) \;=\; \sigma(\nu\mathcal{A} \to \mu^- \rho^+ \mathcal{A}). \tag{3.110}$$

3.4 Cross-section of Coherent ρ^0

In section 10.6 of Griffiths' book [34] one can find information regarding the neutral weak interactions. I will list some basic information from that resource here.

$$\begin{aligned} -\frac{ig_W}{2\sqrt{2}}\gamma^\mu\left(1-\gamma^5\right) \qquad & W^\pm \text{ vertex} \\ -\frac{ig_Z}{2}\gamma^\mu\left(C_V^f - C_A^f\gamma^5\right) \qquad & Z^0 \text{ vertex,}\end{aligned} \tag{3.111}$$

Table 3.1: Table of vector and axial vector couplings.

f	C_V	C_A
ν_e, ν_μ, ν_τ	$\frac{1}{2}$	$\frac{1}{2}$
e^-, μ^-, τ^-	$-\frac{1}{2}+2\sin\theta_W$	$-\frac{1}{2}$
u, c, t	$\frac{1}{2}-\frac{4}{3}\sin^2\theta_W$	$\frac{1}{2}$
d, s, b	$-\frac{1}{2}+\frac{2}{3}\sin^2\theta_W$	$-\frac{1}{2}$

where, in the GWS model, all parameters are determined by the weak mixing angle θ_W, which must itself be measured from experiment as we currently have no method to calculate it. A reasonable measure for the angle is $\theta_W = 28.7^o$, or $\sin^2\theta_W = 0.23$. g_W and g_Z are related to the electromagnetic coupling constant g_e.

$$g_W = \frac{g_e}{\sin\theta_W} \qquad g_Z = \frac{g_e}{\sin\theta_W\cos\theta_W}. \tag{3.112}$$

The GWS vector and axial vector couplings can be gotten from Table 10.1 in [34], shown here in Table 3.1.

Additionally, the W and Z masses are related in a simple way.

$$M_W = M_Z\cos\theta_W. \tag{3.113}$$

For the charged current amplitude, we have:

$$\begin{aligned}
\mathcal{M}_W &= <\rho^+|\bar{u}\left[-i\frac{g}{\sqrt{2}}\gamma^\mu\frac{1}{2}\left(1-\gamma^5\right)V_{ud}\right]\bar{d}|0> \frac{-1}{M_W^2}\bar{u}_\mu\left[-i\frac{g}{\sqrt{2}}\gamma_\alpha\frac{1}{2}\left(1-\gamma^5\right)\right]u_{\nu_\mu}\times \\
&\quad \times A(\rho^+\mathcal{A}\to\rho^+\mathcal{A}) \\
&= V_{ud}\frac{g^2}{8M_W^2} <\rho^+|\bar{u}\gamma^\alpha\bar{d}|0> \bar{u}_\mu\gamma_\alpha(1-\gamma^5)u_{\nu_\mu}A \\
&= \frac{G_F}{\sqrt{2}}V_{ud}M_{\rho^+}f_{\rho^+}\epsilon^\alpha_{\rho^+}\bar{u}_\mu\gamma_\alpha(1-\gamma^5)u_{\nu_\mu}A.
\end{aligned} \tag{3.114}$$

While for the neutral current we have (because $\rho^0 = \frac{1}{\sqrt{2}}(u\bar{u} - d\bar{d})$):

$$\begin{aligned}
\mathcal{M}_Z &= \frac{1}{\sqrt{2}}\Bigg\{\frac{ig}{\cos\theta_W} < \rho^0|\bar{u}\gamma^\alpha\left[\frac{1}{4} - \frac{2}{3}\sin^2\theta_W - \frac{1}{4}\gamma^5\right]u|0> \; + \\
&\quad + \frac{ig}{\cos\theta_W} < \rho^0|\bar{d}\gamma^\alpha\left[-\frac{1}{4} + \frac{1}{3}\sin^2\theta_W + \frac{1}{4}\gamma^5\right]d|0> \Bigg\} \times \\
&\quad \times \frac{1}{M_Z^2}\bar{u}_{\nu_\mu}\left[\frac{-ig}{\cos\theta_W}\gamma_\alpha\left(\frac{1}{4} - \frac{1}{4}\gamma^5\right)\right]u_{\nu_\mu} A(\rho^0\mathcal{A} \to \rho^0\mathcal{A}) \\
&= \frac{1}{\sqrt{2}}\Bigg\{\frac{-ig}{\cos\theta_W}\left(\frac{1}{4} - \frac{2}{3}\sin^2\theta_W\right) < \rho^0|\bar{u}\gamma^\alpha u|0> \; + \\
&\quad + \frac{ig}{\cos\theta_W}\left(-\frac{1}{4} + \frac{1}{3}\sin^2\theta_W\right) < \rho^0|\bar{d}\gamma^\alpha d|0> \Bigg\} \; \times \\
&\quad \times \frac{-1}{M_Z^2}\bar{u}_{\nu_\mu}\left[\frac{-ig}{\cos\theta_W}\gamma^\alpha\left(\frac{1}{4} - \frac{1}{4}\gamma^5\right)\right]u_{\nu_\mu} A \\
&= \frac{1}{\sqrt{2}}\frac{-ig}{\cos\theta_W}\left(\frac{1}{2} - \sin^2\theta_W\right)M_{\rho^0} f_{\rho^0}\epsilon^\alpha_{\rho^0}\frac{-1}{M_Z^2}\left(\frac{-ig}{\cos\theta_W}\frac{1}{4}\right)\bar{u}_{\nu_\mu}\gamma^\alpha(1-\gamma^5)u_{\nu_\mu} A \\
&= \frac{g^2}{8\sqrt{2}M_Z^2\cos^2\theta_W}\left(1 - 2\sin^2\theta_W\right)M_{\rho^0} f_{\rho^0}\epsilon^\alpha_{\rho^0}\bar{u}_{\nu_\mu}\gamma^\alpha(1-\gamma^5)u_{\nu_\mu} A \\
&= \frac{g^2}{8\sqrt{2}M_W^2}\left(1 - 2\sin^2\theta_W\right)M_{\rho^0} f_{\rho^0}\epsilon^\alpha_{\rho^0}\bar{u}_{\nu_\mu}\gamma^\alpha(1-\gamma^5)u_{\nu_\mu} A \\
&= \frac{G_F}{2}\left(1 - 2\sin^2\theta_W\right)M_{\rho^0} f_{\rho^0}\epsilon^\alpha_{\rho^0}\bar{u}_{\nu_\mu}\gamma^\alpha(1-\gamma^5)u_{\nu_\mu} A, \qquad (3.115)
\end{aligned}$$

where $f_{\rho^0} \approx f_{\rho^+}$, $V_{ud} = 1$, isospin conservation gives $M_{\rho^0} = M_{\rho^+}$ and we use the high energy approximation $M_\mu = M_\nu = 0$.

So we can see that for coherent ρ^0:

$$\mathcal{M}(\nu_\mu\mathcal{A} \to \nu_\mu\rho^0\mathcal{A}) = \frac{1}{\sqrt{2}}(1 - 2\sin^2\theta_W)\mathcal{M}(\nu_\mu\mathcal{A} \to \mu^-\rho^+\mathcal{A}), \qquad (3.116)$$

and the coherent ρ^0 cross-section can be written as

$$\frac{d^3\sigma(\nu_\mu\mathcal{A} \to \nu_\mu\rho^0\mathcal{A})}{dQ^2 d\nu dt} = \frac{1}{2}(1 - 2\sin^2\theta_W)^2\frac{d^3\sigma(\nu_\mu\mathcal{A} \to \mu^-\rho^+\mathcal{A})}{dQ^2 d\nu dt}. \qquad (3.117)$$

Chapter 4

The Neutrino Oscillation Magnetic Detector (NOMAD) experiment

4.1 The NOMAD Neutrino Beam

The NOMAD experiment is designed to search for $\nu_\mu \to \nu_\tau$ and $\nu_\mu \to \nu_e$ oscillations in a predominantly ν_μ beam at CERN. Figure 4.1 shows the predicted distributions of neutrino and anti-neutrino flux. The neutrino beam in NOMAD, with a 25 GeV average energy, was produced from the in-flight decays of the secondary mesons, such as $\pi^\pm$, $K^\pm$, K^0. The mesons originated from the 450 GeV protons from the Super Proton Synchrotron (SPS) incident on a beryllium target (made of 11 rods 10 cm long and 2 mm in diameter each separated by 9 cm gaps). The secondary pions and kaons were focused by a pair of coaxial magnetic lenses: a horn and a reflector (shown in Figure 4.2). In this system, charged particles were deflected by the toroidal field between two coaxial conductors carrying equal and opposite currents so that the focusing of particles of one sign implied defocusing particles of the opposite sign. Collimators reduced the anti-neutrinos contamination by intercepting the defocused secondaries. The mesons were allowed to decay within a 290 m long evacuated decay pipe. Shielding made from iron and earth followed which was used to range out muons and absorb hadrons. The average neutrino flight path to the NOMAD detector was 628 m, the detector being 836 m downstream of the Be-target.

The Monte Carlo simulation predicted the relative abundance of neutrino species: $\nu_\mu : \bar{\nu}_\mu : \nu_e : \bar{\nu}_e = 1.00 : 0.061 : 0.0094 : 0.0024$. with average energies of 23.5, 19.2,

37.1, and 31.3 GeV [48].

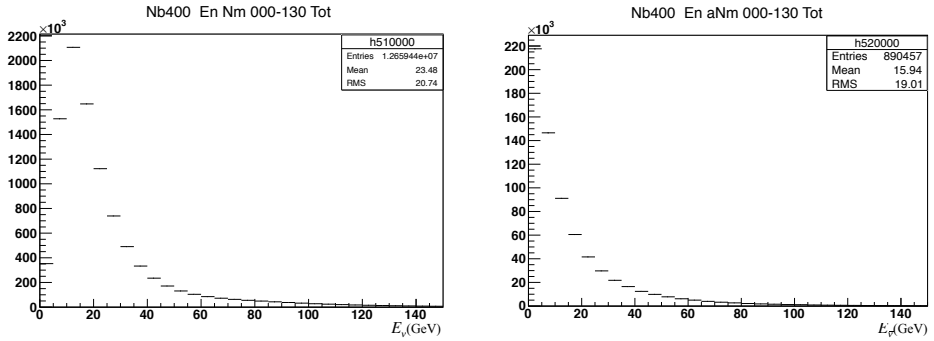

Figure 4.1: Predicted neutrino(ν_μ) and anti-neutrino ($\bar{\nu}_\mu$)flux in NOMAD.

4.2 The NOMAD Detector

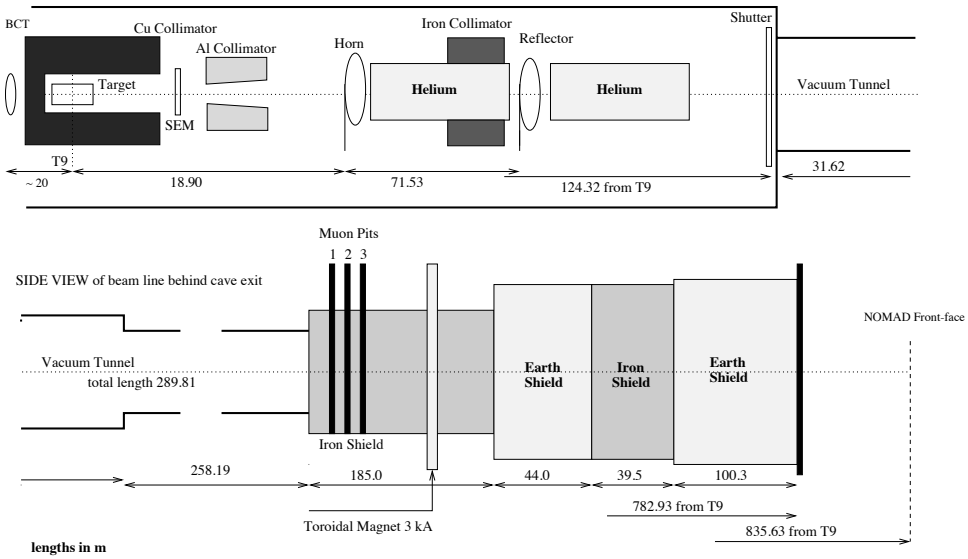

Figure 4.2: Schematic layout of the West Area Neutrino Facility(WANF) beam line [8].

The NOMAD detector was designed to measure and identify most of the particles, including charged and neutral particles, produced in the interaction of neutrino and target [5], which was composed of several sub-detectors. A top view of the NOMAD

detector is shown in Figure 4.3. In this Figure, the fiducial volume of the NOMAD detector consists of 44 drift chambers and with a low average density (around $0.1\,\mathrm{g\,cm^{-3}}$). The drift chambers are located within a dipole magnet providing a 0.4 T magnetic field orthogonal to the neutrino beam line. The existence of magnetic field allows for the determination of the momenta of charged tracks via their curvature with minimal degradation due to multiple scattering. The direction of the magnetic field is chosen as the X reference axis. The incoming neutrinos' direction is called Z axis. Y axis is orthogonal to both of them. On average, the equivalent material in the DC encountered by particles produced in a ν-interaction was about half of a radiation length and a quarter of a hadronic interaction length (λ). The fiducial mass of the NOMAD DC-target, 2.7 tons, was composed primarily of carbon (64%), oxygen (22%), nitrogen (6%), and hydrogen (5%) yielding an effective atomic number, A=12.8, similar to carbon. There were nine modules of transition radiation detectors (TRD) located downstream of the target which are used to separate electrons from pions. Since Pions are about 270 times heavier than electrons, the chance of emitting a transition radiation X-ray is much smaller than electrons. With this TRD, about 99.9% of pions are rejected and 90% electrons are kept. The TRD was followed by an electromagnetic calorimeter (ECAL) including a preshower, a hadronic calorimeter and a muon chamber providing a clean identification of the muons. The energy resolution of this ECAL in NOMAD is $\frac{\sigma(E)}{E} = (1.04 \pm 0.01)\% + \frac{3.22 \pm 0.07}{\%} E(\mathrm{GeV})$. With the muon chamber, about 92% of the muons with momenta above 6 GeV can be reconstructed. In the NOMAD detector, the charged tracks could be reconstructed in the DC with an approximate momentum (p) resolution of $\delta p/p$ 3.5%. The experiment recorded over 1.7 million neutrino interactions in the active drift-chamber (DC) target in the range $O(1) \leq E_\nu \leq 300$ GeV. Besides the drift chamber, the Front Calorimeter (FCAL) was installed to provide additional massive active target for neutrino interactions. This FCAL consisted of 23 iron plates and 4.9 cm thick and separated by

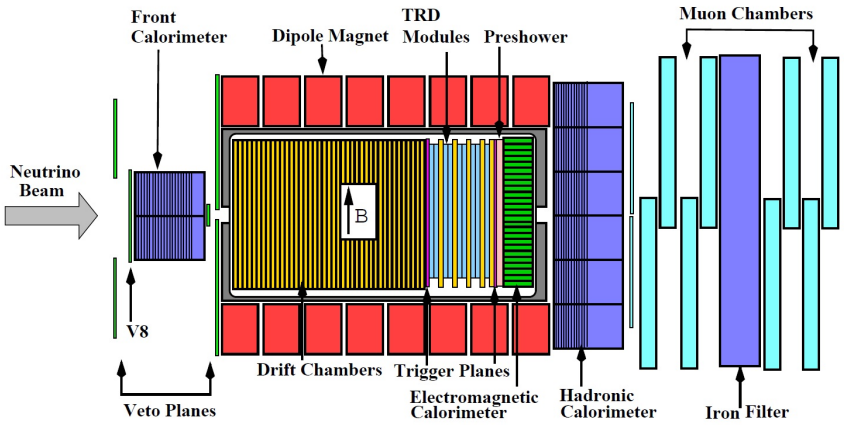

Figure 4.3: Diagram of the NOMAD detector (top view) [5]

1.8 cm gaps. Twenty out of the 22 gaps were instrumented with long scintillators read out on both ends. The depth of FCAL is about 5 nuclear interaction length [48]. The total mass of FCAL in NOMAD is about 17.7 tons. This large mass provides high statistics. There are two main topics are studied with this FCAL: One is the production of opposite sign muon pairs ("dimuons"); The other one is the search for the heavy neutrinos ("sterile neutrinos").

4.3 Reconstruction and Simulation

In the NOMAD experiment, The drift chamber can be used to determine the event topology and to measure the momenta of charged particles. when the neutrinos interact with the target in the drift chamber, the trajectories of charged particles are reconstructed from the coordinate measurements provided by the drift chamber. In order to provide good measurement of the tracks, a very high efficiency of the

track reconstruction is required. Also the measured track parameters do not deviate significantly from the true particle momenta, i.e. the reconstruction program should provide good momentum resolution. The amount of ghost tracks should be minimized. Since in the drift chamber, the amount of matter crossed by a particle between two measurement planes cannot be neglected, the effects of energy losses and multiple scattering must be carefully taken into account [7].

To reconstruct the tracks, first, the pattern recognition (track search) should be performed to decide which individual measurements provided by the detector should be associated together to form an object representing a particle trajectory. Second, a fitting procedure should be applied to this set of measurements in order to extract the parameters describing the trajectory out of which the physical quantities can be computed [7].

To find the particle tracks, first, it is needed to guess possible tracks from hit combinatories and provide initial track parameters. Second, it is attempting to build a track from the given parameters by repeatedly collecting hits, fitting and rejecting possible outliers. The track is claimed to be fitted when no more hits can be added to it [7].

To simulate the Monte Carlo events in NOMAD, Neglib which was built based on LEPTO 6.1 [29] and JETSET [47] is used as the event generator. Rein-Sehgal (RS) model [44], Berger-Sehgal(BS) model [15] are used for the coherent event simulation.

4.4 Neutrino Interaction Candidate in NOMAD Target

Figure 4.4 shows the ν_μ charged current interaction candidate in NOMAD Drift Chamber, we see that there are many hadron tracks, enabling the momentum vector measurements. μ is kinematically separated from the hadron vector.

Figure 4.5 to Figure 4.7 show some other neutrino interactions candidates in NOMAD detector.

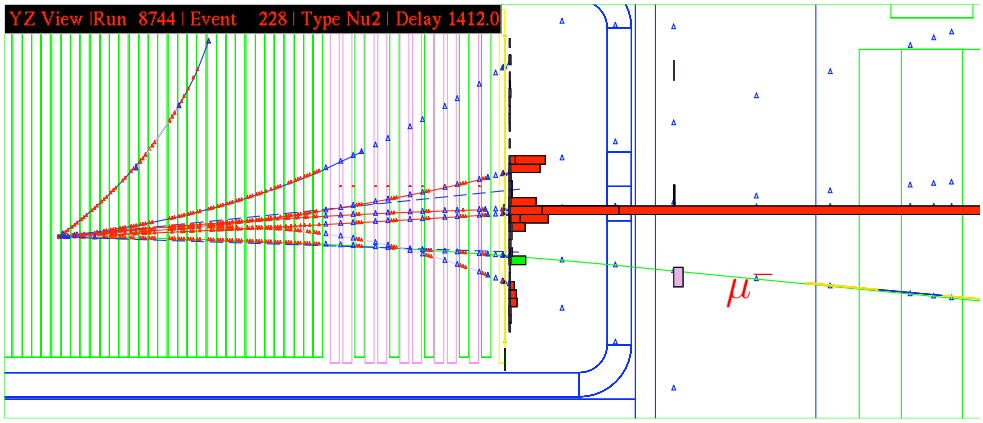

Figure 4.4: ν_μ-CC candidates in NOMAD.

Most difficult to measure among the 4 neutrino species

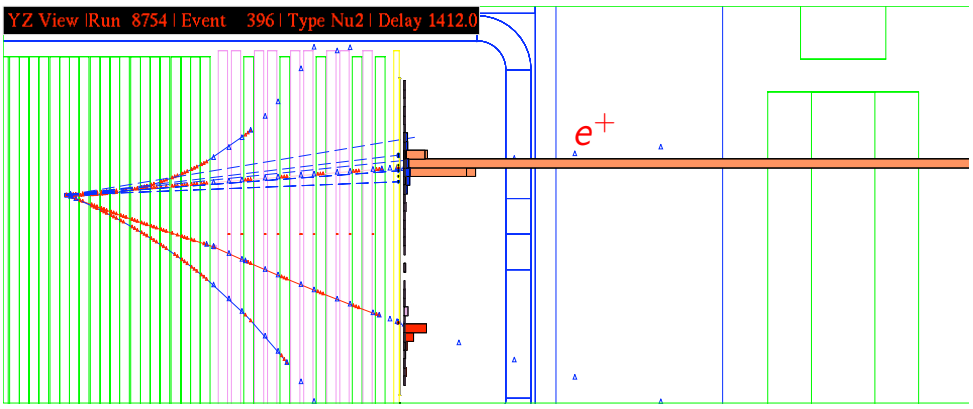

Figure 4.5: $\bar{\nu}_e$-CC candidates in NOMAD.

4.5 Coherent Signature in NOMAD Target

Some candidate coherent interaction events are shown from Figure 4.8 to Figure 4.10. In the charged current coherent process, there are two tracks which are identified as the leading lepton and coherent meson. A coherent ρ^0 candidate event is shown in Figure 4.8. There is a single, forward ρ^0 produced with no accompanying particles in a neutral charged coherent ρ^0 event. The ρ^0 in the final state will promptly decay into a charged pion pair. Therefore, in the NOMAD detector, there will be two tracks detected.

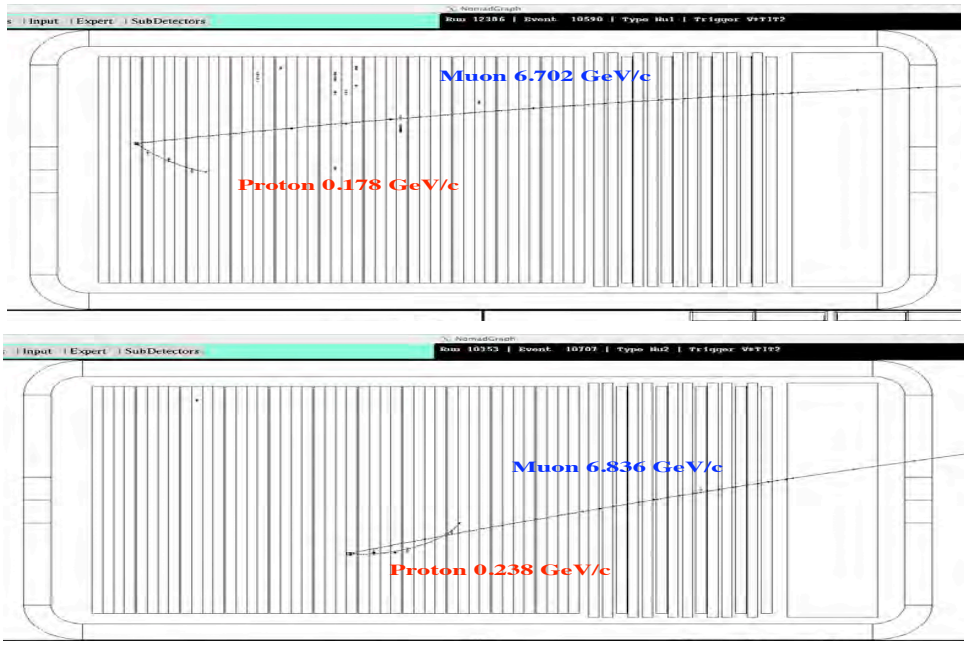

Figure 4.6: QE candidates in NOMAD.

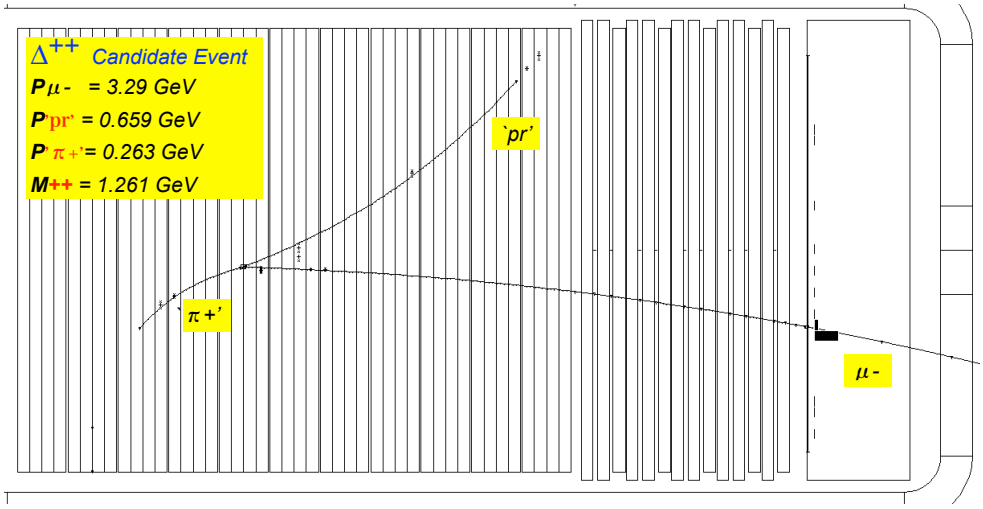

Figure 4.7: Resonance candidates in NOMAD.

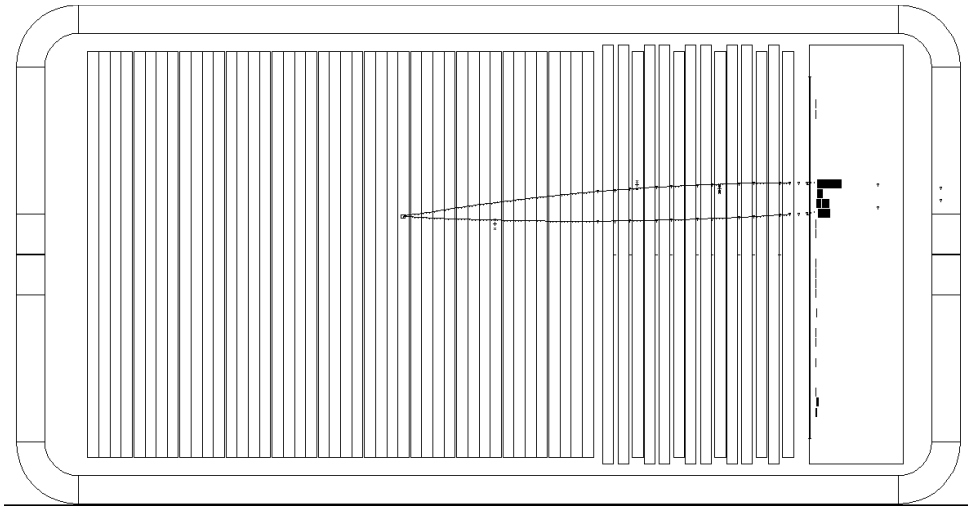

Figure 4.8: Coherent ρ^0 candidate event picture.

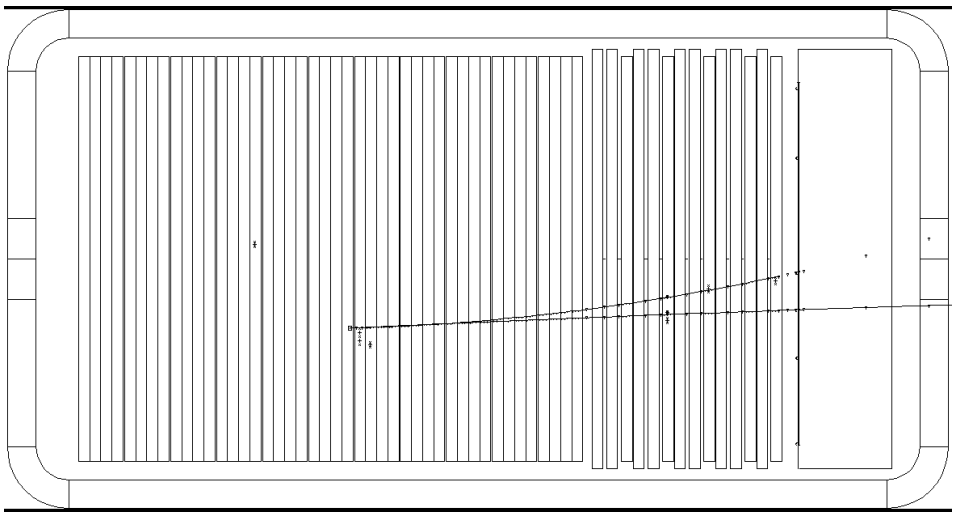

Figure 4.9: Coherent π^+ candidate event picture.

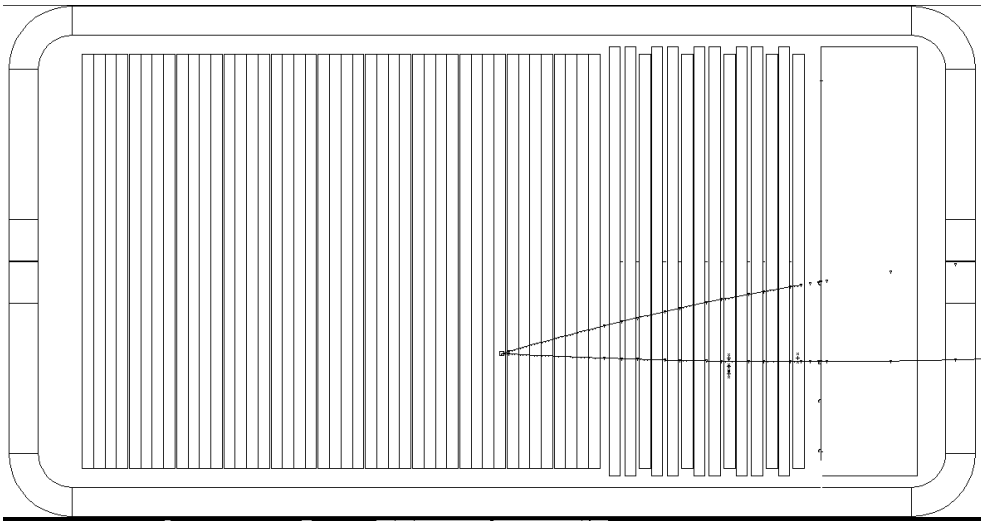

Figure 4.10: Coherent π^- candidate event picture.

Chapter 5

A High Resolution Fine Grained Tracker (FGT) as the Near Detector for ELBNF/DUNE

5.1 Introduction & Salient Physics Goals

In the ELBNF/DUNE project, besides the far detector, a near detector known as HIRESMNU, is also proposed with high resolution within a dipole magnetic field. This near detector is based on the NOMAD detector concept but with some improvements. It combines large statistics with high resolution (for example, momentum and energy) in the reconstruction of neutrino events compared with previous experiments. HIRESMNU is expected to achieve high precision in the measurements of neutrino interactions, structure of nucleons/nuclei, and the elements of the neutrino mass matrix. It is also designed to search for new physics, such as, sterile neutrinos, high Δm^2 oscillations, light dark matter etc. Hopefully, with HIRESMNU, there will be some unexpected discoveries made by the far detector. The fiducial mass of this near detector is 7 tonnes, bigger than the 2.7 tonnes of the NOMAD detector. Different from the NOMAD detector, there is a 4π ECAL coverage in the dipole magnetic field and a 4π μ detector coverage instead of only downstream.

A summary of performance for the fine grained tracker configuration is shown in Table 5.1. All the parameters of the HIRESMNU are not fixed yet, but they have to meet our goals with the design [1].

Constraining the systematic uncertainties in the oscillation studies: The precision of the near detector (ND) measurements will be essential for the neutrino

Table 5.1: Summary of performance for the fine grained tracker configuration [1].

Performance Metric	Value
Vertex resolution	0.1 mm
Angular resolution	2 mrad
E_e resolution	5%
E_μ resolution	5%
$\nu_\mu/\bar{\nu}_\mu$ ID	Yes
$\nu_e/\bar{\nu}_e$ ID	Yes
NCπ^0/CCe rejection	0.1%
NCγ/CCe rejection	0.2%
NCμ/CCe rejection	0.01 %

oscillation studies (νOSCL) in ELBNF/DUNE, so the associated systematic error should be less than the corresponding statistical error. The required systematic precision in the near detector will determine the detector parameters such as resolution, fiducial mass, and so on. To this end, we will pay particular attention to [18]:

(1): Measurement of the relative abundance and energy spectrum of all four species of neutrinos in the LBNE beam: $\nu_\mu, \bar{\nu}_\mu, \nu_e$ and $\bar{\nu}_e$ via the *i*n situ identification of their CC-interactions.

(2): Determination of the absolute ν-flux using the ν-electron scattering.

(3) Identification and precise measurement of π^0, photon, electron and positron yields in ν-induced neutral-current (NC) and charge-current (CC) interactions - the most important background to the ν_e -appearance.

(4) Measurement of NC cross-section relative to CC as a function of the hadronic energy, Ehad, since NC processes constitute the largest background to the ν-CC identification.

(5) Measurement of the $\pi^\pm$ content in CC and NC hadronic jets since the $\pi^\pm \to \mu^\pm$ are the principal background to the $\nu_\mu(\bar{\nu}_\mu)$-CC.

(6) Measurement of the differential cross-section for various exclusive, semi-exclusive and inclusive channels relevant for the νOSCL studies, such as quasi-elastic (QE), res-

onance (Res) and deep-inelastic (DIS) interactions.

(7) Quantification of nuclear-target material cross-section that might affect the ν-nucleus interactions when extrapolating the near detector measurements to the far detector.

Precision neutrino physics: The HIRESMNU in ELBNF/DUNE is designed with a generational advance in the precision measurement of physics parameters, such as the precise measurement of isospin physics, sum-rules, QCD tests, baryon-spin, strange meson and baryon production, charm mesons and electroweak constants. As a case study, we propose to investigate the feasibility of a measurement of the weak-mixing angle, $\sin^2\theta_W$ in the $\nu(\bar{\nu})$-q (DIS) channel at a momentum transfer (Q) in the neighborhood of 4 GeV with a precision approaching 0.2%. The sought precision on $\sin^2\theta_W$ in this experiment will be comparable to that attained by the collider experiments. The HIRESMNU ND will also permit searches for new physics with unprecedented sensitivity; the searches include high- Δm^2 oscillations in $\nu_\mu \to \nu_e$, $\nu_\mu \to \nu_\tau$, $\bar{\nu}_\mu \to \bar{\nu}_e$ and $\nu_e \to \nu_\tau$ channels, rare resonance, heavy neutrinos, and exotic boson [18].

These considerations imply the following requirements:

- Magnetized tracker to identify positive from negative particles throughout the curvature of the particle tracks(B$\sim$0.4T).
- Low density medium to track charged particles ($\rho \sim 0.1\,\mathrm{g\,cm^{-3}}$).
- Large statistics ($\sim 10^8$ neutrino interactions).

5.2 Sub Detectors

The HIRESMNU offers a generational advance in the identification of particles and the precise measurement of their momenta. The most precise neutrino detector to

date is NOMAD whose energy range was $2.5 \leq E_\nu \leq 300$ GeV; the energy range of interest in ELBNF/DUNE is $0.5 \leq E_\nu \leq 100$ GeV.

Figure 5.1 shows the sketch of the proposed HIRESMNU detector. In this figure, the incident neutrino beam comes from the left side. In Figure 5.1, we see that,

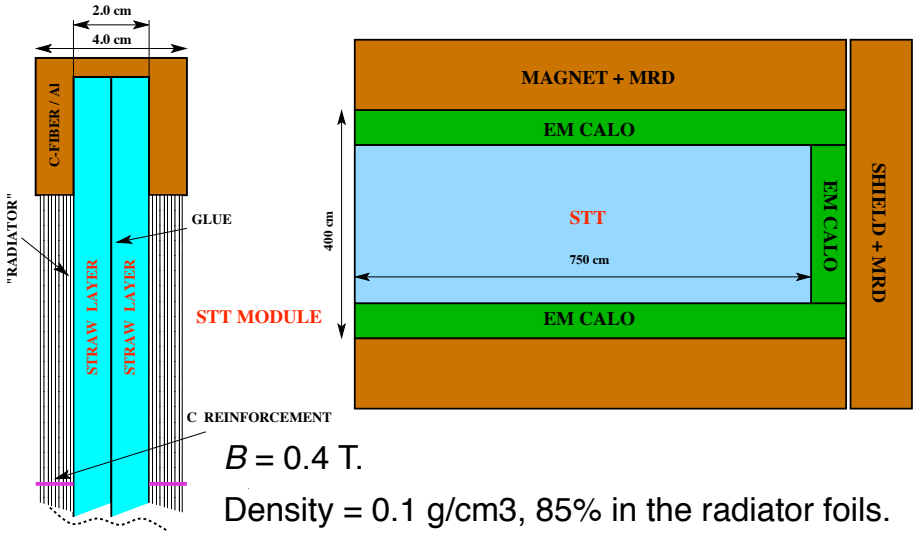

Figure 5.1: Sketch of the proposed HIRESMNU detector showing the inner STT and the 4π ECAL in the dipole magnet with the muon-ID detector(MRD). The internal magnetic volume is approximately 4.5m×4.5m×8m. Also shown is one module of the proposed STT [18]

different from NOMAD with an ECAL (Electomagnetic Calorimeter) at the downstream end, and with a muon-ID detector outside the magnetic field, in HIRESMNU, the near detector (ND) has a 4π ECAL coverage including downstream (DS), sides (Barrel) and upstream (US) ends of the detector. The tracking volume will be fully surrounded by electromagnetic calorimetry. Relative to the NOMAD detector, the HIRESMNU near detector has an enhanced tracking detector, that is composed of straw tubes with 1 cm in diameter. Vertical ($\mathbf{Y}$) and horizontal ($\mathbf{X}$) straws will be al-

ternated and arranged in modules with each module containing a double straw layer. The HIRESMNU ND also has an improved muon identification capability. Compared to the 85% efficiency of muon detection in NOMAD, HIRESMNU will tag 98% of the muons in the ν_μ charged current sample. The trigger in HIRESMNU will have neither geometry bias nor charge bias as NOMAD does. HIRESMNU will accumulate about 60 million neutrino interactions in 5 years, a factor of 30 more events than NOMAD had.

Straw Tube Tracker (STT)

The Straw Tube Tracker (STT) is the particle tracker of HIRESMNU, and locates at the center of the detector. The design of the straw tube follows that of the COMPASS detector [38, 43] similar to the dimensions of HIRESMNU, which is also a low density tracking detector, $\rho \leq 0.1\ \mathrm{g\,cm^{-3}}$. The conceptual transition radiation measurement in ν-interactions is based upon NOMAD-TRD [12]; the design of the transition radiation (TR) detection follows that of the ATLAS Transition Radiation Tracker [4, 3, 2]. The Straw Tube Tracker (STT) will have a total 160 modules. Vertical (Y) and horizontal (X) planes of straws will be alternated and arranged in modules. Each module will consist of a double straw layer (either XX or YY) [18]. Figure 5.2 shows the layout of the straw layers and cross-section of an STT module.

Some parameters for the fine grained tracker are listed in Table 5.2.

Nuclear targets will be installed in the upstream end of the particle tracker (STT). Figure 5.3 shows the sketch of a basis STT module for the measurement of nuclear effects. This nuclear target provides a statistical robust sample ($\times 5$ the far detector statistics) to quantitate the differences in ν-nuclear interaction. Argon gas, same as in the far detector, is proposed to use in pressurized tubes at the upstream end of the STT [18].

Figure 5.4 shows the schematic of the ATLAS transition radiation tracker (TRT).

Table 5.2: Parameters for the fine-grained tracker [1].

Performance Metric	Value
STT detector volume	3×3×7.04 m^3
STT detector mass	8 tons
Number of straws in STT	123,904
Inner magnetic volume	4.5×4.5×8.0m^3
Targets	1.27-cm thick argon ∼50 kg, water and others
Transition radiation radiators	2.4 cm thick
ECAL X_0	10 barrel, 10 backward, 18 forward
Number of scintillator bars in ECAL	32,320
Dipole magnet	2.4-MW power, 60-cm steel thickness
Magnetic field and uniformity	0.4 T; <2% variation over inner volume
MuID configuration	32 RPC planes interspersed between 20-cm thick layers of steel

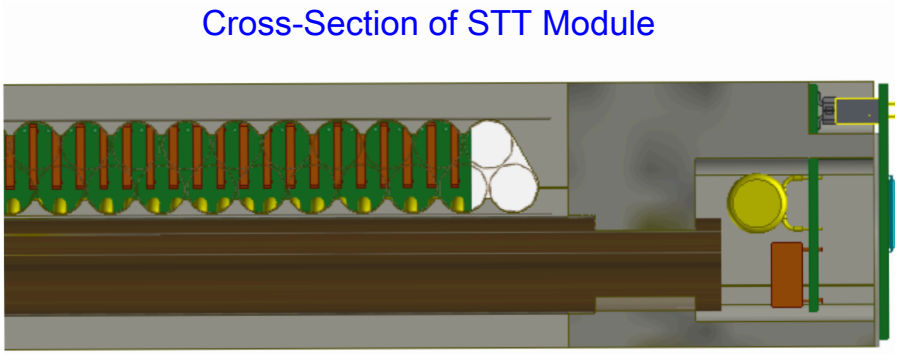

Figure 5.2: Layout of the straw layers and cross-section of an STT Module [18].

The endplug for the STT will be similar to the ATLAS-TRT, which could enable the transition radiation measurement with a mixture of Xenon (70%) and $\mathbf{CO_2}$ (30%) To protect STT against humidity, $\mathbf{CO_2}$ will be flushed through the straws at a forced-flow rate of ∼100 $m^3\,h^{-1}$.

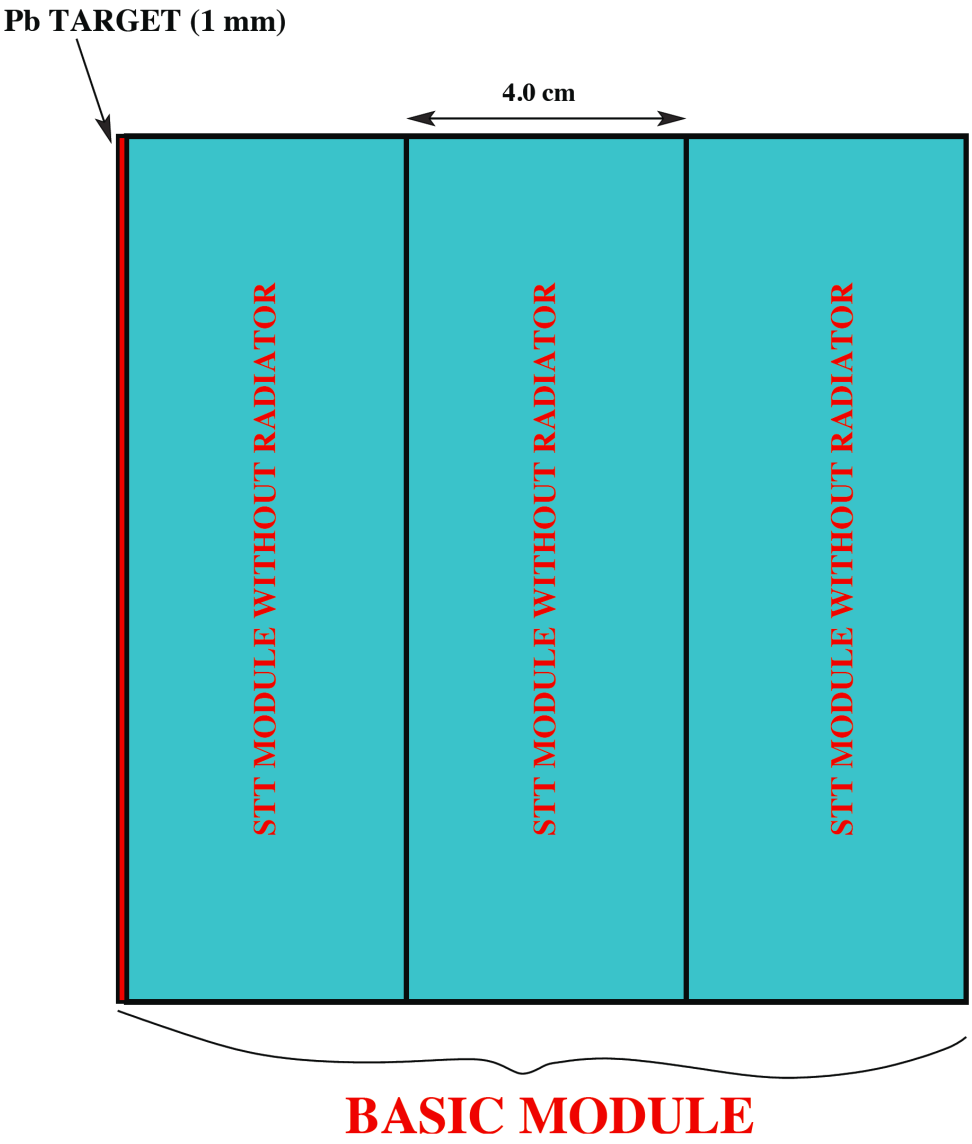

Figure 5.3: Sketch of a basis STT module for the measurement of nuclear effects. Several modules can be placed in the upstream magnetic volume with different target materials(Pb,Fe etc.) of the same thickness in radiation length [18].

Electromagnetic Calorimeter (ECAL)

The tracking volume of HIRESMNU (STT) will be surrounded by a 4π ECAL coverage: the forward or downstream (DS) module, the four side (top-bottom and left-right) of the Barrel module, and the upstream (US) module. This ECAl is a lead-scintillator calorimeter based upon the T2K-ECAL and have transverse and longitu-

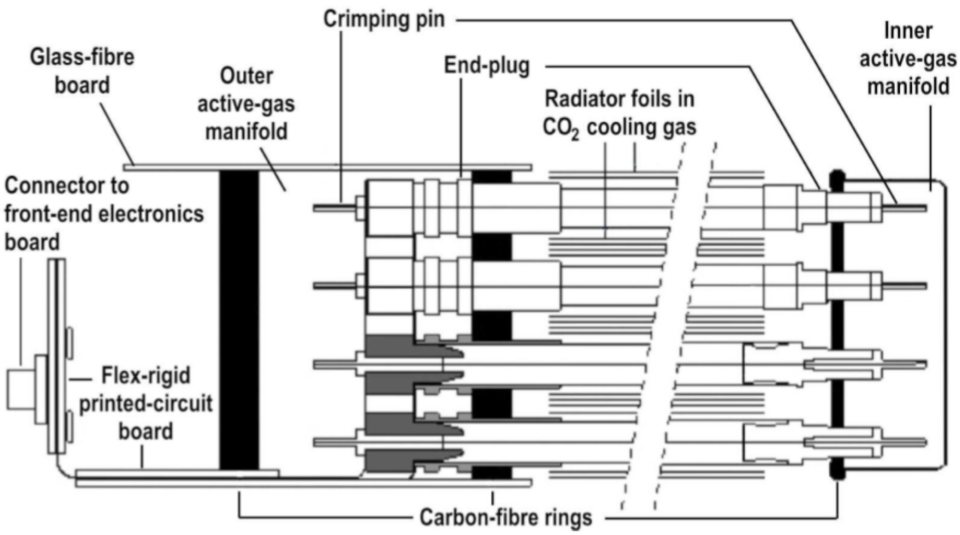

Figure 5.4: Schematic of the ATLAS STT Endplug [18].

dinal segmentation. The ECAL-surrounded STT will be embedded inside the dipole magnet [18].

The most important component of the ECAL in HIRESMNU near detector is the forward, or downstream (DS), module (shown in Figure 5.5) composed of 58 layers of 10-mm-thick (along z-direction) scintillator (Sci) followed by 1.75-mm-thick lead, corresponding to 10 radiation lengths (X_0). The first layer will be composed of 160 horizontal scintillator bars (providing the Y-coordinate of particles), 400-cm long, 2.5-cm wide, and 1-cm thick; followed by the Pb sheet. The 2.5-cm width of the bar is informed by the Moliere-radius of a 2.5 GeV electron–typical of ν_e–induced CC- which is approximately 2cm. The second layer will be composed of 160 vertical scintillator bars (providing the X-coordinate), 400-cm long, 2.5-cm wide, and 1-cm thick; followed by the Pb sheet. The third layer will be a Y-plane of bars, vertically shifted by 1.25 cm; followed by Pb sheet; The fourth layer will be a X-plane of bars, horizontally shifted by 1.25 cm; followed by Pb sheet. This arrangement will repeat itself to complete the DS-ECAL module [18].

Figure 5.5 shows a preliminary schematic of the DS-ECAL containing a total of

9280 Sci-bars with a total Sci-volume of 4.64 m^3. Figure 5.6 shows the engineering details of the module.

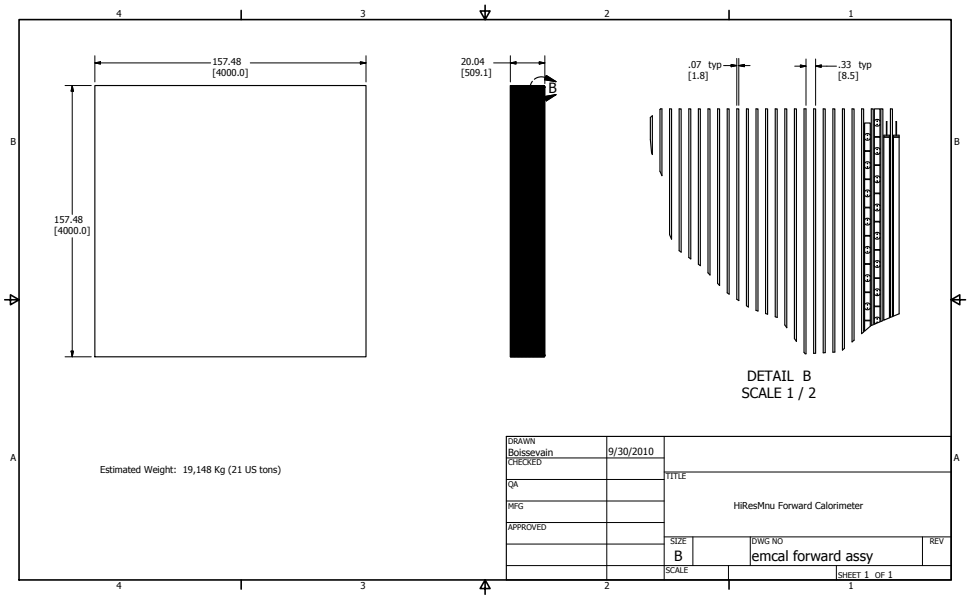

Figure 5.5: Preliminary Schematic of the DownStream or Forward ECAL [18].

At a national lab or fabrication center in India the scintillator bars will be extruded with Kuraray wavelength-shifting fibers and later threaded through the middle of the bars. The fibers will be read out at each end by silicon photomultiplier (SiPM) type photosensors. The two readings allow for a position determination. It follows that the number of readout channels will be twice the number of scintillator bars. In the DS-ECAL, there will be 18,560 SiPMs. The T2K-ECAL used the Hamamatsu photosensors called MPPC which will be adequate for our use. It must be noted that the SiPM technology has undergone a rapid improvement, driving the costs lower and offering better performance.

Since the Barrel-ECAL will surround the sides of the STT, nominally there would be four modules, covering a 8m $\times$ 4m area, corresponding to the top, bottom, left

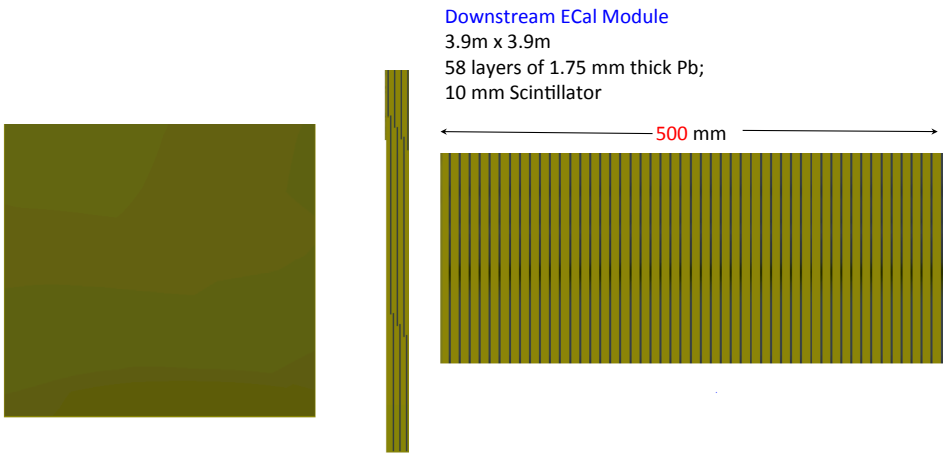

Figure 5.6: DownStream(DS) or Forward ECAL [18].

and right sides. The conceptual design of the Barrel-ECAL is similar to that of the DS-ECAL. A Barrel-ECAL module, Figure 5.7 , will have eight layers of alternating horizontal and vertical scintillator strips every 7 mm of lead, or 10-X_0 deep. The upstream (US) ECAL will be identical to one of the Barrel-ECAL modules (see Figure 5.8). For the scintillator bars, our default assumption is that the dimensions of the bars in the Barrel-ECAL and US-ECAL will remain similar to those in the DS-ECAL, i.e., 400-cm long, 2.5-cm wide, and 1-cm thick. The total number of bars in the eight modules of Barrel-ECAL and the one module of US-ECAL will be 11,520 (4-layers $\times$ 400cm/2.5cm $\times$ 9) correspond ing to 30,000 readout channels.

We have given some thought to reducing the number of channels in the ECAL. Our preliminary optimization studies include (a) reducing the longitudinal granularity in the most important portion, the DS-ECAL; (b) reducing its transverse granularity; and (c) reducing the transverse granularity of the Barrel-ECAL. A detailed GEANT4-

based MC will provide us with better guidance.

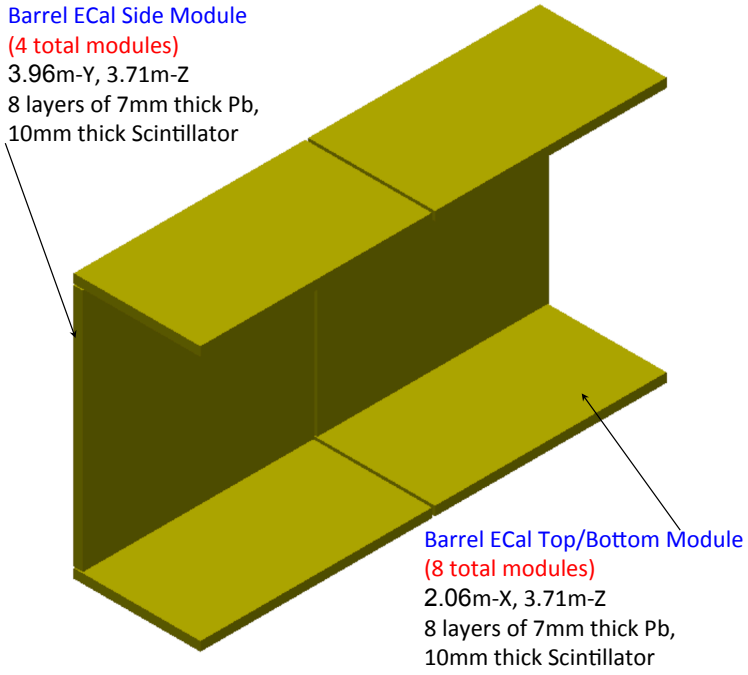

Figure 5.7: Specifications of the Barrel ECAL [18].

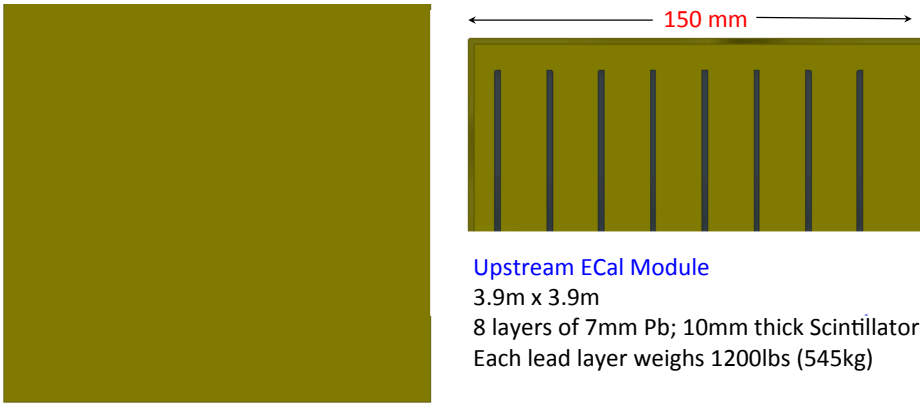

Figure 5.8: UpStream(UP) ECAL [18].

Table 5.3: Parameters of the UA1/NOMAD dipole magnet [18].

Item	Value
Dimension	3.5× 3.5 × 7 m^3
Maximum B-Field	0.7 T
Maximum Current	10,000 A
Resistance(40C)	0.0576
Voltage	576 V
Mass	900 T
Cooling water flow	50 liters/sec
Pressure gredient	15 atm(in .vs. out)
Temperature Diff	30C

Dipole Magnet

In HIRESMNU near detector, the STT particle tracking detector and ECAL modules will both locate inside a 0.4-T dipole magnet with inner dimensions of 4.5-m wide by 4.5-m high by 8.0-m long. The proposed dipole magnet is a larger version of the UA1 dipole magnet [5] which is used by NOMAD, and is currently in use by the near detector of T2K. Because the dipole magnet for HIRESMNU is very similar to the UA1 magnet yoke assembly, Figure 5.9 shows a photograph of the specifications of the UA1 magnet during the NOMAD operation. Table 5.3 summarizes the salient parameters of this magnet at the maximum operating B field of 0.7 T. The HIRESMNU magnet will operate at 0.4 T.

The principal differences between the UA1/NOMAD and the HIRESMNU magnets are: **(a)** size; **(b)** coil-UA1 used Al-coil to minimize the degredation of the energy resolution of the outgoing jets with resistivity $\rho_{Al} = 2.8 \times 10^{-8}\Omega m$; and **(c):** HIRESMNU magnet does not need a hole in the coil to allow passage of the proton beam, as was the case with the UA1 magnet. The HIRESMNU dipole will be composed of 8+8 'C'-Sections, the iron yokes. The coil will be made of copper, with aluminium as another option. Figure 5.10 shows a conceptual engineering drawing of the proposed magnet and 'C' Section.

Figure 5.9: Specs of the UA1/NOMAD dipole magnetic [18].

Resistive Plate Chamber as the Muon Detector (RPC)

In the HIRESMNU design, the muon-ID detector will identify muon tracks which will then be matched with tracks in the STT with measured momenta and charges. Thus, the muon-ID detector is not required to furnish muon momentum, only the μ-ID. However, given the large rate of muons in the ND location, we need a muon-ID detector with such spatial and time resolutions as to precisely reconstruct μ-track segments and permit an unambiguous match with the muon track in the STT. The muon-ID detector can be divided into two systems [18]:

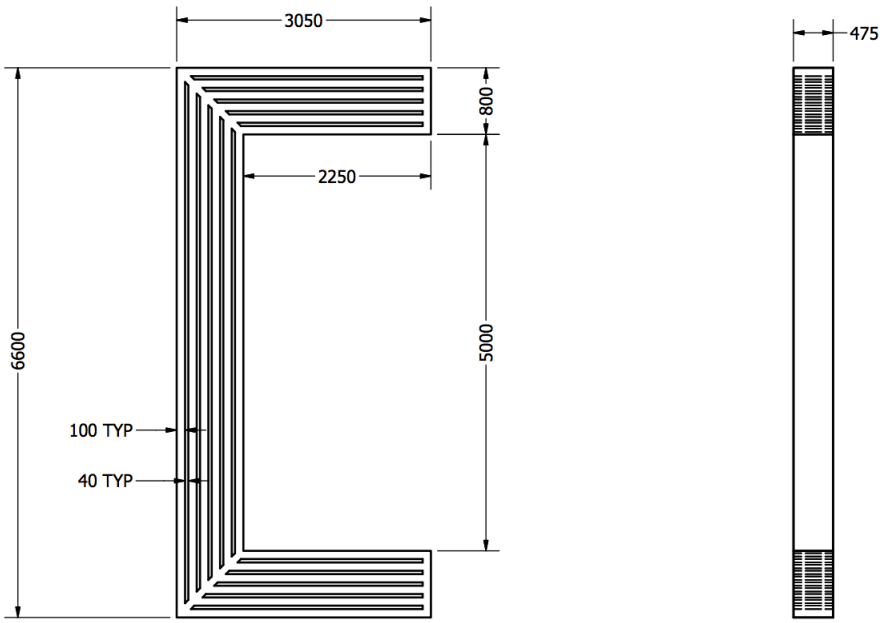

Figure 5.10: Conceptual sketch of one of the C-sections that constitute the magnet return yoke (dimensions are in mm). The vertical dimension is longer that the horizontal one in order to accommodate the magnet coil [18].

- The Muon Range Detector (MRD) instruments the gaps between the plates of the magnet return yoke. The main task of the MRD is to identify muons at low momenta exiting the sides of the detector. The MRD will reconstruct track segments within the magnet return yoke, including those of the stopping (ranging-out) muons [18].

- The External Muon Identifier (EMI) will identify high-energy forward muons. It is located outside the magnet, at the downstream end of the detector. The EMI will consist of two stations separated by a passive concrete/iron absorber. At each station, outside and downstream of the dipole magnet, it will reconstruct muon track segments to be matched with the STT tracks.

Due to the multiple scattering in the material (mainly iron) crossed by the muon tracks reaching both the MRD and the EMI detector, a space resolution in the range of $\simeq$0.75 mm will be adequate to accomplish the tracking task of the muon-ID detectors. For both the MRD and EMI detectors, we have selected the same Resistive Plate Chamber (RPC) technology as that developed for the LHC experiments, OPERA, BaBar and Argo. (An alternative under consideration is glass-based RPCs.) In particular, we follow the design of the RPC detectors used in the OPERA experiment to instrument the gaps within the magnet of the Muon Spectrometer. This type of application is similar to our MRD and has been operational for a few years in OPERA. A sketch of the detector is shown in Figure 5.11. Two electrodes, made of 2 mm Bakelite with linseed oil and volume resistivity $\rho > 5 \times 10^{11} \Omega$cm at T=20 °C, are kept 2 mm apart by means of polycarbonate spacers in a 10 cm lattice configuration. The external surface of the electrodes is painted with graphite of high surface resistivity and protected with a 190 µm thick PET layer that is applied during the installation on each side of the RPC to prevent high voltage discharge. The inner surface of the electrodes is coated with a few-micron-thick polymerized linseed oil layer. The total thickness of an RPC is between 6 and 7 mm [18].

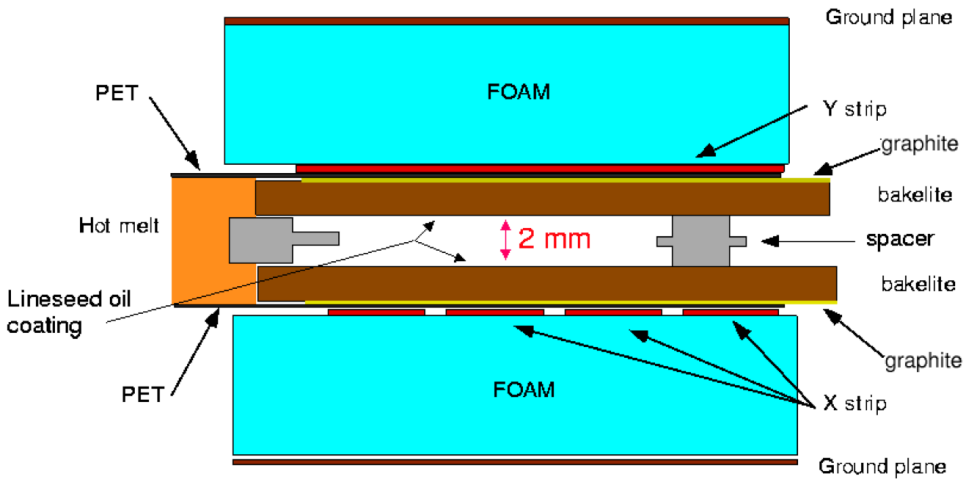

Figure 5.11: Cross-section of a Resistive Plate Chamber with its associated strips for the read out of the induced signal [18].

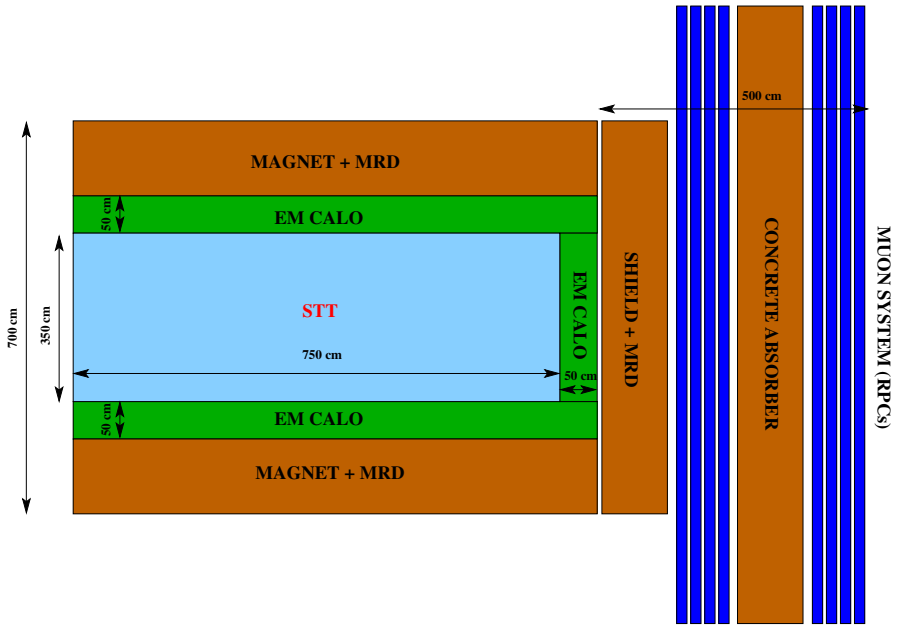

Figure 5.12: Layout of the HIRESMNU with downstream, external muon-ID detector(EMI) and shielding. The EMI specifications are preliminary; detailed simulation studies of EMI will yield a more robust design [18].

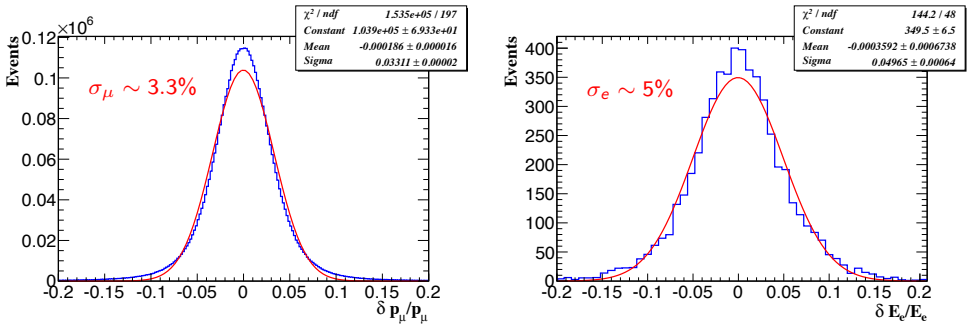

Figure 5.13: Momentum and Energy resolution of HIRESMNU [18].

5.3 How the FGT Helps Accomplish the Above Goals

The FGT offers a generational advance in the precision of the individual particle momentum measurements and identification. The most precise neutrino detector to

date is NOMAD whose energy range is $2.5 \leq E_\nu \leq 300$ GeV; the energy range of interest in LBNE is $0.5 \leq E_\nu \leq 100$GeV. The advancements of the FGT compared with current precision measurement are:

- An Enhanced Tracking Detector.
- 4π Electromagnetic Calorimeter Coverage.
- Improved Muon-Identification.
- No Geometry Bias or Charge Bias Trigger.
- High Event Rate.

Chapter 6

Coherent π^- Measurement in NOMAD

6.1 Signal Signature

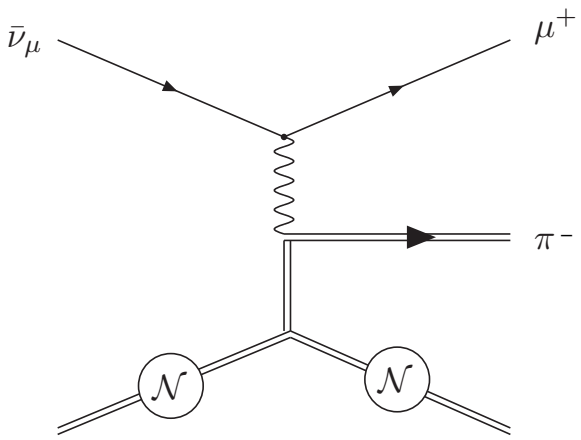

Figure 6.1: Feynman Diagram of Coherent Pion Production.

Figure 6.1 shows the Feynman diagram of coherent π^- process ($\bar{\nu}_\mu + \mathcal{N} \rightarrow \mu^+ + \pi^- + \mathcal{N}$). In the coherent π^- events, there are only two charged particles in the final state, which means in the drift chamber of NOMAD detector, we are looking for the events with the following properties:

- There are only two tracks observed. The one which is longer and triggered the Muon chamber at downstream is identified as Muon.
- The events are all with a low value of Q^2 which is defined in Equation (3.1)($Q^2 \leq 1GeV^2$).

- In the selected signal events, the direction of the outgoing lepton is collinear with the incoming neutrino direction.

6.2 Background

The background of coherent π^- events comes from several sources:

- The biggest background comes from ν_μ charged current events. In some of the ν_μ charged current events, π^- are also produced, and could be identified as coherent π^- events especially when other particles (except π^- and μ^+) have very small energy.

- Another background comes from coherent ρ^0 events: The decay of the ρ^0 produces π^+ and π^-, which might also be classified as coherent Pion events.

- Neutral current events are also a background source in coherent π^- analysis when there are only two tracks observed and one of them is classified as Muon.

6.3 Neutrino and Anti-neutrino Beams

In the NOMAD experiment, the neutrino beam is produced by extracting part of the 450 GeV proton beam circulating in the SPS (Super Proton Synchrotron) and allowing it to interact with a beryllium target. Figure 4.2 show the schematic layout of the the WANF beam line[8]. The two toroidal magnetic lenses, referred to as the horn and the reflector, focused charged particles of a given sign (positive for a predominantly ν_μ beam); The polarity of these magnetic elements could be changed within minutes in order to produce an anti-neutrino beam ($\bar{\nu}_\mu$ beam) [8], which are called neutrino beam mode (positive focusing data: FocP) and anti-neutrino beam mode (negative focusing data: FocN).

The principle of the focusing is illustrated in Figure 6.2. The reflector provided additional focusing for high momentum particles by horn. The magnetic field was

provided by current sheets flowing in the inner and outer conductors of the lenses. The field was measured to be azimuthally symmetric to better than 1.5%. Its value at a radial position r from the beam axis and for a current I is given by [8]

$$B = \frac{\mu_0 I}{2\pi r} \tag{6.1}$$

The current (100 kA for the horn and 120 kA for the reflector) was provided by the discharge of capacitor banks and lasted 6.8 ms. The thickness of the inner conductor was minimized to reduce secondary interactions while maintaining adequate strength to withstand the magnetic forces.

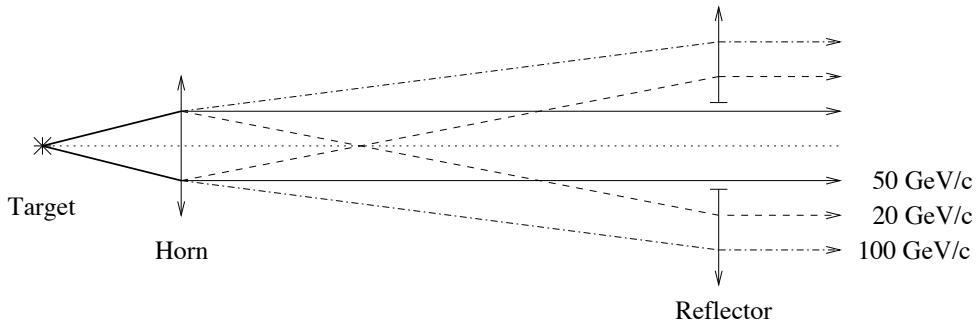

Figure 6.2: Principle of the focusing. The lines are representative trajectories of particles of three different momenta [8].

Positively charged particles (mainly π^+ and K^+ mesons) produced around zero degrees with respect to the primary proton beam are focused into a near parallel beam by a system of magnetic lenses and subsequently decay producing neutrinos.

The effect of the horn and the reflector on particles of different sign is illustrated in Figures 6.3 and 6.4, which show angular distributions of positive and negative pions at a plane just upstream of the horn and immediately downstream of it. Upstream of the horn, pions of both positive and negative charges emerging from the target have very similar angular distributions, with the bulk of the particles within 10 mrad, which is the acceptance of the collimators. While traversing the horn, positive pions with both momentum around 50 GeV/c are focused into a near-parallel beam leading to an overall enhancement at small angles of up to a factor of 30 (Figure 6.3).

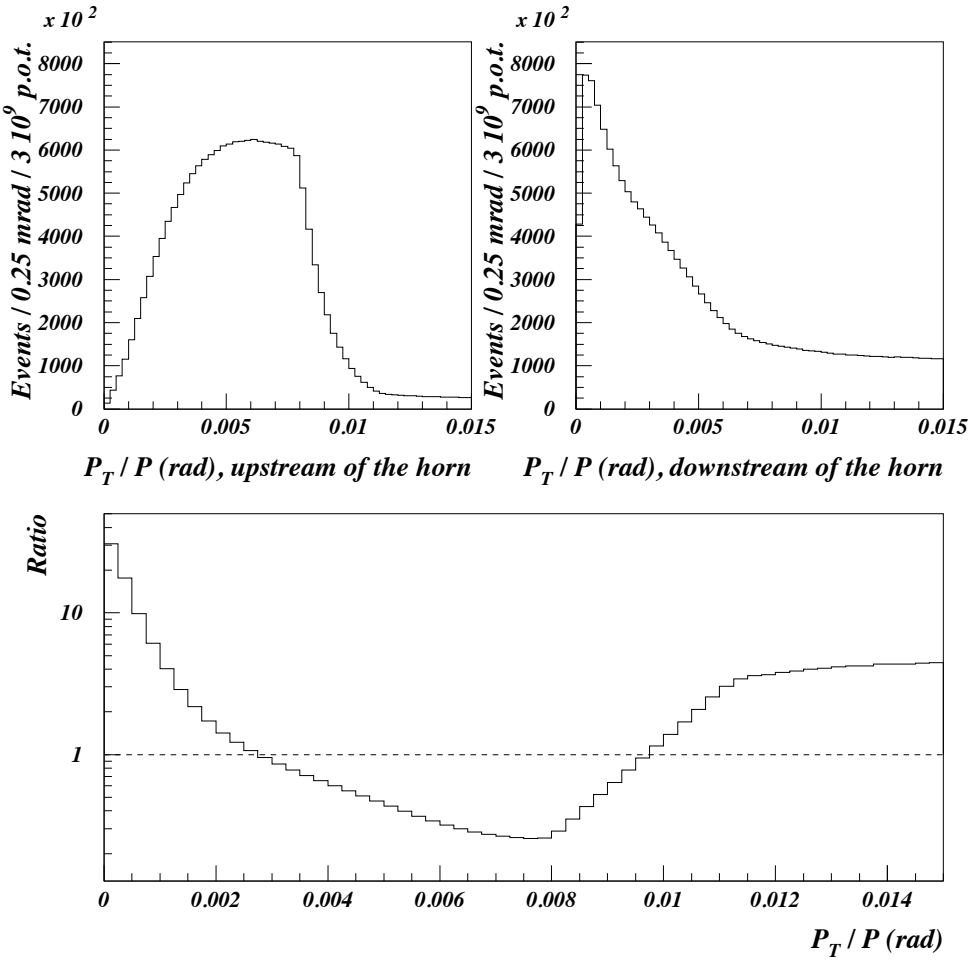

Figure 6.3: Distribution of the angle between the π^+ momentum vector and the beam line direction, P_T/P, just upstream of the horn (top left),right after it(top right) and the ratio of the latter to the former(bottom) [8].

Negative pions are strongly defocused resulting in their reduction at small angles by as much as a factor of 5 (Figure 6.4). The reflector provides an additional focusing for positive particles of momentum both higher and power than 50 GeV/c that were respectively underfocused and overfocused by horn [8].

6.4 Neutrino Beam Mode

In the NOMAD data, all of the incoming neutrinos originating from the neutrino beam mode are dominated by the Muon neutrinos ν_μ, but still with a about 3% percentage contamination of the anti-neutrinos $\bar{\nu}_\mu$. At first, we are going to measure

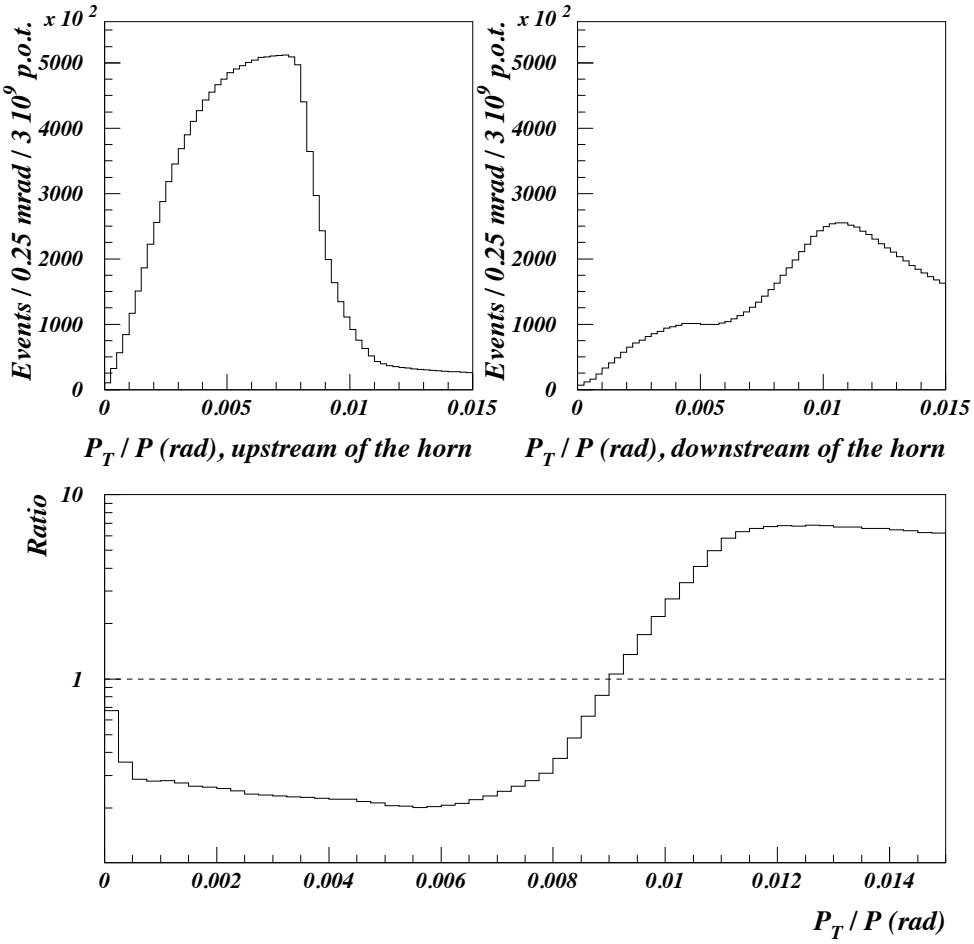

Figure 6.4: Distribution of the angle between the π^- momentum vector and the beam line direction, P_T/P, just upstream of the horn (top left),right after it(top right) and the ratio of the latter to the former(bottom) [8].

the coherent π^- events in the neutrino beam mode.

Normalization of Events Samples

In the analysis, to ensure the Monte Carlo matches well with the NOMAD experimental data, all the Monte Carlo components are initially normalized based on coherent events and inclusive charged current events.

The initial normalization factors in the analysis are shown in Table 6.1 and Table 6.2. Where 1,436,000 is the number of the ν_μ inclusive charged current events from the reference [52]. The ratio between neutral current and charged current ν_μ

Table 6.1: Normalization of Neutrino Beam Mode events [52, 8].

Mode	Event Number
ν_μ CC	1,436,000
ν_μ NC	1,436,000 × 0.37
$\bar{\nu}_\mu$ CC	1,436,000 × 0.025
$\bar{\nu}_\mu$ NC	1,436,000 × 0.025 × 0.37

Table 6.2: Ratios between interaction mode.

Ratio	Value
NC/CC	0.37
non-DIS/DIS	0.055
QE/RES	0.75

events also comes from this work, but not published yet. These initial normalization factors should provide us with a reasonable description of the data. Later we will fine-tune certain normalization factors to improve the fit.

Preselection of $\bar{\nu}_\mu$ CC and Coh π Events

To select the $\bar{\nu}_\mu$ charged current process, some variables cuts were applied during this analysis, including:

- Fermi Momentum Cut: Pfermi Cut(<1.0 GeV): Fermi Momentum(Pfermi) cut is applied to all the Monte Carlo events and helps us remove the non-physical events.

- W2s Cut: Invariant hadronic mass (W2s: $W^2 = (q+P)^2$>1.96 GeV^2), which is only applied to deep inelastic charged current and neutral current events, which will remove most of the background from deep inelastic interactions.

- Fiducial Volume: The drift chamber (DC) target is $3\times3\times4m^3$ and perpendicular to the neutrino beam direction. A reduced volume is necessary because some interactions in the magnet can create vertexes close to or outer the edges of

the drift chamber active area. In my research, the fiducial volume chosen is |X|<130 cm, |Y-5|<130 cm, and Z<405 cm with minimum z varying depending on experiment setup.

Table 6.3: Minimum value for the fiducial volume in NOMAD.

run No.	≤8375	[8376,9344]	[9345,14164]	≥14165
min z (cm)	265	115	5	35

- Muon Identification: Since this analysis is searching for coherent π^- ($\bar{\nu}_\mu + \mathcal{N} \rightarrow \mu^+ + \pi^- + \mathcal{N}$), Muon identification ($\mu^+$) becomes very critical. The first identification is a loose identification of Phase II which means that a track in drift chamber can be matched to a hit in the Muon chamber within 40 cm in the first station or within 50 cm in the second condition. This identification is stored in the DSTs (Data Summary Type). Then, the selection of Muon can be tightened by considering the goodness of fit between the track and the hit in the Muon chamber, and accepting only those combinations with the total χ^2 less than 20, over the four degrees of freedom of the fit.

- Tube/Veto Cut: Tube/Veto cut is applied to remove the charged particles and only let the neutral particles pass through the drift chamber. Then, the events originating mainly from the Muon contaminants can be rejected.

- Track Number Cut (ncand): In the $\bar{\nu}_\mu$ charged current interactions, there are two or more than two charged tracks observed. In coherent π^- interactions, there are only two charged tracks observed, including Muon and Pion.

- Muon Momentum ($\vec{P}_\mu$) Cut: To ensure the quality of the momentum's measurement, the Muon momentum should be greater than 1.5 GeV.

- Charge Identification: In a coherent π^- event, the hadron is π^-. To select the events with a negative hadron, Charge Identification is applied.

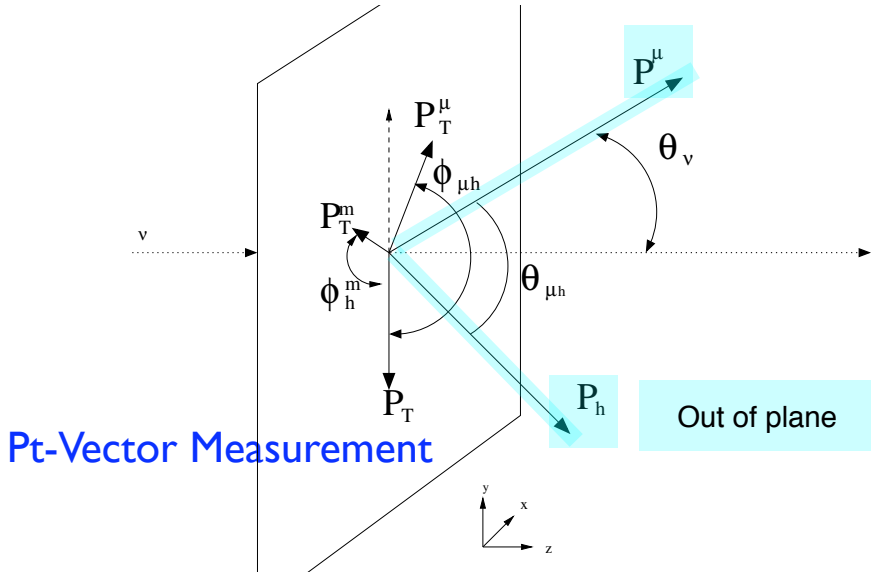

Figure 6.5: Reconstruction of the event kinematics for individual events.

- Angle Cut: To select the coherent π^- events, 2 angle cuts have been applied. The angle θ which is the angle between the outgoing lepton μ and the meson π, should be less than 177.5° and greater than 0.5 Rad.

- Missing Transverse Momentum (P_T^m) Cut: Figure 6.5 shows the reconstruction of the event kinematics for individual event. To choose the coherent events, the transverse momentum of the lepton must be less that 0.5 GeV.

- Neutral Vertex and Cluster Cut: neutral vertex and cluster cut are used to cut off the the coherent ρ^0 background especially when the two neutral vertex or cluster are both from the primary vertex.

$$|t| = [(E_\mu - p_\mu^z) + (E_\pi - p_\pi^z)]^2 + [(p_\mu^x + p_\pi^x) + (p_\mu^y + p_\pi^y)]^2 \tag{6.2}$$

$$|t_{min}| = [(Q^2 + m_\pi^2)/2E_\pi]^2 \tag{6.3}$$

$$t' = |t - t_{min}| \tag{6.4}$$

In the analysis, besides the variables mentioned in the preselection section, there are three other variable are also used and very important in the analysis of coherent processes, they are $|t|$, $|t_{min}|$, and $|t'|$ which are defined in Equation (6.2), Equation (6.3) and Equation (6.4). Where $|t|$ represents the magnitude of the square of nucleus' 4-momentum transferred to the nucleus.

Table 6.4: Cut table of Monte Carlo events in generated level.

	$N_{\bar{\nu}}^{CC}$	N_{ν}^{CC}	N^{NC}	TotBkg	N_{MC}
Total	47790.3	1645469	628612.1	2274081	2321871
Pfermi<1.0	47380.6	1631201	623116.4	2254318	2301698
W2s>1.96(CCDIS)	40610.1	1555351	589725.7	2145077	2185687
|GenX, (GenY-5)|<130 cm Zmin < GenZ < 405 cm	36076.4	1436828	544853.6	1981682	2017758
2.5<Evis<300	35900.0	1436001	544603.7	1980605	2016505

Table 6.4 shows the preselection of $\bar{\nu}_\mu$ charged current events in generated level. The normalization factor to the total inclusive $\bar{\nu}_\mu$ charged current events is $0.025 \times 1.436 \times 10^6$ after normalization, Z-weight, and flux(beam) reweight. $N_{\bar{\nu}_\mu}^{CC}$ represents the number of $\bar{\nu}_\mu$ charged current events including $\bar{\nu}_\mu$ charged current deep inelastic events($\bar{\nu}_\mu$ CCDIS), $\bar{\nu}_\mu$ charged current quasi-elastic events($\bar{\nu}_\mu$ CCQE), and $\bar{\nu}_\mu$ charged current resonance events($\bar{\nu}_\mu$ CCRES). $N_{\nu_\mu}^{CC}$ represents the number of ν_μ charged current events including ν_μ charged current deep inelastic events(ν_μ CCDIS), ν_μ charged current quasi-elastic events(ν_μ CCQE), and $\bar{\nu}_\mu$ charged current resonance events(ν_μ CCRES). N^{NC} represents the number of $\bar{\nu}_\mu$ neutral current events and ν_μ neutral current events. It is obvious that, after all the normalization, the total ν_μ charged current events has been normalized to 1,436,000; and the total $\bar{\nu}_\mu$ charged current events has been normalized to 35,900, which is equal to 1,436,000 $\times$ 0.025.

Table 6.5: Reconstructed variable cut table after normalization and reweighted.

	$N_{\bar{\nu}}^{CC}$	N_{ν}^{CC}	N^{NC}	TotBkg	N_{MC}	N_{data}	N_{data}/N_{MC}
Total	38919.5	1434877	464599.6	1899476	1938396	4018980	2.073
Pfermi<1.0	38595.7	1422826	460710.6	1883537	1922133	4018980	2.091
W2s>1.96(CCDIS)	33404.4	1357502	459376.8	1816879	1850283	4018980	2.169
FV cut	27615.3	1202210	405951.5	1608162	1635777	2515946	1.538
PhaseII	25478.2	1065825	14718.7	1080544	1106022	1151014	1.041
Nmu=1	25361.4	1058265	12319.5	1070584	1095946	1138941	1.039
veto/tube	25234.0	1055009	12263.2	1067273	1092507	1109323	1.015
ncand>=2	23411.5	1029563	12179.9	1041743	1065155	1079287	1.013
$\|\vec{p}_{\mu}\|$>2.5	23277.8	1023853	11742.4	1035595	1058873	1072094	1.012
μ^{+}	23172.5	8257.5	6011.7	14269.3	37441.7	52834	1.411
DeltaP/P<=0.2	23096.9	7311.7	5819.0	13130.7	36227.7	50085	1.383
thetamupi<177.5	23094.4	7311.7	5818.4	13130.1	36224.5	47549	1.313
Evis<300GeV	23093.2	7309.9	5817.5	13127.4	36220.6	47119	1.301
Ehad<300GeV	23093.2	7309.3	5817.3	13126.6	36219.8	47117	1.301
Nuhat>0	19838.1	2321.7	518.2	2840.0	22678.1	24898	1.098
Ybj<0.5	16157.8	585.7	250.4	836.1	16994.0	18060	1.063

Table 6.5 shows the preselection of $\bar{\nu}_\mu$ charged current events in reconstructed level. From this table, it is obvious that there is still about 6.3 % disagreement between Monte Carlo events and NOMAD data after all the cuts. We are going to vary the normalization factors to get better matches between Monte Carlo events and NOMAD data.

To ensure that the Monte Carlo matches the NOMAD data well, the following method was used to fit the Monte Carlo events with NOMAD data. The initial step needed to do is to choose the variables will be used to fit. The principle of choosing the variables used for fitting is they should give a good separation of signal from background. After checking the distributions of some kinematic variables, the three variables selected for fitting are as follows: $\hat{\nu}$ ($\hat{\nu}$ is defined in Equation 6.5), Ybj (Ybj is defined in Equation 6.6), and the missing transverse momentum P_T^m. The normalization factors for $\bar{\nu}_\mu$ charged current events, ν_μ charged current events, and neutral current events are $k_{norm}^{\bar{\nu}_\mu CC}$, $k_{norm}^{\nu_\mu CC}$ and k_{norm}^{NC}.

$$\hat{\nu} = \frac{P_T^{lep} - P_T^m}{P_T^{hadron}}. \tag{6.5}$$

$$y = \frac{p \cdot q}{k \cdot p} = \frac{M(E - E')}{EM} = 1 - \frac{E'}{E} = \frac{\nu}{E}, \tag{6.6}$$

where the variables, p, q, E, E', ν have been defined at the beginning of chapter 3.

The procedure includes the following steps:

- Create the 3D distribution with respect to missing transverse momentum P_T^m, Bjorken variable Ybj, and $\hat{\nu}$;
- Divide the distribution into equi-populated $5 \times 5 \times 5 = 125$ cubes. Because the events are not distributed uniformly, the volumes of the cubes are not the same.
- Run through all the possible normalization:

– Set the default value of $k_{norm}^{\bar{\nu}_\mu CC}$ at 0.9 and vary it in steps of 0.001 from 0.9 to 1.1;

– Set the default value of k_{norm}^{NC} at 1.9 and vary it in steps of 0.001 from 1.9 to 2.5;

– Set the default value of $k_{norm}^{\nu_\mu CC}$ at 1.5 and vary it in steps of 0.001 from 1.4 to 1.5;

Then the total number of Monte Carlo events after normalization becomes

$$\begin{aligned} N_{MC} = & N_{\bar{\nu}_\mu}^{CC} \times k_{norm}^{\bar{\nu}_\mu CC} + \\ & N^{NC} \times k_{norm}^{NC} + \\ & N_{\nu_\mu}^{CC} \times k_{norm}^{\nu_\mu CC} \end{aligned}$$

- Calculate the χ^2 for each cube and sum over all of them.

  $\chi^2 = \frac{(N_{data}-N_{MC})^2}{\sigma_{data}^2+\sigma_{MC}^2}$

  While $\sigma_{data} = \sqrt{N_{data}}$, and $\sigma_{MC} = \sqrt{\sum_j (\sqrt{N_{MC}(j)})^2}$, index j represents the Monte Carlo events($\bar{\nu}_\mu CC$, ν_μ CC and NC).

- Get the parameter corresponding the minimum χ^2.

$$k_{norm}^{\bar{\nu}_\mu CC} = 0.961 \pm 0.018$$

(shown in Figure 6.6)

$$k_{Norm}^{NC} = 2.052 \pm 0.052$$

(shown in Figure 6.7)

$$k_{norm}^{\nu_\mu CC} = 1.445 \pm 0.051$$

(shown in Figure 6.8)

Since the total number of points I used for fit is 125, the minimum χ^2 equals to 979.61, then the value χ^2/DOF is 7.837 (DOF means degree of freedom). Compared to the χ^2 before this 3D fit, it is reduced.

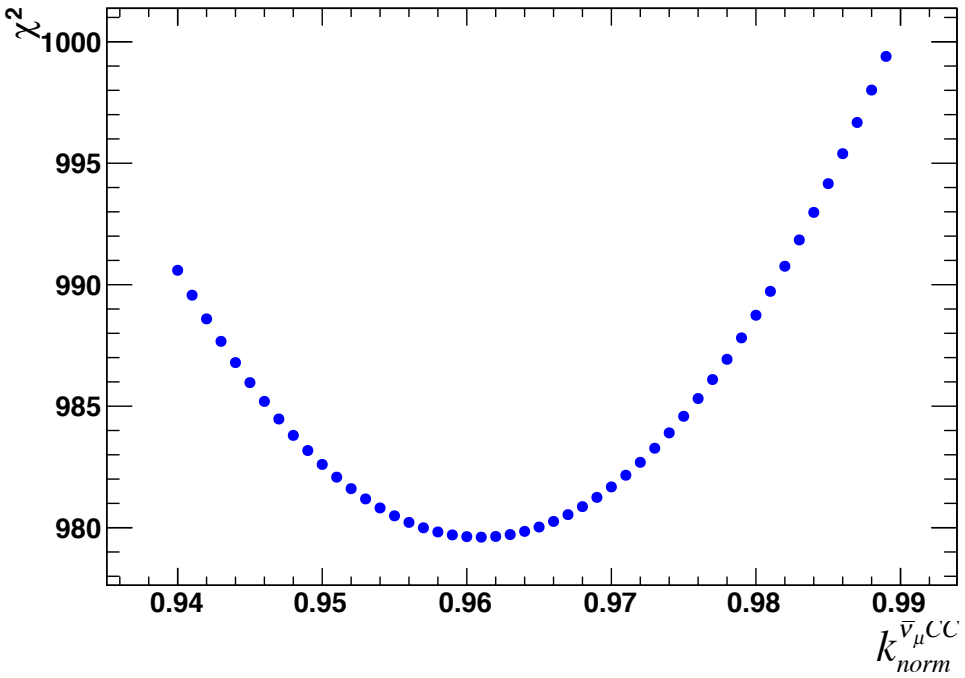

Figure 6.6: χ^2 distribution with respect to $k_{norm}^{\bar{\nu}_\mu CC}$, fix $k_{norm}^{NC} = 1.062$, $k_{norm}^{\nu_\mu CC} = 1.445$ using 125 points.

- After fitting with the 3D distribution of P_T^m, Ybj, and $\hat{\nu}$, I also created the 2D distributions of Ybj and $\hat{\nu}$, and fitted the MC events to the Data as a check. The normalization factors I got from this 2D fit are

  $k_{norm}^{'\bar{\nu}_\mu CC} = 1.103 \pm 0.016$;

  $k_{norm}^{'\nu_\mu} = 0.989 \pm 0.016$;

  where $k_{norm}^{'\nu_\mu}$ is applied on both the ν_μ charged and neutral current events. The total points I used for this 2D fit is 50, and The minimum χ^2 is 228.125, then the χ^2/DOF equals to 4.56. Which means the χ^2/DOF is reduced from 7.80 to

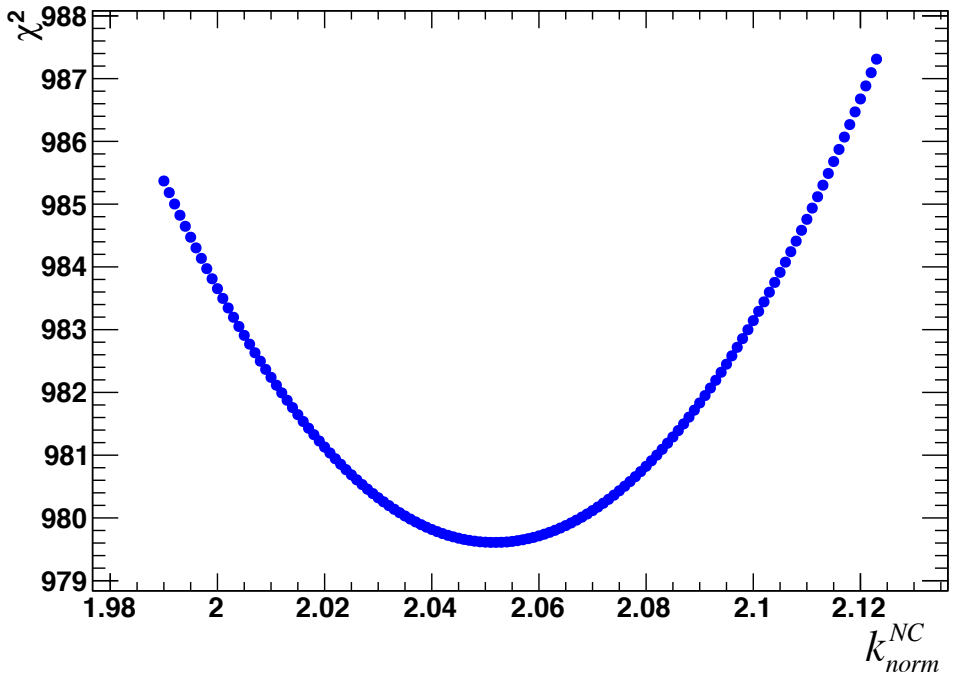

Figure 6.7: χ^2 distribution with respect to k_{norm}^{NC}, fix $k_{norm}^{\bar{\nu}_\mu CC} = 0.961$, $k_{norm}^{\nu_\mu CC} = 1.445$ using 125 points.

4.56 by this 2D fit. Then the new full normalization factors I got after the 2D fit are

$p_{norm}^{\bar{\nu}_\mu CC} = 0.961 \times 1.103 = 1.06$;

$p_{norm}^{NC} = 2.052 \times 0.989 = 2.03$;

$p_{norm}^{\nu_\mu CC} = 1.445 \times 0.989 = 1.43$;

- After fitting with the 2D distribution of Ybj and $\hat{\nu}$ cut, I refitted the $\bar{\nu}_\mu$ charged current events again with Ybj distribution as a check. For this 1D fit, all the events are divided into 5 equi-populated bins according to the Ybj distribution. The minimum value of χ^2 is 25.600, then the value χ^2/DOF equals to 5.120. Compared to χ^2/DOF before this 1D fit, it is reduced by a factor of 1.98.

  $p_{norm}^{'\bar{\nu}_\mu CC} = 0.961 \times 1.103 \times 0.975 = 1.03$;

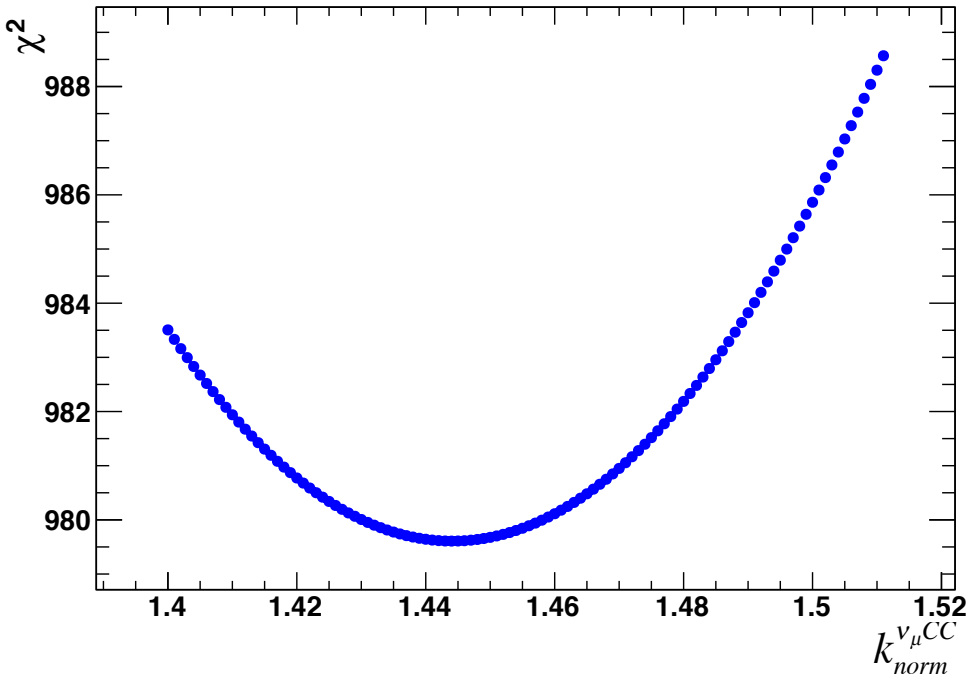

Figure 6.8: χ^2 distribution with respect to $k_{norm}^{\nu_\mu CC}$, fix $k_{norm}^{\bar{\nu}_\mu CC} = 0.961$, $k_{norm}^{NC} = 2.052$ using 125 points.

$p_{norm}^{NC} = 2.052 \times 0.989 = 2.03;$

$p_{norm}^{\nu_\mu CC} = 1.445 \times 0.989 = 1.43;$

- Get the total normalization factor

  $p_{norm}^{'\bar{\nu}_\mu CC} = 0.961 \times 1.103 \times 0.975 = 1.03$, which means the total $\bar{\nu}_\mu$ charged current events

  $N_{\bar{\nu}_\mu}^{CC} = 1436000 \times 0.025 \times 1.03 = 36977;$

This fit procedure is only used to define the center value of the background scale factors. The large value of χ^2 from the fit can be explained by the systematic uncertainties which were not included in the χ^2 calculation. These systematic uncertainties on the background subtraction will be estimated using a different ways of background normalization (which will be shown in section 6.8).

The first two columns of Table 6.6 show the number of generated and reconstructed $\bar{\nu}_\mu$ charged current events in 7 visible energy (Evis) bins. By calculating the ratio between the reconstructed and generated values in each bin, we can get the corresponding efficiency, which are shown in the last column of Table 6.6. The elements in the last column of Table 6.6 construct the 7 dimensional efficiency vector, and it is going to be used to calculated the corrected signal. Besides the efficiency vector, the efficiency matrix is also used to calculate the fully corrected signal.

Table 6.6: The efficiency (ratio between Reconstructed $\bar{\nu}_\mu$ CC and Simulated $\bar{\nu}_\mu$ CC events) in 7 E_ν bins.

Evis(GeV)	Generated $N_{\bar{\nu}}^{CC}$	Reconstructed $N_{\bar{\nu}}^{CC}$	Efficiency
2.5-8.0	3970.6	1160.3	0.292
8.0-15.0	6179.3	2566.7	0.415
15.0-20.0	3933.6	1777.5	0.452
20.0-30.0	6098.3	2905.4	0.476
30.0-50.0	7618.3	3782.4	0.496
50.0-100.0	6608.1	3288.7	0.498
100.0-300.0	1491.9	677.0	0.454
2.5-300.0	35900.0	16157.8	0.450

Table 6.7 and Table 6.8 show the generated, reconstructed $\bar{\nu}_\mu$ charged current events, charged current (CC) background, neutral current (NC) background, number of data before normalization with the factor from fit, and raw signal, reconstructed $\bar{\nu}_\mu$ charged current events, background after normalization with respect to Evis. With these numbers, we can calculated the fully corrected signal (The fully corrected signal is the $\bar{\nu}_\mu$ charged current events in this section). Where Normalized Signal equals to the reconstructed signal times the normalization factor I got from fit ($p_{norm}^{'\bar{\nu}_\mu CC} = 1.03$, $p_{norm}^{NC} = 2.03$, $p_{norm}^{\nu_\mu CC} = 1.43$). Raw signal equals to the Number of data in each bin (N_{data}) minus total normalized background in the same bin (Tot-Bkg). Using the Raw signal in each Evis bin divide by the efficiency in the corresponding bin, we get the fully corrected signal in the 7 Evis bins shown in Table 6.9.

Table 6.7: Reconstructed $\bar{\nu}_\mu$ CC events without normalization with the factor from fit.

Evis(GeV)	$N^{CC}_{\bar{\nu}_\mu}$ generated	$N^{CC}_{\bar{\nu}_\mu}$ reconstructed	CC-Bkg	NC-bkg	Tot-Bkg	N_{MC}	N_{data}
2.5-8.0	3970.6	1160.3	21.1	34.2	55.3	1215.6	1260
8.0-15.0	6179.3	2566.7	77.7	44.0	121.7	2688.4	2513
15.0-20.0	3933.6	1777.5	54.3	27.5	81.8	1859.2	1733
20.0-30.0	6098.3	2905.4	95.3	39.3	134.6	3040.0	2997
30.0-50.0	7618.3	3782.4	129.7	50.1	179.8	3962.2	4067
50.0-100.0	6608.1	3288.7	151.1	42.2	193.3	3481.9	4217
100.0-300.0	1491.9	677.0	56.6	13.1	69.7	756.7	1273
2.5-300.0	35900.0	16157.8	585.7	250.4	856.1	16994.0	18060

Table 6.8: Raw signal and fully corrected data after normalization.

Evis(GeV)	$N^{CC}_{\bar{\nu}_\mu}$ Reconstructed	Normalized Signal	Raw Signal	Tot-Bkg	N_{MC}	N_{data}	N_{data}/N_{MC}
2.5-8.0	1160.3	1199.2	1160.4	99.6	1298.8	1260	0.970
8.0-15.0	2566.7	2652.6	2312.7	200.3	2852.9	2513	0.881
15.0-20.0	1777.5	1837.0	1599.6	133.4	1970.4	1733	0.880
20.0-30.0	2905.4	3002.7	2781.0	216.0	3218.7	2997	0.931
30.0-50.0	3782.4	3853.2	3780.0	287.0	4140.2	4067	0.982
50.0-100.0	3288.7	3398.8	3915.4	301.6	3700.4	4217	1.140
100.0-300.0	677.0	699.7	1165.5	107.5	807.2	1273	1.577
2.5-300.0	16157.8	16698.8	16714.7	1345.3	18044.1	18060	1.001

Table 6.9: Fully corrected signal got from efficiency vector (shown in Table 6.6).

Evis(GeV)	Raw Signal	Efficiency	Full Corrected Signal
2.5-8.0	1160.4	0.292	3970.9
8.0-15.0	2312.7	0.415	5567.8
15.0-20.0	1599.6	0.452	3539.9
20.0-30.0	2781.0	0.476	5793.8
30.0-50.0	3780.0	0.496	7613.5
50.0-100.0	3915.4	0.498	7830.8
100.0-300.0	1165.5	0.454	2568.4
2.5-300.0	16714.7	0.450	37137.3

Where, in Table 6.9, the Fully Corrected Signal equals to the Raw Signal divide by Efficiency (Ratio of Reconstructed Signal and Generated Signal). Aside from the efficiency vector, the fully corrected signal in 7 Evis bins are also calculated from the efficiency matrix, which is shown in Table 6.13, which are going to be used as denominator of ratio between the coherent π^- and $\bar{\nu}_\mu$ charged current events.

Table 6.10 shows the number of $\bar{\nu}_\mu$ charged current events as a function of E_ν and Evis before multiple the normalization factor got from the fit. Using the elements in this table times the normalization factors and divide by the generated $\bar{\nu}_\mu$ charged current events in Table 6.6, we can get the efficiency matrix which are shown in Table 6.11.

After get the efficiency matrix, to calculate the Raw signal, the background after normalization is still needed to be considered. The background matrix after normalization is shown in Table 6.12.

Table 6.11 shows the efficiency matrix of $\bar{\nu}_\mu$ charged current event selection in neutrino beam mode analysis. Table 6.12 shows the background matrix in each Evis and E_ν bin. The Raw Signal in each Evis bin can be calculated from the number of NOMAD data minus the number of background after normalization in each bin. The fully corrected signal can be calculated using the number of Raw Signal divide by the efficiency in the same Evis bin, which are shown in Table 6.13.

Table 6.10: $\bar{\nu}_\mu$ CC events as a function of E_ν (Evis) before normalization with the factor got from fit.

E_ν \ Evis	2.5-8.0	8.0-15.0	15.0-20.0	20.0-30.0	30.0-50.0	50.0-100.0	100.0-300.0	2.5-300.0
2.5-8.0	827.4	9.4	0.1	0	0	0	0	837.0
8.0-15.0	331.0	2028.6	22.6	0.1	0	0	0	2382.3
15.0-20.0	1.4	505.2	1221.3	30.0	0.1	0.1	0	1758.1
20.0-30.0	0.4	21.8	527.5	2354.7	44.8	0.4	0	2949.6
30.0-50.0	0.1	1.6	5.7	517.3	3340.8	61.2	0	3926.8
50.0-100.0	0	0.1	0.2	3.1	396.4	3099.6	41.3	3540.6
100.0-300.0	0	0	0	0	0.3	127.4	635.6	763.4
2.5-300.0	1160.3	2566.7	1777.5	2905.4	3782.4	3288.7	677.0	16157.8

Table 6.11: $\bar{\nu}_\mu$ CC efficiency matrix.

E_ν \ Evis	2.5-8.0	8.0-15.0	15.0-20.0	20.0-30.0	30.0-50.0	50.0-100.0	100.0-300.0	2.5-300.0
2.5-8.0	0.21	0	0	0	0	0	0	0.02
8.0-15.0	0.08	0.33	0.01	0	0	0	0	0.07
15.0-20.0	0	0.08	0.31	0	0	0	0	0.05
20.0-30.0	0	0	0.13	0.39	0.01	0	0	0.08
30.0-50.0	0	0	0	0.08	0.44	0.01	0	0.11
50.0-100.0	0	0	0	0	0.05	0.47	0.03	0.10
100.0-300.0	0	0	0	0	0	0.02	0.43	0.02
2.5-300.0	0.29	0.42	0.45	0.48	0.50	0.50	0.45	0.45

Table 6.12: $\bar{\nu}_\mu$ Background matrix(the elements in this table is the total background in each bin).

E_ν \ Evis	2.5-8.0	8.0-15.0	15.0-20.0	20.0-30.0	30.0-50.0	50.0-100.0	100.0-300.0	2.5-300.0
2.5-8.0	13.2	0	0	0	0	0	0	13.2
8.0-15.0	38.0	81.4	2.0	0	0	0	0	121.4
15.0-20.0	0	54.3	42.6	0	0	0	0	96.9
20.0-30.0	0	0	53.4	98.5	8.4	0	0	160.3
30.0-50.0	0	0	0	75.6	142.8	16.2	0	234.6
50.0-100.0	0	0	0	0	103.3	170.1	10.5	283.9
100.0-300.0	0	0	0	0	0	113.1	96.1	209.2
2.5-300.0	51.2	135.7	98.0	174.1	254.5	299.4	106.6	1119.5

Table 6.13: Fully corrected signal got from efficiency matrix.

Evis(GeV)	Raw signal	Efficiency	Fully Corrected Signal
2.5-8.0	1208.8	0.29	4168.3
8.0-15.0	2377.3	0.42	5660.2
15.0-20.0	1635.0	0.45	3633.3
20.0-30.0	2822.9	0.48	5881.0
30.0-50.0	3812.5	0.50	7625.0
50.0-100.0	3917.6	0.50	7835.2
100.0-300.0	1166.4	0.45	2592.0
2.5-300.0	16940.5	0.45	37645.6

Artificial Neural Network Method

To separate signal from background, besides the cuts on kinematic variables, neural network is trained using Monte Carlo events for future separation. Artificial neural networks (ANN or just NN) are widely used in physics data analysis [21]. Most of the neural networks are multilayer perceptions: input layer, at least one hidden layer and output layer. All the layers are made up of interconnected neurons.

1. Input layer. The neurons in a input layer receive the inputs, normalize them and forward them to the first hidden layer [21].

2. Hidden layer. The input to each neuron in a hidden layer is a linear combination of the outputs of the previous layer. The output is a sigmoid function of that combination. A sigmoid function is defined as

$$S(x) = \frac{1}{1+e^{-x}}$$

3. Outputlayer. Each neuron in any subsequent layer is computed as a linear combination of the outputs of the previous layer.

In physics analysis with neural network, at first, we need to take multiple kinematic variables $(I_1, I_2...)$ as input and use a single output to indicate signal or background. $(f = f(I_1, I_2...))$ The neural network should be trained and validated with independent Monte Carlo samples before being used in analysis, to make sure that there

is no over training. The neural network is trained using Monte Carlo events(signal and background) with output equals to 1 for signal and 0 for the background. The aim of using neutral network is to minimize the total error of weighted examples, which is defined as the sum of in quadrature, divided by two, of the error on each individual output neuron. The output of the neural network is the probability of signal against background.

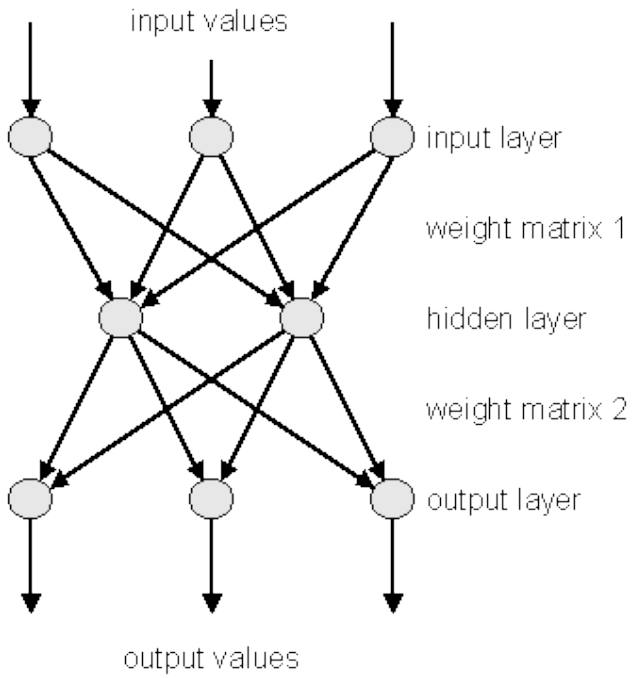

Figure 6.9: An example of the structure of an artificial neutral network [21].

We use TMultiLayerPerceptron class in root to build neural networks. The structure of NN is showed in figure 6.9.

Kinematic Analysis

When the neural network is being used to separate the Coherent π^- signal from background, the first thing we need to decide is which values will be inputs. In this analysis, the following three variables were used as input:

- p_T^m: missing transverse momentum, which is the measurement of the neutrino beam divergence.
- X_{bj}: the fraction of the nucleon's momentum carried by the struck quark.
- ζ_π: $E_\pi \times (1 - \cos(\theta_\pi))$, which means the forwardness of the outgoing Pions.

The principle of choosing input variables includes good separation power and good agreement between Monte Carlo events and data. Using the neural network, there is only one output variable in the coherent π^- analysis, which could be used to separate the signal from background.

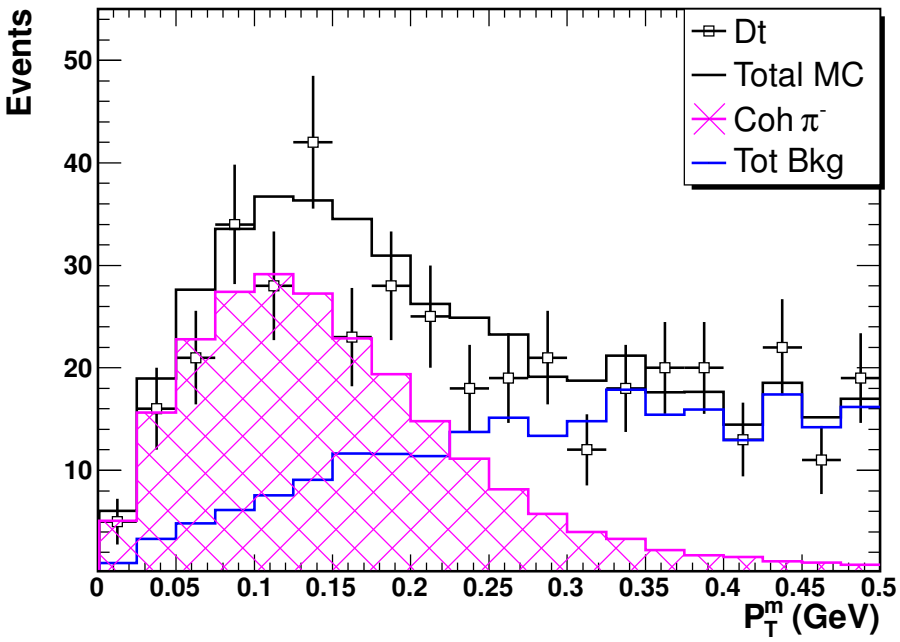

Figure 6.10: P_T^m distribution of the neutrino beam mode data (positive focusing data: FocP).

The distributions of P_T^m, Xbj, and ζ are shown from Figure 6.10 to Figure 6.12. In these figures, the total Monte Carlo events (Tot MC) is the sum of the signal (Coherent π^-) and total background (Tot Bkg).

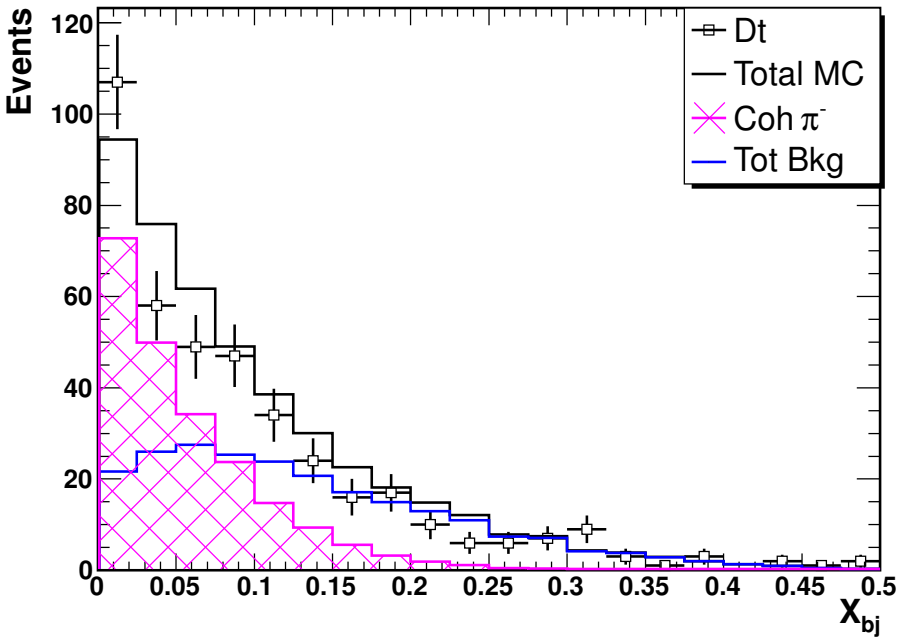

Figure 6.11: Xbj distribution of the neutrino beam mode data (positive focusing data: FocP).

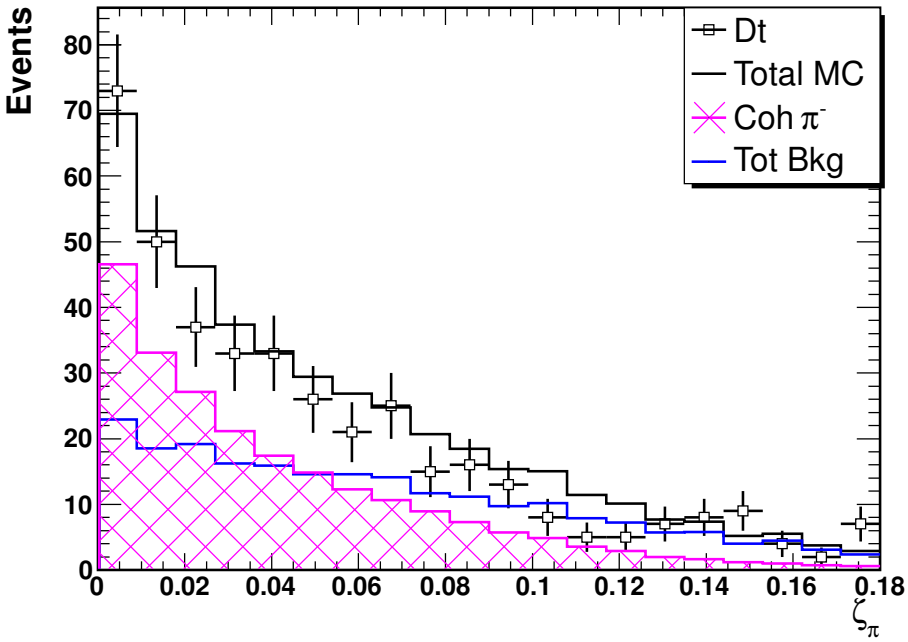

Figure 6.12: ζ distribution of the neutrino beam mode data (positive focusing data: FocP).

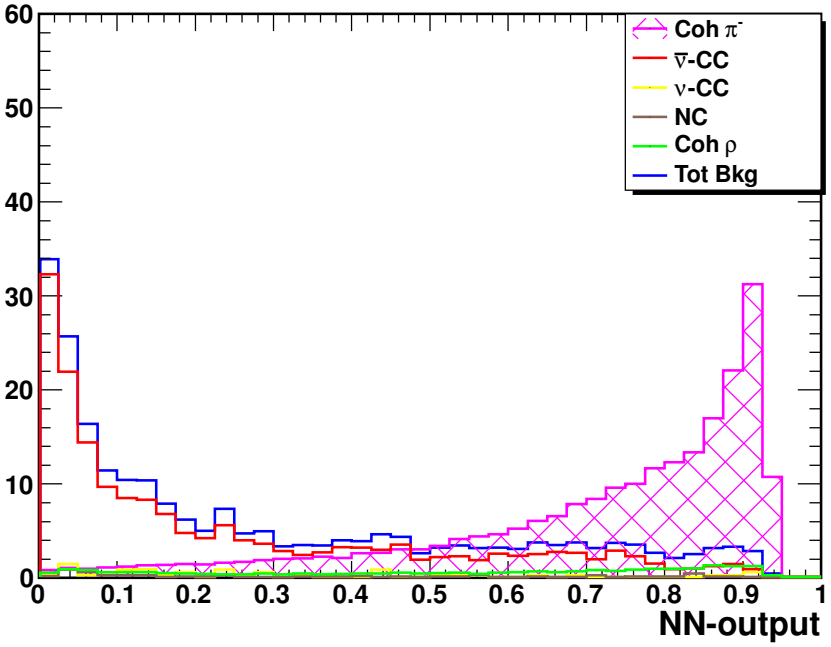

Figure 6.13: The NN distribution comparison of background and signal.

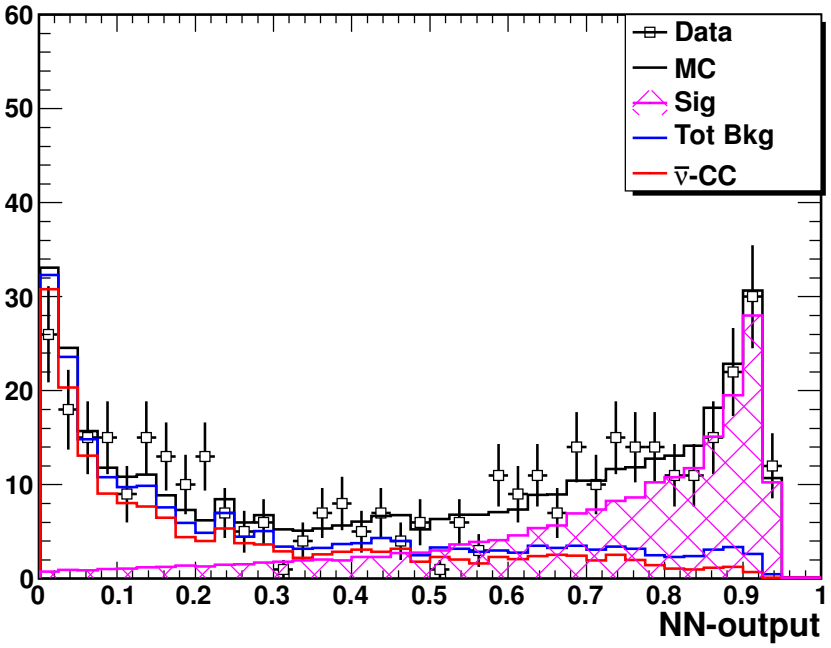

Figure 6.14: The NN distribution comparison of Data and MC.

Figure 6.13 shows the output of the neural network including the distributions of signal (Coherent π^-), $\bar{\nu}_\mu$ CC background, ν_μ CC background, NC background, Coherent ρ^-, total background (TotBkg: sum of CC background, NC background and background from coherent ρ^-) as a function of NN output value, and so on. NN-output is a value from 0 to 1, it is obvious that Background dominates the region NN output less than 0.3, and Signal dominates the region NN output greater than 0.7.

With the output of neural network, the events in background and signal region can be normalized. Let's use BN to represent the Background Normalization factor and SN represent the Signal Normalization factor. They are calculated as following steps:

At first, all the events are divided into 7 bins according to visible energy (Evis) from 2.5 to 300 GeV (Evis={2.5, 8, 15, 20, 30, 50, 100, 300}).

Then fit the Monte Carlo events to NOMAD data bin by bin. The background normalization factor (BN), signal normalization factor (SN), and the number of corrected signal ($N_{corr-sig}$) in each bin are calculated with the following formulas (BNtemp is a temporary factor used to calculate SN):

$\text{BNtemp} = \frac{N_{data}^{b[i]}}{N_{bkg}^{b[i]}}$

$\text{SN} = \frac{(N_{data}^{s[i]} - bntemp \times N_{bkg}^{s[i]})}{N_{sig}^{s[i]}}$;

$\text{BN} = \frac{(N_{data}^{b[i]} - sntemp \times N_{sig}^{b[i]})}{N_{bac}^{b[i]}}$;

$N_{corr-sig} = N_{data}^{s[i]} - N_{bkg}^{s[i]} \times BN$

Where i is the index of Evis bin number. $N_{data}^{s[i]}$ is the number of NOMAD data events in signal region. $N_{data}^{b[i]}$ is the number of NOMAD data events in background region. $N_{bkg}^{s}[i]$ is the number of background events in signal region. $N_{sig}^{b}[i]$ is the number of signal events in background region. $N_{bkg}^{b}[i]$ is the number of background events in background region. $N_{sig}^{s}[i]$ is the number of signal events in signal region.

Coherent π^- in Neutrino Mode

After we got the number of the $\bar{\nu}_\mu$ charged current events in 7 visible energy (Evis) bins, in this section, we will measure the number of coherent π^- in each Evis bin. Both of them are going to be used to calculate the ratio between coherent π^- and $\bar{\nu}_\mu$ charged current interactions.

Table 6.14: Normalization of the MC events.

$\bar{\nu}_\mu$ CC	35900
$\bar{\nu}_\mu$ CC DIS	34028.5
$\bar{\nu}_\mu$ NC DIS	341.05
$\bar{\nu}_\mu$ QE	802.1
$\bar{\nu}_\mu$ RES	1069.5
$\bar{\nu}$ cohPi	417.1
$\bar{\nu}$ cohRho	250.3
ν_μ CC	1436001
ν_μ QE	32084.0
ν_μ RES	42778.6
ν_μ CC DIS	1361138
ν_μ NC DIS	531320.7

Table 6.14 shows the numbers of normalized Monte Carlo events with beamweight (flux reweight) and Z-weight. These numbers are calculated from:

The total number of ν_μ charged current events within Fiducial Volume is normalized to 1436000 [52]; The total number of $\bar{\nu}_\mu$charged current events equals to 0.025 $\times$ 1436000 [8];

The ratio between neutral current and charged current events N^{NC}/N^{CC} equals to 0.37, ratio between non-deep inelastic and deep inelastic events $N^{non-Dis}/N^{Dis}$ equals to 0.055; ratio between quasi-elastic and resonance events N^{QE}/N^{RES} equals to 0.75; ratio between coherent π and quasi-elastic events $N^{Coh-\pi}/N^{QE}$ equals to 0.26; $N^{Coh-\rho}/N^{Coh-\pi}$ equals to 0.6;

Table 6.15: Summary of event reduction in different data and MC samples for the preselection cuts.

	$N_{\bar{\nu}}^{CC}$	N_{ν}^{CC}	N^{NC}	Cohρ^-	TotBkg	Cohπ^-	N_{data}	Ratio
Total	47790.3	1645469	628612.1	289.6	2322161	735.8	–	–
Pfermi	47380.6	1631201	623116.4	289.6	2301988	735.8	–	–
W2S	40610.1	1555351	589725.7	289.6	2185977	735.8	–	–
Gen-FV	36076.4	1436828	544853.6	257.6	2018015	638.3	–	–
E_π>0.5(Coh only)	36076.4	1436828	544853.6	250.3	2018009	417.1	–	–
2.5<Evis<300	35900.0	1436001	544603.7	250.3	2016755	417.1	–	–
total	38919.5	1434877	464599.6	247.4	1938643	590.2	4018980	2.07
pfermi	38595.7	1422826	460710.6	247.4	1922380	590.2	4018980	2.08
W2	33404.4	1357502	460710.6	247.4	1850530	590.2	4018980	2.17
Rec-Fidu	29777.2	1255851	427703.2	219.6	1712318	528.1	3135328	1.83
E_π>0.5(Coh only)	29777.2	1255851	426469.6	201.7	1712300	400.1	3135328	1.83
Ph2mu	27445.9	1111808	15116.2	175.5	1154546	357.6	1240972	1.07
Tube/Veto	27282.6	1107721	15038.4	174.5	1150216	355.3	1185892	1.03
Ncand=2	4218.0	133866.6	567.5	141.1	138793.2	309.2	145171	1.04
μ^+/E_μ	4212.1	253.9	305.4	139.7	4911.1	307.9	10163	1.95
Had-	2568.2	150.4	230.0	138.5	3087.0	305.8	6607	1.95
θ_{μ^+,π^-}<177.5	2566.1	150.4	229.3	138.5	3084.2	305.6	4612	1.36
Fit Matrix error	2548.0	140.1	224.4	137.2	3049.6	303.5	4192	1.25
P_π>1.0	967.8	111.6	137.5	129.2	1346.0	249.8	2180	1.37
θ_{μ^+,π^-}<0.5	689.8	85.0	132.3	128.6	1035.7	239.1	1667	1.31
P_T^m<0.5	296.5	30.1	12.2	116.1	454.9	231.4	754	1.10
$(p_\pi - p_{neu})/(p_\pi + p_{neu}) > 0$	230.0	15.5	8.1	65.8	319.4	230.9	568	1.03
nV0 cut	222.8	14.6	7.9	56.6	301.9	230.7	556	1.04
Nclu cut	190.7	11.2	6.4	25.1	233.5	225.0	470	1.03
mgg<0.5	190.7	11.2	6.4	25.1	233.5	225.0	470	1.03
19512<Run<21270	190.7	11.2	6.4	25.1	233.5	225.0	415	0.91

Table 6.15 shows the summary of event reduction in different data and Monte Carlo samples for the preselection cuts. From this table, we can see that even after all the variable cuts, there is still about 9% disagreement between the Monte Carlo events and NOMAD data.

To get better matches between Monte Carlo events and NOMAD data, neural network training is used in this analysis which has been introduced in previous sections.

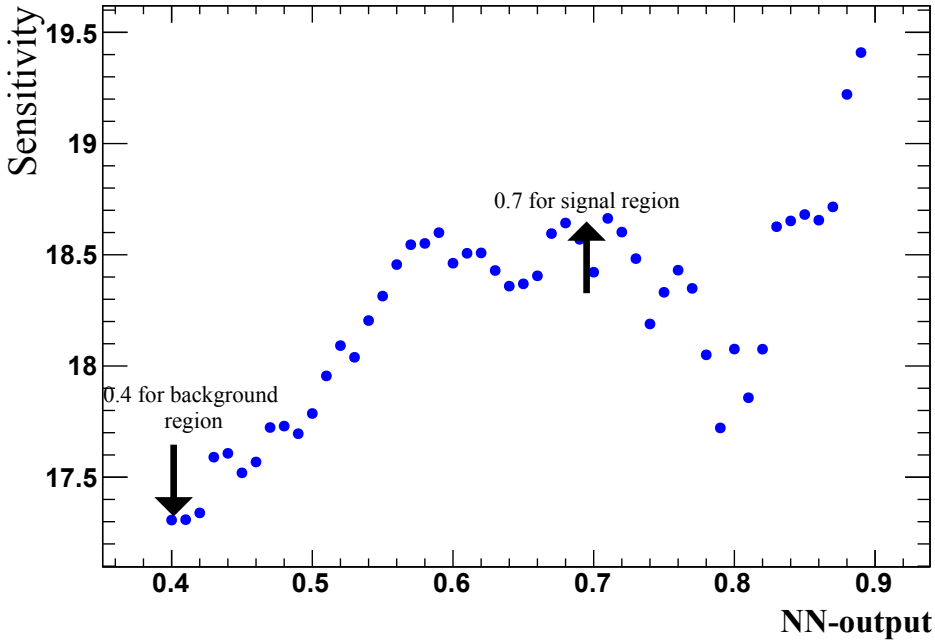

Figure 6.15: The distribution of sensitivity of the neural network in coherent π^- analysis of neutrino beam mode.

Figure 6.15 shows the distributions of the sensitivity which is defined as

$$Sensitivity = \frac{N^{Corr-Sig}}{\sqrt{N^{Corr-Sig} + N^{Norm-Bkg}}}, \tag{6.7}$$

where $N^{Corr-Sig}$ is the number of corrected signal events, $N^{Norm-Bkg}$ is the number of normalized background events. This figure is plotted from the result in Table 6.16. The sensitivity gave us a tool to find the optimal cut values to define the signal and

background regions. Combine the distribution of the sensitivity and Figure 6.13, we finally chose 0.7 as the cut value of signal region and 0.4 as the cut value of background region, then the signal region is from 0.7 to 1 and the background region is from 0 to 0.4. The background region is going to be used to calibrate the background of NOMAD data. The region from 0.4 to 0.7 is not ideal region either for background normalization or measurement of signal. Because the ratio of signal to background is too close to 1.

Some kinematic variable distributions in background (control) region and signal region after neural network are shown from Figure 6.16 to Figure 6.35. It is obvious that there is a good agreement between Monte Carlo events and NOMAD data after the neural network analysis. In these figures, "Dt" represents NOMAD data; "Total MC" represents total Monte Carlo events; "Tot Bkg" represents total background events; "$\bar{\nu}$ CC" represents $\bar{\nu}_\mu$ charged current events; "ν CC" represents ν_μ charged current events; "NC" represents the combination of $\bar{\nu}_\mu$ and ν_μ neutral current events; "Coh π^-" represents the coherent π^- events, which is also the signal in this analysis, "Coh ρ^-" represents the coherent ρ^- events. All the variable distributions are consistent with the theoretical prediction. For example, the signal (coherent π^- events) is with a lower value of Q^2 compared to the background. The Bjorken variable Xbj is defined as

$$Xbj = \frac{Q^2}{2M\nu}, \tag{6.8}$$

when the target is at rest. Xbj is also very small compared to the background. The missing transverse momentum P_T^m of signal is smaller compared to the background. ζ_π which represent the forwardness of the outgoing hadron is also a smaller value compared to the background, which means the meson Pion is very forward outgoing. The magnitudes of the square of the 4 momentum transfer to the nucleus |t| of signal is also very small compared to the background. The angle between the leading lepton μ^+ and the outgoing meson π^- of signal is smaller compared to the background. All

other variable distributions also gave a good agreement between the Monte Carlo events and NOMAD data and are also consistent with the theoretical predictions. In next step, the neural network analysis will be used to separate the signal from background.

Table 6.16 gives out the result of total number of background (Tot-Bkg), background normalization factor (BN), normalized background, number of Data, Raw signal (Raw Sig: which equals to the number of data minus the normalized background), Efficiency (Eff: which equals to the raw signal divide by the number of Data), and corrected signal (Corr-Sig: which equals to raw signal divide by efficiency) with different NN cut values. The corrected signal error includes the statistical error and the error comes from the background normalization.

Figure 6.36 shows a coherent π^- sample picture after all the kinematic cuts and neural network output cut of NOMAD events. In this figure, there are only two tracks are observed. The longer one is identified as Muon (μ^+) which is also called leading lepton. The shorter one is identified as Pion (π^-). Some values of this event are listed in Table 6.17. These values are consistent with the theoretical prediction described before, such as the small 4-momentum transfer Q^2, the small missing transverse momentum P_T^m, the small value of forwardness of meson ζ_π, the small value of angle between Muon and Pion.

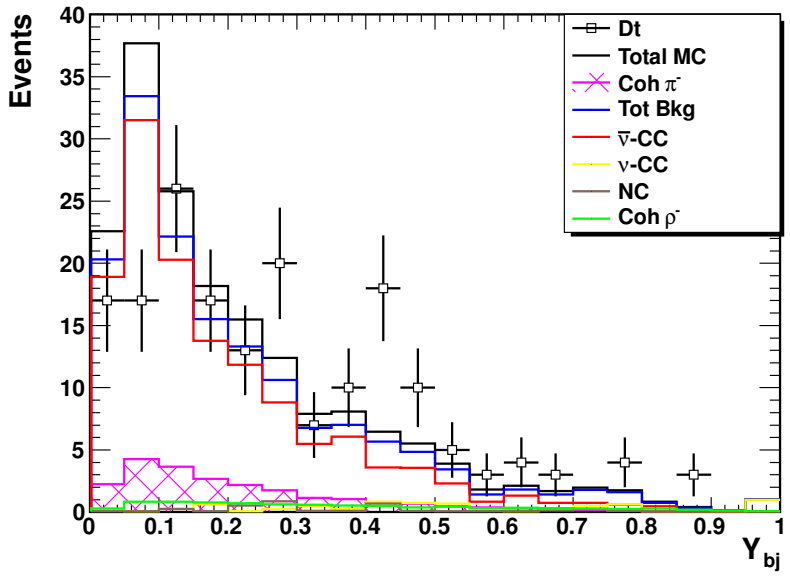

Figure 6.16: The Y_{bj} distribution from different contributions, ν-CC, $\bar{\nu}$-CC, NC, $\bar{\nu}$-Cohρ^- and Cohπ^- in *background (control) region* and the Comparison between Data (points with error bars) and MC(histogram).

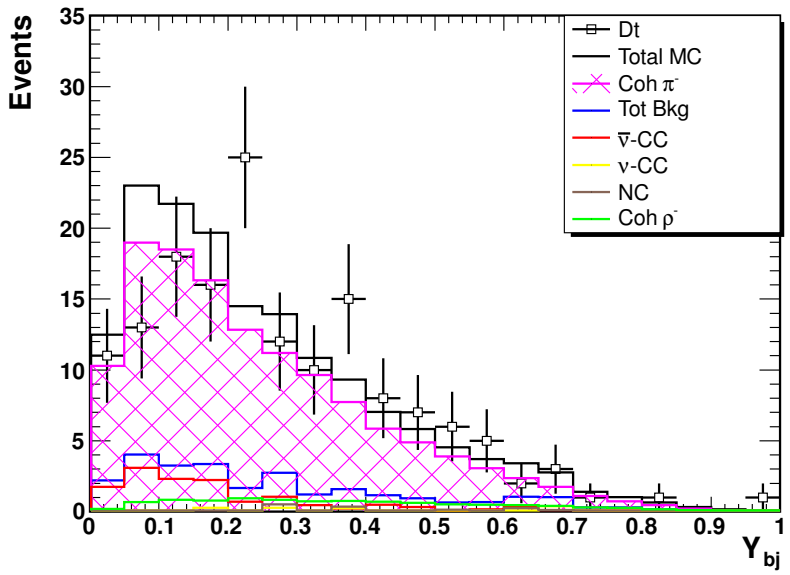

Figure 6.17: The Y_{bj} distribution from different contributions, ν-CC, $\bar{\nu}$-CC, NC, $\bar{\nu}$-Cohρ^- and Cohπ^- in *signal (>0.7) region* and the Comparison between Data (points with error bars) and MC(histogram).

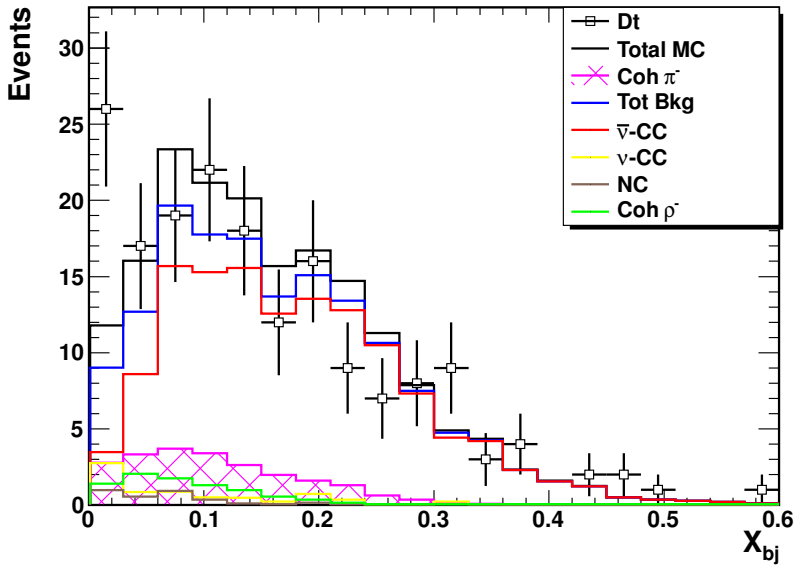

Figure 6.18: The X_{bj} distribution from different contributions, ν-CC, $\bar{\nu}$-CC, NC, $\bar{\nu}$-Cohρ^- and Cohπ^- in *background (control) region* and the Comparison between Data (points with error bars) and MC(histogram).

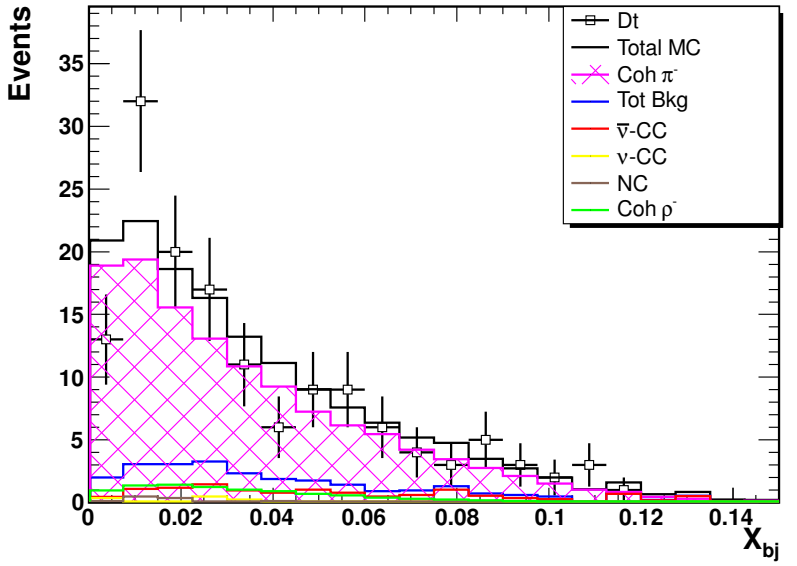

Figure 6.19: The X_{bj} distribution from different contributions, ν-CC, $\bar{\nu}$-CC, NC, $\bar{\nu}$-Cohρ^- and Cohπ^- in *signal (>0.7) region* and the Comparison between Data (points with error bars) and MC(histogram).

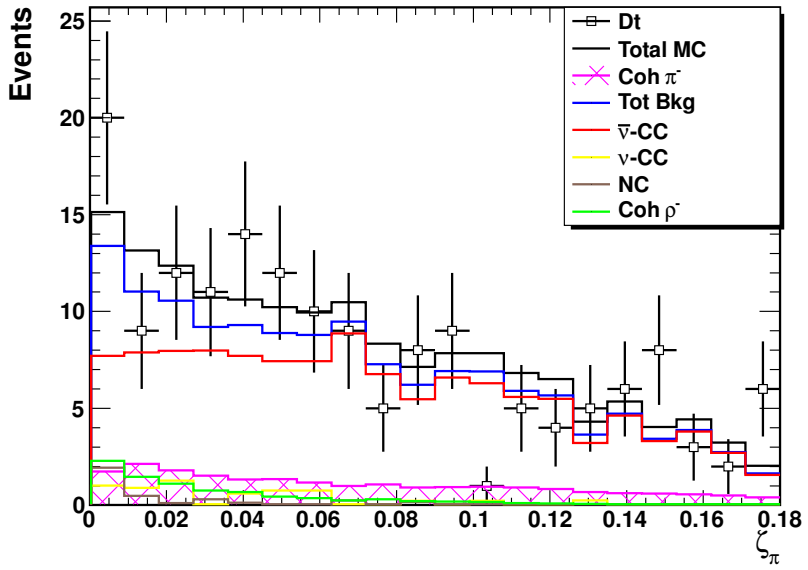

Figure 6.20: The ζ_π distribution from different contributions, ν-CC, $\bar{\nu}$-CC, NC, $\bar{\nu}$-Cohρ^- and Cohπ^- in *background (control) region* and the Comparison between Data (points with error bars) and MC(histogram).

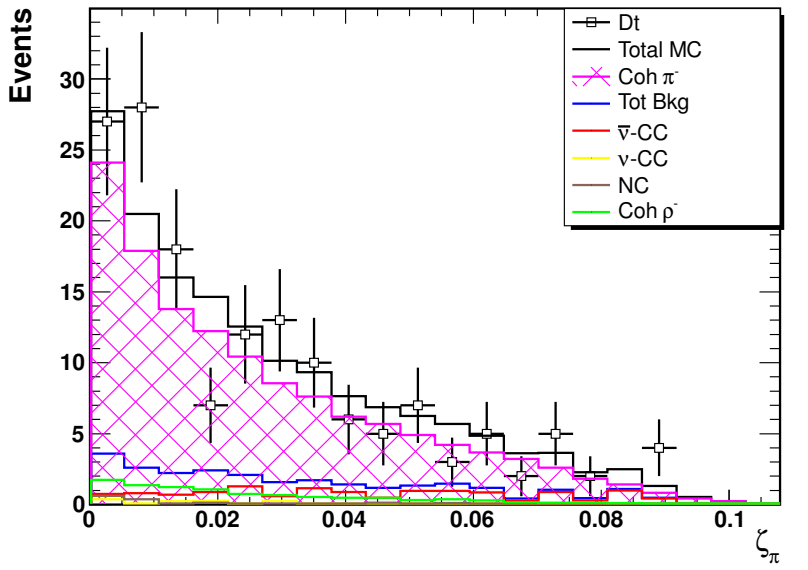

Figure 6.21: The ζ_π distribution from different contributions, ν-CC, $\bar{\nu}$-CC, NC, $\bar{\nu}$-Cohρ^- and Cohπ^- in *signal (>0.7) region* and the Comparison between Data (points with error bars) and MC(histogram).

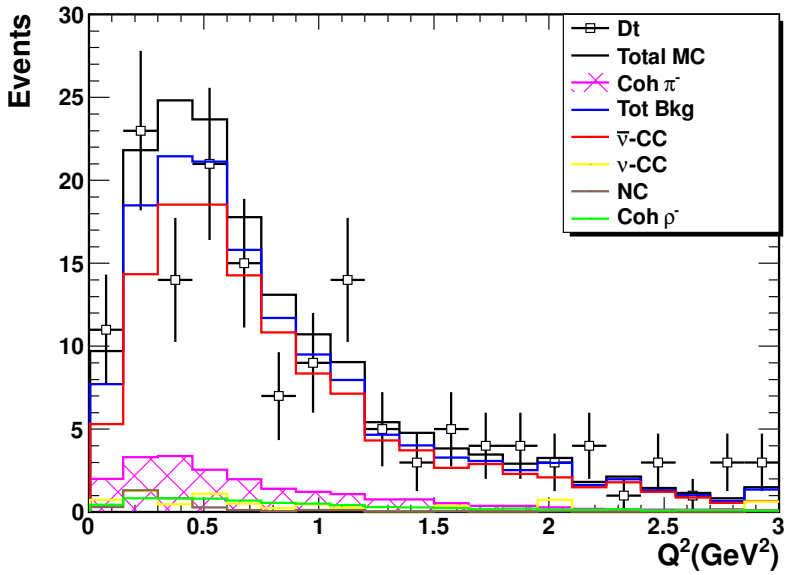

Figure 6.22: The Q^2 distribution from different contributions, ν-CC, $\bar{\nu}$-CC, NC, $\bar{\nu}$-Cohρ^- and Cohπ^- in *background (control) region* and the Comparison between Data (points with error bars) and MC(histogram).

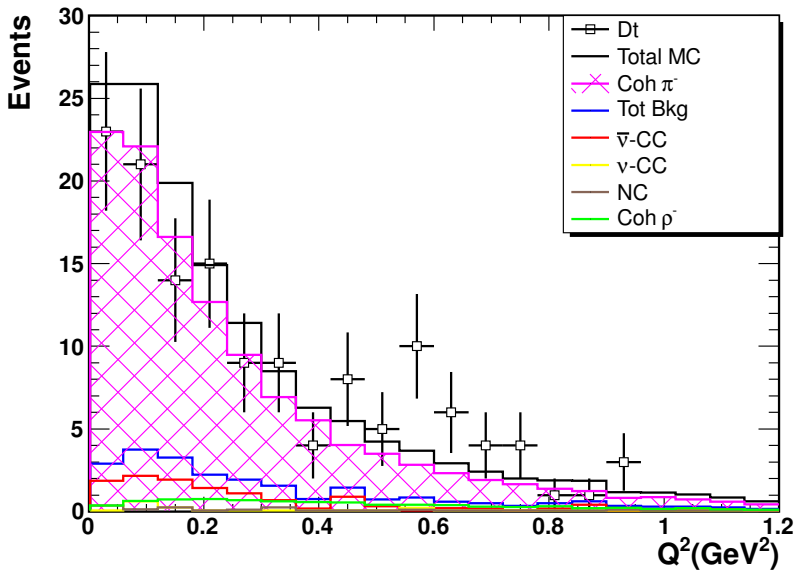

Figure 6.23: The Q^2 distribution from different contributions, ν-CC, $\bar{\nu}$-CC, NC, $\bar{\nu}$-Cohρ^- and Cohπ^- in *signal (>0.7) region* and the Comparison between Data (points with error bars) and MC(histogram).

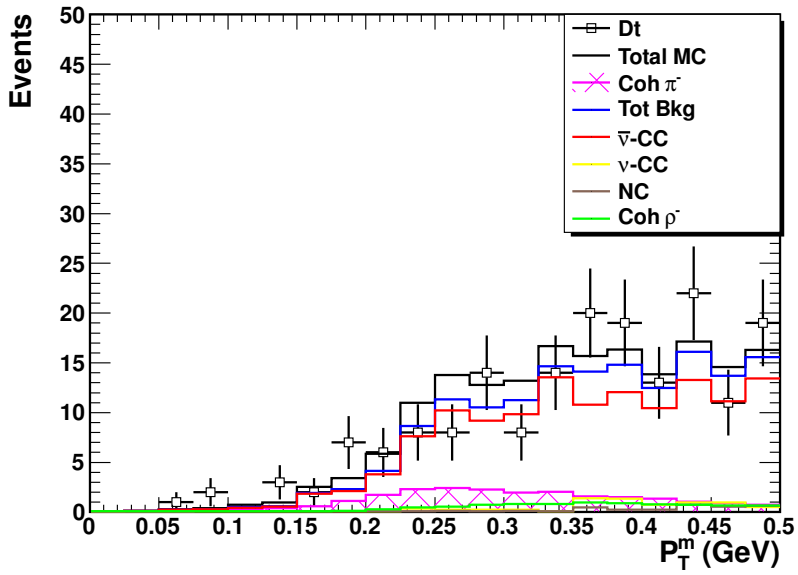

Figure 6.24: The P_T^m distribution from different contributions, ν-CC, $\bar{\nu}$-CC, NC, $\bar{\nu}$-Cohρ^- and Cohπ^- in *background (control) region* and the Comparison between Data (points with error bars) and MC(histogram).

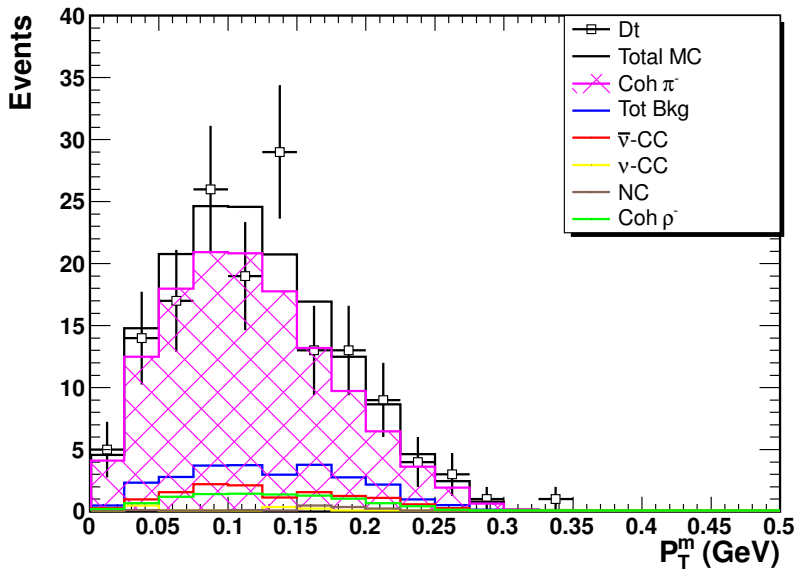

Figure 6.25: The P_T^m distribution from different contributions, ν-CC, $\bar{\nu}$-CC, NC, $\bar{\nu}$-Cohρ^- and Cohπ^- in *signal (>0.7) region* and the Comparison between Data (points with error bars) and MC(histogram).

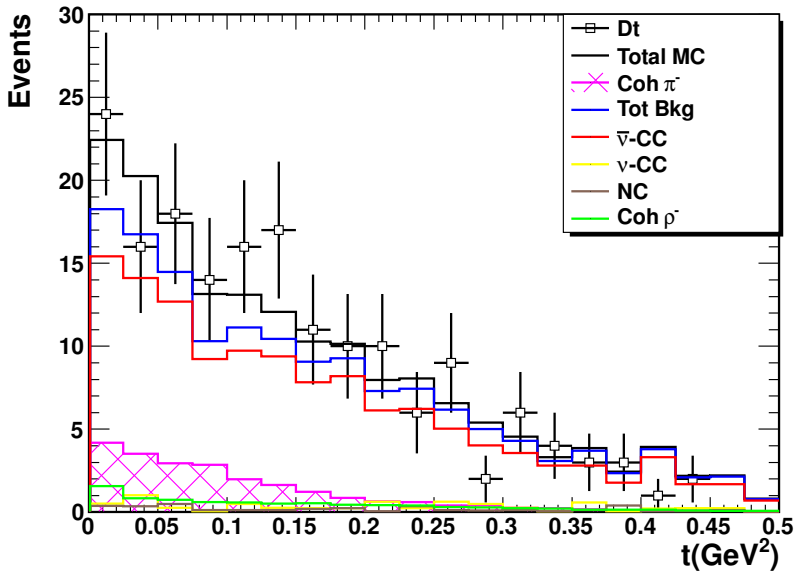

Figure 6.26: The t distribution from different contributions, ν-CC, $\bar{\nu}$-CC, NC, $\bar{\nu}$-Cohρ^- and Cohπ^- in *background (control) region* and the Comparison between Data (points with error bars) and MC(histogram).

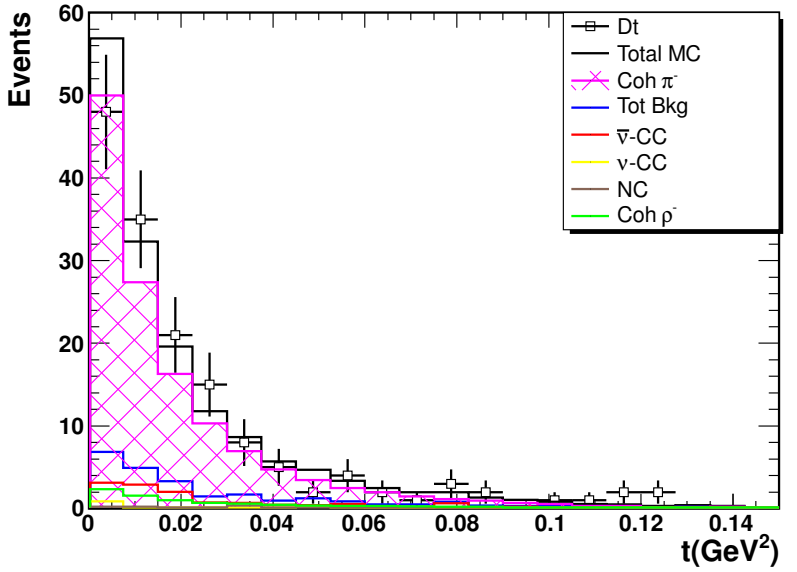

Figure 6.27: The t distribution from different contributions, ν-CC, $\bar{\nu}$-CC, NC, $\bar{\nu}$-Cohρ^- and Cohπ^- in *signal (>0.7) region* and the Comparison between Data (points with error bars) and MC(histogram).

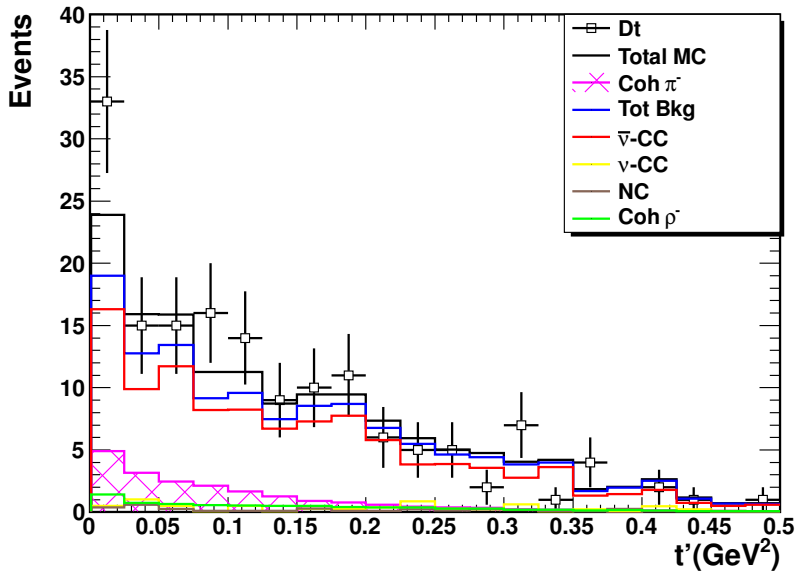

Figure 6.28: The t' distribution from different contributions, ν-CC, $\bar{\nu}$-CC, NC, $\bar{\nu}$-Cohρ^- and Cohπ^- in *background (control) region* and the Comparison between Data (points with error bars) and MC(histogram).

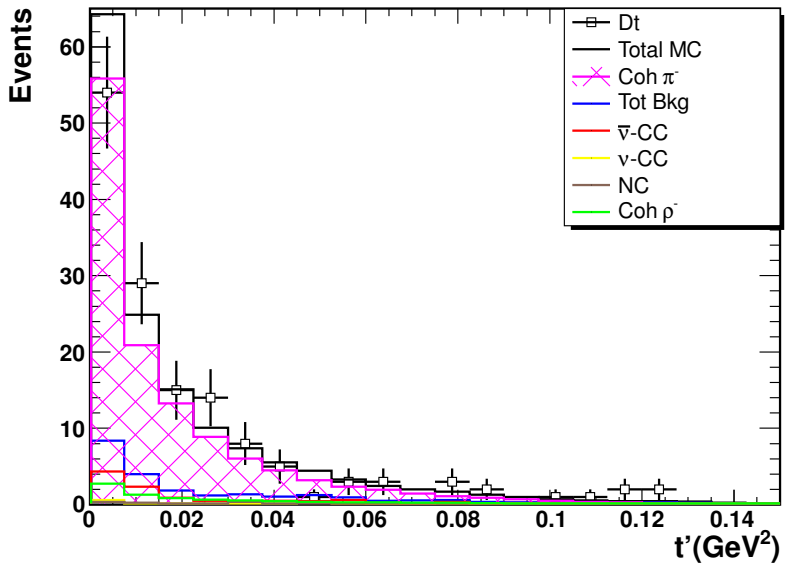

Figure 6.29: The t' distribution from different contributions, ν-CC, $\bar{\nu}$-CC, NC, $\bar{\nu}$-Cohρ^- and Cohπ^- in *signal (>0.7) region* and the Comparison between Data (points with error bars) and MC(histogram).

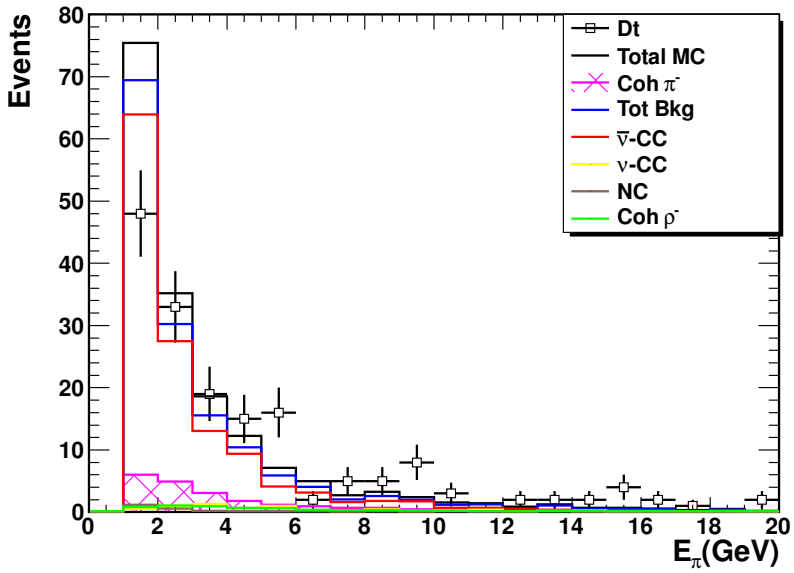

Figure 6.30: The E_π distribution from different contributions, ν-CC, $\bar{\nu}$-CC, NC, $\bar{\nu}$-Cohρ^- and Cohπ^- in *background (control) region* and the Comparison between Data (points with error bars) and MC(histogram).

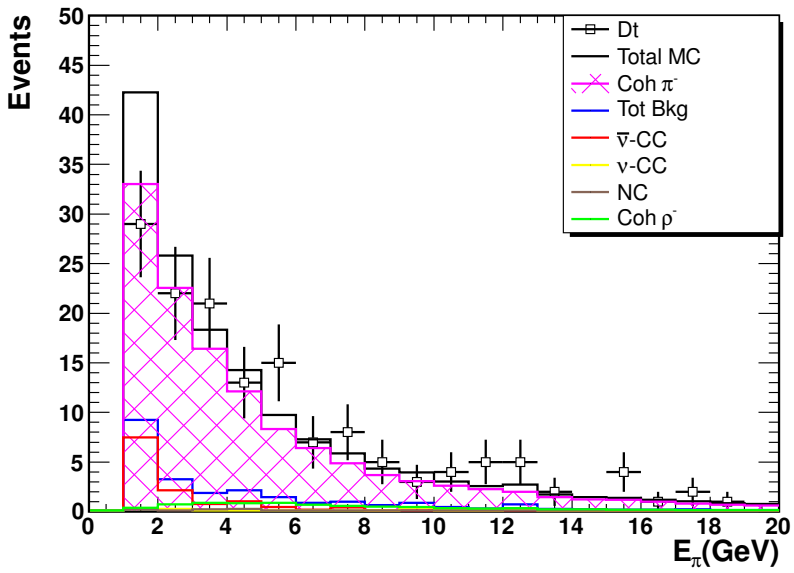

Figure 6.31: The E_π distribution from different contributions, ν-CC, $\bar{\nu}$-CC, NC, $\bar{\nu}$-Cohρ^- and Cohπ^- in *signal (>0.7) region* and the Comparison between Data (points with error bars) and MC(histogram).

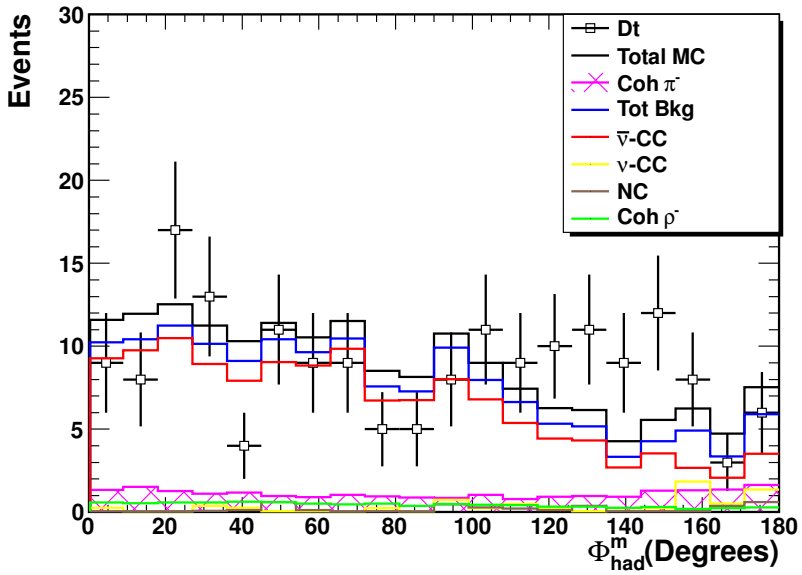

Figure 6.32: The Φ_{had}^{PT} distribution from different contributions, ν-CC, $\bar{\nu}$-CC, NC, $\bar{\nu}$-Cohρ^- and Cohπ^- in *background (control) region* and the Comparison between Data (points with error bars) and MC(histogram).

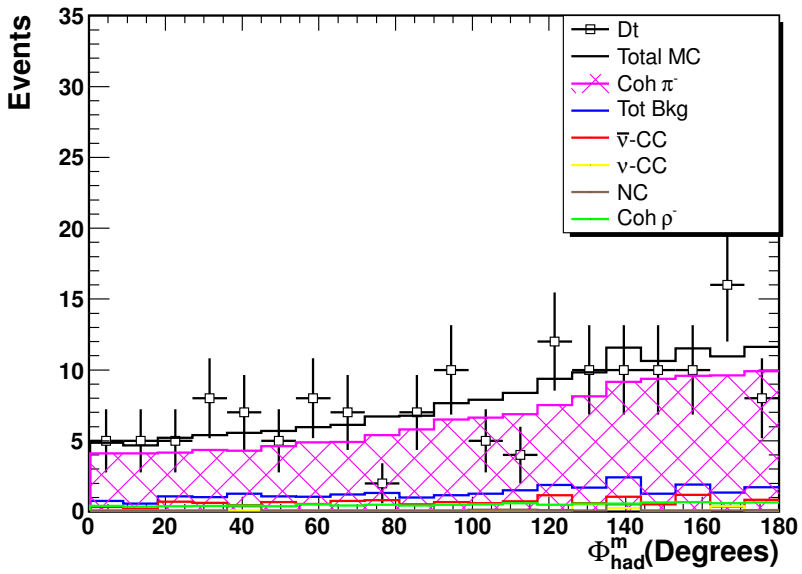

Figure 6.33: The Φ_{had}^{PT} distribution from different contributions, ν-CC, $\bar{\nu}$-CC, NC, $\bar{\nu}$-Cohρ^- and Cohπ^- in *signal (>0.7) region* and the Comparison between Data (points with error bars) and MC(histogram).

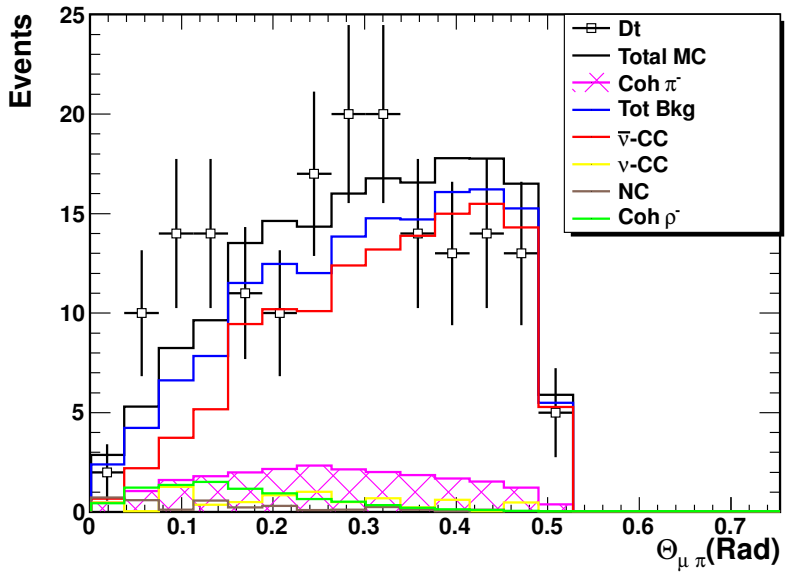

Figure 6.34: The angleθ between Muon and Pion distribution from different contributions, ν-CC, $\bar{\nu}$-CC, NC, $\bar{\nu}$-Cohρ^- and Cohπ^- in *background (control) region* and the Comparison between Data (points with error bars) and MC(histogram).

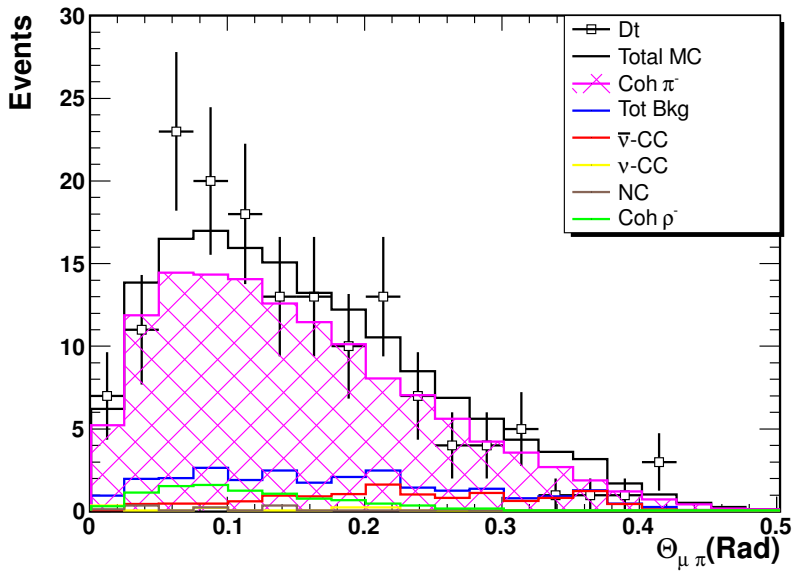

Figure 6.35: The angle θ distribution from different contributions, ν-CC, $\bar{\nu}$-CC, NC, $\bar{\nu}$-Cohρ^- and Cohπ^- in *signal (>0.7) region* and the Comparison between Data (points with error bars) and MC(histogram).

Table 6.16: The NN cut table (the beam(flux) reweight is applied to all the $\bar{\nu}_\mu$-CC events).

NN	Tot-Bkg	BN	Norm-Bkg	Data	Raw Sig.	Eff.	Corr-Sig. (Err = Stat., BN)
0.4	70.6	0.95	67.1	238	171	0.48	356 ± 36.72 ± 17.12
0.41	68.9	0.95	65.5	235	169	0.478	354.9 ± 36.63 ± 16.81
0.42	67.7	0.95	64.3	233	169	0.475	355.1 ± 36.62 ± 16.59
0.43	65.2	0.948	61.8	233	171	0.473	362.2 ± 36.66 ± 16.07
0.44	64.1	0.948	60.7	231	170	0.47	362 ± 36.65 ± 15.87
0.45	62	0.949	58.9	226	167	0.467	357.5 ± 36.42 ± 15.45
0.46	60.6	0.949	57.5	224	166	0.465	358.2 ± 36.41 ± 15.19
0.47	58.8	0.948	55.7	223	167	0.462	362.4 ± 36.46 ± 14.82
0.48	57.1	0.948	54.1	220	166	0.459	361.4 ± 36.37 ± 14.49
0.49	56	0.949	53.1	217	164	0.456	359.4 ± 36.32 ± 14.3
0.5	55	0.948	52.1	216	164	0.453	361.9 ± 36.43 ± 14.14
0.51	53.8	0.946	50.9	216	165	0.45	367.1 ± 36.59 ± 13.92
0.52	52.3	0.944	49.4	215	166	0.446	370.9 ± 36.7 ± 13.66
0.53	51.6	0.945	48.8	212	163	0.443	368.5 ± 36.72 ± 13.57
0.54	50	0.943	47.2	211	164	0.439	373.3 ± 36.88 ± 13.28
0.55	48.3	0.942	45.5	209	163	0.435	376 ± 36.94 ± 12.94
0.56	47.1	0.941	44.3	208	164	0.43	380.3 ± 37.14 ± 12.73
0.57	45.6	0.94	42.9	206	163	0.426	382.5 ± 37.23 ± 12.47
0.58	44.6	0.94	41.9	203	161	0.422	381.9 ± 37.32 ± 12.3
0.59	42.9	0.94	40.3	200	160	0.418	382.4 ± 37.34 ± 11.97
0.6	41.9	0.942	39.5	195	156	0.413	376.6 ± 37.26 ± 11.81
0.61	40.5	0.942	38.1	192	154	0.408	377.1 ± 37.36 ± 11.56
0.62	39.6	0.942	37.3	189	152	0.403	376.5 ± 37.49 ± 11.44
0.63	38	0.944	35.8	184	148	0.398	372.3 ± 37.4 ± 11.11
0.64	36.5	0.945	34.5	179	144	0.392	368.6 ± 37.41 ± 10.86
0.65	35	0.946	33.1	175	142	0.386	367.8 ± 37.49 ± 10.56
0.66	33.9	0.945	32	172	140	0.38	368.2 ± 37.67 ± 10.37
0.67	32.3	0.943	30.4	170	140	0.373	373.9 ± 38.02 ± 10.07
0.68	30.5	0.943	28.8	166	137	0.367	374.3 ± 38.14 ± 9.686
0.69	29.4	0.944	27.7	161	133	0.36	370.6 ± 38.26 ± 9.509
0.7	27.7	0.947	26.2	154	128	0.351	363.8 ± 38.26 ± 9.183
0.71	26	0.944	24.6	152	127	0.343	371.4 ± 38.77 ± 8.836
0.72	25.1	0.945	23.7	147	123	0.335	368.3 ± 39.06 ± 8.735
0.73	23.8	0.947	22.5	141	118	0.326	362.8 ± 39.18 ± 8.49
0.74	22.6	0.952	21.5	133	111	0.318	351.1 ± 39.14 ± 8.292
0.75	20.8	0.95	19.7	129	109	0.308	354.7 ± 39.58 ± 7.852
0.76	19.3	0.949	18.3	125	107	0.299	357.1 ± 40.04 ± 7.524
0.77	17.9	0.951	17	119	102	0.289	352.9 ± 40.31 ± 7.206
0.78	16.6	0.955	15.9	111	95.1	0.279	341 ± 40.34 ± 6.937
0.79	15.6	0.96	15	103	88	0.268	328.4 ± 40.47 ± 6.771
0.8	14.5	0.956	13.9	101	87.1	0.256	340.1 ± 41.8 ± 6.614
0.81	13.4	0.959	12.9	94	81.1	0.245	331.3 ± 42.17 ± 6.389
0.82	12.7	0.956	12.2	91	78.8	0.233	338.5 ± 43.54 ± 6.365
0.83	11.7	0.949	11.2	90	78.8	0.22	357.8 ± 45.55 ± 6.209
0.84	11.2	0.949	10.6	85	74.4	0.208	358.2 ± 46.97 ± 6.264
0.85	9.86	0.949	9.36	79	69.6	0.194	358.1 ± 48.23 ± 5.908
0.86	8.48	0.95	8.05	72	63.9	0.18	355.9 ± 49.7 ± 5.496
0.87	7.34	0.949	6.97	65	58	0.163	357.1 ± 52.08 ± 5.258
0.88	6.09	0.943	5.74	60	54.3	0.145	375.1 ± 55.92 ± 4.905
0.89	4.93	0.94	4.64	52	47.4	0.124	381.3 ± 60.45 ± 4.625

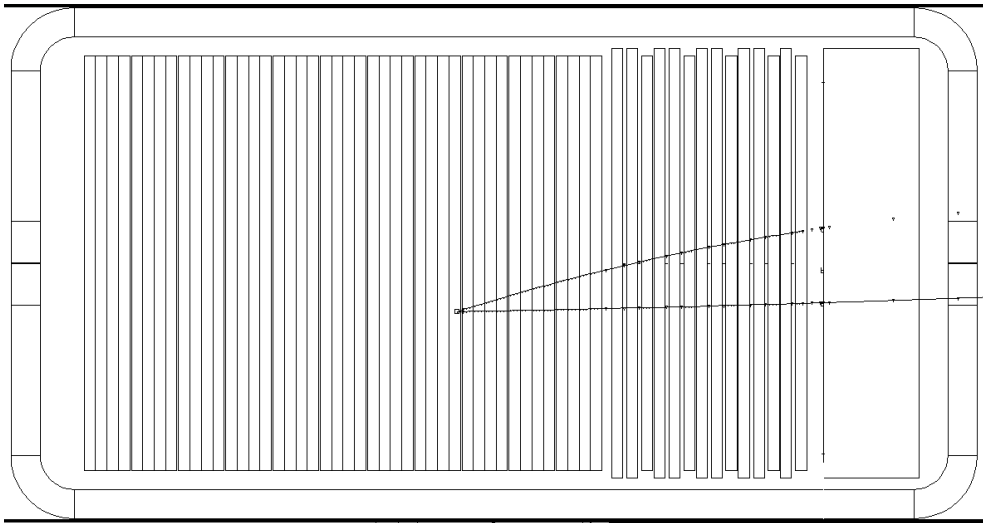

Figure 6.36: Coherent π^- event picture originated by $\bar{\nu}_\mu$ contamination in the neutrino mode.

Table 6.17: Kinematic information of a coherent π^- event corresponding to Figure 6.36 survived from preselection and Neural Network.

Anti-neutrino Beam Mode							
Run	Event	NN(lh)	XVR	YVR	ZVR		
19796	11602	0.606	24.3	-37.8	291		
P_T^m	Φ_{LH}	Φ_{mPtH}	$\Theta_{\mu\pi}$	t	ζ	Xbj	Ybj
0.0919	177	20.6	0.308	0.0256	0.0857	0.125	0.0799
Ncand	Nprim	Nsecond	Nvzero	nhitMuon	nhithad		
2	2	0	0	14	13		
particle	E	|P|	Px	Py	Pz	Θ	Φ
Muon	25.3	25.3	-0.271	-0.633	25.3	1.56	66.9
Pion	2.19	2.19	0.21	0.568	2.1	16.1	69.7

Determination of the Coherent π^- Cross-section

Instead of calculating the absolute cross-section of coherent π^- interactions in NOMAD, the R defined in Equation 6.9 is calculated as the ratio between the cross-section of coherent π^- events and inclusive $\bar{\nu}_\mu$ charged current cross-section.

$$R = \frac{\sigma(Coh\pi^-)}{\sigma(\bar{\nu}_\mu CC)}. \tag{6.9}$$

We calculated R instead of the absolute cross-sections for two reasons: one is normalization; the other one is, some systematic uncertainties can be removed because they share the same systematic uncertainties. The numbers of inclusive $\bar{\nu}_\mu$ charged current events in each bin have been shown in Table 6.13. Next step, we are going to calculate the coherent π^- in each bin.

Table 6.18: BN and SN table in 7 visible energy (Evis) bins, calculated from variable BN depends on the Evis(R=$\frac{\sigma(Coh\pi^-)}{\sigma(\bar{\nu}_\mu CC)}$).

Evis(GeV)	BN	SN	δ_{BN}	R$\times 10^{-3}$(Stat.)
2.5-8.0	0.7865	0.6167	0.2622	14.520$\pm$ 5.224
8.0-15.0	0.835	0.8941	0.1996	16.490$\pm$ 3.333
15.0-20.0	1.213	0.5591	0.3541	7.851 $\pm$ 3.217
20.0-30.0	0.8609	1.179	0.2712	12.760$\pm$ 2.608
30.0-50.0	0.8089	0.9373	0.2715	7.362 $\pm$ 1.795
50.0-100.0	1.658	0.9211	0.627	4.094 $\pm$ 1.668
100.0-300.0	0.4954	1.943	1.251	3.894 $\pm$ 2.341
2.5-300.0	0.9444	0.8886	0.1165	9.845 $\pm$ 1.047

Table 6.18 and Table 6.19 show the result of R (ratio between coherent π^- and $\bar{\nu}_\mu$ charged current events.) in 7 visible energy (Evis) bins which are calculated from variable BN and fixed BN.

Figure 6.37 shows the distribution of BN as a function of visible energy (Evis) in 7 bins, which are corresponding to the result in Table 6.18.

Table 6.19: BN and SN table in 7 visible energy (Evis) bins, using a fixed BN(R=$\frac{\sigma(Coh\pi^-)}{\sigma(\bar{\nu}_\mu CC)}$).

Evis(GeV)	BN	SN	δ_{BN}	R$\times 10^{-3}$(Stat.)
2.5-8.0	0.9444	0.6167	0.1165	13.770± 5.257
8.0-15.0	0.9444	0.8941	0.1165	16.080± 3.327
15.0-20.0	0.9444	0.5591	0.1165	8.492 ± 2.966
20.0-30.0	0.9444	1.179	0.1165	12.600± 2.588
30.0-50.0	0.9444	0.9373	0.1165	7.138 ± 1.780
50.0-100.0	0.9444	0.9211	0.1165	4.748 ± 1.406
100.0-300.0	0.9444	1.943	0.1165	3.615 ± 2.294
2.5-300.0	0.9444	0.8886	0.1165	9.845 ± 1.047

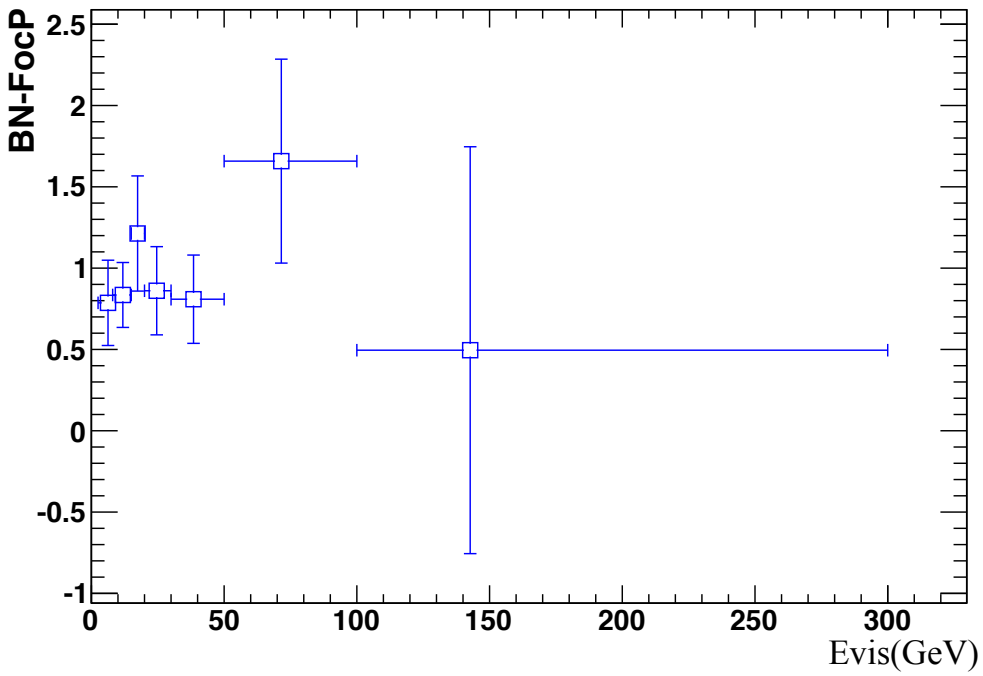

Figure 6.37: The distribution of BN as a function of visible energy (Evis) in 7 bins(the beam(flux) reweight is applied to all the $\bar{\nu}_\mu$-CC events).

Table 6.20: Signal in signal region, and Generated signal information calculated from variable BN.

Evis(GeV)	Sig-S	Sig-Gen	Efficiency
2.5 - 8.0	19.262	98.158	0.197
8.0 - 15.0	39.467	104.391	0.378
15.0 - 20.0	20.909	51.016	0.410
20.0 - 30.0	27.114	63.615	0.426
30.0 - 50.0	26.177	59.890	0.437
50.0 - 100.0	15.043	34.827	0.432
100.0 - 300.0	1.908	5.195	0.367
2.5 - 300.0	150	417.1	0.360

Table 6.21: Norm-bkg, Corr-sig as a function of Evis in 7 bins calculated from variable BN.

Evis	Tot-bkg	BN	Norm-bkg	Data	Raw-sig	Eff	Corr-Sig. (Err=Stat., BN)
2.5 - 8.0	3.89	0.787	3.06	15	11.9	0.197	60.53 ± 21.15 ± 5.17
8.0 - 15.0	8.04	0.835	6.71	42	35.3	0.378	93.34 ± 18.38 ± 4.243
15.0 - 20.0	3.55	1.21	4.31	16	11.7	0.41	28.52 ± 11.28 ± 3.068
20.0 - 30.0	4.67	0.861	4.02	36	32	0.426	75.03 ± 15.04 ± 2.972
30.0 - 50.0	5.52	0.809	4.46	29	24.5	0.437	56.13 ± 13.25 ± 3.428
50.0 - 100.0	3.1	1.66	5.14	19	13.9	0.432	32.08 ± 12.27 ± 4.502
100.0 - 300.0	0.591	0.495	0.293	4	3.71	0.367	10.09 ± 5.724 ± 2.015
2.5 - 300.0	29.4	0.944	27.7	161	133	0.36	370.6 ± 38.26 ± 9.509

Table 6.20 shows the Efficiency as a function of visible energy (Evis) in 7 bins, which are calculated from ratio of the signal in signal region (Sig-S) after all the kinematic variable cuts and generated signal (Sig-Gen).

Table 6.21 shows the result of total background (Tot-bkg), BN, normalized background (Norm-bkg), data, raw signal (Raw-sig), Efficiency (Eff), corrected signal (Corr-Sig) in 7 Evis bins. Norm-bkg equals to Tot-bkg times BN. Raw-sig equals to data minus Norm-bkg. The Corr-Sig equals to the Raw-sig divide by Efficiency. Table 6.22 and Table 6.23 show the result of R=$\frac{\sigma(Coh\pi^-)}{\sigma(\bar{\nu}_\mu CC)}$ calculated from variable BN of neutrino beam mode data (Positive focusing data: FocP) in 7 Evis and E_ν bins.

Figure 6.38 and Figure 6.39 show the distributions of R=$\frac{\sigma(Coh\pi^-)}{\sigma(\bar{\nu}_\mu CC)}$ and R×E in both linear scale (top) and log scale (bottom), where R is calculated using a variable BN.

Table 6.22: Corrected signal (Corr-Sig) as a function of Evis in 7 bins calculated from variable BN(R=$\frac{\sigma(Coh\pi^-)}{\sigma(\bar{\nu}_\mu CC)}$).

Evis	<E>	Corr-Sig	$\bar{\nu}_\mu$-CC	R $\times 10^{-3}$(Stat.)
2.5 - 8	6.25	60.53	4168.3	14.520 ± 5.224
8 - 15	11.84	93.34	5660.2	16.490 ± 3.333
15 - 20	17.40	28.52	3633.3	7.851 ± 3.217
20 - 30	24.60	75.03	5881.0	12.760 ± 2.608
30 - 50	38.47	56.13	7625.0	7.362 ± 1.795
50 - 100	71.54	32.08	7835.2	4.094 ± 1.668
100 - 300	142.70	10.09	2592.0	3.894 ± 2.341
2.5 - 300	25.00	370.6	37645.6	9.845 ± 1.047

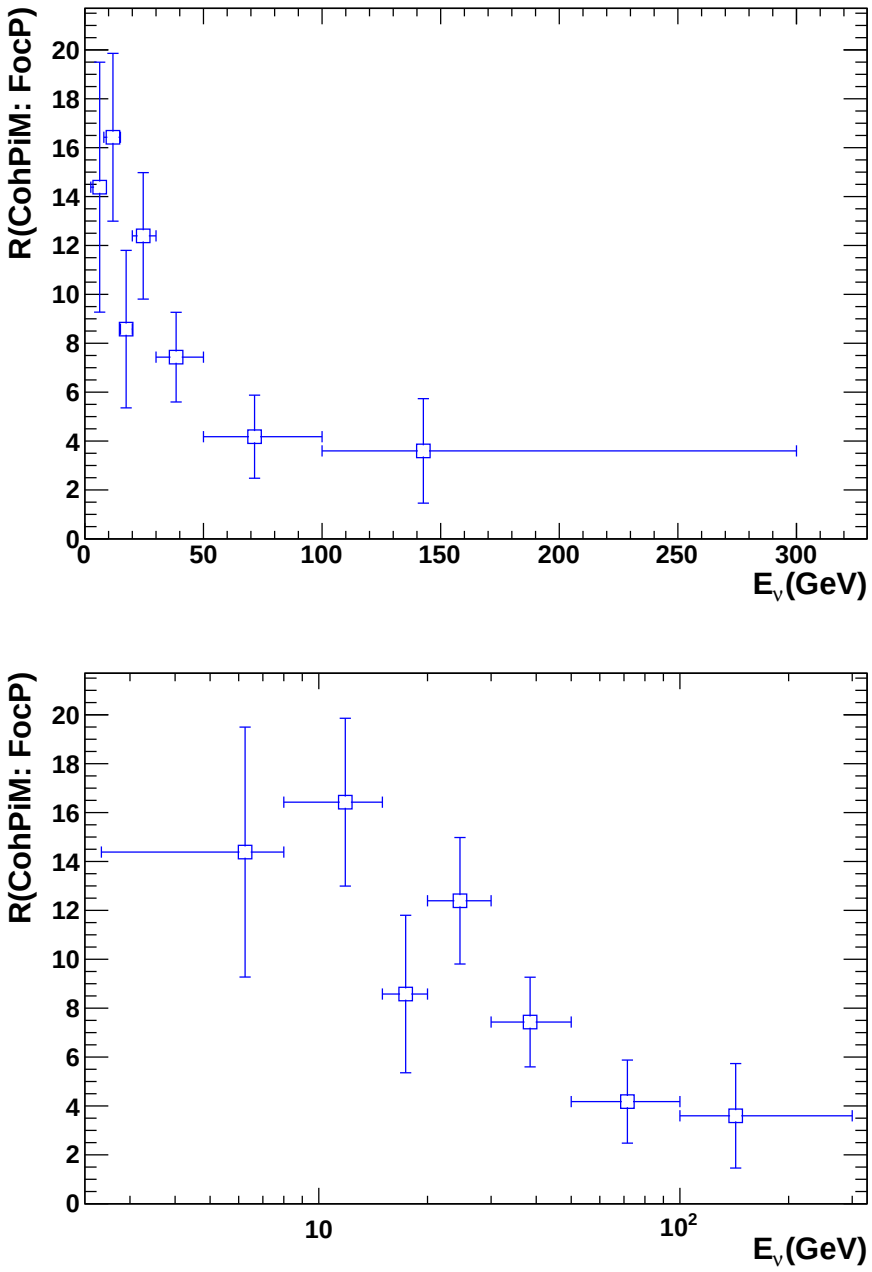

Figure 6.38: R=$\frac{\sigma(Coh\pi^-)}{\sigma(\bar{\nu}_\mu CC)}$ distribution in both linear scale (top) and log scale (bottom), calculated using a variable BN which depends on the Evis(the beam(flux) reweight is applied to all the $\bar{\nu}_\mu$-CC events).

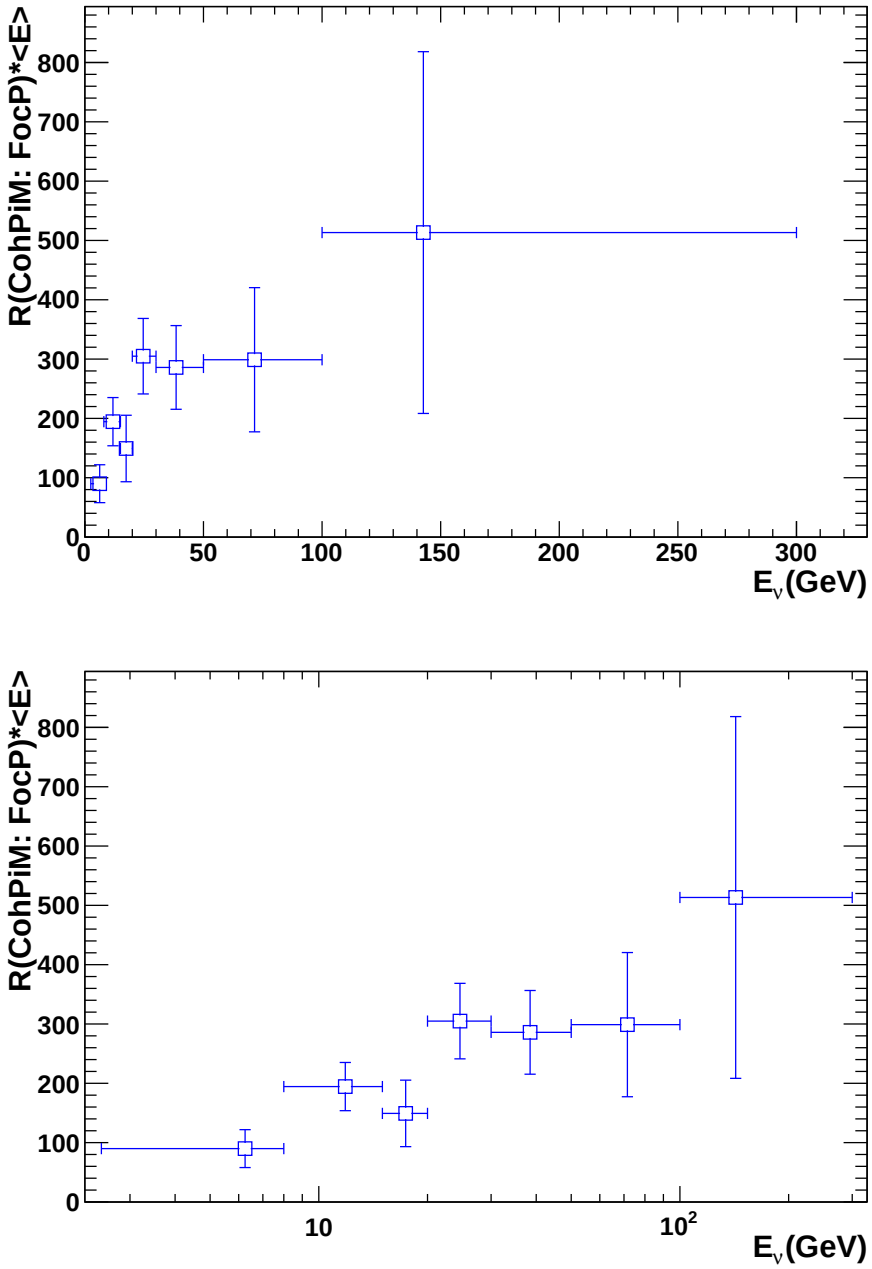

Figure 6.39: R×<E> distribution in both linear scale (top) and log scale (bottom), calculated using a variable BN which depends on the Evis(the beam(flux) reweight is applied to all the $\bar{\nu}_\mu$-CC events).

Table 6.23: Corrected signal (Corr-Sig-Enus) as a function of E_ν in 7 bins calculated from variable BN(R=$\frac{\sigma(Coh\pi^-)}{\sigma(\bar{\nu}_\mu CC)}$).

E_ν	<E>	Corr-Sig-Enus	$\bar{\nu}_\mu$-CC	R $\times 10^{-3}$(Stat.)
2.5 - 8	6.25	59.961 $\pm$ 21.310	4168.3	14.385 $\pm$ 5.112
8 - 15	11.84	92.977 $\pm$ 19.428	5660.2	16.426 $\pm$ 3.432
15 - 20	17.40	31.166 $\pm$ 11.704	3633.3	8.578 $\pm$ 3.221
20 - 30	24.60	72.886 $\pm$ 15.214	5881.0	12.393 $\pm$ 2.587
30 - 50	38.47	56.672 $\pm$ 13.981	7625.0	7.432 $\pm$ 1.834
50 - 100	71.54	32.738 $\pm$ 13.313	7835.2	4.178 $\pm$ 1.699
100 - 300	142.70	9.323 $\pm$ 5.539	2592.0	3.597 $\pm$ 2.137
2.5 - 300	25.00	370.6 $\pm$ 39.42	37645.6	9.845 $\pm$ 1.047

Table 6.24: Norm-bkg, Corr-sig as a function of Evis in 7 bins, calculated from a fixed BN.

Evis	Tot-bkg	BN	Norm-bkg	Data	Raw-sig	Eff	Corr-Sig. (Err=Stat., BN)
2.5 - 8	3.89	0.944	3.67	15	11.3	0.197	57.42 ± 21.79 ± 2.297
8 - 15	8.04	0.944	7.59	42	34.4	0.378	91.01 ± 18.67 ± 2.477
15 - 20	3.55	0.944	3.35	16	12.6	0.41	30.85 ± 10.73 ± 1.01
20 - 30	4.67	0.944	4.41	36	31.6	0.426	74.12 ± 15.17 ± 1.277
30 - 50	5.52	0.944	5.21	29	23.8	0.437	54.42 ± 13.5 ± 1.471
50 - 100	3.1	0.944	2.93	19	16.1	0.432	37.21 ± 10.99 ± 0.8365
100 - 300	0.591	0.944	0.558	4	3.44	0.367	9.371 ± 5.943 ± 0.1876
2.5 - 300	29.4	0.944	27.7	161	133	0.36	370.6 ± 38.26 ± 9.509

Table 6.25 and Table 6.26 show the result of R=$\frac{\sigma(Coh\pi^-)}{\sigma(\bar{\nu}_\mu CC)}$ calculated from a fixed BN of neutrino beam mode data (Positive focusing data: FocP) in 7 Evis and E_ν bins.

Table 6.25: Corrected signal (Corr-sig) as a function of Evis in 7 bins, calculated from a fixed BN(R=$\frac{\sigma(Coh\pi^-)}{\sigma(\bar{\nu}_\mu CC)}$).

Evis(GeV)	<E>	Corr-Sig	$\bar{\nu}_\mu$-CC	R $\times 10^{-3}$(Stat.)
2.5 - 8	6.25	57.42	4168.3	13.770 ± 5.257
8 - 15	11.84	91.01	5660.2	16.080 ± 3.327
15 - 20	17.40	30.85	3633.3	8.492 ± 2.966
20 - 30	24.60	74.12	5881.0	12.600 ± 2.588
30 - 50	38.47	54.42	7625.0	7.138 ± 1.780
50 - 100	71.54	37.21	7835.2	4.748 ± 1.406
100 - 300	142.70	9.371	2592.0	3.615 ± 2.294
2.5 - 300	25.00	370.6	37645.6	9.845 ± 1.047

Table 6.26: Corrected signal (Corr-sig) as a function of E_ν in 7 bins calculated from a fixed BN(R=$\frac{\sigma(Coh\pi^-)}{\sigma(\bar{\nu}_\mu CC)}$).

E_ν	<E>	Corr-Sig	$\bar{\nu}_\mu$-CC	R $\times 10^{-3}$(Stat.)
2.5 - 8	6.25	56.921 ± 21.438	4168.3	13.656 ± 5.143
8 - 15	11.84	90.749 ± 19.359	5660.2	16.321 ± 3.420
15 - 20	17.40	33.195 ± 10.867	3633.3	9.136 ± 2.991
20 - 30	24.60	72.066 ± 15.065	5881.0	12.254 ± 2.562
30 - 50	38.47	55.295 ± 13.771	7625.0	7.252 ± 1.806
50 - 100	71.54	37.439 ± 11.369	7835.2	4.778 ± 1.451
100 - 300	142.70	8.743 ± 5.409	2592.0	3.373 ± 2.087
2.5 - 300	25.00	370.6 ± 39.42	37645.6	9.845 ± 1.047

Figure 6.40 and Figure 6.41 show the distributions of R=$\frac{\sigma(Coh\pi^-)}{\sigma(\bar{\nu}_\mu CC)}$ and R×E distributions in both linear scale (top) and log scale (bottom), where R is calculated from a fixed BN.

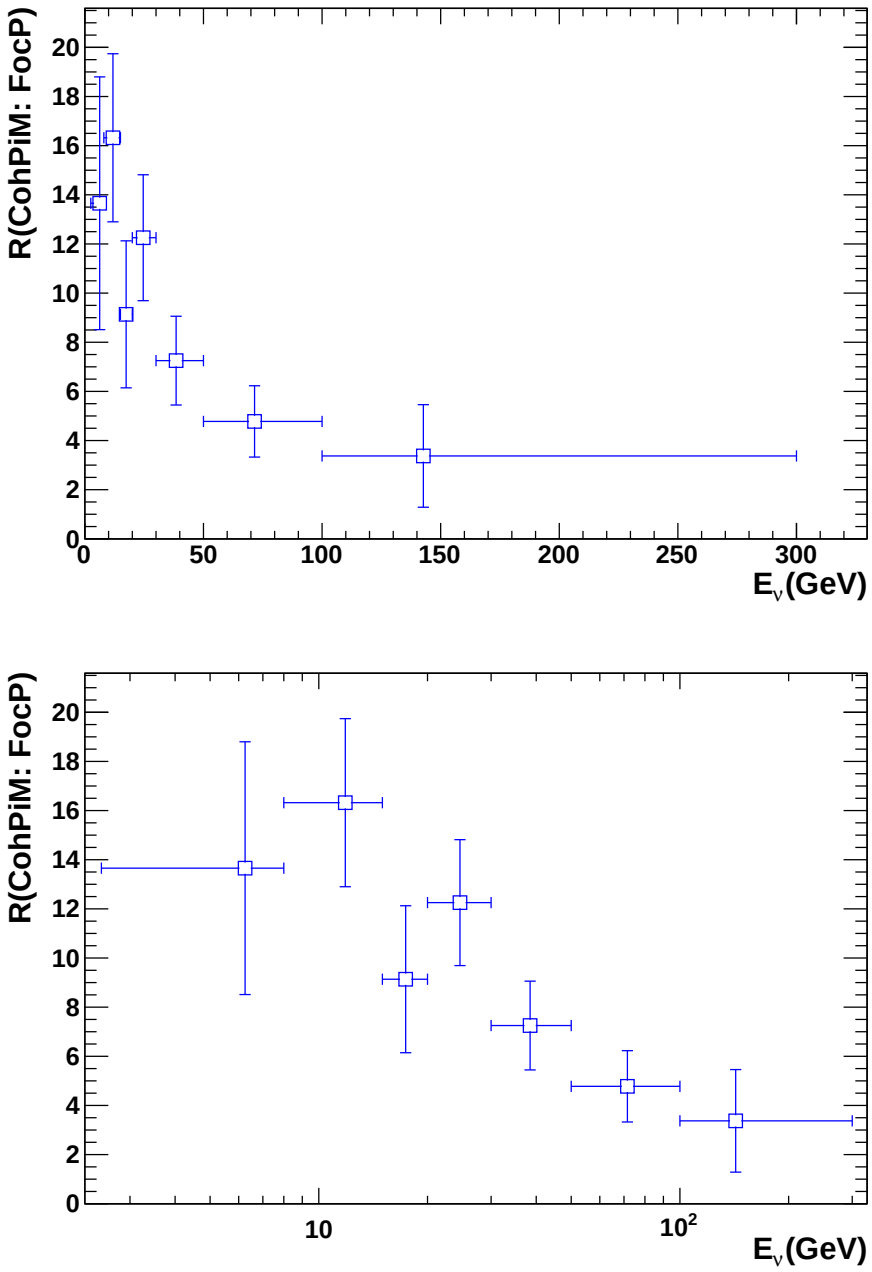

Figure 6.40: R=$\frac{\sigma(Coh\pi^-)}{\sigma(\bar{\nu}_\mu CC)}$ distribution in both linear scale (top) and log scale (bottom), calculated from a fixed BN (the beam(flux) reweight is applied to all the $\bar{\nu}_\mu$-CC events).

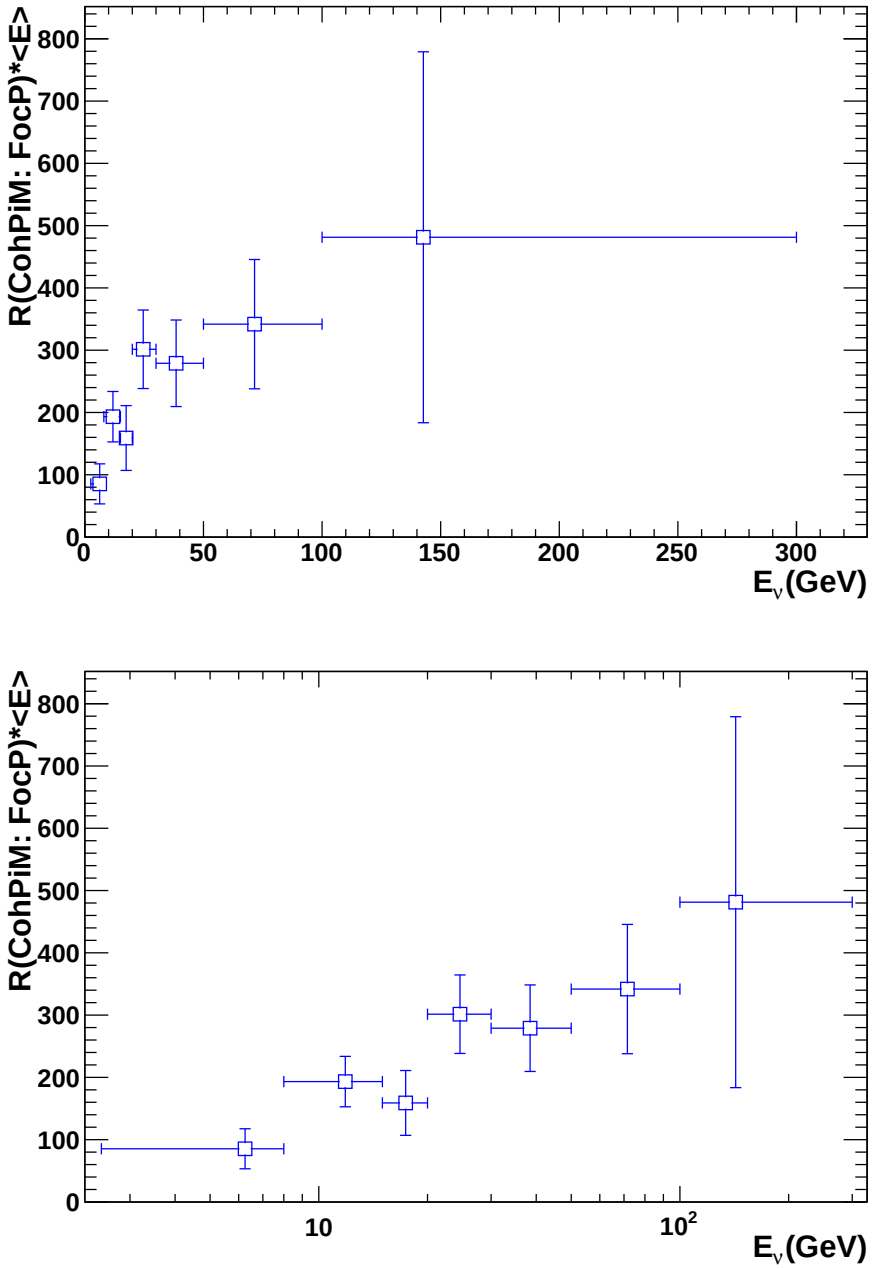

Figure 6.41: R×<E> distribution in both linear scale (top) and log scale (bottom), calculated from a fixed BN (the beam(flux) reweight is applied to all the $\bar{\nu}_\mu$-CC events).

Similar to the analysis of the Neutrino Beam Mode NOMAD data, the NOMAD data generated from Anti-neutrino Beam Mode is also analyzed with the same method. With the anti-neutrino beam mode data, the ratio R which is the ratio between the coherent π^- events and $\bar{\nu}_\mu$ charged current events is also calculated. Combine the results of R from neutrino and anti-neutrino beam mode together, the averaged value of R is calculated and compared to the result of coherent π^+.

Normalization of Event Samples

Same as the process in the neutrino beam mode analysis, in the anti-neutrino beam mode analysis, all the Monte Carlo events are also normalized based on coherent events and inclusive charged current events.

Table 6.27: Normalization of (Anti-)Neutrino Beam Mode events [8].

Mode	Event Number
ν_μ CC	13,000
ν_μ NC	13,000 $\times$ 0.35
$\bar{\nu}_\mu$ CC	35,000
$\bar{\nu}_\mu$ NC	35,000 $\times$ 0.35

Table 6.28: Ratios between interaction mode.

Ratio	Value
NC/CC	0.37
non-DIS/DIS	0.055
QE/RES	0.75

Preselection of $\bar{\nu}_\mu$ CC Events

Table 6.29: Cut table of Monte Carlo events in generated level.

	$N_{\bar{\nu}}^{CC}$	N_{ν}^{CC}	N^{NC}	TotBkg	N_{MC}
Total	45462.8	14987.6	21038.9	36026.5	81489.3
Pfermi<1.0	45073.8	14859.9	20853.3	35713.2	80787.0
W2s>1.96(CCDIS)	39409.3	14157.7	18721.1	32878.8	72288.1
|GenX, (GenY-5)|<130 cm Zmin < GenZ < 405 cm	35012.3	13073.7	16851.4	29925.1	64937.4
2.5<Evis<300	35000	13000	16800	29800	64800

Table 6.29 shows the preselection of $\bar{\nu}_\mu$ charged current events in generated level. From this table, we can see that all the $\bar{\nu}_\mu$ charged current events has been normalized to 35,000, and ν_μ charged current events has been normalized to 13,000 which are consistent with the prediction shown in Table 6.27.

Table 6.30 shows the preselection of $\bar{\nu}_\mu$ charged current events in reconstructed level with kinematic variable cuts. Similar to the result in the neutrino beam mode data analysis, there is also a disagreement about 15% between the normalized Monte Carlo events and anti-neutrino beam mode NOMAD data. To get a better agreement, the Monte Carlo events was refitted. Through this refitting process, the new normalization factors can be calculated and used to normalize the Monte Carlo events.

Table 6.30: Reconstructed variable cut table after normalization and reweighted.

	$N_{\bar{\nu}}^{CC}$	N_{ν}^{CC}	N^{NC}	TotBkg	N_{MC}	N_{data}	N_{data}/N_{MC}
Total	37718.5	12846.4	13049.0	50767.6	63613.9	189609	2.981
Pfermi<1.0	37404.5	12740.5	12939.0	50343.5	63084.1	189609	3.006
W2s>1.96(CCDIS)	32812.3	12175.0	12862	45674.3	57849.3	189609	3.278
FV cut	27076.9	10795.2	10953.7	38030.6	48825.8	103952	2.129
PhaseII	25286.1	9615.8	330.9	25617.0	35232.7	43627	1.238
Nmu=1	25199.1	9523.1	282.3	25481.4	35004.6	43257	1.236
veto/tube	25064.6	9495.8	281.0	25345.6	34841.4	41900	1.203
ncand>=2	23152.5	9287.8	278.6	23431.1	32718.9	38213	1.168
$\|\vec{p}_{\mu}\|$>2.5	23055.4	9235.7	267.6	23323.0	32558.7	38009	1.167
μ^{+}	22969.9	101.0	143.0	244.0	23213.9	27055	1.165
DeltaP/P<=0.2	22926.1	86.6	138.9	225.5	23151.7	26879	1.161
thetamupi<177.5	22923.4	86.6	138.9	225.5	23149.0	26545	1.147
Evis<300GeV	22922.4	86.6	138.9	225.5	23147.9	26479	1.144
Ehad<300GeV	22922.4	86.6	138.9	225.5	23147.9	26479	1.144
19512<Run<21270	22922.4	86.6	138.9	225.5	23147.9	26479	1.144

To ensure the Monte Carlo events match the NOMAD data well, the same fitting method as used in analysis of neutrino beam mode is also applied to anti-neutrino mode. During this fitting process, two variables are used: Ybj and $\hat{\nu}$. The normalization factors for $\bar{\nu}_\mu$ charged current events, ν_μ charged current events and neutral current events are $k_{norm}^{\bar{\nu_\mu}}$, $k_{norm}^{\nu_\mu CC}$, and k_{norm}^{NC}.

The procedure includes the following steps:

- Create the 2D distribution of Ybj, and $\hat{\nu}$;
- Divide the distribution into equal-populated $5 \times 10 = 50$ cubes. Because the events do not distribute uniformly, the volumes of the cubes are not the same.
- Run through all the possible normalization,
  - Set the default of $k_{norm}^{\bar{\nu}_\mu CC}$ at 1.15 and vary it in steps of 0.001 from 1.1 to 1.2;
  - Set $k_{norm}^{NC} = 4.7$ and vary it in steps of 0.001 from 4.6 to 4.8;
  - Set $k_{norm}^{\nu_\mu CC} = 0.1$ and vary it in steps of 0.001 from 0.0 to 0.2;

  Then the total number of Monte Carlo events after normalization becomes

$$\begin{aligned} N_{MC} = & N_{\bar{\nu}_\mu}^{CC} \times k_{norm}^{\bar{\nu}_\mu CC} + \\ & N^{NC} \times k_{norm}^{NC} + \\ & N_{\nu_\mu}^{CC} \times k_{norm}^{\nu_\mu CC} \end{aligned}$$

- Calculate the χ^2 for each cube and sum over all of them.

$$\chi^2 = \frac{(N_{data} - N_{MC})^2}{\sigma_{data}^2 + \sigma_{MC}^2}$$

While $\sigma_{data} = \sqrt{N_{data}}$, and $\sigma_{MC} = \sqrt{\sum_j (\sqrt{N_{MC}(j)})^2}$, index i represent the Monte Carlo events ($\bar{\nu}_\mu$CC, ν_μCC and NC);

- Get the parameter corresponding the minimum χ^2.

  $k_{norm}^{\bar{\nu}_\mu CC} = 1.114 \pm 0.015$

  $$k_{norm}^{NC} = 4.67$$

  $$k_{norm}^{\nu_\mu CC} = 0.0$$

  Since the total points I used for this 2D fit is equal to 50 and the minimum χ^2 is 247.2, then the value χ^2/DOF equals to 4.944.

The normalization factors got from this fit procedure will be used to calculated the number of $\bar{\nu}_\mu$ charged current in the anti-neutrino beam mode. Same method was used in this anti-neutrino beam mode data analysis as in the neutrino beam mode data analysis.

Table 6.31 shows the number of $\bar{\nu}_\mu$-CC events, background from charged current events (CC-Bkg), background from neutral current events (NC-Bkg), total background (Tot-Bkg), total Monte Carlo events (Tot-MC), number of data (N_{data}) after all the cuts in 7 Evis bins without normalization (not multiply Norm factors I got from the fit).

The first two columns of Table 6.33 show the generated and reconstructed $\bar{\nu}_\mu$ charged current events in 7 visible energy (Evis) bins. Analogous to the calculations in the neutrino beam mode data analysis, the efficiency vector can also be calculated from the ratio between the elements in these two columns (Reconstructed $\bar{\nu}_\mu$ charged current events divide by the Generated $\bar{\nu}_\mu$ charged current events) which is shown in the last column of Table 6.33.

Table 6.31: Reconstructed $\bar{\nu}_\mu$ charged current events without normalization.

Evis(GeV)	$N^{CC}_{\bar{\nu}_\mu}$ generated	$N^{CC}_{\bar{\nu}_\mu}$ constructed	CC-Bkg	NC-bkg	Tot-Bkg	N_{MC}	N_{data}
2.5-8.0	1583.3	1168.5	0.8	6.5	7.3	1175.8	1042
8.0-15.0	8550.9	5598.0	3.6	18.3	22.0	5620.0	5165
15.0-20.0	6424.7	4016.0	3.9	14.7	18.7	4034.7	4039
20.0-30.0	7976.4	5038.1	10.2	25.0	35.1	5073.2	5891
30.0-50.0	5868.9	3988.4	21.0	35.8	56.9	4045.3	5262
50.0-100.0	3879.0	2652.2	29.3	31.4	60.7	2712.8	4024
100.0-300.0	716.8	461.3	17.7	7.2	24.9	486.1	1056
2.5-300.0	35000	22922.4	86.6	138.9	225.5	23147.9	26479

Table 6.32: Raw signal and fully corrected data after normalization.

Evis(GeV)	$\bar{\nu}_\mu$-CC reconstructed	normalized signal	Raw signal	Tot-Bkg	N_{MC}	N_{data}	N_{data}/N_{MC}
2.5-8.0	1168.5	1301.7	1011.6	30.4	1332.1	1042	0.782
8.0-15.0	5598.0	6236.2	5079.5	85.5	6321.7	5165	0.817
15.0-20.0	4016.0	4473.8	3970.4	68.6	4542.4	4039	0.889
20.0-30.0	5038.1	5612.4	5774.2	116.8	5729.2	5891	1.028
30.0-50.0	3988.4	4443.1	5094.8	167.2	4610.3	5262	1.141
50.0-100.0	2652.2	2954.5	3877.4	146.6	3101.1	4024	1.298
100.0-300.0	461.3	513.8	1022.4	33.6	547.4	1056	1.929
2.5-300.0	22922.4	25535.5	25830.3	648.7	26184.2	26479	1.011

Table 6.33: The efficiency (ratio between Rec-$\bar{\nu}_\mu$ CC and Gen-$\bar{\nu}_\mu$ CC events) in 7 E_ν bins.

Evis(GeV)	Generated $N^{CC}_{\bar{\nu}_\mu}$	Reconstructed $N^{CC}_{\bar{\nu}_\mu}$	Efficiency
2.5-8.0	1583.3	1168.5	0.738
8.0-15.0	8550.9	5598.0	0.655
15.0-20.0	6424.7	4016.0	0.625
20.0-30.0	7976.4	5038.1	0.632
30.0-50.0	5868.9	3988.4	0.680
50.0-100.0	3879.0	2652.2	0.684
100.0-300.0	716.8	461.3	0.644
2.5-300.0	35000	22922.4	0.655

Table 6.32 shows the reconstructed $\bar{\nu}_\mu$, normalized signal, Raw signal which equals to the number of data minus the total background, total background (Tot-Bkg), total number of MC events (N_{MC}) which equals to the sum of normalized signal and the total background, number of data (N_{data}). These numbers will be used to calculated the fully corrected signal.

Table 6.34: Fully corrected signal get from efficiency vector (shown in Table 6.33).

Evis(GeV)	Raw signal	Efficiency	Full Corrected Signal
2.5-8.0	1011.6	0.738	1370.7
8.0-15.0	5079.5	0.655	7755.0
15.0-20.0	3970.4	0.625	6352.6
20.0-30.0	5774.2	0.632	9136.4
30.0-50.0	5094.8	0.680	7492.4
50.0-100.0	3877.4	0.684	5668.7
100.0-300.0	1022.4	0.644	1587.6
2.5-300.0	25830.3	0.655	39435.6

Using the Raw signal in Table 6.32 divide by the efficiency in the same energy bin shown in Table 6.33, we get the fully corrected signal which are shown in Table 6.34.

Table 6.35: $\bar{\nu}_\mu$ charged current events as a function of E_ν (Evis) before normalization.

E_ν \ Evis	2.5-8.0	8.0-15.0	15.0-20.0	20.0-30.0	30.0-50.0	50.0-100.0	100.0-300.0	2.5-300.0
2.5-8.0	572.9	15.7	0.3	0.2	0.5	0.1	0.1	589.7
8.0-15.0	585.0	4214.1	74.0	7.2	3.5	1.8	1.0	4886.6
15.0-20.0	6.9	1288.5	2779.0	109.8	6.6	3.0	1.7	4195.5
20.0-30.0	2.6	72.5	1143.9	4214.7	116.3	8.4	4.9	5563.4
30.0-50.0	0.8	5.8	16.9	695.5	3485.1	86.7	5.8	4296.7
50.0-100.0	0.2	1.2	1.6	10.1	374.0	2445.2	52.1	2884.4
100.0-300.0	0.1	0.2	0.2	0.6	2.5	106.8	395.7	506.1
2.5-300.0	1168.5	5598.0	4016.0	5038.1	3988.5	2652	461.3	22922.4

Table 6.36: Background as a function of E_ν and Evis before normalization.

E_ν \ Evis	2.5-8.0	8.0-15.0	15.0-20.0	20.0-30.0	30.0-50.0	50.0-100.0	100.0-300.0	2.5-300.0
2.5-8.0	0	0	0	0	0	0	0	0
8.0-15.0	1.9	1.1	0	0	0	0	0	3.0
15.0-20.0	0.9	2.5	0.4	0	0	0	0	3.8
20.0-30.0	1.7	4.7	3.3	2.3	0.2	0	0	12.2
30.0-50.0	1.2	5.4	5.8	9.5	7.3	0.1	0.1	29.4
50.0-100.0	0.7	3.9	4.1	9.9	19.0	12.4	0.3	50.2
100.0-300.0	0.3	0.7	1.2	3.2	9.3	18.8	6.8	40.2
2.5-300.0	6.7	18.3	14.8	24.9	35.8	31.3	7.2	139

Table 6.37: Raw signal and fully corrected data after normalization.

Evis(GeV)	$\bar{\nu}_\mu$-CC reconstructed	normalized signal	Raw signal	Tot-Bkg	N_{MC}	N_{data}
2.5-8.0	1168.5	1301.7	1010.7	31.3	1333.0	1042
8.0-15.0	5598.0	6236.2	5079.5	85.5	6231.7	5165
15.0-20.0	4016.0	4473.8	3969.9	69.1	4542.9	4039
20.0-30.0	5038.1	5612.4	5774.7	116.3	5728.7	5891
30.0-50.0	3988.4	4443.1	5094.8	167.2	4610.3	5262
50.0-100.0	2652.2	2954.5	3877.8	146.2	3100.7	4024
100.0-300.0	461.3	513.8	1022.4	33.6	547.4	1056
2.5-300.0	22922.4	25535.5	25829.9	649.1	26184.6	26479

Table 6.38: Fully corrected signal get from efficiency matrix.

Evis(GeV)	Raw signal	Efficiency	Full Corrected Signal
2.5-8.0	1010.7	0.738	1369.5
8.0-15.0	5079.5	0.655	7755.0
15.0-20.0	3969.9	0.625	6351.8
20.0-30.0	5774.7	0.632	9137.2
30.0-50.0	5094.8	0.680	7492.4
50.0-100.0	3877.8	0.684	5669.3
100.0-300.0	1022.4	0.644	1587.6
2.5-300.0	25829.9	0.655	39435.0

Coherent π^- in Anti-neutrino Mode

Table 6.39: Normalization of the MC events.

$\bar{\nu}_\mu$ CC	35000
$\bar{\nu}_\mu$ CC QE	782.0
$\bar{\nu}_\mu$ CC RES	1042.7
$\bar{\nu}_\mu$ CC DIS	33175.4
$\bar{\nu}_\mu$ NC DIS	12250
$\bar{\nu}_\mu$ cohPi	406.6
$\bar{\nu}_\mu$ cohRho	244.0
ν_μ CC	13000
ν_μ QE generated	290.5
ν_μ RES generated	387.3
ν_μ CC DIS generated	12322.3
ν_μ NC DIS generated	4550

Total ν_μ-CC events with in Fiducial Volume is normalized to 13000 events; $\bar{\nu}_\mu$-CC events equals to 35000 events; NC/CC equals to 0.35, non-Dis/Dis equals to 0.055;QE/RES equals to 0.75; Coh-π/QE equals to 2$\times$ 0.26; Coh-ρ/ Coh-π equals to 0.6.

Table 6.40: Summary of event reduction in different data and MC samples for the preselection cuts.

	$N^{CC}_{\bar{\nu}_\mu}$	$N^{CC}_{\nu_\mu}$	N^{NC}	Cohρ^-	TotBkg	Cohπ^-	N_{data}	Ratio
Total	45462.8	14987.6	21038.9	282.6	81771.9	658.4	–	–
Pfermi	45073.8	14859.9	20853.3	282.6	81069.6	658.4	–	–
W2S	39409.3	14157.7	18721.1	282.6	72570.7	658.4	–	–
Gen-FV	35012.3	13073.7	16851.4	250.9	65188.3	572.8	–	–
E_π>0.5(Coh only)	35012.3	13073.7	16851.4	250.9	65188.3	407.2	–	–
2.5<Evis<300	35000.0	13000.0	16800	244.0	65044.0	406.6	–	–
total	37718.5	12846.4	13049.0	242.3	63856.3	543.7	189609	2.94
pfermi	37404.5	12740.5	12939.0	242.3	63326.3	543.7	189609	2.96
W2	32812.3	12175.0	12862	242.3	58091.6	543.7	189609	3.24
Rec-Fidu	29244.2	11271.13	11651.2	214.8	52381.2	487.5	137286	2.60
E_π>0.5(Coh only)	29244.2	11271.1	11651.1	196.4	52362.8	376.0	137286	2.60
Ph2mu	27325.2	10009.6	341.0	169.0	37844.8	365.3	48963	1.28
Tube/Veto	27153.4	9975.1	339.1	168.1	37635.6	363.2	46123	1.21
Ncand=2	4534.5	1035.5	17.2	136.6	5723.8	320.2	7065	1.17
μ^+/E_μ	4529.3	2.8	10.0	135.1	4677.2	318.9	5519	1.10
Had-	2752.2	1.5	8.0	134.1	2895.8	316.8	3558	1.08
θ_{μ^+,π^-}<177.5	2750.2	1.5	8.0	134.1	2893.8	316.6	3293	1.03
Fit Matrix error	2732.3	1.3	8.0	133.0	2874.6	314.5	3230	1.01
P_π>1.0	1045.7	1.0	5.2	124.2	1176.2	264.8	1542	1.07
θ_{μ^+,π^-}<0.5	740.4	0.8	5.0	123.6	869.9	254.9	1252	1.13
P_T^m<0.5	327.3	0.2	0.6	113.0	441.1	246.8	789	1.14
$(p_\pi - p_{neu})/(p_\pi + p_{neu}) > 0$	257.9	0.1	0.3	64.6	323.0	246.3	651	1.14
nV0 cut	250.0	0.1	0.3	56.0	306.5	246.1	630	1.14
Nclu cut	216.0	0.1	0.2	25.3	241.5	240.0	531	1.10
mgg<0.5	216.0	0.1	0.2	25.3	241.5	240.0	531	1.10
19512<Run<21270	216.0	0.1	0.2	25.3	241.5	240.0	531	1.10

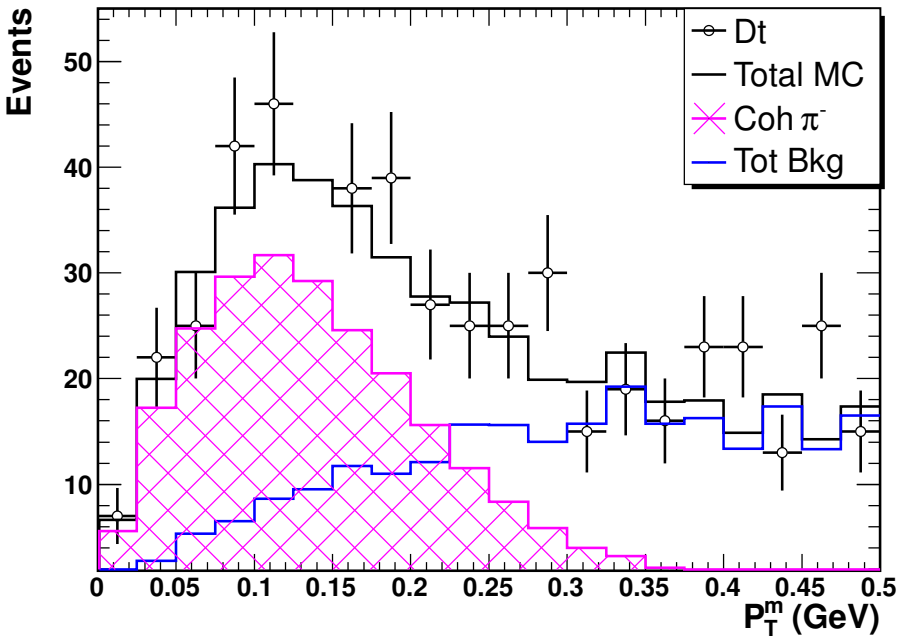

Figure 6.42: P_T^m distribution of the anti-neutrino beam mode data (negative focusing data: FocN).

The distributions of missing transverse momentum P_T^m, the Bjorken variable Xbj, the outgoing meson forwardness ζ are shown from Figure 6.42 to Figure 6.44. These three variables were used during the neural network analysis.

Figure 6.47 shows the distribution of sensitivity (defined in Equation (6.7)) in anti-neutrino beam mode. From this figure, we could see that, in the anti-neutrino beam mode analysis, the best cut value for the signal is 0.8, however, to be consistent with the event selection in the neutrino beam mode, we also chose 0.4 and 0.7 for background and signal region.

Similar to the analysis of neutrino beam mode, in this anti-neutrino beam mode analysis, some kinematic variable distributions after neural network are shown from Figure 6.48 to Figure 6.67. It is obvious that there is also a good agreement between Monte Carlo events and NOMAD data after the neural network analysis. Same to the

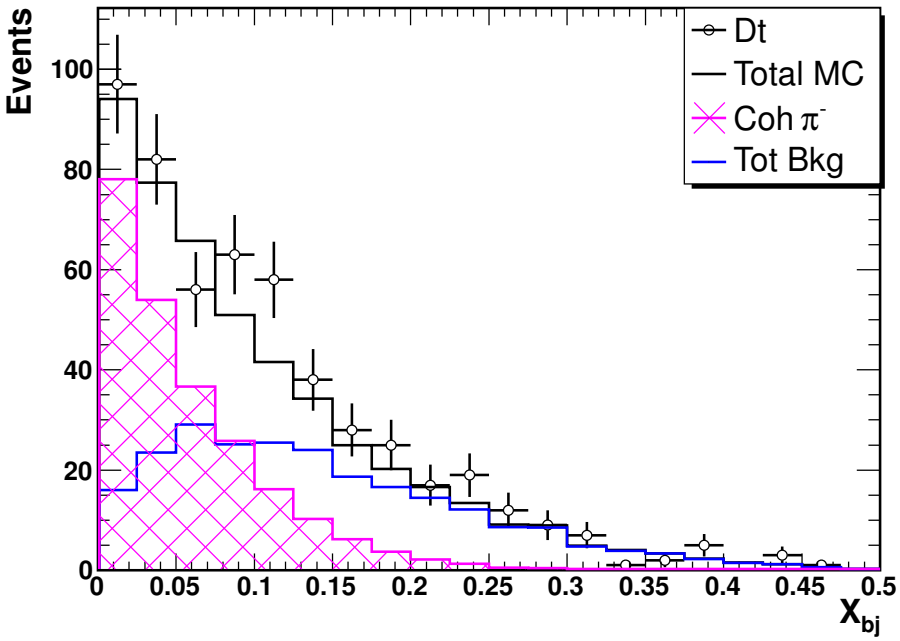

Figure 6.43: Xbj distribution of the anti-neutrino beam mode data (negative focusing data: FocN).

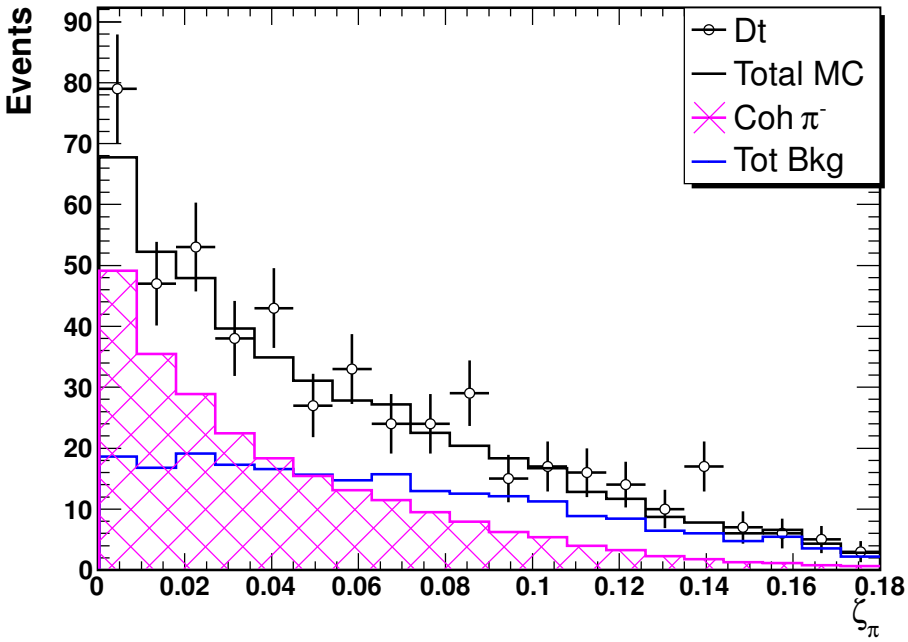

Figure 6.44: ζ distribution of the anti-neutrino beam mode data (negative focusing data: FocN).

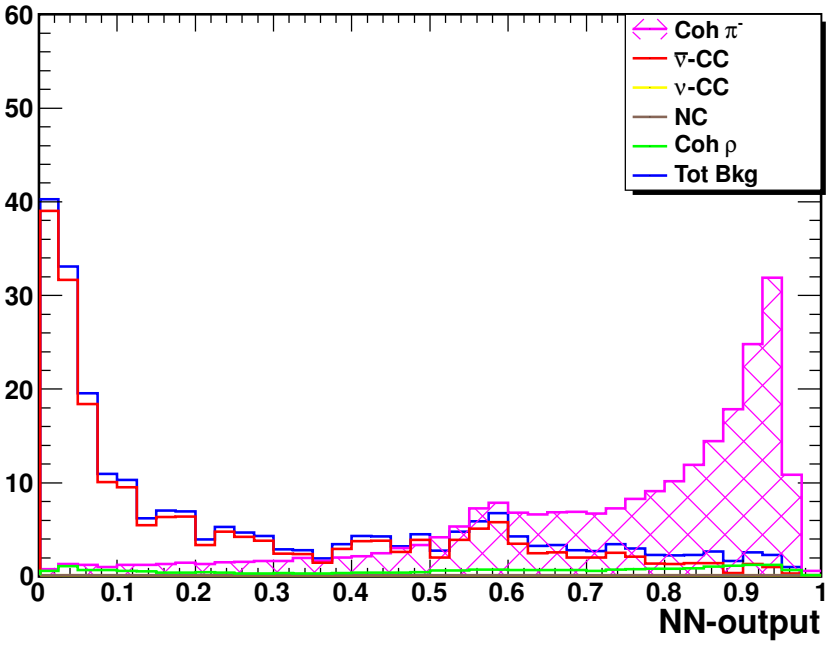

Figure 6.45: The NN distribution comparison of background and signal.

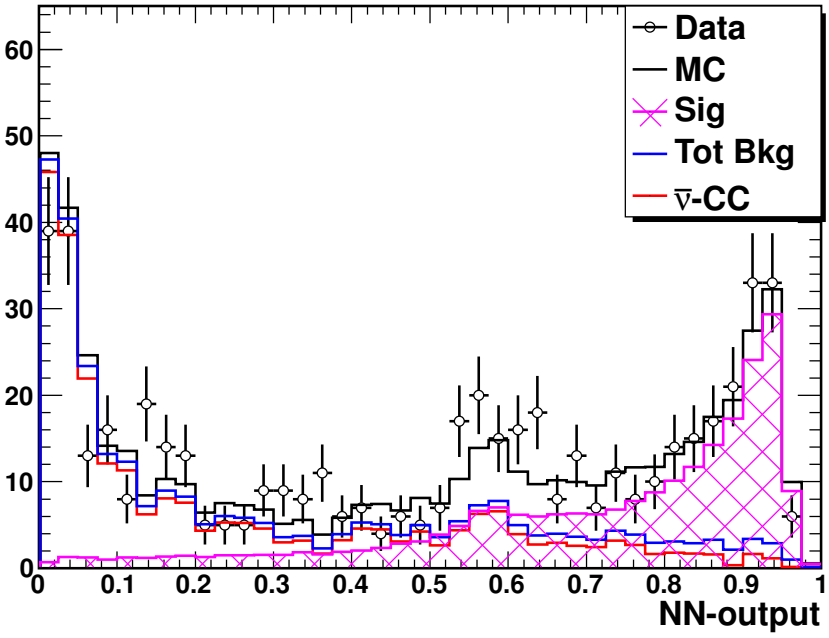

Figure 6.46: The NN distribution comparison of Data and MC.

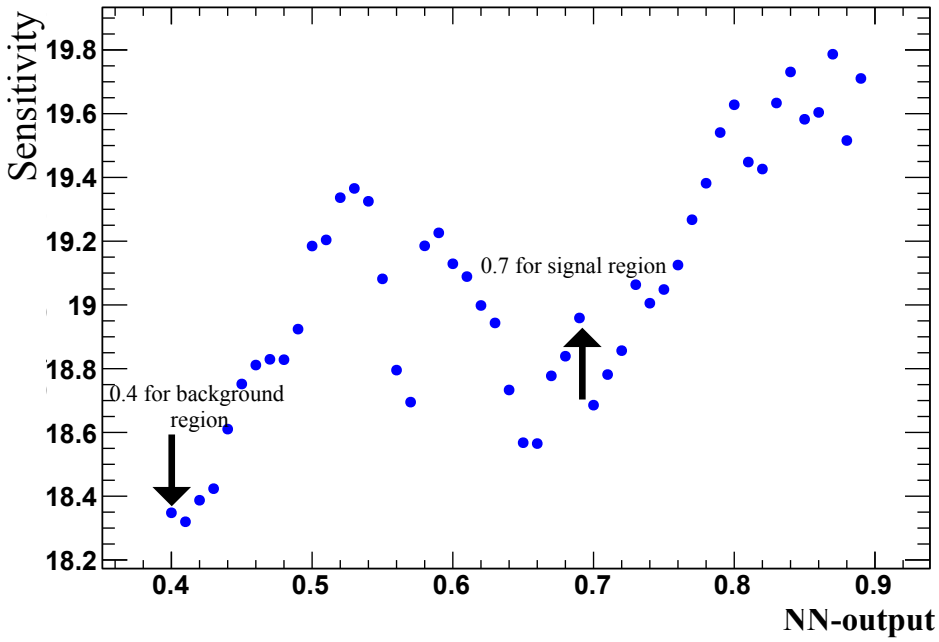

Figure 6.47: The distribution of sensitivity of the neural network in coherent π^- analysis of anti-neutrino beam mode.

plots in neutrino beam mode, in these figures, "Dt" represents NOMAD data; "Total MC" represents total Monte Carlo events; "Tot Bkg" represents total background events; "$\bar{\nu}$ CC" represents $\bar{\nu}_\mu$ charged current events; "ν CC" represents ν_μ charged current events; "NC" represents the combination of $\bar{\nu}_\mu$ and ν_μ neutral current events; "Coh π^-" represents the coherent π^- events; which is also the signal in this analysis; "Coh ρ^-" represents the coherent ρ^- events.

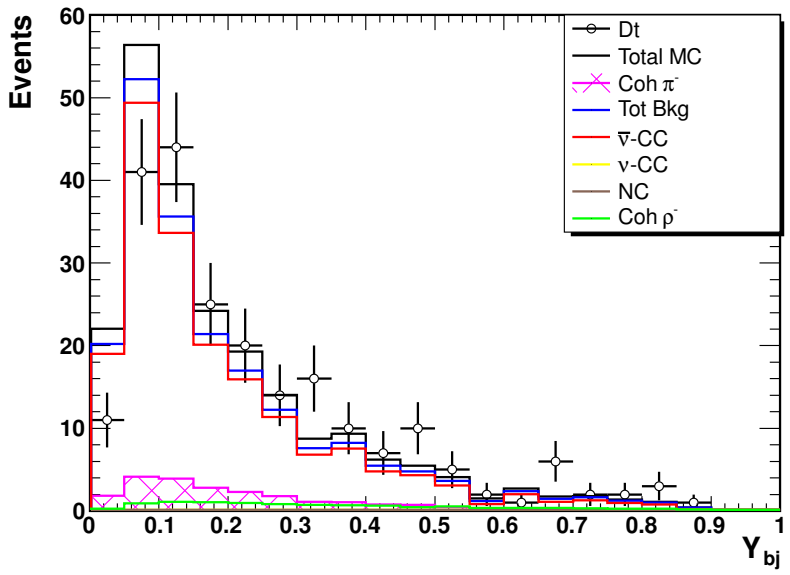

Figure 6.48: The Y_{bj} distribution from different contributions, ν-CC, $\bar{\nu}$-CC, NC, $\bar{\nu}$-Cohρ^- and Cohπ^- in *background (control) region* and the Comparison between Data (points with error bars) and MC (histogram).

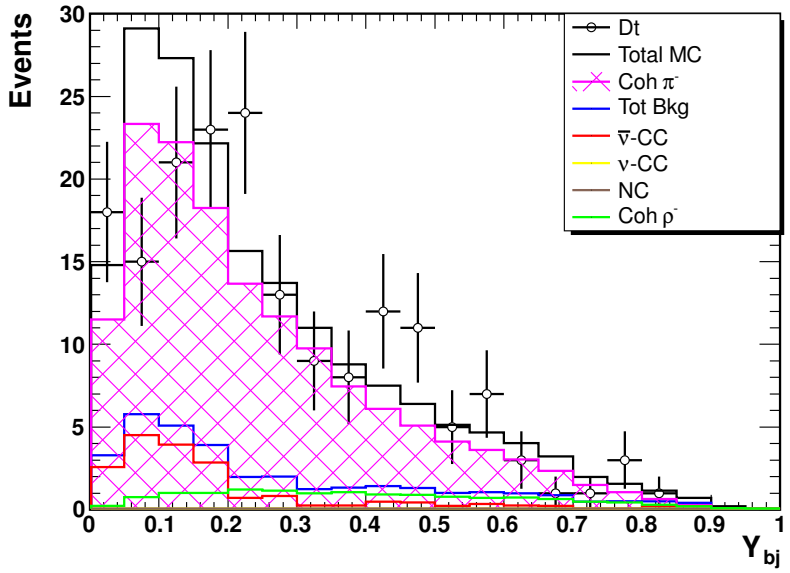

Figure 6.49: The Y_{bj} distribution from different contributions, ν-CC, $\bar{\nu}$-CC, NC, $\bar{\nu}$-Cohρ^- and Cohπ^- in *signal (>0.7) region* and the Comparison between Data (points with error bars) and MC (histogram).

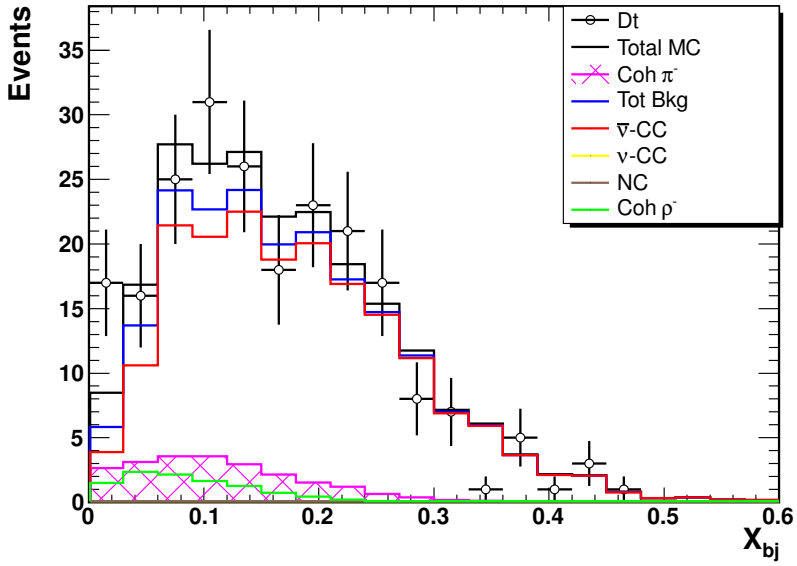

Figure 6.50: The X_{bj} distribution from different contributions, ν-CC, $\bar{\nu}$-CC, NC, $\bar{\nu}$-Cohρ^- and Cohπ^- in *background (control) region* and the Comparison between Data (points with error bars) and MC (histogram).

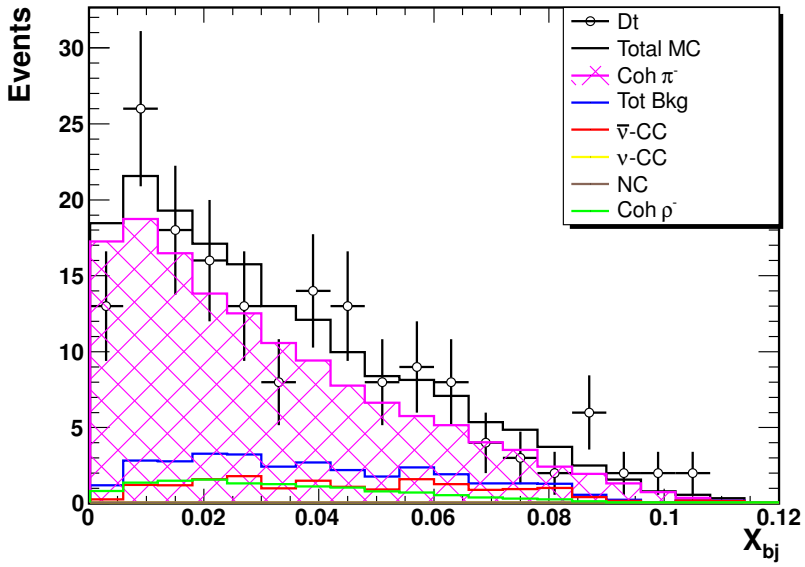

Figure 6.51: The X_{bj} distribution from different contributions, ν-CC, $\bar{\nu}$-CC, NC, $\bar{\nu}$-Cohρ^- and Cohπ^- in *signal (>0.70) region* and the Comparison between Data (points with error bars) and MC (histogram).

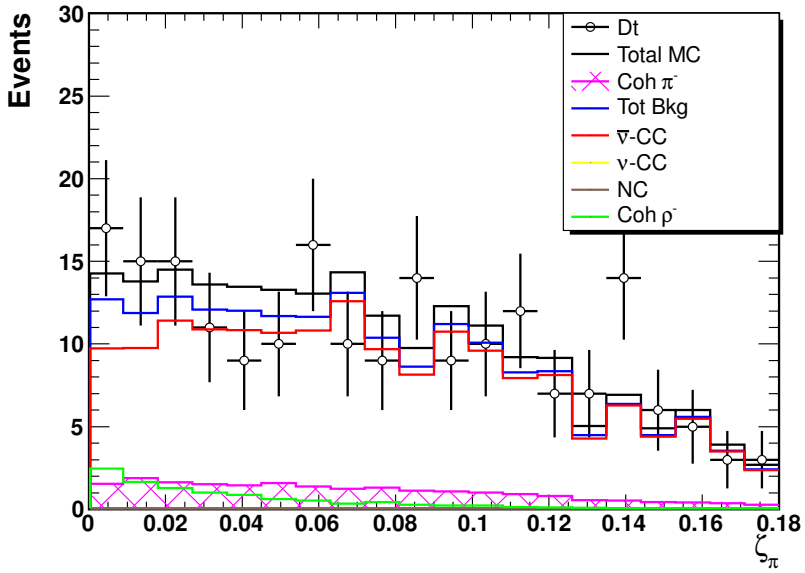

Figure 6.52: The ζ_π distribution from different contributions, ν-CC, $\bar{\nu}$-CC, NC, $\bar{\nu}$-Cohρ^- and Cohπ^- in *background (control) region* and the Comparison between Data (points with error bars) and MC (histogram).

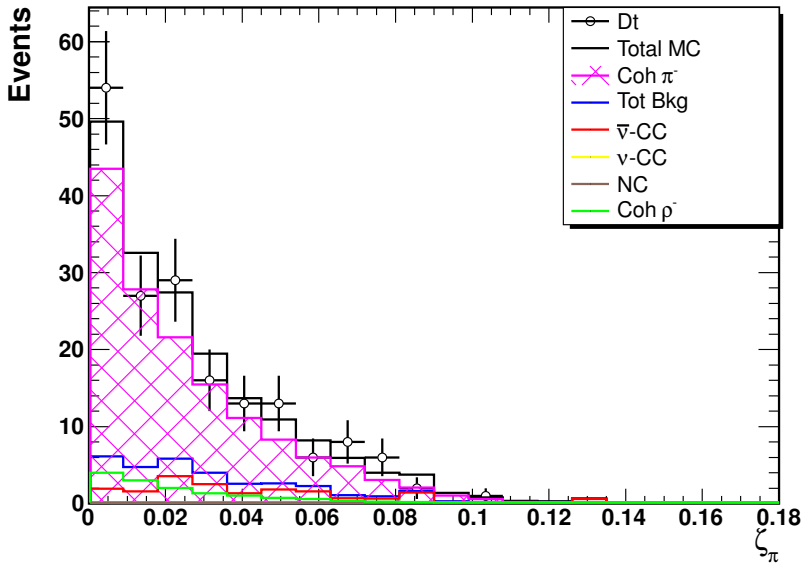

Figure 6.53: The ζ_π distribution from different contributions, ν-CC, $\bar{\nu}$-CC, NC, $\bar{\nu}$-Cohρ^- and Cohπ^- in *signal (>0.7) region* and the Comparison between Data points with error bars) and MC (histogram).

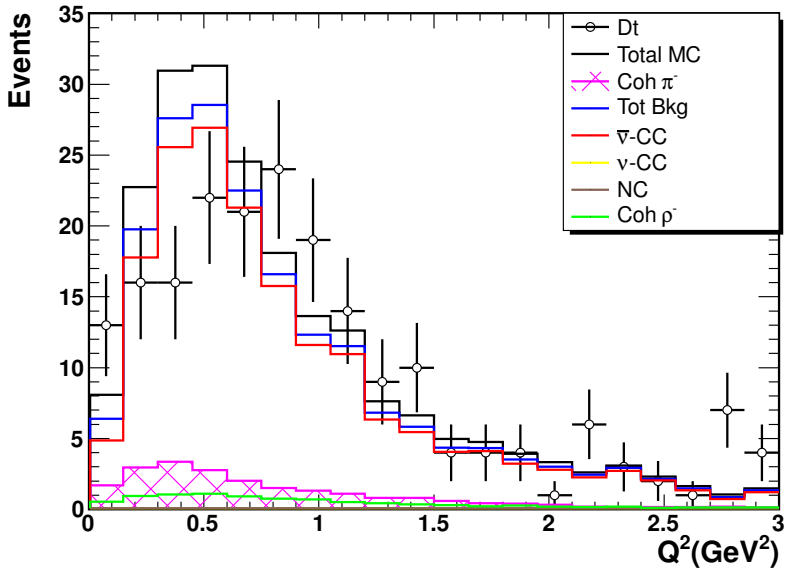

Figure 6.54: The Q^2 distribution from different contributions, ν-CC, $\bar{\nu}$-CC, NC, $\bar{\nu}$-Cohρ^- and Cohπ^- in *background (control) region* and the Comparison between Data (points with error bars) and MC (histogram).

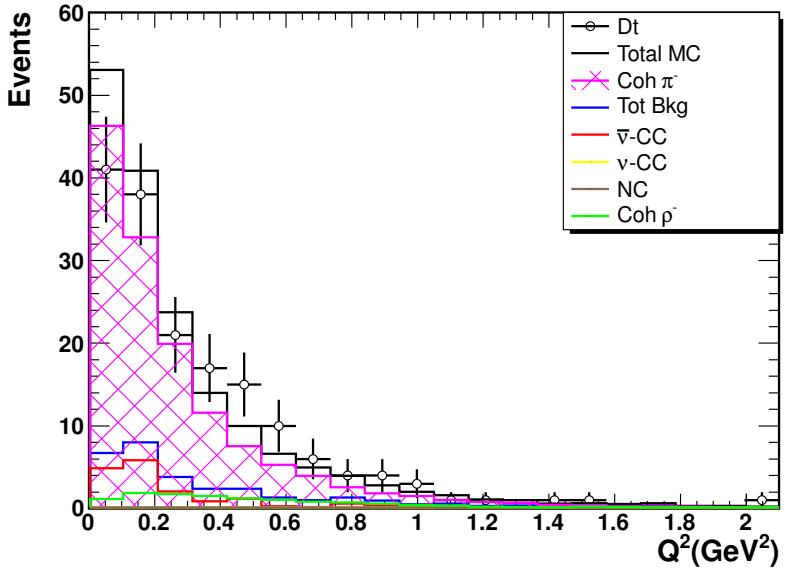

Figure 6.55: The Q^2 distribution from different contributions, ν-CC, $\bar{\nu}$-CC, NC, $\bar{\nu}$-Cohρ^- and Cohπ^- in *signal (>0.7) region* and the Comparison between Data (points with error bars) and MC (histogram).

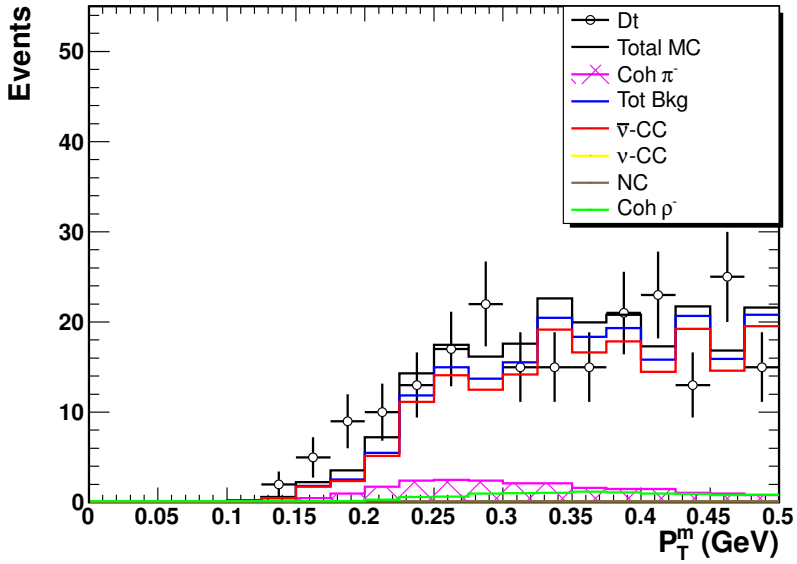

Figure 6.56: The P_T^m distribution from different contributions, ν-CC, $\bar{\nu}$-CC, NC, $\bar{\nu}$-Cohρ^- and Cohπ^- in *background (control) region* and the Comparison between Data (points with error bars) and MC (histogram).

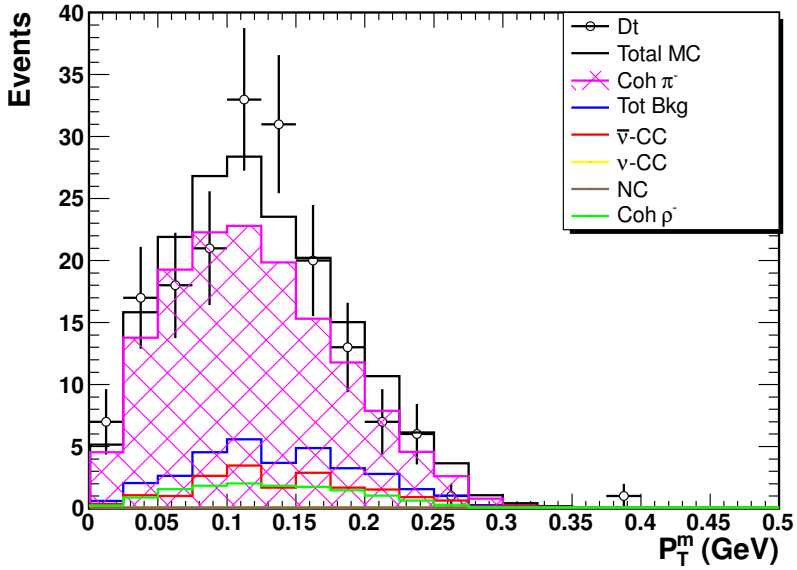

Figure 6.57: The P_T^m distribution from different contributions, ν-CC, $\bar{\nu}$-CC, NC, $\bar{\nu}$-Cohρ^- and Cohπ^- in *signal (>0.7) region* and the Comparison between Data (points with error bars) and MC (histogram).

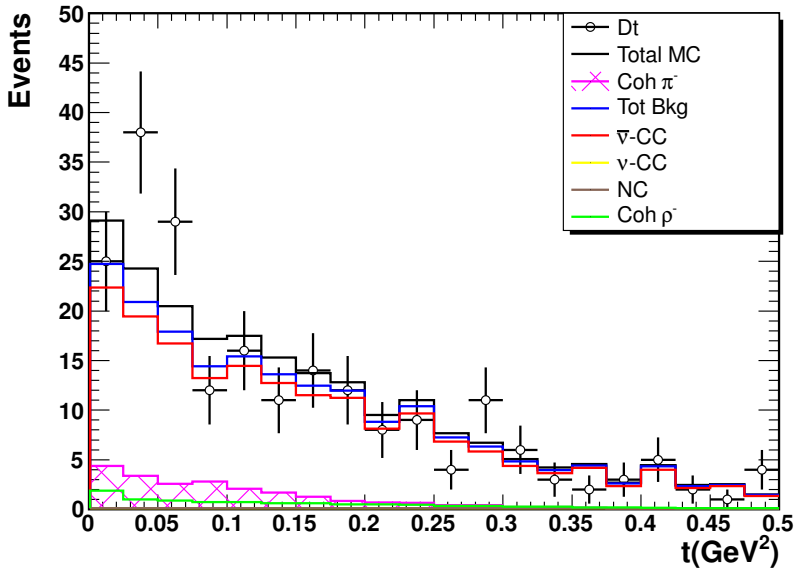

Figure 6.58: The t distribution from different contributions, ν-CC, $\bar{\nu}$-CC, NC, $\bar{\nu}$-Cohρ^- and Cohπ^- in *background (control) region* and the Comparison between Data (points with error bars) and MC (histogram).

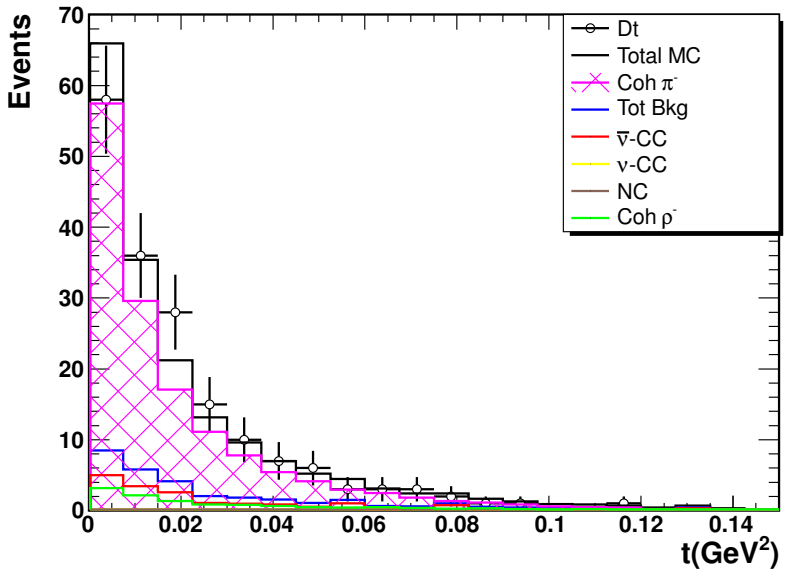

Figure 6.59: The t distribution from different contributions, ν-CC, $\bar{\nu}$-CC, NC, $\bar{\nu}$-Cohρ^- and Cohπ^- in *signal (>0.7) region* and the Comparison between Data (points with error bars) and MC (histogram).

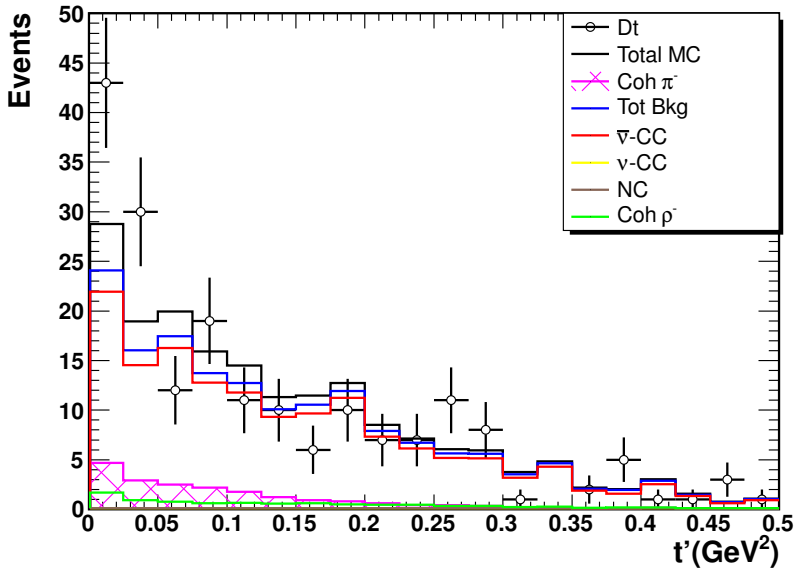

Figure 6.60: The t' distribution from different contributions, ν-CC, $\bar{\nu}$-CC, NC, $\bar{\nu}$-Cohρ^- and Cohπ^- in *background (control) region* and the Comparison between Data (points with error bars) and MC (histogram).

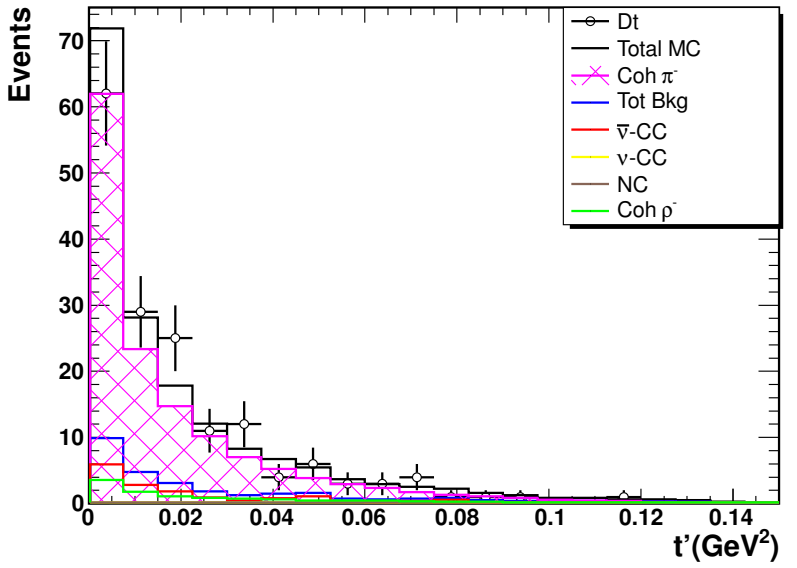

Figure 6.61: The t' distribution from different contributions, ν-CC, $\bar{\nu}$-CC, NC, $\bar{\nu}$-Cohρ^- and Cohπ^- in *signal (>0.7) region* and the Comparison between Data (points with error bars) and MC (histogram).

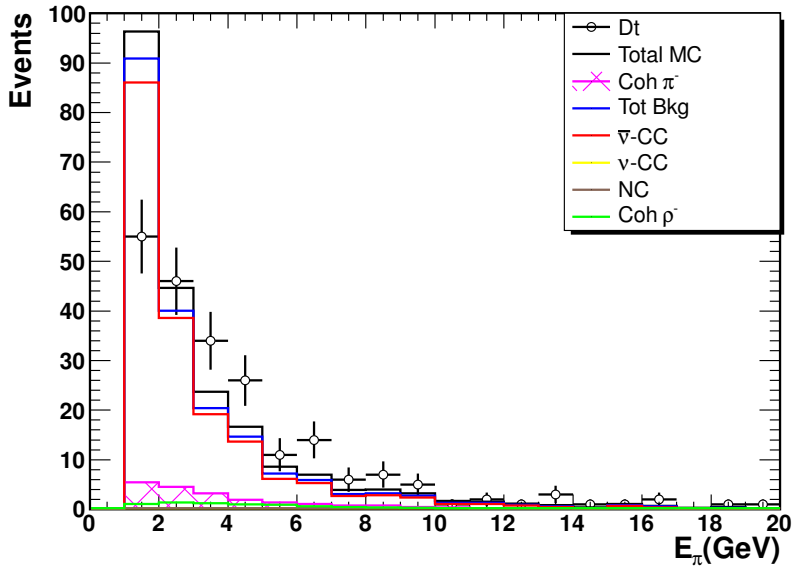

Figure 6.62: The E_π distribution from different contributions, ν-CC, $\bar{\nu}$-CC, NC, $\bar{\nu}$-Cohρ^- and Cohπ^- in *background (control) region* and the Comparison between Data (points with error bars) and MC (histogram).

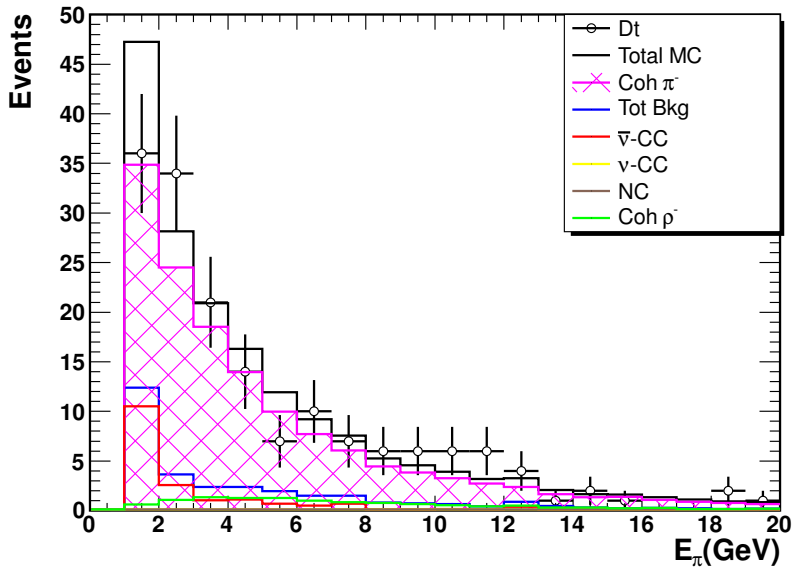

Figure 6.63: The E_π distribution from different contributions, ν-CC, $\bar{\nu}$-CC, NC, $\bar{\nu}$-Cohρ^- and Cohπ^- in *signal (>0.7) region* and the Comparison between Data (points with error bars) and MC (histogram).

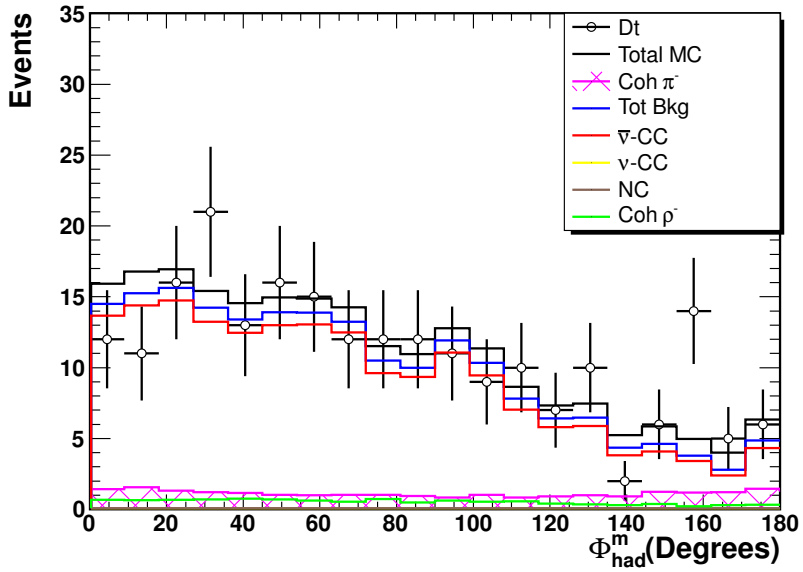

Figure 6.64: The Φ_{had}^{PT} distribution from different contributions, ν-CC, $\bar{\nu}$-CC, NC, $\bar{\nu}$-Cohρ^- and Cohπ^- in *background (control) region* and the Comparison between Data (points with error bars) and MC (histogram).

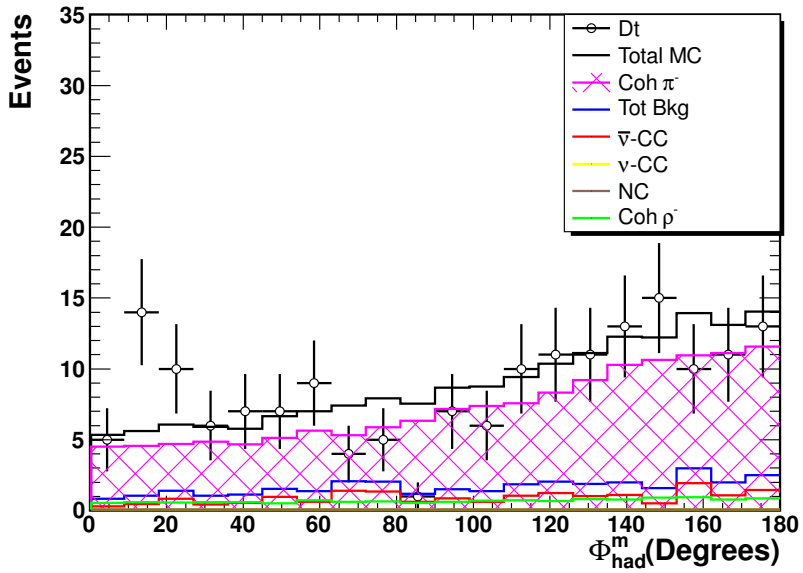

Figure 6.65: The Φ_{had}^{PT} distribution from different contributions, ν-CC, $\bar{\nu}$-CC, NC, $\bar{\nu}$-Cohρ^- and Cohπ^- in *signal (>0.7) region* and the Comparison between Data (points with error bars) and MC (histogram).

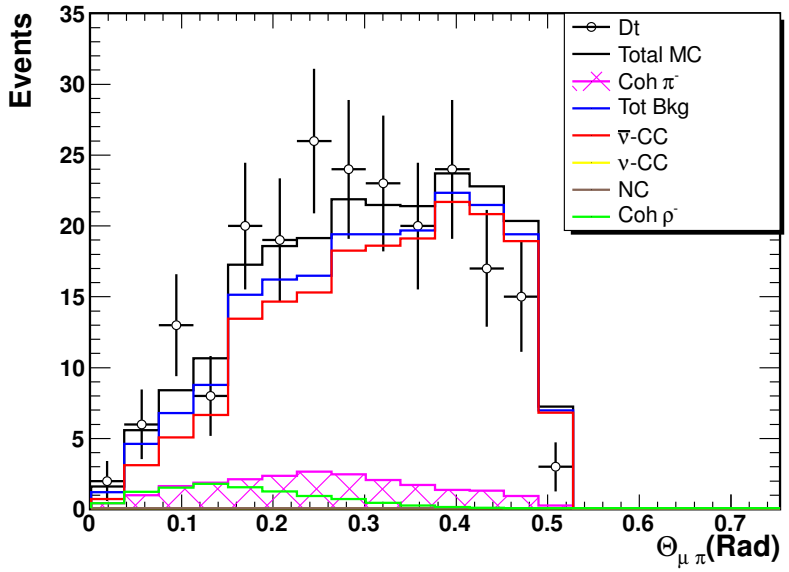

Figure 6.66: The angleθ between muon and pion distribution from different contributions, ν-CC, $\bar{\nu}$-CC, NC, $\bar{\nu}$-Cohρ^- and Cohπ^- in *background (control) region* and the Comparison between Data (points with error bars) and MC (histogram).

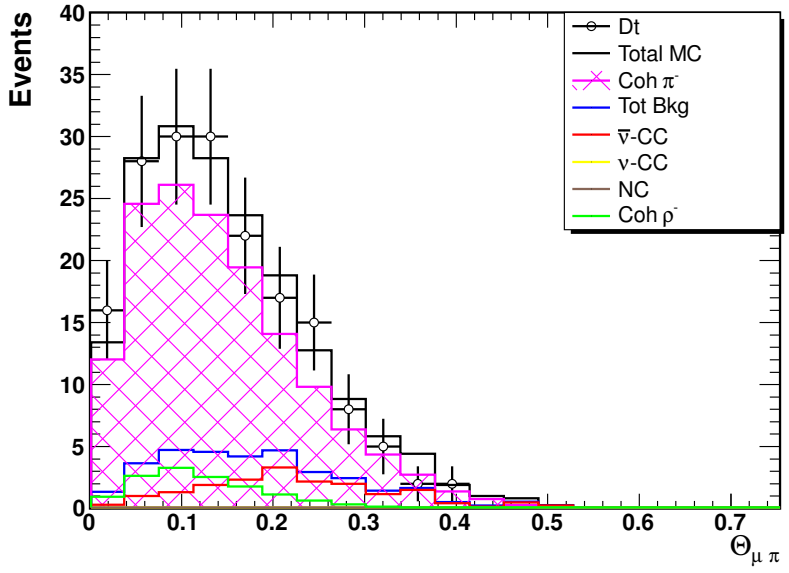

Figure 6.67: The angle θ distribution from different contributions, ν-CC, $\bar{\nu}$-CC, NC, $\bar{\nu}$-Cohρ^- and Cohπ^- in *signal (>0.7) region* and he Comparison between Data points with error bars and MC (histogram).

Table 6.41: The NN cut table (the beam(flux) reweight is applied to all the $\bar{\nu}_\mu$-CC and ν_μ-CC events).

NN	Tot-Bkg	BN	Norm-Bkg	Data	Raw Sig.	Eff.	Corr-Sig. (Err = Stat., BN)
0.4	76.6	1.19	91.5	311	219	0.533	411.5 ± 39.61 ± 19.29
0.41	74.4	1.2	89	306	217	0.531	408.7 ± 39.37 ± 18.82
0.42	72.9	1.2	87.2	304	217	0.529	410 ± 39.32 ± 18.51
0.43	71.2	1.2	85.1	301	216	0.527	409.9 ± 39.19 ± 18.14
0.44	69.1	1.19	82.4	300	218	0.524	415.1 ± 39.2 ± 17.69
0.45	68	1.19	81.1	300	219	0.522	419.6 ± 39.29 ± 17.5
0.46	66.2	1.19	78.9	297	218	0.519	420.3 ± 39.22 ± 17.14
0.47	64.9	1.19	77.4	294	217	0.516	419.9 ± 39.18 ± 16.9
0.48	63.8	1.19	76.1	291	215	0.513	418.9 ± 39.14 ± 16.7
0.49	63	1.19	75	290	215	0.51	421.8 ± 39.26 ± 16.59
0.5	60.3	1.19	71.7	289	217	0.506	429.5 ± 39.29 ± 16
0.51	59.2	1.19	70.3	286	216	0.503	429.2 ± 39.3 ± 15.81
0.52	58.2	1.19	69.1	285	216	0.498	433.5 ± 39.49 ± 15.69
0.53	56.6	1.19	67.2	281	214	0.494	433.2 ± 39.48 ± 15.4
0.54	54.8	1.19	65.1	275	210	0.488	430 ± 39.39 ± 15.06
0.55	52.7	1.19	62.9	265	202	0.483	418.8 ± 39.05 ± 14.67
0.56	50.6	1.2	60.6	254	193	0.476	406 ± 38.69 ± 14.27
0.57	47.9	1.2	57.4	245	188	0.469	399.7 ± 38.44 ± 13.71
0.58	44.3	1.19	52.9	244	191	0.461	415 ± 38.76 ± 12.92
0.59	42.1	1.19	50.3	238	188	0.453	414.5 ± 38.77 ± 12.48
0.6	40.1	1.2	47.9	230	182	0.445	408.8 ± 38.65 ± 12.08
0.61	38.4	1.2	46	224	178	0.439	405.7 ± 38.62 ± 11.75
0.62	36.6	1.2	43.9	217	173	0.432	400.5 ± 38.51 ± 11.38
0.63	35.2	1.2	42.2	211	169	0.425	397 ± 38.52 ± 11.12
0.64	33.7	1.2	40.5	203	162	0.419	387.6 ± 38.27 ± 10.78
0.65	32.5	1.21	39.2	196	157	0.412	380.3 ± 38.21 ± 10.58
0.66	31	1.21	37.4	191	154	0.406	378.7 ± 38.24 ± 10.27
0.67	29.5	1.2	35.5	189	154	0.399	385.1 ± 38.54 ± 9.929
0.68	28.6	1.2	34.4	186	152	0.392	386.5 ± 38.76 ± 9.771
0.69	27.2	1.2	32.8	183	150	0.385	389.7 ± 39.01 ± 9.492
0.7	26.3	1.21	31.7	175	143	0.379	378.4 ± 38.86 ± 9.335
0.71	25.2	1.21	30.4	172	142	0.372	380.9 ± 39.13 ± 9.112
0.72	24.2	1.2	29.2	169	140	0.365	382.7 ± 39.36 ± 8.896
0.73	22.9	1.2	27.5	167	139	0.358	389.1 ± 39.71 ± 8.574
0.74	21.3	1.2	25.7	161	135	0.351	385.3 ± 39.68 ± 8.158
0.75	20.2	1.2	24.3	157	133	0.344	385.7 ± 39.87 ± 7.873
0.76	18.9	1.2	22.8	153	130	0.336	387.3 ± 40.14 ± 7.56
0.77	18	1.2	21.6	150	128	0.328	391.7 ± 40.66 ± 7.373
0.78	16.6	1.2	19.9	146	126	0.319	394.6 ± 40.98 ± 6.979
0.79	15.7	1.2	18.8	143	124	0.311	399.8 ± 41.59 ± 6.793
0.8	14.8	1.2	17.8	139	121	0.301	402.3 ± 42.16 ± 6.611
0.81	13.4	1.2	16.1	131	115	0.292	393.7 ± 42.16 ± 6.188
0.82	12.8	1.2	15.4	126	111	0.282	392.2 ± 42.73 ± 6.099
0.83	11.6	1.2	14	122	108	0.271	399 ± 43.6 ± 5.773
0.84	10.9	1.2	13	117	104	0.259	401.9 ± 44.61 ± 5.653
0.85	10.3	1.2	12.3	110	97.7	0.247	395.4 ± 45.28 ± 5.577
0.86	9.44	1.2	11.3	104	92.7	0.234	395.3 ± 46.32 ± 5.409
0.87	8.21	1.2	9.83	98	88.2	0.22	401.1 ± 47.71 ± 5.012
0.88	7.34	1.2	8.83	88	79.2	0.203	389.5 ± 48.9 ± 4.853
0.89	6.8	1.2	8.16	82	73.8	0.186	396.5 ± 51.47 ± 4.904

Figure 6.68 shows a coherent π^- event picture after all the kinematic cut and neural network output cut of NOMAD events.

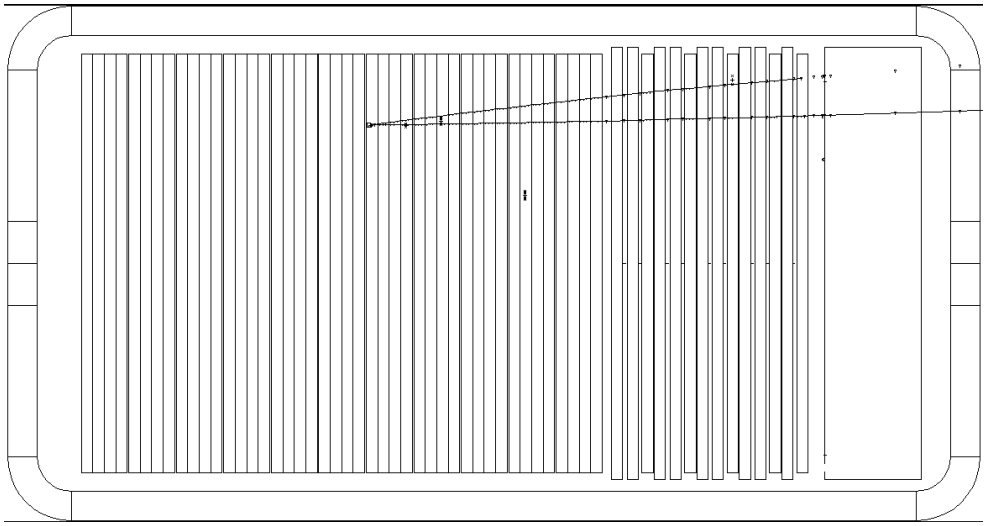

Figure 6.68: Coherent π^- event picture originated by $\bar{\nu}_\mu$ contamination in the anti-neutrino mode.

Table 6.42: Kinematic information of a coherent π^- event corresponding to Figure 6.68 survived from preselection and Neural Network.

Neutrino Beam Mode							
Run	Event	NN(lh)	XVR	YVR	ZVR		
20896	22826	0.621	-32	107	223		
P_T^m	Φ_{LH}	Φ_{mPtH}	$\Theta_{\mu\pi}$	t	ζ	Xbj	Ybj
0.204	167	71.9	0.124	0.0332	0.0363	0.0602	0.25
Ncand	Nprim	Nsecond	Nvzero	nhitmuon	nhithad		
2	2	0	0	47	15		
particle	E	|P|	Px	Py	Pz	Θ	Φ
Muon	27.3	27.3	0.397	-0.784	27.3	1.84	-63.2
Pion	8.59	8.59	-0.201	0.763	8.56	5.27	-75.3

Table 6.43: BN and SN table in 7 Bins, calculated from variable BN depends on the Evis(R=$\frac{\sigma(Coh\pi^-)}{\sigma(\bar{\nu}_\mu CC)}$).

Evis(GeV)	BN	SN	δ_{BN}	R$\times 10^{-3}$(Stat.)
2.5-8.0	0.4263	0.37	0.2307	9.442 ± 6.266
8.0-15.0	1.056	0.7615	0.2013	13.680 ± 2.762
15.0-20.0	1.289	0.8975	0.3096	11.550 ± 2.674
20.0-30.0	1.373	0.926	0.3261	8.325 ± 1.939
30.0-50.0	1.333	1.337	0.4512	8.190 ± 2.017
50.0-100.0	2.131	1.742	1.102	6.144 ± 2.400
100.0-300.0	3.164	2.606	4.47	4.100 ± 4.915
2.5-8.0	1.202	0.9585	0.1343	9.883 ± 1.018

Table 6.44: BN, and δ_{BN} table, using a fixed BN(R=$\frac{\sigma(Coh\pi^-)}{\sigma(\bar{\nu}_\mu CC)}$).

Evis(GeV)	BN	SN	δ_{BN}	R$\times 10^{-3}$(Stat.)
2.5-8.0	1.202	0.37	0.1343	5.186 ± 7.655
8.0-15.0	1.202	0.7615	0.1343	13.240 ± 2.787
15.0-20.0	1.202	0.8975	0.1343	11.710 ± 2.596
20.0-30.0	1.202	0.926	0.1343	8.584 ± 1.841
30.0-50.0	1.202	1.337	0.1343	8.343 ± 1.925
50.0-100.0	1.202	1.742	0.1343	6.903 ± 2.016
100.0-300.0	1.202	2.606	0.1343	5.160 ± 3.576
2.5-8.0	1.202	0.9585	0.1343	9.883 ± 1.018

Table 6.45: Signal in signal region, and Generated signal information calculated from variable BN.

Evis(GeV)	Sig-S	Sig-Gen	Efficiency
2.5 - 8.0	8.664	34.980	0.248
8.0 - 15.0	50.945	139.361	0.366
15.0 - 20.0	32.407	81.768	0.396
20.0 - 30.0	34.583	82.141	0.421
30.0 - 50.0	20.115	45.861	0.438
50.0 - 100.0	8.947	19.996	0.447
100.0 - 300.0	1.083	2.498	0.434
2.5 - 300.0	156.7	406.6	0.385

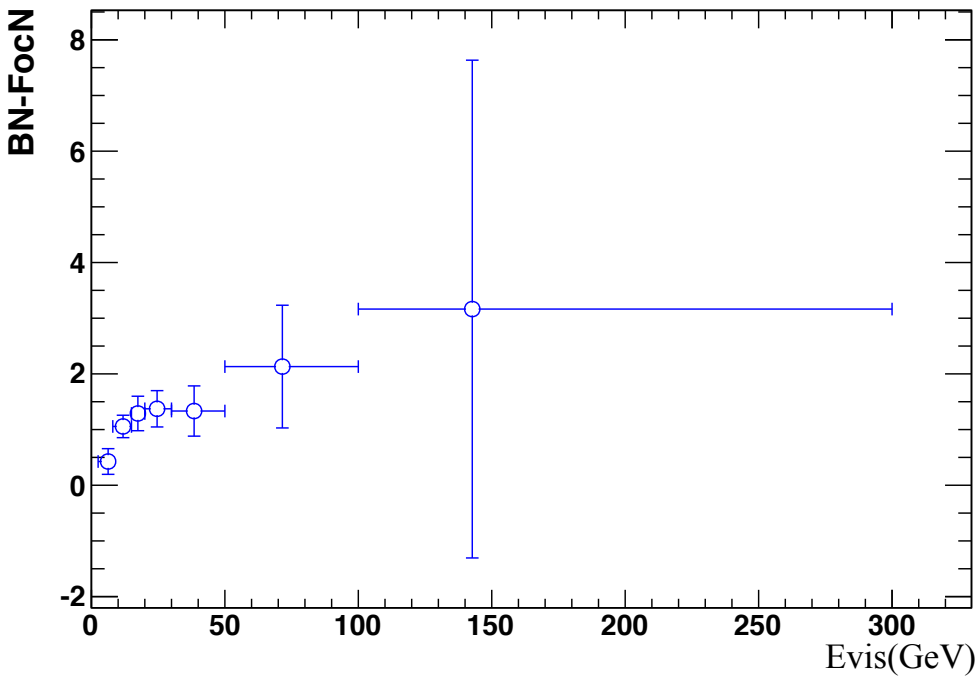

Figure 6.69: The distribution of BN as a function of visible energy(Evis) in 7 bins (the beam(flux) reweight is applied to all the $\bar{\nu}_\mu$-CC events).

Table 6.46: Norm-bkg, Corr-sig as a function of Evis in 7 bins calculated from variable BN.

Evis	Tot-bkg	BN	Norm-bkg	Data	Raw-sig	Eff	Corr-Sig. (Err=Stat., BN)
2.5 - 8.0	1.86	0.426	0.794	4	3.21	0.248	12.94 ± 8.411 ± 1.735
8.0 - 15.0	8.71	1.06	9.21	48	38.8	0.366	106.1 ± 20.87 ± 4.798
15.0 - 20.0	4.59	1.29	5.91	35	29.1	0.396	73.39 ± 16.61 ± 3.586
20.0 - 30.0	5.81	1.37	7.98	40	32	0.421	76.06 ± 17.13 ± 4.499
30.0 - 50.0	3.83	1.33	5.1	32	26.9	0.438	61.36 ± 14.59 ± 3.941
50.0 - 100.0	2.07	2.13	4.42	20	15.6	0.447	34.83 ± 12.61 ± 5.103
100.0 - 300.0	0.372	3.16	1.18	4	2.82	0.434	6.509 ± 6.795 ± 3.835
2.5 - 300.0	27.2	1.2	32.8	183	150	0.385	389.7 ± 39.01 ± 9.492

Table 6.47: Corrected signal (Corr-Sig) as a function of Evis in 7 bins calculated from variable BN(R=$\frac{\sigma(Coh\pi^-)}{\sigma(\bar{\nu}_\mu CC)}$).

Evis(GeV)	<E>	Corr-Sig	$\bar{\nu}_\mu$-CC	R $\times 10^{-3}$(Stat.)
2.5 - 8	6.25	12.94	1370.7	9.442 ± 6.266
8 - 15	11.84	106.1	7755.0	13.680 ± 2.762
15 - 20	17.40	73.39	6352.6	11.550 ± 2.674
20 - 30	24.60	76.06	9136.4	8.325 ± 1.939
30 - 50	38.47	61.36	7492.4	8.190 ± 2.017
50 - 100	71.54	34.83	5668.7	6.144 ± 2.400
100 - 300	142.70	6.509	1587.6	4.100 ± 4.915
2.5 - 300	25.00	389.7	39435.6	9.883 ± 1.018

Table 6.48: Corrected signal (Corr-Sig-Enus) as a function of E_ν in 7 bins calculated from variable BN(R=$\frac{\sigma(Coh\pi^-)}{\sigma(\bar{\nu}_\mu CC)}$).

E_ν	<E>	Corr-Sig-Enus	$\bar{\nu}_\mu$-CC	R $\times 10^{-3}$(Stat.)
2.5 - 8	6.25	13.162 ± 8.164	1370.7	9.602 ± 5.956
8 - 15	11.84	106.167 ± 21.991	7755.0	13.690 ±2.836
15 - 20	17.40	74.131 ± 17.080	6352.6	11.669 ±2.689
20 - 30	24.60	76.719 ± 17.907	9136.4	8.397 ±1.960
30 - 50	38.47	60.443 ± 15.147	7492.4	8.067 ±2.022
50 - 100	71.54	34.634 ± 13.077	5668.7	6.110 ±2.307
100 - 300	142.70	5.943 ± 6.872	1587.6	3.743 ±4.329
2.5 - 300	25.00	389.7 ± 40.15	39435.6	9.883 ±1.018

Figure 6.70 and Figure 6.71 show the distributions of R=$\frac{\sigma(Coh\pi^-)}{\sigma(\bar{\nu}_\mu CC)}$ and R×E distributions in both linear scale and log scale, where R is calculated from variable BN.

Table 6.49 and Table 6.50 show the results calculated using a fixed BN of anti-neutrino beam mode data (Negative focusing data: FocN).

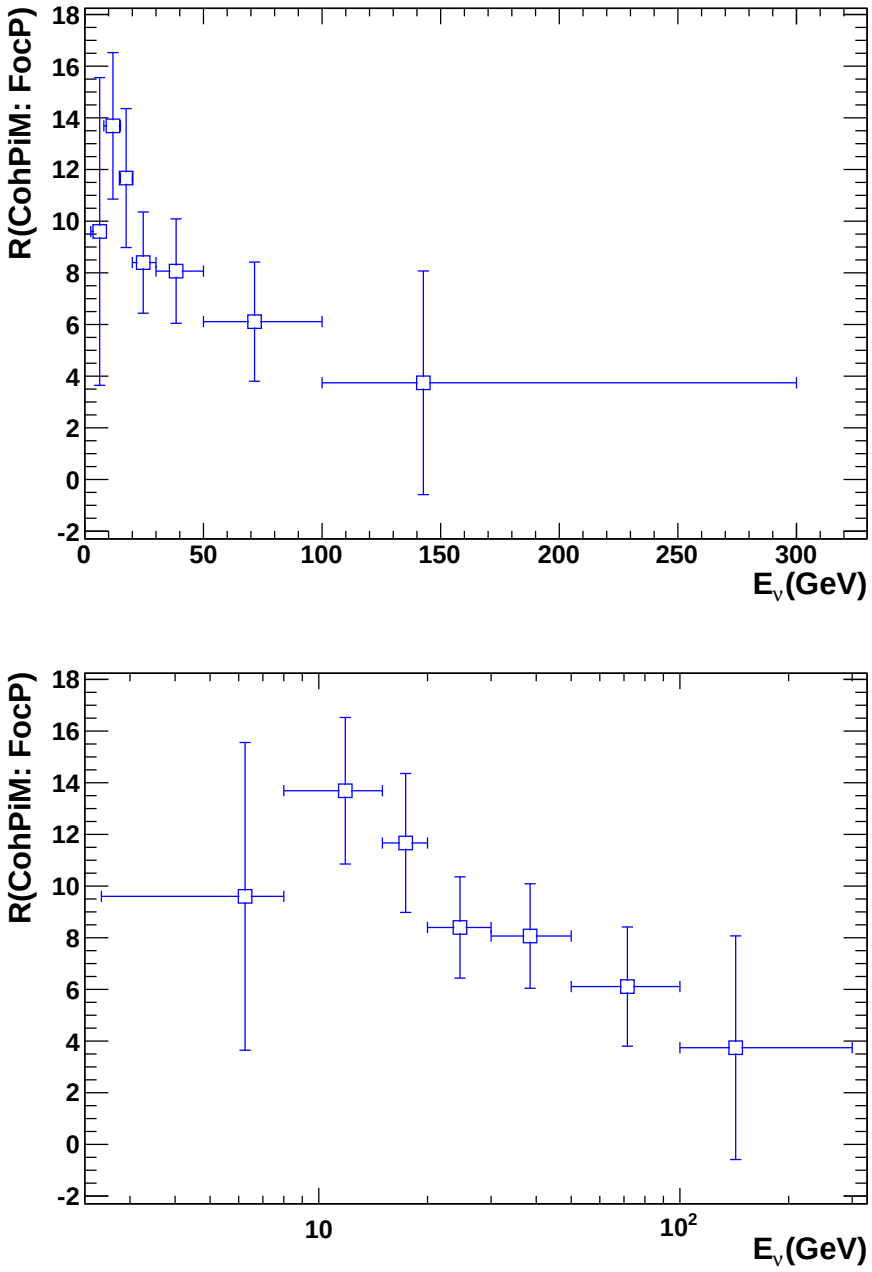

Figure 6.70: R=$\frac{\sigma(Coh\pi^-)}{\sigma(\bar{\nu}_\mu CC)}$ distribution in both linear scale (top) and log scale (bottom), calculated from variable BN which depends on the Evis (the beam(flux) reweight is applied to all the $\bar{\nu}_\mu$-CC events).

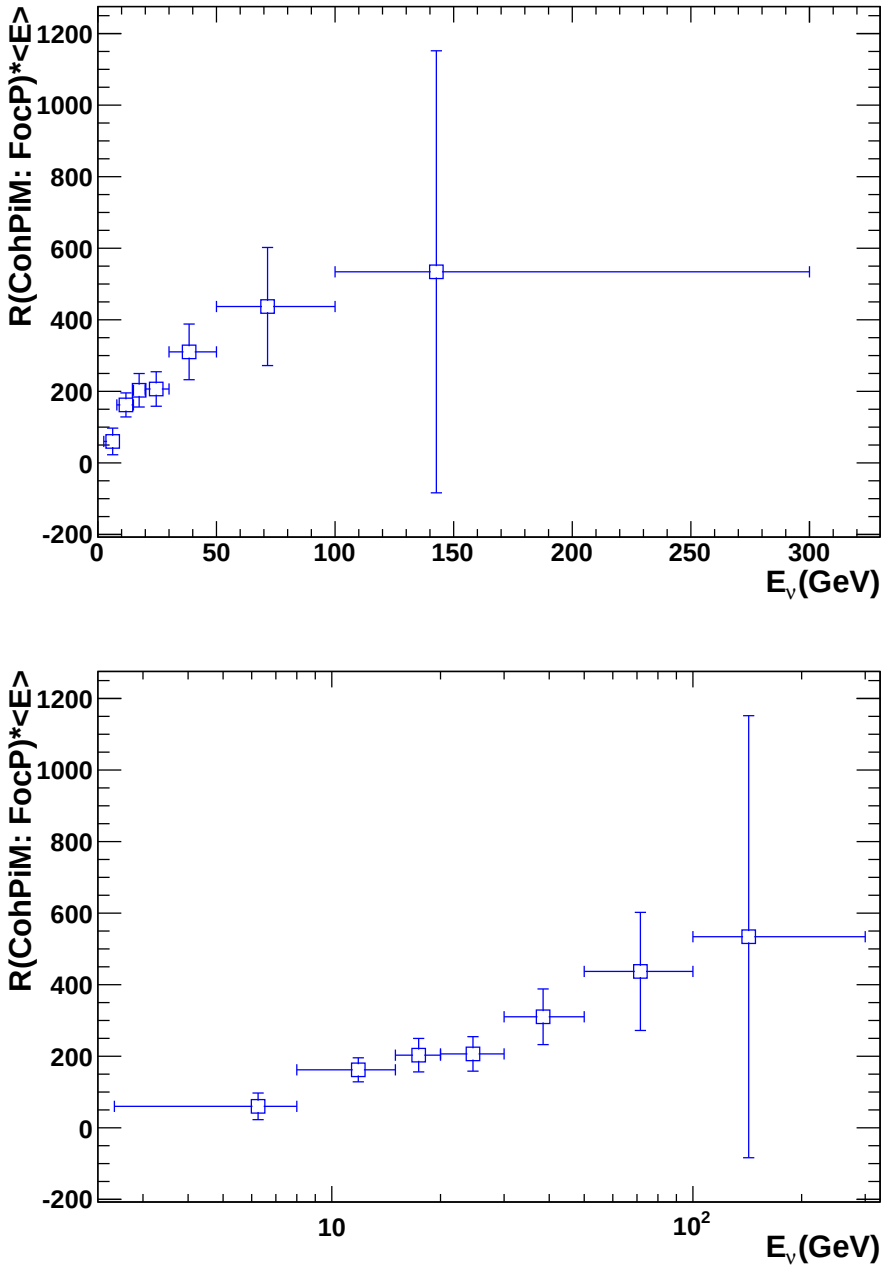

Figure 6.71: R×<E> distribution in both linear scale (top) and log scale (bottom), calculated from variable BN which depends on the Evis (the beam(flux) reweight is applied to all the $\bar{\nu}_\mu$-CC events).

Table 6.49: Norm-bkg, Corr-sig as a function of Evis in 7 bins, calculated from a fixed BN.

Evis	Tot-bkg	BN	Norm-bkg	Data	Raw-sig	Eff	Corr-Sig. (Err=Stat., BN)
2.5 - 8	1.86	1.2	2.24	4	1.76	0.248	7.108 ± 10.44 ± 1.01
8 - 15	8.71	1.2	10.5	48	37.5	0.366	102.6 ± 21.37 ± 3.202
15 - 20	4.59	1.2	5.52	35	29.5	0.396	74.39 ± 16.42 ± 1.555
20 - 30	5.81	1.2	6.98	40	33	0.421	78.42 ± 16.72 ± 1.853
30 - 50	3.83	1.2	4.6	32	27.4	0.438	62.51 ± 14.38 ± 1.173
50 - 100	2.07	1.2	2.49	20	17.5	0.447	39.13 ± 11.41 ± 0.6221
100 - 300	0.372	1.2	0.447	4	3.55	0.434	8.192 ± 5.676 ± 0.1152
2.5 - 300	27.2	1.2	32.8	183	150	0.385	389.7 ± 39.01 ± 9.492

Table 6.50: Corrected signal (Corr-sig) as a function of Evis in 7 bins, calculated from a fixed BN(R=$\frac{\sigma(Coh\pi^-)}{\sigma(\bar{\nu}_\mu CC)}$).

Evis(GeV)	<E>	Corr-Sig	$\bar{\nu}_\mu$-CC	R $\times 10^{-3}$(Stat.)
2.5 - 8	6.25	7.108	1370.7	5.186 ± 7.655
8 - 15	11.84	102.6	7755.0	13.240± 2.787
15 - 20	17.40	74.39	6352.6	11.710± 2.596
20 - 30	24.60	78.42	9136.4	8.584 ± 1.841
30 - 50	38.47	62.51	7492.4	8.343 ± 1.925
50 - 100	71.54	39.13	5668.7	6.903 ± 2.016
100 - 300	142.70	8.192	1587.6	5.160 ± 3.576
2.5 - 300	25.00	389.7	39435.6	9.883 ± 1.018

Table 6.51: Corrected signal (Corr-Sig-Enus) as a function of E_ν in 7 bins, calculated from a fixed BN(R=$\frac{\sigma(Coh\pi^-)}{\sigma(\bar{\nu}_\mu CC)}$).

E_ν	<E>	Corr-Sig-Enus	$\bar{\nu}_\mu$-CC	R $\times 10^{-3}$(Stat.)
2.5 - 8	6.25	7.745 ± 9.921	1370.7	5.650 ± 7.238
8 - 15	11.84	102.432 ± 22.304	7755.0	13.209 ± 2.876
15 - 20	17.40	75.069 ± 16.589	6352.6	11.817 ± 2.611
20 - 30	24.60	79.013 ± 17.020	9136.4	8.648 ± 1.863
30 - 50	38.47	61.795 ± 14.368	7492.4	8.248 ± 1.918
50 - 100	71.54	38.911 ± 11.736	5668.7	6.864 ± 2.070
100 - 300	142.70	7.436 ± 5.009	1587.6	4.684 ± 3.155
2.5 - 300	25.00	389.7 ± 40.15	39435.6	9.883 ± 1.018

Figure 6.72 and Figure 6.73 show the distributions of R=$\frac{\sigma(Coh\pi^-)}{\sigma(\bar{\nu}_\mu CC)}$ and R×E distributions while R is calculated from a fixed BN.

6.6 Comparison of Neutrino Mode and Anti-neutrino Mode

With the result of R in Neutrino Beam Mode and Anti-neutrino Beam Mode, we could calculate the average value of <R>. We use $<R^->$ to denote this average value, "-" means this is the R of coherent π^-. To explain how to calculate $<R^->$, let's take a simple example: for the variables $A \pm \delta A$ and $B \pm \delta B$, the average value of C and δ C are calculated as:

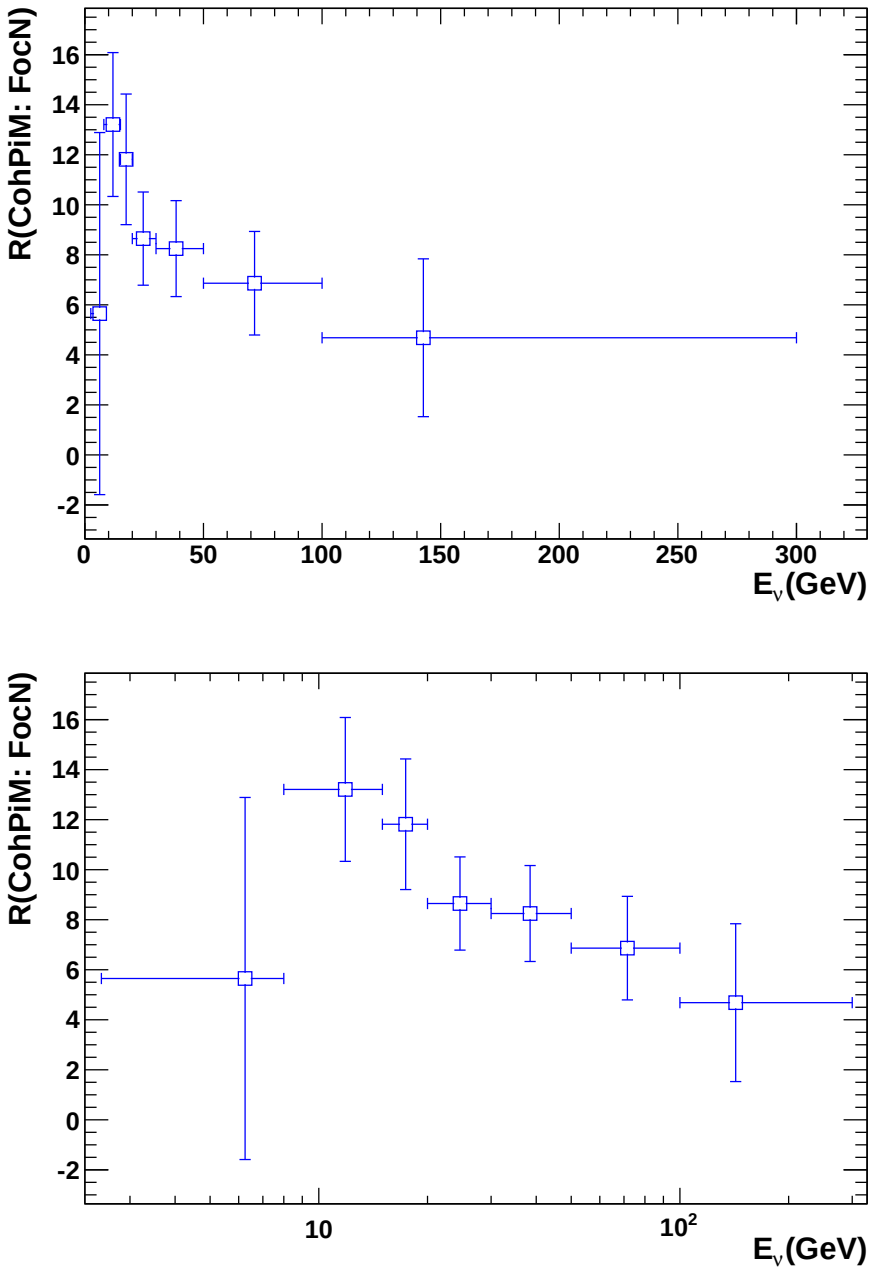

Figure 6.72: R=$\frac{\sigma(Coh\pi^-)}{\sigma(\bar{\nu}_\mu CC)}$ distribution in both linear scale (top) and log scale (bottom), calculated from a fixed BN (the beam(flux) reweight is applied to all the $\bar{\nu}_\mu$-CC events).

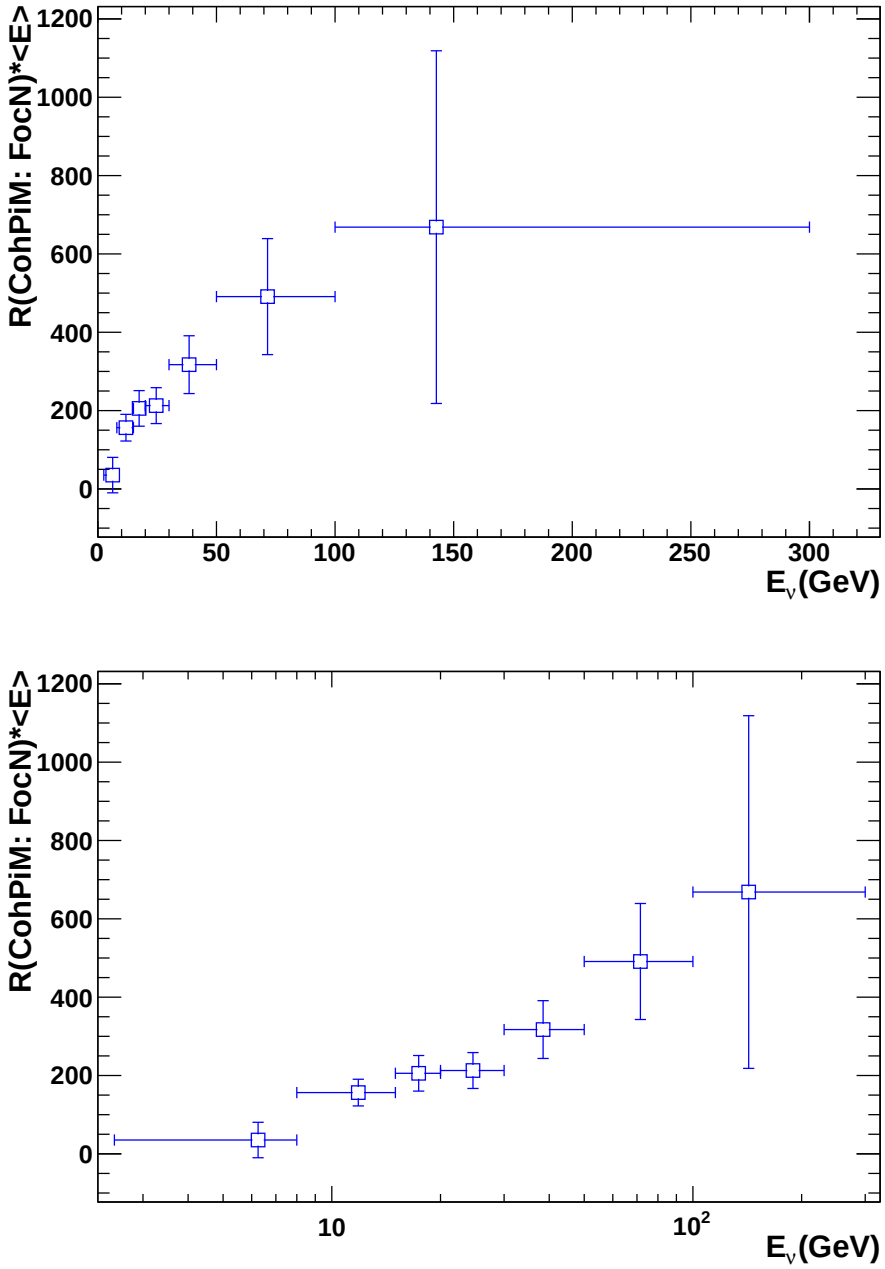

Figure 6.73: R×<E> distribution in both linear scale (top) and log scale (bottom), calculated from a fixed BN (the beam(flux) reweight is applied to all the $\bar{\nu}_\mu$-CC events).

$$C = \frac{\frac{A}{\delta A^2} + \frac{B}{\delta B^2}}{\frac{1}{\delta A^2} + \frac{1}{\delta B^2}} \tag{6.10}$$

$$\delta C = \sqrt{\frac{1}{\frac{1}{\delta A^2} + \frac{1}{\delta B^2}}} \tag{6.11}$$

Using Equation (6.10) and Equation (6.11), the averaged value of R(Cohπ^-) in neutrino beam mode (positive focusing data: FocP) and anti-neutrino beam mode (negative focusing data: FocN) are calculated and shown in Table 6.52.

Table 6.52: Comparison of R=$\frac{\sigma(Coh\pi^-)}{\sigma(\bar{\nu}_\mu CC)}$:FocP and R=$\frac{\sigma(Coh\pi^-)}{\sigma(\bar{\nu}_\mu CC)}$:FocN as a function of Evis using variable BN.)

Evis(GeV)	R(Cohπ^-: FocP)	R(Cohπ^-: FocN)	<R>
2.5-8.0	14.520 ± 5.224	9.442 ± 6.266	12.438 ± 4.012
8.0-15.0	16.490 ± 3.333	13.68 ± 2.762	14.824 ± 2.127
15.0-20.0	7.851 ± 3.217	11.55 ± 2.674	10.039 ± 2.056
20.0-30.0	12.760 ± 2.608	8.325 ± 1.939	9.904 ± 1.556
30.0-50.0	7.362 ± 1.795	8.19 ± 2.017	7.728 ± 1.341
50.0-100.0	4.094 ± 1.668	6.144 ± 2.400	4.762 ± 1.370
100.0-300.0	3.894 ± 2.341	4.100 ± 4.915	3.932 ± 2.114
2.5-300.0	9.845 ± 1.047	9.883 ± 1.018	9.865 ± 0.730

Table 6.53: Comparison of R=$\frac{\sigma(Coh\pi^-)}{\sigma(\bar{\nu}_\mu CC)}$:FocP and R=$\frac{\sigma(Coh\pi^-)}{\sigma(\bar{\nu}_\mu CC)}$:FocN as a function of E_ν using variable BN.

E_ν(GeV)	R(Cohπ^-: FocP)	R(Cohπ^-: FocN)	<R>
2.5-8.0	14.385 ± 5.112	9.602 ± 5.956	12.356 ± 3.879
8.0-15.0	16.426 ± 3.432	13.690 ±2.836	14.800 ± 2.186
15.0-20.0	8.578 ± 3.221	11.669 ±2.689	10.400 ± 2.064
20.0-30.0	12.393 ± 2.587	8.397 ±1.960	9.854 ± 1.562
30.0-50.0	7.432 ± 1.834	8.067 ±2.022	7.719 ± 1.358
50.0-100.0	4.178 ± 1.699	6.110 ±2.307	4.857 ± 1.368
100.0-300.0	3.597 ± 2.137	3.743 ±4.329	3.626 ± 1.916
2.5-300.0	9.845 ± 1.047	9.883 ± 1.018	9.865 ± 0.730

Table 6.52 and Table 6.53 show the comparison of R(Cohπ^-) in Neutrino Beam Mode and Anti-neutrino Beam Mode in 7 bins before and after smearing matrix

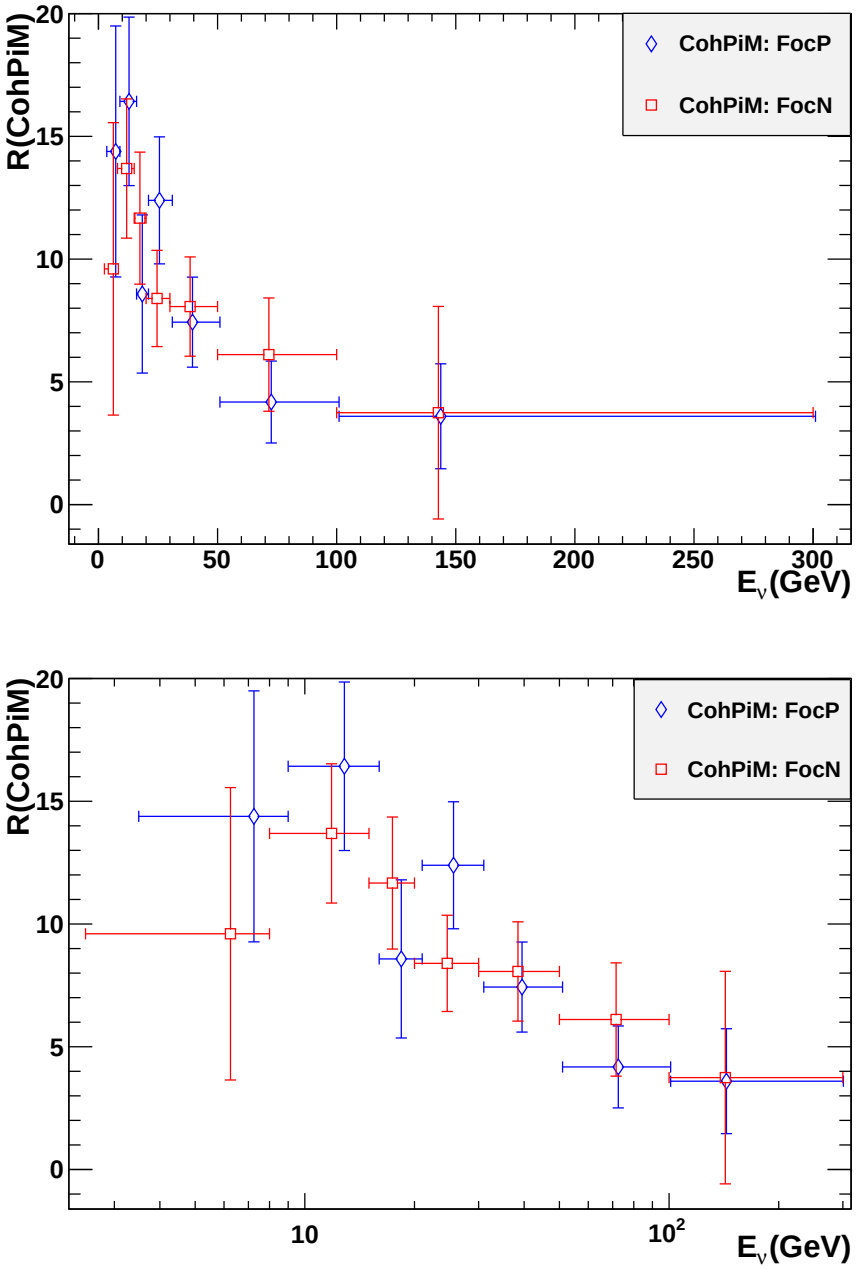

Figure 6.74: Comparison of R=$\frac{\sigma(Coh\pi^-)}{\sigma(\bar{\nu}_\mu CC)}$:FocP and R=$\frac{\sigma(Coh\pi^-)}{\sigma(\bar{\nu}_\mu CC)}$:FocN as a function of E_ν using variable BN.

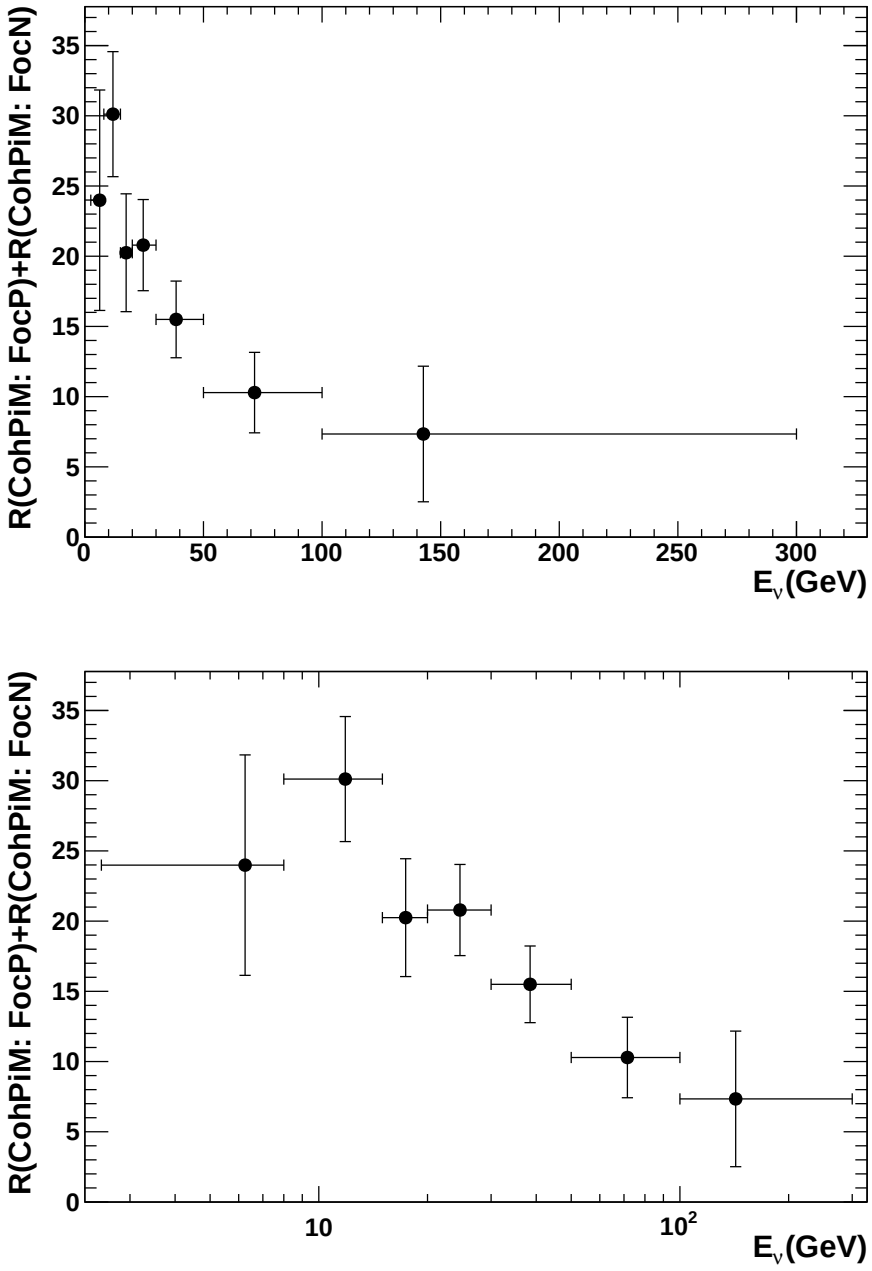

Figure 6.75: Distribution of the sum of R=$\frac{\sigma(Coh\pi^-)}{\sigma(\bar{\nu}_\mu CC)}$:FocP and R=$\frac{\sigma(Coh\pi^-)}{\sigma(\bar{\nu}_\mu CC)}$:FocN as a function of E_ν using variable BN.

correction. From these two tables, it is obvious that in each bins, the R=$\frac{\sigma(Coh\pi^-)}{\sigma(\bar{\nu}_\mu CC)}$ are similar in this two beam modes. There are overlap in each bins. In the whole bin from 2.5 to 300 GeV, R=$\frac{\sigma(Coh\pi^-)}{\sigma(\bar{\nu}_\mu CC)}$ are very close to each other in this two beam modes.

6.7 Comparison of Coherent π^- and Coherent π^+

With the average value of R(R=$\frac{\sigma(Coh\pi^-)}{\sigma(\bar{\nu}_\mu CC)}$), let's compare the average value with the result of coherent π^+ which got by Xinchun Tian. In Table 6.54, it gives out that the

Table 6.54: Comparison of R=$\frac{\sigma(Coh\pi^-)}{\sigma(\bar{\nu}_\mu CC)}$ and R=$\frac{\sigma(Coh\pi^+)}{\sigma(\nu_\mu CC)}$ as a function of Evis using variable BN.

Evis(GeV)	R(Cohπ^-)	R(Cohπ^+)	R(Cohπ^-) / R(Cohπ^+)
2.5-8.0	12.438 ± 4.012	7.06 ± 1.02	1.762 ± 0.623
8.0-15.0	14.824 ± 2.127	7.23 ± 0.37	2.053 ± 0.313
15.0-20.0	10.039 ± 2.056	6.43 ± 0.36	1.561 ± 0.331
20.0-30.0	9.904 ± 1.556	5.39 ± 0.27	1.837 ± 0.303
30.0-50.0	7.728 ± 1.341	4.52 ± 0.24	1.710 ± 0.310
50.0-100.0	4.762 ± 1.370	3.08 ± 0.23	1.546 ± 0.460
100.0-300.0	3.932 ± 2.114	2.06 ± 0.31	1.909 ± 1.066
2.5-300.0	9.865 ± 0.730	4.86 ± 0.12	2.030 ± 0.158

ratio between R=$\frac{\sigma(Coh\pi^-)}{\sigma(\bar{\nu}_\mu CC)}$ and R=$\frac{\sigma(Coh\pi^+)}{\sigma(\nu_\mu CC)}$ is 2.030 ± 0.158, which is consistent to the theoratical prediction, because in NOMAD beam, the ratio between the number of ν_μ and $\bar{\nu}_\nu$ is 2:1.

Table 6.55 shows the comparison between R=$\frac{\sigma(Coh\pi^-)}{\sigma(\bar{\nu}_\mu CC)}$ and R=$\frac{\sigma(Coh\pi^+)}{\sigma(\nu_\mu CC)}$ after smearing matrix correction.

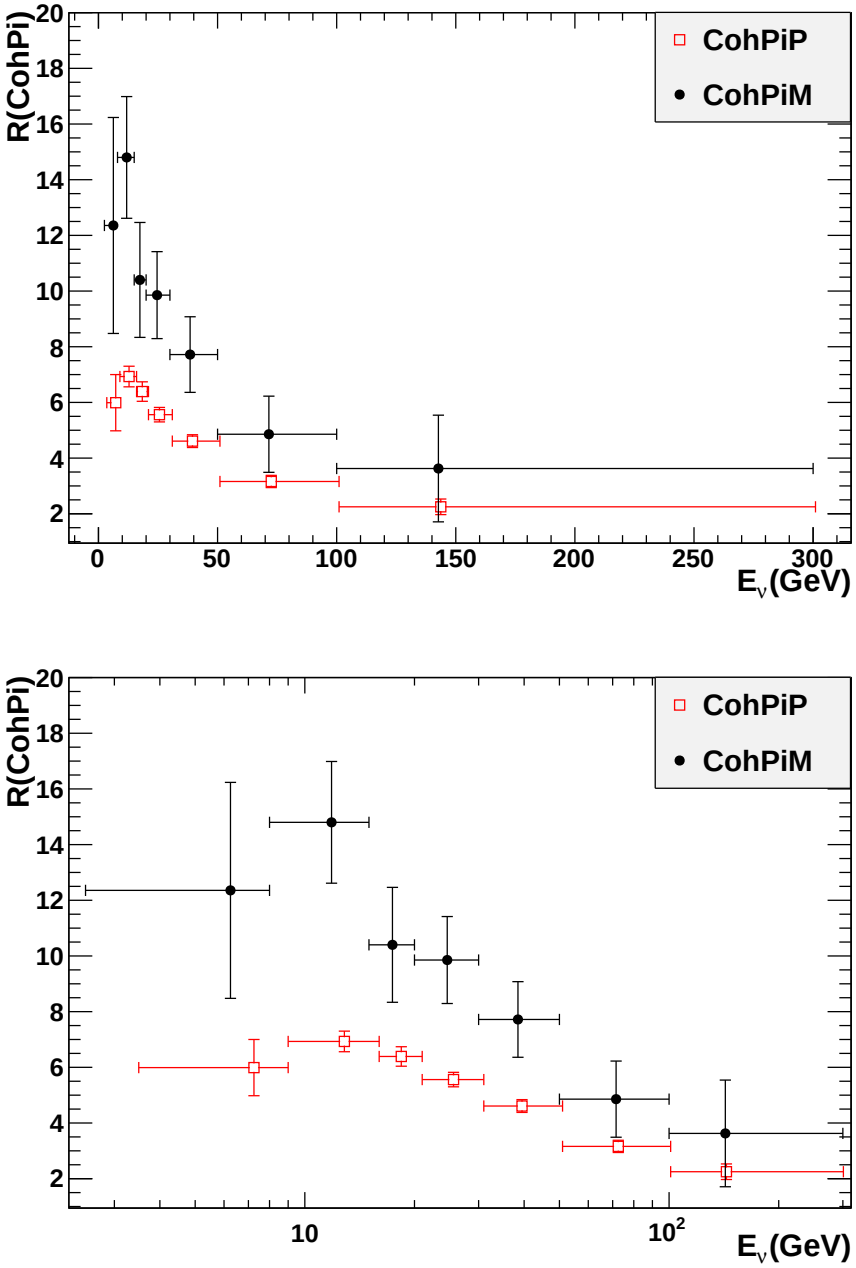

Figure 6.76: Comparison of R=$\frac{\sigma(Coh\pi^-)}{\sigma(\bar{\nu}_\mu CC)}$ and R=$\frac{\sigma(Coh\pi^+)}{\sigma(\nu_\mu CC)}$ using variable BN.

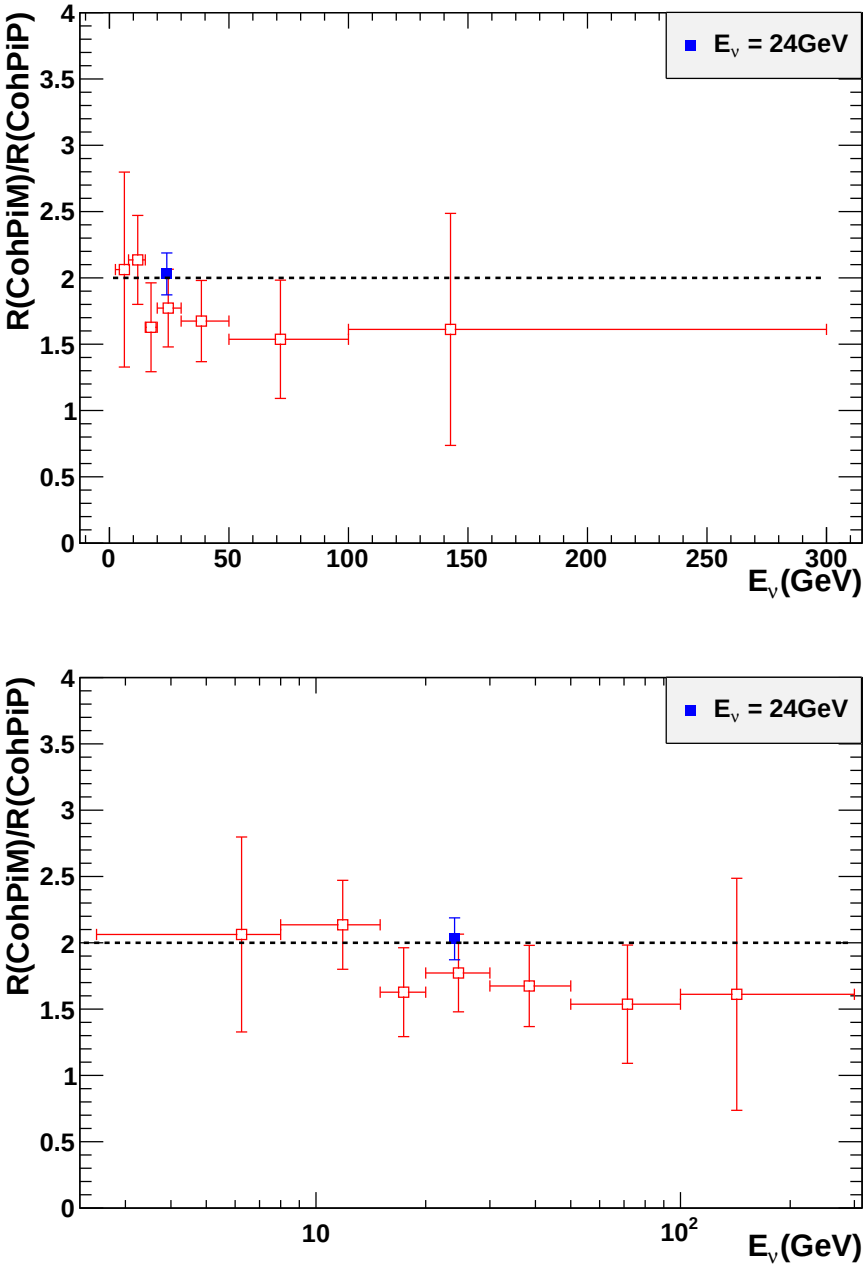

Figure 6.77: Comparison of R=$\frac{\sigma(Coh\pi^-)}{\sigma(\bar{\nu}_\mu CC)}$ and R=$\frac{\sigma(Coh\pi^+)}{\sigma(\nu_\mu CC)}$ using variable BN.

Table 6.55: Comparison of R=$\frac{\sigma(Coh\pi^-)}{\sigma(\bar{\nu}_\mu CC)}$ and =$\frac{\sigma(Coh\pi^+)}{\sigma(\nu_\mu CC)}$ as a function of E_ν using variable BN.

E_ν(GeV)	R(Cohπ^-)	R(Cohπ^+)	R(Cohπ^-) / R(Cohπ^+)
2.5-8.0	12.356 ± 3.879	5.99 ± 1.01	2.063 ± 0.735
8.0-15.0	14.800 ± 2.186	6.93 ± 0.37	2.136 ± 0.335
15.0-20.0	10.400 ± 2.064	6.39 ± 0.35	1.628 ± 0.335
20.0-30.0	9.854 ± 1.562	5.56 ± 0.26	1.772 ± 0.293
30.0-50.0	7.719 ± 1.358	4.61 ± 0.23	1.674 ± 0.306
50.0-100.0	4.857 ± 1.368	3.16 ± 0.22	1.537 ± 0.446
100.0-300.0	3.626 ± 1.916	2.25 ± 0.28	1.612 ± 0.875
2.5-300.0	9.865 ± 0.730	4.86 ± 0.12	2.030 ± 0.158

6.8 Systematic Uncertainties

Background Subtraction Procedure

In the procedure of the normalization of background, there are two methods have been used. One is to normalize the background bin by bin with variable normalization factor. The other one is to normalize the background by the normalization factor of the whole bin from 2.5 to 300 GeV. From this subsection, we would give out the result of analysis using a single background normalization factor. The difference between these two ways of normalization of background is considered as a systematic uncertainty which is shown in Table 6.61. In Table 6.61, δ_R equals to the R calculated from a fixed BN minus the R calculated from variable BN. $\frac{\delta_R}{R}$ equals δ_R divide by the R calculated from a fixed BN.

Table 6.56 shows the comparison of R=$\frac{\sigma(Coh\pi^-)}{\sigma(\bar{\nu}_\mu CC)}$ in neutrino beam mode and anti-neutrino beam mode calculated from a single background normalization.

The averaged value of R=$\frac{\sigma(Coh\pi^-)}{\sigma(\bar{\nu}_\mu CC)}$ in neutrino beam mode and anti-neutrino beam mode are calculated by the Equation (6.10) and Equation (6.11), and are shown in Table 6.57.

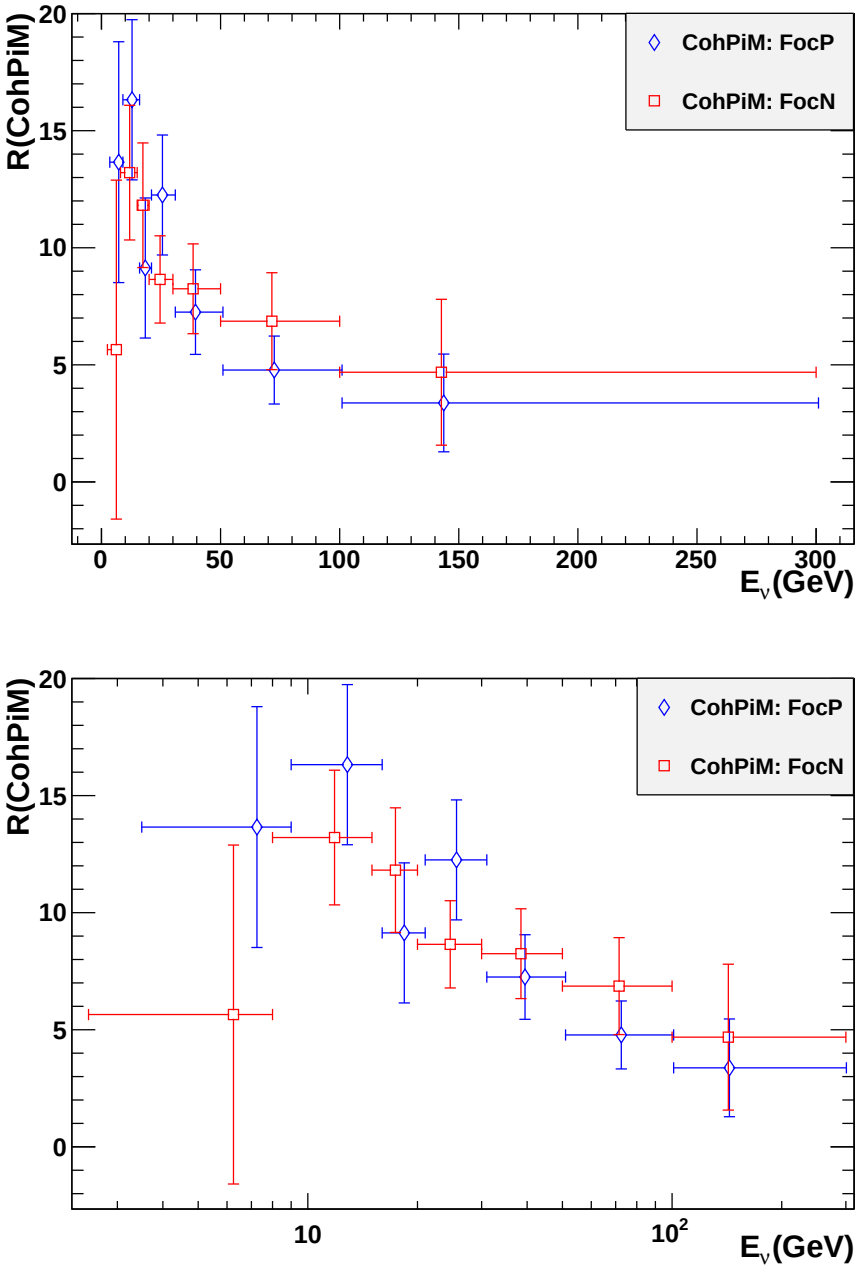

Figure 6.78: Comparison of R=$\frac{\sigma(Coh\pi^-)}{\sigma(\bar{\nu}_\mu CC)}$:FocP and R=$\frac{\sigma(Coh\pi^-)}{\sigma(\bar{\nu}_\mu CC)}$:FocN calculated from a fixed BN.

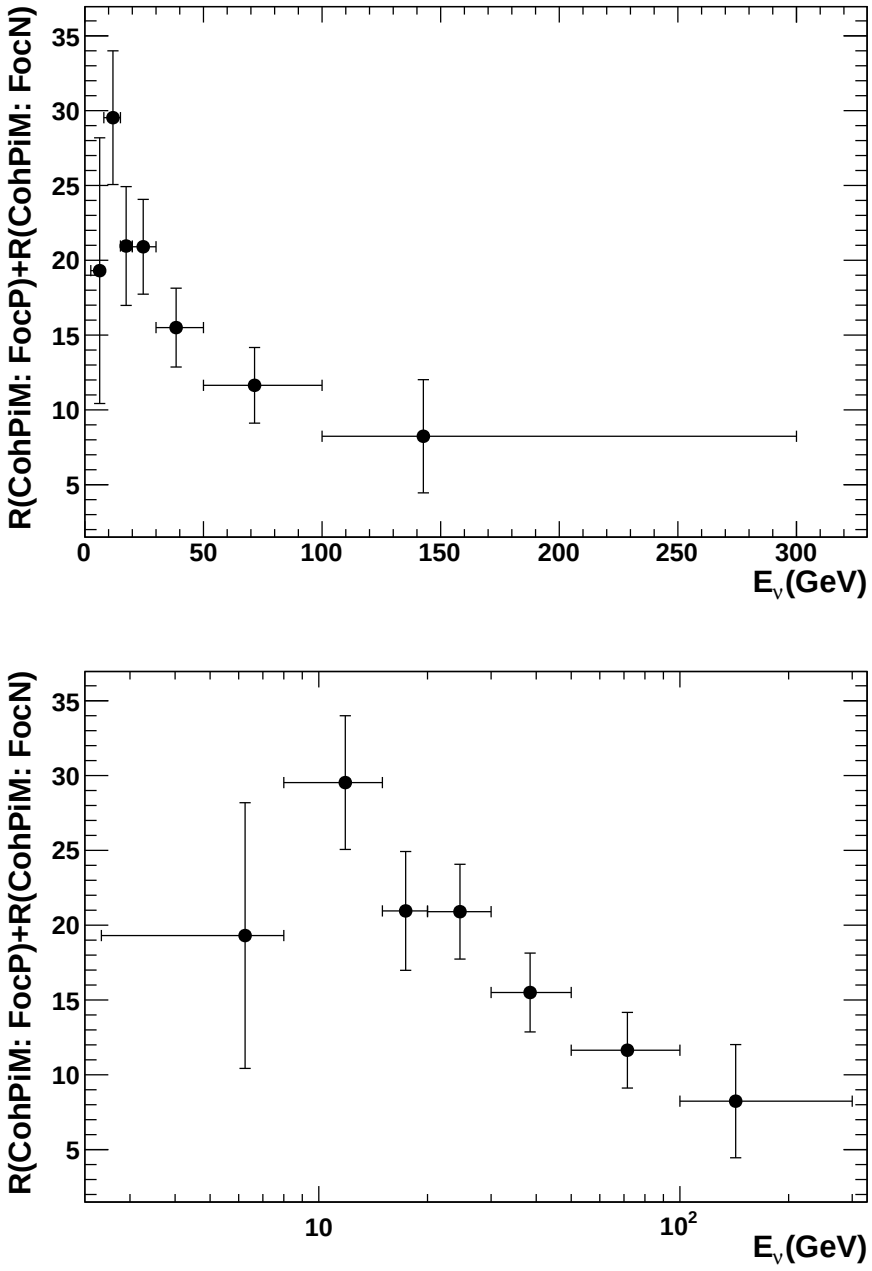

Figure 6.79: Distribution of the sum of R=$\frac{\sigma(Coh\pi^-)}{\sigma(\bar{\nu}_\mu CC)}$:FocP and R=$\frac{\sigma(Coh\pi^-)}{\sigma(\bar{\nu}_\mu CC)}$:FocN calculated from a fixed BN.

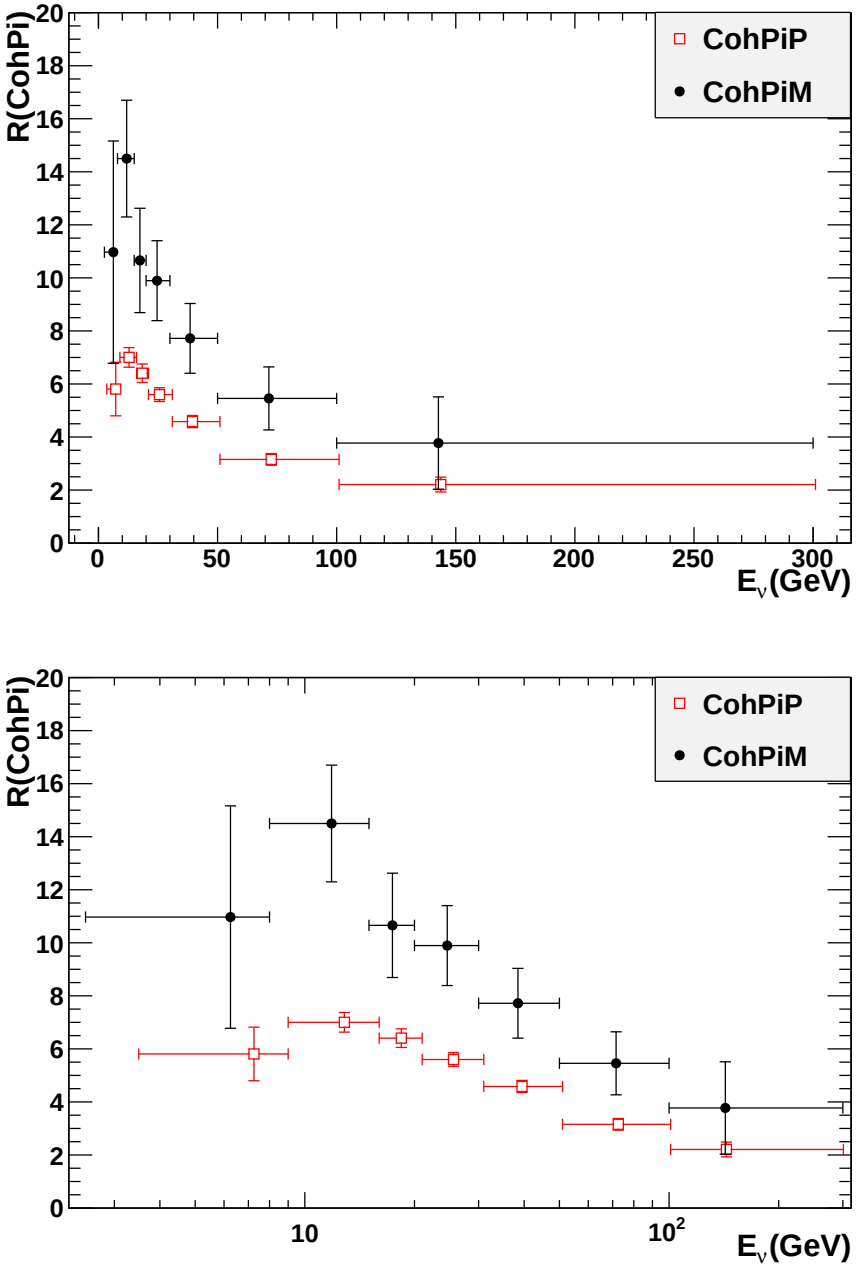

Figure 6.80: Comparison of R=$\frac{\sigma(Coh\pi^-)}{\sigma(\bar{\nu}_\mu CC)}$ and R=$\frac{\sigma(Coh\pi^+)}{\sigma(\nu_\mu CC)}$ calculated from a fixed BN.

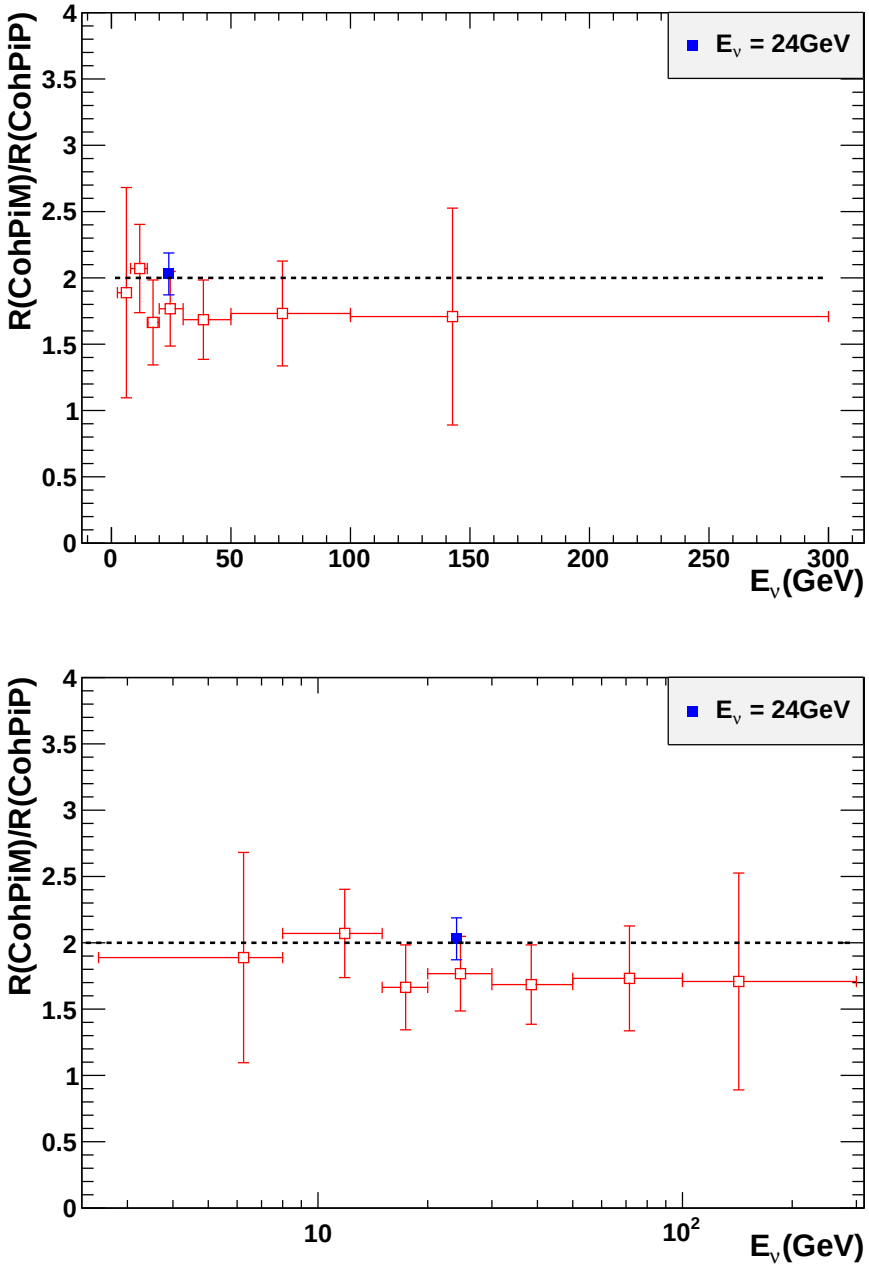

Figure 6.81: Comparison of R=$\frac{\sigma(Coh\pi^-)}{\sigma(\bar{\nu}_\mu CC)}$ and R=$\frac{\sigma(Coh\pi^+)}{\sigma(\nu_\mu CC)}$ calculated from a fixed BN.

Table 6.56: Comparison of R=$\frac{\sigma(Coh\pi^-)}{\sigma(\bar{\nu}_\mu CC)}$:FocP and R=$\frac{\sigma(Coh\pi^-)}{\sigma(\bar{\nu}_\mu CC)}$:FocN calculated from a fixed BN.

E_ν(GeV)	R(Cohπ^-: FocP)	R(Cohπ^-: FocN)	<R>
2.5-8.0	13.656± 5.143	5.650± 7.238	10.97 ± 4.192
8.0-15.0	16.321± 3.420	13.209± 2.876	14.498 ± 2.201
15.0-20.0	9.136± 2.991	11.817± 2.611	10.658 ± 1.967
20.0-30.0	12.254± 2.562	8.648± 1.863	9.895 ± 1.507
30.0-50.0	7.252± 1.806	8.248± 1.918	7.720 ± 1.315
50.0-100.0	4.778± 1.451	6.864± 2.070	5.465 ± 1.188
100.0-300.0	3.373± 2.087	4.684± 3.155	3.772 ± 1.741
2.5-300	9.845± 1.047	9.883± 1.018	9.865 ± 0.730

Table 6.57: Comparison of R=$\frac{\sigma(Coh\pi^-)}{\sigma(\bar{\nu}_\mu CC)}$ and R=$\frac{\sigma(Coh\pi^+)}{\sigma(\nu_\mu CC)}$ calculated from a fixed BN.

E_ν(GeV)	R(Cohπ^-)	R(Cohπ^+)	R(Cohπ^-)/R(Cohπ^+)
2.5-8.0	10.970 ± 4.192	5.809±1.01	1.888± 0.793
8.0-15.0	14.498 ± 2.201	7.002±0.37	2.071± 0.333
15.0-20.0	10.658 ± 1.967	6.405±0.35	1.664± 0.320
20.0-30.0	9.895 ± 1.507	5.599±0.26	1.767± 0.281
30.0-50.0	7.720 ± 1.315	4.582±0.23	1.685± 0.299
50.0-100.0	5.465 ± 1.188	3.156±0.22	1.732± 0.395
100.0-300.0	3.772 ± 1.741	2.208±0.28	1.708± 0.817
2.5-300.0	9.865 ± 0.730	4.86± 0.12	2.030± 0.158

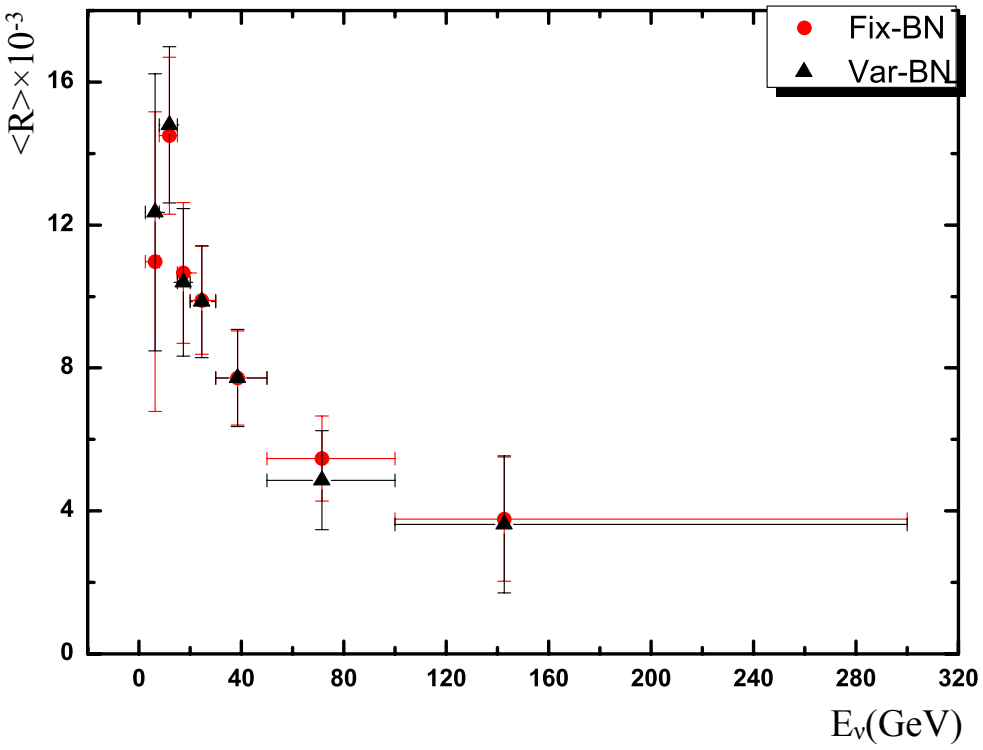

Figure 6.82: Comparison of R=$\frac{\sigma(Coh\pi^-)}{\sigma(\bar{\nu}_\mu CC)}$ calculated from a fixed BN to R=$\frac{\sigma(Coh\pi^-)}{\sigma(\bar{\nu}_\mu CC)}$ calculated from variable BN.

Table 6.58: Comparison between different background subtractions.

E_ν(GeV)	FixBN(ν-Mode)	VarBN(ν-Mode)	FixBN($\bar{\nu}$-Mode)	VarBN($\bar{\nu}$-Mode)	<R>(ν-Mode)	<R>($\bar{\nu}$-Mode)
2.5-8	13.656±5.143	14.385±5.112	5.650±7.238	9.652±5.956	10.97±4.192	12.356±3.879
8-15	16.321±3.420	16.426±3.432	13.209±2.876	13.690±2.836	14.498±2.201	14.800±2.186
15-20	9.136±2.991	8.578±3.221	11.817±2.611	11.669±2.689	10.658±1.967	10.400±2.064
20-30	12.254±2.562	12.393±2.587	8.648±1.863	8.397±1.960	9.895±1.507	9.854±1.562
30-50	7.252±1.806	7.432±1.834	8.248±1.918	8.067±2.022	7.720±1.315	7.719±1.358
50-100	4.778±1.451	4.178±1.699	6.864±2.070	6.110±2.307	5.465±1.188	4.857±1.386
100-300	3.373±2.087	3.597±2.137	4.684±3.155	3.743±4.329	3.772±1.741	3.626±1.916

Smearing matrix for Cohπ^-:FocP

Table 6.59: Smearing matrix of Cohπ^-:FocP

Evis\ E_ν	2.5-8.0	8.0-15.0	15.0-20.0	20.0-30.0	30.0-50.0	50.0-100.0	100.0-300.0
2.5-8.0	28.68	1.09	0.01	0	0	0	0
8.0-15.0	1.06	56.72	1.45	0.02	0	0	0
15.0-20.0	0	1.51	28.31	1.25	0	0	0
20.0-30.0	0	0	1.55	37.55	1.34	0	0
30.0-50.0	0	0	0.01	1.43	36.44	1.03	0
50.0-100.0	0	0	0	0	1.11	20.96	0.23
100.0-300.0	0	0	0	0	0	0.35	2.86

Smearing matrix for Cohπ^-:FocN

Table 6.60: Smearing matrix of Cohπ^-:FocN

Evis\ E_ν	2.5-8.0	8.0-15.0	15.0-20.0	20.0-30.0	30.0-50.0	50.0-100.0	100.0-300.0
2.5-8.0	12.98	0.93	0	0	0	0	0
8.0-15.0	1.09	76.38	2.28	0.02	0	0	0
15.0-20.0	0.01	2.33	45.38	2.48	0.01	0	0
20.0-30.0	0	0.03	1.76	48.52	1.63	0	0
30.0-50.0	0	0	0	1.13	28.01	0	0
50.0-100.0	0	0	0	0	0.58	12.02	0.22
100.0-300.0	0	0	0	0	0	0.12	1.37

Table 6.61: Systematic on Background Subtraction.

E_ν(GeV)	δ_R-ν mode	$\frac{\delta_R}{R}$-ν mode	δ_R-$\bar{\nu}$ mode	$\frac{\delta_R}{R}$-$\bar{\nu}$ mode
2.5-8	-0.729	-0.053	-4.002	-0.708
8-15	-0.105	-0.006	-0.481	-0.036
15-20	0.558	0.061	0.148	0.013
20-30	-0.139	-0.011	0.251	0.029
30-50	-0.18	-0.025	0.181	0.022
50-100	0.6	0.126	0.754	0.109
100-300	-0.224	-0.066	0.941	0.201

Systematic from Final State Interaction

Another very important systematic uncertainty comes from the final state interaction, when the mesons are produced within the nucleus and interact with the nucleons. Coherent process is not sensitive to the final state interactions, because the pion in the final state does not emerge from the nucleons. However final state interactions are affecting the background processes as well as the $\bar{\nu}_\mu$ charged current events and ν_μ charged current events. Therefore, we used NUANCE event generator to estimate such effect by turning on/off the final state interaction(FSI) effect. Table 6.62 shows the final state interaction error as a function of energy in 14 bins of coherent π^+ in neutrino beam mode analysis.

Use of Different Signal Models

In this analysis, the Rein-Sehgal(RS) Model [44] is used to simulate the Coherent π^- interaction in NOMAD detector. The RS model used by both NUANCE and NEUGEN, describes the weak current only in terms of the pion field; The Q^2 dependence of the cross-section is assumed to have a dipole form. Other calculations reply on meson-dominance models [15] which include the dominant contributions from the ρ and a_1 mesons, for example, Berger-Sehgal(BS) Model [15]. The Monte Carlo Coher-

Table 6.62: Final state interaction (FSI) error as a function of energy in 14 bins

Evis(GeV)	FSI
2.5-6.0	6.5051
6.0-8.0	10.5073
8.0-10.0	6.4971
10.0-12.0	4.6806
12.0-15.0	3.9991
15.0-20.0	4.5252
20.0-25.0	2.4506
25.0-30.0	2.3983
30.0-40.0	1.7477
40.0-50.0	1.6448
50.0-70.0	0.7053
70.0-100.0	-2.8253
100.0-130.0	-7.0350
130.0-300.0	17.7462
2.5-300.0	3.7120

ent π^- events used above are simulated by RS Model. As a check, the BS Model is also used to simulate the coherent π^- interactions. In this section, we will give out the result of the analysis using the coherent π^- events simulated by the BS Model and compared it with the result of the RS Model. Because the momentum of the hadron in BS model is lower than in the RS model, the efficiency is lower. Thus, according to the theory, the corrected signal of BS Model should be more than the corrected signal in RS model. The difference between the result of BS and RS model is also considered as systematic uncertainty shown in Table 6.80. In Table 6.80, δ_R equals to the R calculated from analysis with RS model simulation minus the R calculated from analysis with BS model simulation. $\frac{\delta_R}{R}$ equals δ_R divide by the R calculated from analysis with RS model simulation.

Similar to the analysis with the coherent π^- events simulated using the Rein-Sehgal (RS) model, the coherent π^- events simulated using the Berger-Sehgal (BS) Model are used in the analysis of neutrino beam mode data and anti-neutrino beam mode data. In this section, the results of the analysis with the coherent π^- events

simulated using BS model are given out and compared with the result of analysis with the coherent π^- events simulated using the RS model.

Neutrino Beam Mode Analysis:

Table 6.63 and Table 6.64 show the result of background and signal normalization factors (BN and SN) calculated from variable BN and fixed BN.

Table 6.63: BN and SN table in 7 Bins using variable BN depends on the Evis in 7 bins.

Evis(GeV)	BN	SN	δ_{BN}	R $\times 10^{-3}$(Stat.)
2.5 - 8	0.8302	0.5041	0.2787	14 $\pm$ 6.215
8 - 15	0.7921	1.08	0.2023	22.09 $\pm$ 4.389
15 - 20	1.354	0.7222	0.4074	11.2 $\pm$ 4.198
20 - 30	0.8784	1.236	0.3057	15.14 $\pm$ 3.199
30 - 50	0.8652	0.9873	0.2973	8.492 $\pm$ 2.17
50 - 100	1.85	0.9401	0.7219	4.556 $\pm$ 2.135
100 - 300	0.6892	1.756	1.561	3.639 $\pm$ 2.803
2.5 - 300	0.9848	0.9612	0.1266	11.97 $\pm$ 1.324

Table 6.64: BN and SN table in 7 Bins using a fixed BN.

Evis(GeV)	BN	SN	δ_{BN}	R $\times 10^{-3}$(Stat.)
2.5 - 8	0.9848	0.5041	0.1266	13.1 $\pm$ 6.253
8 - 15	0.9848	1.08	0.1266	21.22 $\pm$ 4.443
15 - 20	0.9848	0.7222	0.1266	12.12 $\pm$ 3.85
20 - 30	0.9848	1.236	0.1266	14.91 $\pm$ 3.177
30 - 50	0.9848	0.9873	0.1266	8.265 $\pm$ 2.145
50 - 100	0.9848	0.9401	0.1266	5.53 $\pm$ 1.708
100 - 300	0.9848	1.756	0.1266	3.412 $\pm$ 2.634
2.5 - 300	0.9848	0.9612	0.1266	11.97 $\pm$ 1.324

Table 6.65: Norm-bkg, Corr-sig as a function of Evis in 7 bins using variable BN.

Evis(GeV)	Tot-bkg	BN	Norm-bkg	Data	Raw-sig	Eff	Corr-Sig. (Err=Stat., BN)
2.5 - 8.0	3.72	0.83	3.09	12	8.91	0.153	58.37 ± 25 ± 6.791
8.0 - 15.0	7.06	0.792	5.59	40	34.4	0.275	125 ± 24.3 ± 5.192
15.0 - 20.0	2.93	1.35	3.96	17	13	0.32	40.68 ± 14.79 ± 3.724
20.0 - 30.0	4.17	0.878	3.66	33	29.3	0.33	89.03 ± 18.41 ± 3.867
30.0 - 50.0	5.05	0.865	4.37	27	22.6	0.349	64.75 ± 15.98 ± 4.299
50.0 - 100.0	3.05	1.85	5.65	18	12.4	0.346	35.7 ± 15.47 ± 6.365
100.0 - 300.0	0.554	0.689	0.382	3	2.62	0.278	9.434 ± 6.563 ± 3.117
2.5 - 300.0	26.5	0.985	26.1	150	124	0.275	450.6 ± 48.34 ± 12.23

The total background (Tot-bkg), background normalization (BN), normalized background (Norm-bkg), Data, raw signal(Raw-sig), Efficiency (Eff), corrected signal (Corr-Sig) of the analysis using BS model are shown in Table 6.65. The total number corrected signal in the whole bin from 2.5 to 300 GeV is 450.6±49.86, which is bigger than the total number of corrected signal in the result of RS model which is 370.6±38.26±9.509.

Table 6.66: Corrected signal (Corr-Sig) as a function of Evis in 7 bins using variable BN.

Evis(GeV)	<E>	Corr-Sig	$\bar{\nu}_\mu$-CC	R $\times 10^{-3}$(Stat.)
2.5 - 8	6.25	58.37	4168.3	14 ± 6.215
8 - 15	11.84	125	5660.2	22.09 ± 4.389
15 - 20	17.40	40.68	3633.3	11.2 ± 4.198
20 - 30	24.60	89.03	5881.0	15.14 ± 3.199
30 - 50	38.47	64.75	7625.0	8.492 ± 2.17
50 - 100	71.54	35.7	7835.2	4.556 ± 2.135
100 - 300	142.70	9.434	2592.0	3.639 ± 2.803
2.5 - 300	25.00	450.6	37645.6	11.97 ± 1.324

Table 6.67: Corrected signal (Corr-Sig-Enus) as a function of E_ν in 7 bins using variable BN.

E_ν(GeV)	<E>	Corr-Sig-Enus	$\bar{\nu}_\mu$-CC	R $\times 10^{-3}$(Stat.)
2.5 - 8	6.25	58.31	4168.3	14± 6.079
8 - 15	11.84	124.3	5660.2	21.96± 4.523
15 - 20	17.40	42.76	3633.3	11.77± 4.129
20 - 30	24.60	87.30	5881.0	14.84± 3.210
30 - 50	38.47	65.32	7625.0	8.567± 2.222
50 - 100	71.54	36.51	7835.2	4.660± 2.186
100 - 300	142.70	8.558	2592.0	3.301± 2.493
2.5 - 300	25.00	450.6	37645.6	11.97± 1.324

Table 6.68: Norm-bkg, Corr-sig as a function of Evis in 7 bins using a fixed BN(the the beam(flux) reweight is applied to both of the $\bar{\nu}_\mu$-CC events and ν_μ-CC events).

Evis(GeV)	Tot-bkg	BN	Norm-bkg	Data	Raw-sig	Eff	Corr-Sig. (Err=Stat., BN)
2.5 - 8.0	3.72	0.985	3.66	12	8.34	0.153	54.61 ± 25.88 ± 3.085
8.0 - 15.0	7.06	0.985	6.95	40	33	0.275	120.1 ± 24.94 ± 3.248
15.0 - 20.0	2.93	0.985	2.88	17	14.1	0.32	44.05 ± 13.94 ± 1.157
20.0 - 30.0	4.17	0.985	4.11	33	28.9	0.33	87.68 ± 18.61 ± 1.601
30.0 - 50.0	5.05	0.985	4.98	27	22	0.349	63.02 ± 16.26 ± 1.831
50.0 - 100.0	3.05	0.985	3.01	18	15	0.346	43.33 ± 13.33 ± 1.116
100.0 - 300.0	0.554	0.985	0.546	3	2.45	0.278	8.844 ± 6.823 ± 0.2527
2.5 - 300.0	26.5	0.985	26.1	150	124	0.275	450.6 ± 48.34 ± 12.23

Table 6.68 shows the result of total background (Tot-bkg), background normalization (BN), normalized background (Norm-bkg), Data, raw signal (Raw-sig), Efficiency (Eff), and corrected signal (Corr-Sig) which are calculated using a single background normalization.

Table 6.69: Corrected signal (Corr-Sig) as a function of Evis in 7 bins using a fixed BN.

Evis(GeV)	<E>	Corr-Sig	$\bar{\nu}_\mu$-CC	R $\times 10^{-3}$(Stat.)
2.5 - 8	6.25	54.61	4168.3	13.1 $\pm$ 6.253
8 - 15	11.84	120.1	5660.2	21.22 $\pm$ 4.443
15 - 20	17.40	44.05	3633.3	12.12 $\pm$ 3.85
20 - 30	24.60	87.68	5881.0	14.91 $\pm$ 3.177
30 - 50	38.47	63.02	7625.0	8.265 $\pm$ 2.145
50 - 100	71.54	43.33	7835.2	5.53 $\pm$ 1.708
100 - 300	142.70	8.844	2592.0	3.412 $\pm$ 2.634
2.5 - 300	25.00	450.6	37645.6	11.97 $\pm$ 1.324

Table 6.70: Corrected signal (Corr-Sig-Enus) as a function of E_ν in 7 bins using a fixed BN.

E_ν(GeV)	<E>	Corr-Sig-Enus	$\bar{\nu}_\mu$-CC	R $\times 10^{-3}$(Stat.)
2.5 - 8	6.25	54.60	4168.3	13.10 $\pm$6.116
8 - 15	11.84	119.53	5660.2	21.12 $\pm$4.565
15 - 20	17.40	45.64	3633.3	12.562$\pm$3.816
20 - 30	24.60	86.13	5881.0	14.645$\pm$3.178
30 - 50	38.47	64.05	7625.0	8.4 $\pm$2.177
50 - 100	71.54	43.53	7835.2	5.556 $\pm$1.778
100 - 300	142.70	8.14	2592.0	3.14 $\pm$2.332
2.5 - 300	25.00	450.6	37645.6	11.97 $\pm$1.324

Anti-neutrino Beam Mode Analysis:

Table 6.71: BN and SN table in 7 Bins using variable BN depends on the Evis in 7 bins.

Evis(GeV)	BN	SN	δ_{BN}	R $\times 10^{-3}$(Stat.)
2.5 - 8.0	0.3439	0.2867	0.1952	8.538 $\pm$ 6.822
8.0 - 15.0	1.055	0.8238	0.1975	16.42 $\pm$ 3.478
15.0 - 20.0	1.24	0.9688	0.2968	13.77 $\pm$ 3.141
20.0 - 30.0	1.283	0.9928	0.3057	10.12 $\pm$ 2.333
30.0 - 50.0	1.479	1.35	0.4713	9.046 $\pm$ 2.372
50.0 - 100.0	2.006	1.759	1.039	6.767 $\pm$ 2.685
100.0 - 300.0	1.727	2.658	3.158	4.309 $\pm$ 4.224
2.5 - 300.0	1.17	1.009	0.1294	11.6 $\pm$ 1.226

Table 6.72: BN and SN table in 7 Bins using a fixed BN.

Evis(GeV)	BN	SN	δ_{BN}	R $\times 10^{-3}$(Stat.)
2.5 - 8.0	1.17	0.2867	0.1294	2.363 $\pm$ 8.942
8.0 - 15.0	1.17	0.8238	0.1294	15.97 $\pm$ 3.494
15.0 - 20.0	1.17	0.9688	0.1294	13.91 $\pm$ 3.064
20.0 - 30.0	1.17	0.9928	0.1294	10.33 $\pm$ 2.236
30.0 - 50.0	1.17	1.35	0.1294	9.474 $\pm$ 2.199
50.0 - 100.0	1.17	1.759	0.1294	7.597 $\pm$ 2.24
100.0 - 300.0	1.17	2.658	0.1294	4.655 $\pm$ 3.52
2.5 - 300.0	1.17	1.009	0.1294	11.6 $\pm$ 1.226

Table 6.73: Norm-bkg, Corr-sig as a function of Evis in 7 bins using variable BN.

Evis(GeV)	Tot-bkg	BN	Norm-bkg	Data	Raw-sig	Eff	Corr-Sig. (Err=Stat., BN)
2.5 - 8.0	2.02	0.344	0.694	3	2.31	0.197	11.7 ± 9.351
8.0 - 15.0	8.64	1.05	9.12	45	35.9	0.282	127.4 ± 26.97
15.0 - 20.0	4.33	1.24	5.37	34	28.6	0.327	87.46 ± 19.95
20.0 - 30.0	5.91	1.28	7.58	39	31.4	0.34	92.43 ± 21.32
30.0 - 50.0	3.87	1.48	5.73	31	25.3	0.373	67.77 ± 17.77
50.0 - 100.0	2.15	2.01	4.32	19	14.7	0.383	38.36 ± 15.22
100.0 - 300.0	0.346	1.73	0.597	3	2.4	0.351	6.841 ± 6.706
2.5 - 300.0	27.3	1.17	31.9	174	142	0.31	457.6 ± 48.36

The total background (Tot-bkg), background normalization (BN), normalized background (Norm-bkg), Data, raw signal (Raw-sig), Efficiency (Eff), corrected signal (Corr-Sig) of the analysis using BS model are shown in Table 6.46. The total number corrected signal in the whole bin from 2.5 to 300 GeV is 457.6±48.36, which is bigger than the total number of corrected signal in the result of RS model which is 389.7±39.01±9.492.

Table 6.74: Corrected signal (Corr-sig) as a function of Evis in 7 bins using variable BN.

Evis(GeV)	<E>	Corr-Sig	$\bar{\nu}_\mu$-CC	R $\times 10^{-3}$(Stat.)
2.5 - 8	6.25	11.7	1370.7	8.538 ± 6.822
8 - 15	11.84	127.4	7755.0	16.42 ± 3.478
15 - 20	17.40	87.46	6352.6	13.77 ± 3.141
20 - 30	24.60	92.43	9136.4	10.12 ± 2.333
30 - 50	38.47	67.77	7492.4	9.046 ± 2.372
50 - 100	71.54	38.36	5668.7	6.767 ± 2.685
100 - 300	142.70	6.841	1587.6	4.309 ± 4.224
2.5 - 300	25.00	457.6	39435.6	11.6 ± 1.226

Table 6.75: Corrected signal (Corr-Sig-Enus) as a function of E_ν in 7 bins using variable BN.

E_ν(GeV)	<E>	Corr-Sig-Enus	$\bar{\nu}_\mu$-CC	R $\times 10^{-3}$(Stat.)
2.5 - 8	6.25	12.2	1370.7	8.899 ± 6.476
8 - 15	11.84	127.5	7755.0	16.44 ± 3.565
15 - 20	17.40	87.20	6352.6	13.73 ± 3.124
20 - 30	24.60	93.89	9136.4	10.28 ± 2.383
30 - 50	38.47	66.77	7492.4	8.911 ± 2.367
50 - 100	71.54	38.28	5668.7	6.753 ± 2.768
100 - 300	142.70	6.079	1587.6	3.829 ± 3.606
2.5 - 300	25.00	457.6	39435.6	11.6 ± 1.226

Table 6.76: Norm-bkg, Corr-sig as a function of Evis in 7 bins using a fixed BN.

Evis(GeV)	Tot-bkg	BN	Norm-bkg	Data	Raw-sig	Eff	Corr-Sig. (Err=Stat., BN)
2.5 - 8.0	2.02	1.17	2.36	3	0.638	0.197	3.239 ± 12.26
8.0 - 15.0	8.64	1.17	10.1	45	34.9	0.282	123.8 ± 27.09
15.0 - 20.0	4.33	1.17	5.06	34	28.9	0.327	88.38 ± 19.47
20.0 - 30.0	5.91	1.17	6.91	39	32.1	0.34	94.4 ± 20.43
30.0 - 50.0	3.87	1.17	4.53	31	26.5	0.373	70.98 ± 16.48
50.0 - 100.0	2.15	1.17	2.52	19	16.5	0.383	43.07 ± 12.7
100.0 - 300.0	0.346	1.17	0.405	3	2.6	0.351	7.39 ± 5.588
2.5 - 300.0	27.3	1.17	31.9	174	142	0.31	457.6 ± 48.36

Table 6.77: Corrected signal (Corr-sig) as a function of Evis in 7 bins using a fixed BN.

Evis(GeV)	<E>	Corr-Sig	$\bar{\nu}_\mu$-CC	R $\times 10^{-3}$(Stat.)
2.5 - 8	6.25	3.239	1370.7	2.363 $\pm$ 8.942
8 - 15	11.84	123.8	7755.0	15.97 $\pm$ 3.494
15 - 20	17.40	88.38	6352.6	13.91 $\pm$ 3.064
20 - 30	24.60	94.4	9136.4	10.33 $\pm$ 2.236
30 - 50	38.47	70.98	7492.4	9.474 $\pm$ 2.199
50 - 100	71.54	43.07	5668.7	7.597 $\pm$ 2.24
100 - 300	142.70	7.39	1587.6	4.655 $\pm$ 3.52
2.5 - 300	25.00	457.6	39435.6	11.6 $\pm$ 1.226

Table 6.78: Corrected signal (Corr-Sig-Enus) as a function of E_ν in 7 bins using a fixed BN.

E_ν(GeV)	<E>	Corr-Sig-Enus	$\bar{\nu}_\mu$-CC	R $\times 10^{-3}$(Stat.)
2.5 - 8	6.25	4.407	1370.7	3.215 $\pm$ 8.418
8 - 15	11.84	123.5	7755.0	15.93 $\pm$ 3.609
15 - 20	17.40	88.03	6352.6	13.86 $\pm$ 3.049
20 - 30	24.60	96.00	9136.4	10.51 $\pm$ 2.281
30 - 50	38.47	70.04	7492.4	9.348 $\pm$ 2.186
50 - 100	71.54	42.83	5668.7	7.556 $\pm$ 2.314
100 - 300	142.70	6.584	1587.6	4.147 $\pm$ 3.005
2.5 - 300	25.00	457.6	39435.6	11.6 $\pm$ 1.226

Table 6.79: Comparison between RS and BS signal model simulation.

E_ν(GeV)	RS(ν-mode)	BS(ν-mode)	RS($\bar{\nu}$-mode)	BS($\bar{\nu}$-mode)	<R>(RS)	<R>(BS)
2.5-8	13.656±5.143	13.100±6.116	5.650±7.238	3.215±8.418	10.97± 4.192	9.685±4.948
8-15	16.321±3.420	21.12±4.565	13.209±2.876	15.930±3.609	14.498±2.201	17.926±2.831
15-20	9.136±2.991	12.562±3.816	11.817±2.611	13.86±3.049	10.658±1.967	13.354±2.382
20-30	12.254±2.562	14.645±3.178	8.648±1.863	10.510±2.281	9.895±1.507	11.916±1.853
30-50	7.252±1.806	8.400±2.177	8.248±1.918	9.348±2.183	7.720±1.315	8.872±1.543
50-100	4.778±1.451	5.556±1.778	6.864±2.070	7.556±2.314	5.465±1.188	6.298±1.410
100-300	3.373±2.087	3.140±2.332	4.684±3.155	4.147±3.005	3.772±1.741	3.519±1.842
2.5-300	9.845±1.047	11.97±1.324	9.883±1.018	11.6±1.226	9.865±0.730	11.771±0.9

Table 6.80: Systematic on signal modeling.

E_ν(GeV)	δ_R-ν mode	$\frac{\delta_R}{R}$-ν mode	δ_R-$\bar{\nu}$ mode	$\frac{\delta_R}{R}$-$\bar{\nu}$ mode
2.5-8	0.556	0.041	2.435	0.431
8-15	-4.799	-0.293	-2.721	-0.206
15-20	-3.426	-0.375	-2.043	-0.173
20-30	-2.391	-0.195	-1.862	-0.215
30-50	-1.148	-0.158	-1.1	-0.133
50-100	-0.768	-0.161	-0.692	-0.101
100-300	0.233	0.069	0.537	0.115
2.5-300	-2.125	-0.216	-1.717	-0.174

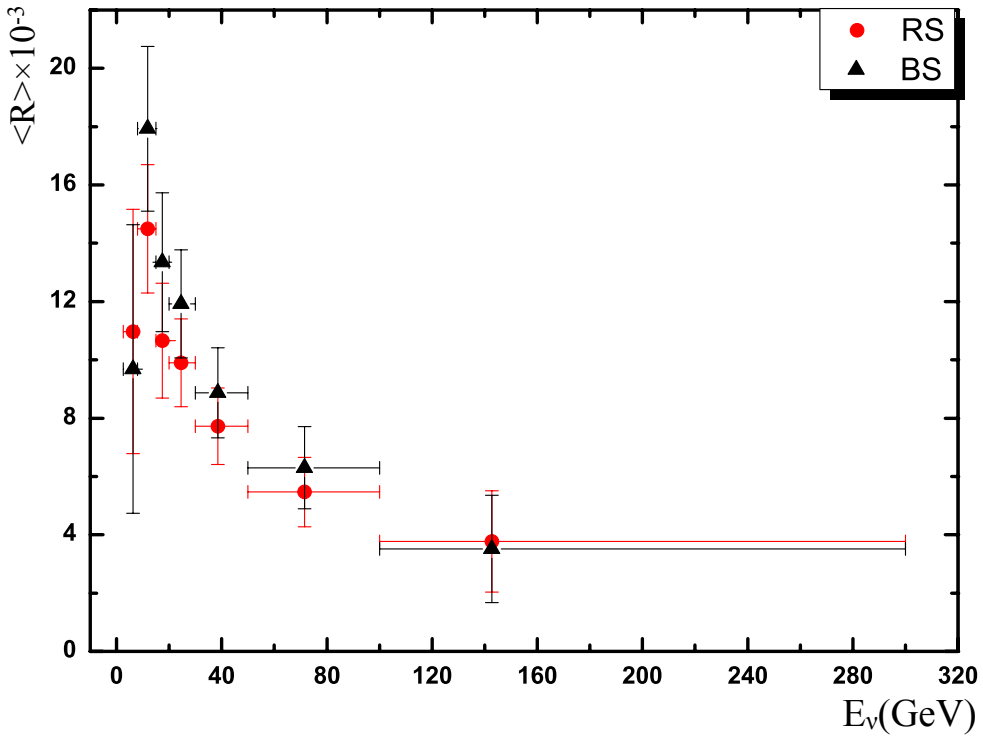

Figure 6.83: Comparison of R=$\frac{\sigma(Coh\pi^-)}{\sigma(\bar{\nu}_\mu CC)}$ between BS and RS Model calculated from a fixed BN.

Table 6.81: Comparison of R=$\frac{\sigma(Coh\pi^-)}{\sigma(\bar{\nu}_\mu CC)}$:FocP and R=$\frac{\sigma(Coh\pi^-)}{\sigma(\bar{\nu}_\mu CC)}$:FocN as a function of Evis using variable BN.

Evis(GeV)	R(Cohπ^-:FocP)	R(Cohπ^-:FocN)	<R>
2.5 - 8.0	14 ± 6.215	8.538 ± 6.822	11.523 ± 4.594
8.0 - 15.0	22.09 ±4.389	16.42 ± 3.478	18.607 ± 2.726
15.0 - 20.0	11.2 ±4.198	13.77 ± 3.141	12.848 ± 2.515
20.0 - 30.0	15.14 ±3.199	10.12 ± 2.333	11.863 ± 1.885
30.0 - 50.0	8.492 ±2.17	9.046 ± 2.372	8.744 ± 1.601
50.0 - 100.0	4.556 ±2.135	6.767 ± 2.685	5.412 ± 1.671
100.0 - 300.0	3.639 ±2.803	4.309 ± 4.224	3.844 ± 2.336
2.5 - 300.0	11.97 ±1.324	11.6 ± 1.226	11.771 ± 0.900

Table 6.82: Comparison of R=$\frac{\sigma(Coh\pi^-)}{\sigma(\bar{\nu}_\mu CC)}$:FocP and R=$\frac{\sigma(Coh\pi^-)}{\sigma(\bar{\nu}_\mu CC)}$:FocN as a function of E_ν using variable BN.

E_ν(GeV)	R(Cohπ^-:FocP)	R(Cohπ^-:FocN)	<R>
2.5 - 8.0	14 ± 6.079	8.899 ± 6.476	11.611 ±4.432
8.0 - 15.0	21.96± 4.523	16.44 ± 3.565	18.555 ±2.800
15.0 - 20.0	11.77± 4.129	13.73 ± 3.124	13.017 ±2.491
20.0 - 30.0	14.84± 3.210	10.28 ± 2.383	11.900 ±1.913
30.0 - 50.0	8.567± 2.222	8.911 ± 2.367	8.728 ±1.620
50.0 - 100.0	4.660± 2.186	6.753 ± 2.768	5.464 ±1.716
100.0 - 300.0	3.301± 2.493	3.829 ± 3.606	3.472 ±2.051
2.5 - 300.0	11.97± 1.324	11.6 ± 1.226	11.771 ±0.900

Table 6.83: Comparison of R=$\frac{\sigma(Coh\pi^-)}{\sigma(\bar{\nu}_\mu CC)}$:FocP and R=$\frac{\sigma(Coh\pi^-)}{\sigma(\bar{\nu}_\mu CC)}$:FocN as a function of Evis calculated from a fixed BN.

Evis(GeV)	R(Cohπ^-:FocP)	R(Cohπ^-:FocN)	<R>
2.5 - 8.0	13.1 ± 6.253	2.363 ± 8.942	9.574 ±5.124
8.0 - 15.0	21.22± 4.443	15.97 ± 3.494	17.976 ±2.746
15.0 - 20.0	12.12± 3.85	13.91 ± 3.064	13.216 ±2.397
20.0 - 30.0	14.91± 3.177	10.33 ± 2.236	11.847 ±1.829
30.0 - 50.0	8.265± 2.145	9.474 ± 2.199	8.854 ±1.535
50.0 - 100.0	5.53 ± 1.708	7.597 ± 2.24	6.290 ±1.358
100.0 - 300.0	3.412± 2.634	4.655 ± 3.52	3.858 ±2.109
2.5 - 300.0	11.97± 1.324	11.6 ± 1.226	11.771 ±0.900

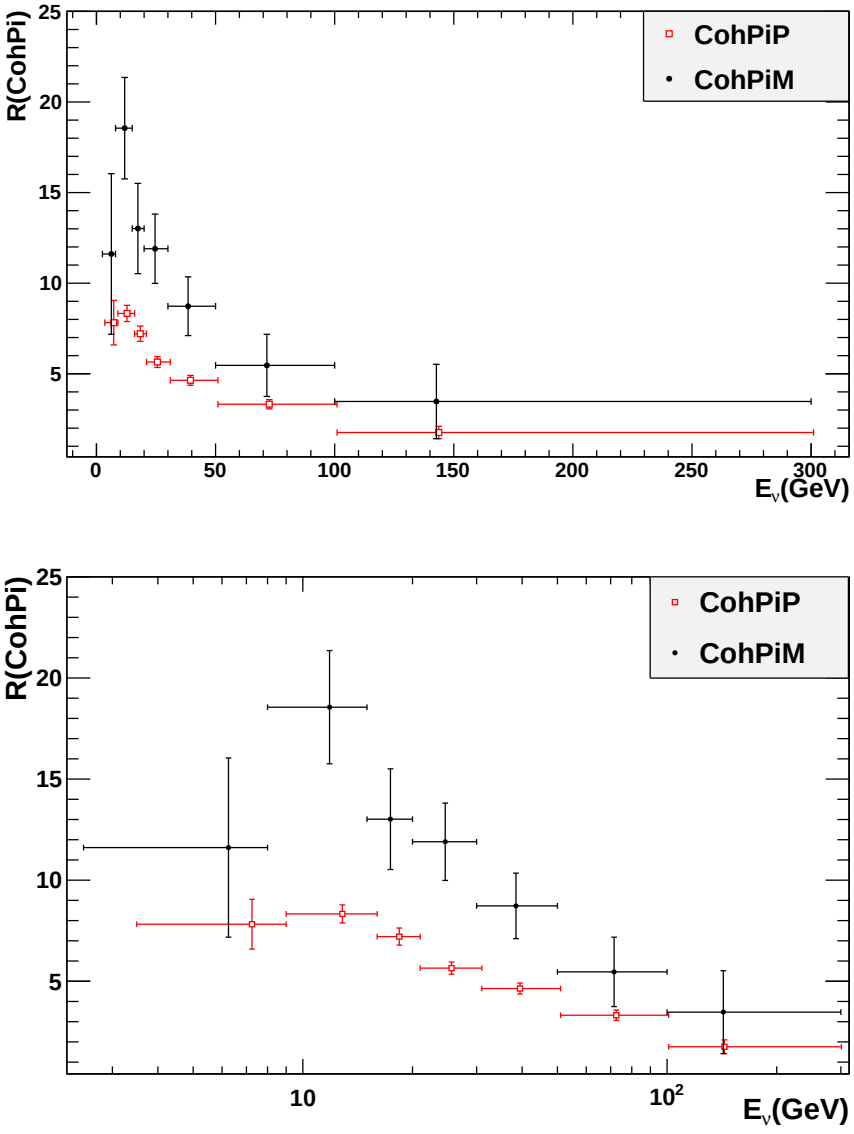

Figure 6.84: Comparison of R=$\frac{\sigma(Coh\pi^-)}{\sigma(\bar{\nu}_\mu CC)}$ and R=$\frac{\sigma(Coh\pi^+)}{\sigma(\nu_\mu CC)}$ as a function of E_ν using variable BN.

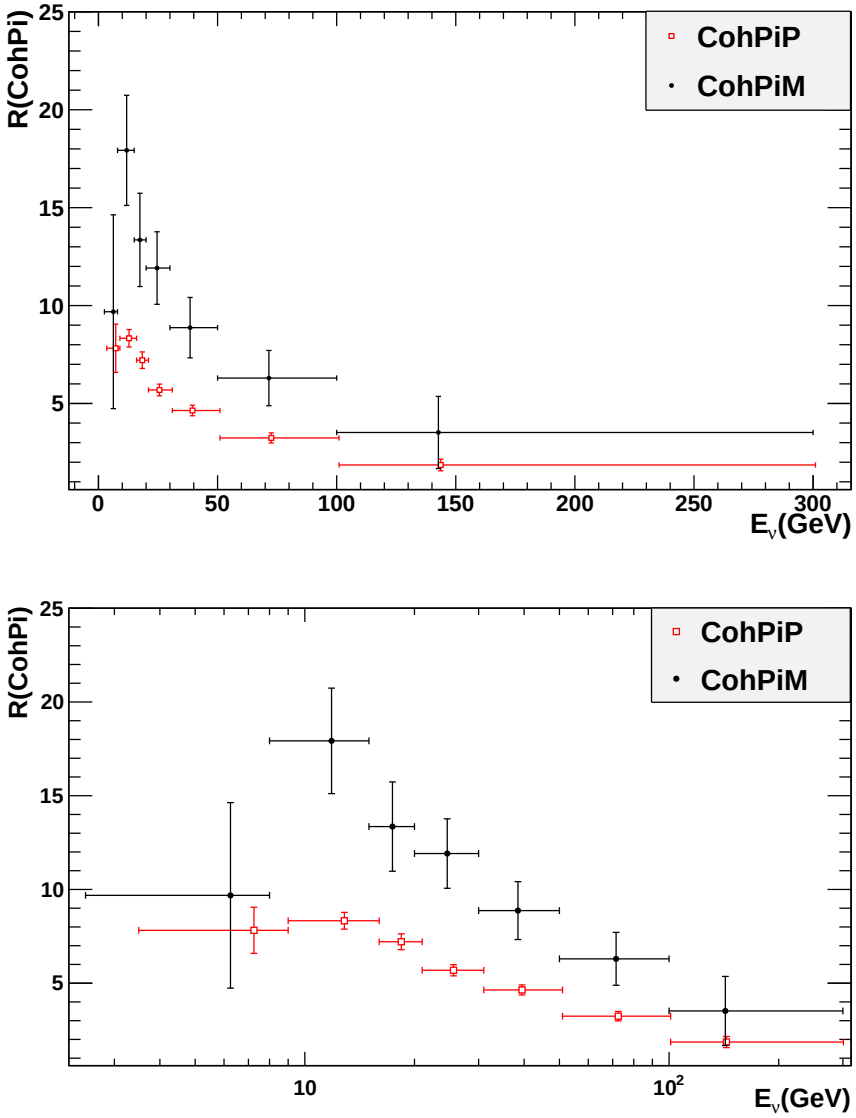

Figure 6.85: Comparison of R=$\frac{\sigma(Coh\pi^-)}{\sigma(\bar{\nu}_\mu CC)}$ and R=$\frac{\sigma(Coh\pi^+)}{\sigma(\nu_\mu CC)}$ as a function of E_ν calculated from a fixed BN.

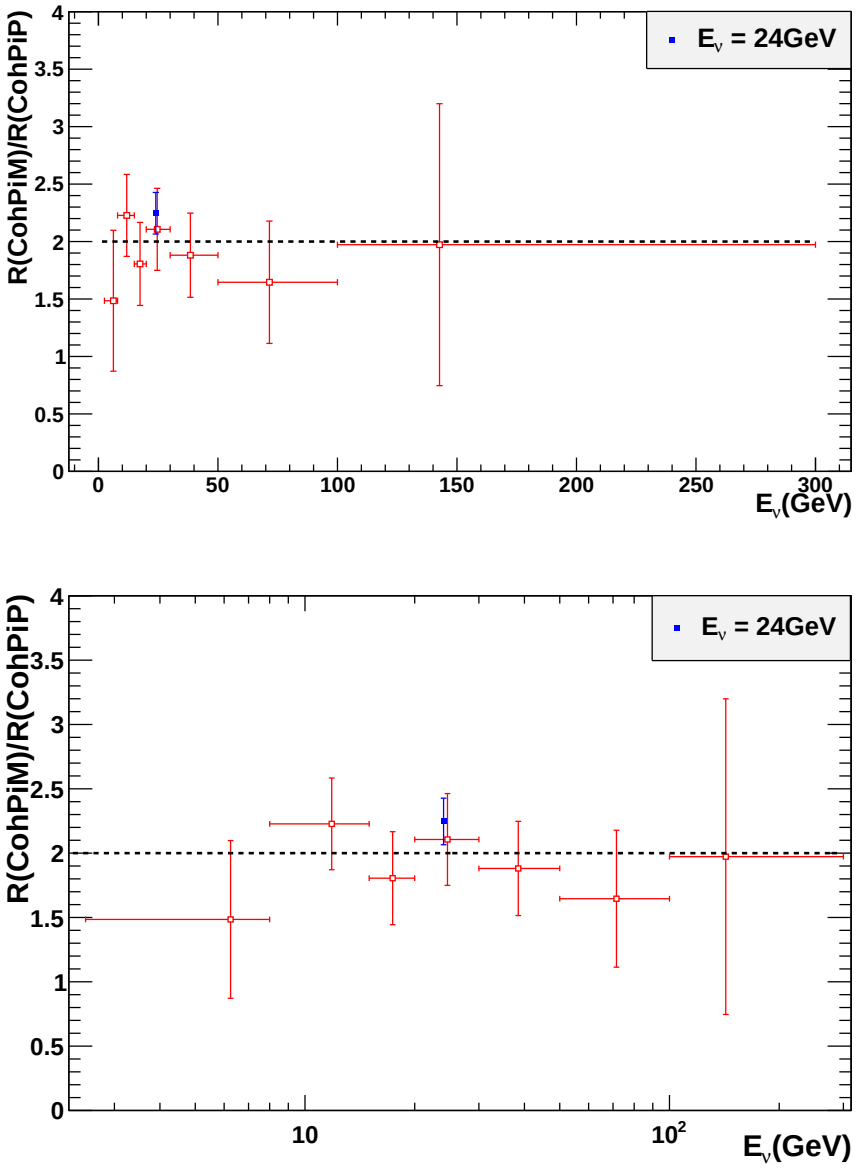

Figure 6.86: Ratio between R=$\frac{\sigma(Coh\pi^-)}{\sigma(\bar{\nu}_\mu CC)}$ and R=$\frac{\sigma(Coh\pi^+)}{\sigma(\nu_\mu CC)}$ as a function of E_ν using variable BN.

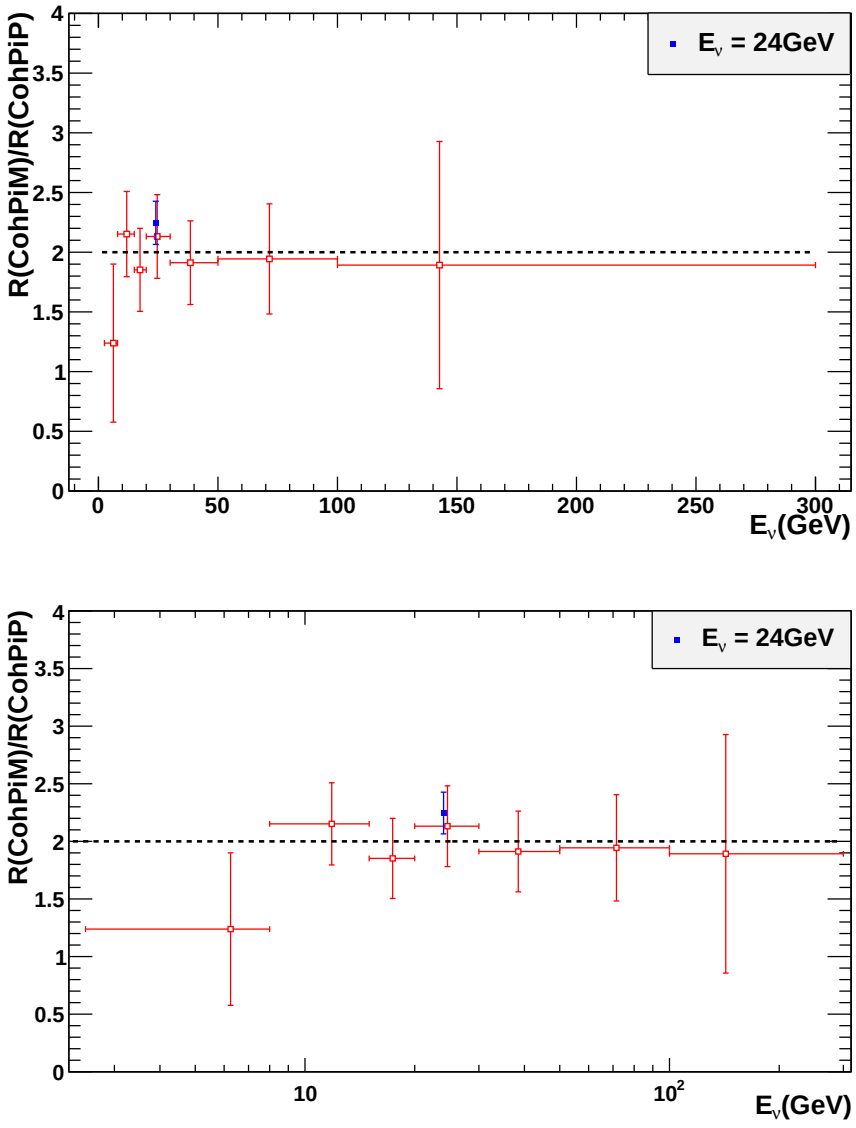

Figure 6.87: Ratio between of R=$\frac{\sigma(Coh\pi^-)}{\sigma(\bar{\nu}_\mu CC)}$ and R=$\frac{\sigma(Coh\pi^+)}{\sigma(\nu_\mu CC)}$ as a function of E_ν calculated from a fixed BN.

Table 6.84: Comparison of R=$\frac{\sigma(Coh\pi^-)}{\sigma(\bar{\nu}_\mu CC)}$:FocP and R=$\frac{\sigma(Coh\pi^-)}{\sigma(\bar{\nu}_\mu CC)}$:FocN as a function of E_ν calculated from a fixed BN.

E_ν(GeV)	R(Cohπ^-:FocP)	R(Cohπ^-:FocN)	<R>
2.5 - 8.0	13.10 ± 6.116	3.215 ± 8.418	9.685 ±4.948
8.0 - 15.0	21.12 ± 4.565	15.93 ± 3.609	17.926 ±2.831
15.0 - 20.0	12.562± 3.816	13.86 ± 3.049	13.354 ±2.382
20.0 - 30.0	14.645± 3.178	10.51 ± 2.281	11.916 ±1.853
30.0 - 50.0	8.4 ± 2.177	9.348 ± 2.186	8.872 ±1.543
50.0 - 100.0	5.556 ± 1.778	7.556 ± 2.314	6.298 ±1.410
100.0 - 300.0	3.14 ± 2.332	4.147 ± 3.005	3.519 ±1.842
2.5 - 300.0	11.97 ± 1.324	11.6 ± 1.226	11.771 ±0.900

Table 6.85: Ratio between R=$\frac{\sigma(Coh\pi^-)}{\sigma(\bar{\nu}_\mu CC)}$ and R=$\frac{\sigma(Coh\pi^+)}{\sigma(\nu_\mu CC)}$ as a function of E_ν using variable BN.

E_ν(GeV)	R(Cohπ^-)	R(Cohπ^+)	R(Cohπ^-)/R(Cohπ^+)
2.5-8.0	11.611 ± 4.432	7.82 ±1.230	1.485 ± 0.613
8.0-15.0	18.555 ± 2.800	8.33 ±0.446	2.227 ± 0.357
15.0-20.0	13.017 ± 2.491	7.21 ±0.423	1.805 ± 0.361
20.0-30.0	11.900 ± 1.913	5.65 ±0.303	2.106 ± 0.357
30.0-50.0	8.728 ± 1.620	4.64 ±0.272	1.881 ± 0.366
50.0-100.0	5.464 ± 1.716	3.32 ±0.256	1.646 ± 0.532
100.0-300.0	3.472 ± 2.051	1.76 ±0.342	1.973 ± 1.227
2.5-300.0	11.771 ± 0.900	5.24 ±0.134	2.246 ± 0.181

Table 6.86: Ratio between R=$\frac{\sigma(Coh\pi^-)}{\sigma(\bar{\nu}_\mu CC)}$ and R=$\frac{\sigma(Coh\pi^+)}{\sigma(\nu_\mu CC)}$ as a function of E_ν calculated from a fixed BN.

E_ν(GeV)	R(Cohπ^-)	R(Cohπ^+)	R(Cohπ^-)/R(Cohπ^+)
2.5-8.0	9.685 ± 4.948	7.82 ± 1.230	1.238 ± 0.662
8.0-15.0	17.926 ± 2.813	8.33 ± 0.446	2.152 ± 0.357
15.0-20.0	13.354 ± 2.382	7.21 ± 0.423	1.852 ± 0.348
20.0-30.0	11.916 ± 1.853	5.69 ± 0.298	2.132 ± 0.350
30.0-50.0	8.872 ± 1.543	4.64 ± 0.268	1.912 ± 0.350
50.0-100.0	6.298 ± 1.410	3.24 ± 0.255	1.944 ± 0.461
100.0-300.0	3.519 ± 1.842	1.86 ± 0.297	1.892 ± 1.035
2.5-300.0	11.771 ± 0.900	5.24 ± 0.134	2.246 ± 0.181

Table 6.87: Variation of Selection Cuts.

E(GeV)	$E_\pi - \sigma$	$E_\pi + \sigma$	$\theta_{\mu\pi} - \sigma$	$\theta_{\mu\pi} + \sigma$	$P_T^m - \sigma$	$P_T^m + \sigma$	$\|t\| - \sigma$	$\|t\| + \sigma$	$LH - \sigma$	$LH + \sigma$
2.5-6.0	11.6801	14.9215	-0.0029	1.2152	-0.6940	1.6924	3.1682	4.8313	7.9703	2.0819
6.0-8.0	-8.7922	-13.2404	0.1911	-2.2089	-3.2015	-0.1998	-11.6918	7.8951	-6.5333	3.0169
8.0-10.0	2.9775	-0.3931	0.6583	-0.2867	1.3526	0.0433	-6.7592	3.8665	-0.2399	1.7187
10.0-12.0	2.3871	-3.4039	-0.0359	0.6659	-1.5546	-0.1880	-5.0496	9.1302	-2.7272	1.0839
12.0-15.0	0.1747	-1.2485	2.1770	1.7885	0.7135	1.4232	-3.2093	5.4010	0.8625	1.5466
15.0-20.0	1.0206	0.7432	0.4749	-0.3013	-0.1227	0.0429	-6.9257	3.4628	-0.8809	0.8849
20.0-25.0	-0.5879	1.8357	1.1529	0.1288	0.9869	0.4498	-2.6667	5.2470	0.5167	2.3634
25.0-30.0	1.0098	-0.3757	0.3817	0.9409	0.9814	-0.1689	-2.1256	5.3498	1.5725	1.5785
30.0-40.0	0.8639	-1.2536	0.4798	-1.2473	0.1509	-0.3995	-6.4679	4.9091	-0.2745	2.1057
40.0-50.0	-0.1103	-1.1908	0.8992	-1.5585	-0.5193	0.8160	-8.4046	5.0322	1.8468	2.2545
50.0-70.0	0.5876	1.4756	0.6383	-0.4734	-0.7513	-0.1182	-9.1249	5.5142	-2.7839	0.9751
70.0-100.0	-0.0111	-1.6245	1.9125	-0.3689	3.0378	-1.6033	-10.5984	7.0058	-6.2656	2.6411
100.0-130.0	3.1054	-1.0962	-0.4299	-1.6977	-0.2720	-0.0633	-21.2723	-3.5256	-2.0776	3.8175
130.0-300.0	-0.4959	-3.8586	-0.9748	6.6181	-0.8720	-1.7911	3.5501	-0.8281	2.5231	6.4279
2.5-300.0	0.6386	-0.6010	0.7517	-0.0230	0.2123	0.0910	-5.8974	5.0962	-0.6228	0.3345

Variation of Selection Cuts

Table 6.87 shows the variation of the preslection variable cuts of coherent π^+ in Neutrino Beam Mode Data analysis. For the variable E_π, $\theta_{\mu\pi}$, P_T^m, and the slope of t, change the parameters that we care about by $\pm\,\sigma$, and get the fully corrected signal as N', assuming the nominal is N, the error is $(N' - N)/N$.

Variation of Neutrino and Anti-neutrino Flux

As the description in NOMAD flux, the neutrinos in the beam originate from the decay of mesons produced through four different mechanisms: proton-Be interactions in the target, proton interactions downstream of the target in material other than beryllium, re-interactions of particles in the target and interactions of particles downstream of the target. These four sources all contribute the systematic uncertainties which are described in paper [8].

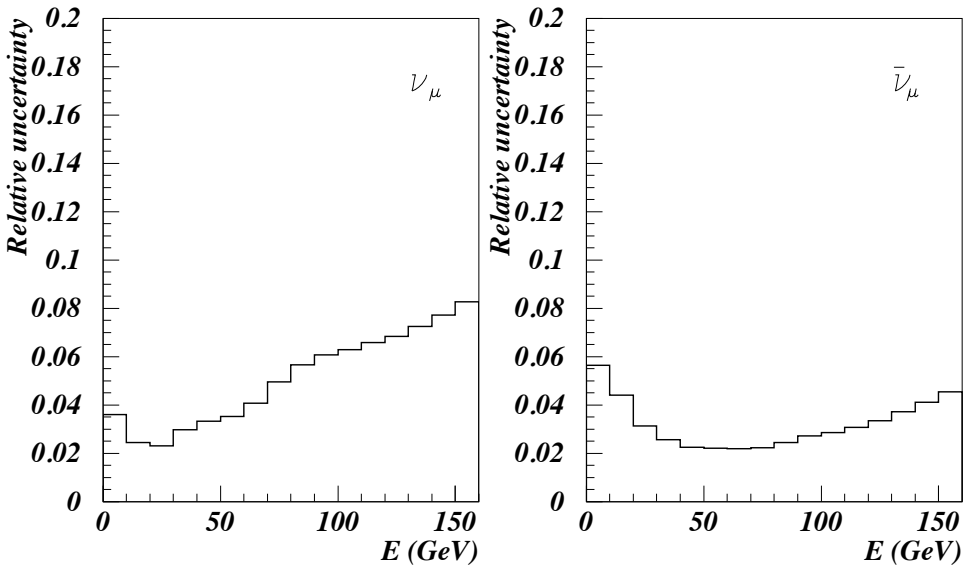

Figure 6.88: Total energy-dependent uncertainties on the yields of each of the neutrino species(ν_μ and $\bar{\nu}_\mu$).

Figure 6.88 shows the energy-dependent uncertainties of neutrino and anti-neutrino flux [8].

Cross-section Uncertainties

Table 6.88: The error of cross-section of charged current resonance and coherent ρ events in 14 bins.

Evis(GeV)	CCres-σ	CCRes+σ	CCCoh$\rho-\sigma$	CCCoh$\rho-\sigma$
2.5-6.0	7.3905	-1.5665	1.4230	-1.0336
6.0-8.0	-4.7827	-2.9778	-5.8231	1.2684
8.0-10.0	0.6041	-1.4013	1.3472	1.6682
10.0-12.0	-2.4972	0.8300	-1.4289	-0.1821
12.0-15.0	0.9553	1.1081	-0.6609	1.0299
15.0-20.0	-0.9298	-0.5188	-1.7648	0.6175
20.0-25.0	0.4320	2.4922	-1.5011	2.6735
25.0-30.0	2.2773	1.2459	-0.5308	3.9376
30.0-40.0	-0.0182	-1.8955	-2.3173	1.2494
40.0-50.0	1.7604	2.7377	-3.1267	3.4498
50.0-70.0	-2.9851	-0.0075	-2.4287	2.3243
70.0-100.0	-6.4030	2.6083	-2.7508	0.7109
100.0-130.0	-2.2339	-5.3554	-6.4215	1.7497
130.0-300.0	2.4863	9.4299	-1.1441	8.1019
2.5-300.0	-0.3841	0.4714	-1.6963	1.6761

Table 6.88 shows the uncertainties originated from the calculation of cross-sections of charged current resonance and coherent events. Similar to the calculation of the variation of selection cuts, the error of cross-section is also calculated by changing the parameter by $\pm\sigma$, and get the new fully corrected signal as N', assuming the nominal is N, then the error is $(N'-N)/N$. The σ of charged current resonance is 7% which is from the NOMAD measurement [46]. The σ of charged current coherent ρ^+ is 8% which is also from the NOMAD measurement [45]. In this table, we only listed the charged current and resonance and coherent ρ^+ processes error, compared to these two, the quasi-elastic is negligible, we use control region to reweight essentially DIS. Therefore only these two need to be considered.

Table 6.89: Summary of experimental measurements of coherent π^- production in $\bar{\nu}_\mu$ CC interactions.

Experiment	Pub. Year	E_ν(GeV)	σ(Coh-π^-) $(10^{-40} cm^2/nucleus)$	$\frac{\sigma(Coh\pi^2))}{\sigma CC}$ $\times 10^{-3}$
BEBC	1986	40(5-200)	175±25	9±1
SKAT	1986	7(3-20)	113±35	18±5
FNAL 15'BC	1989	70(40-300)	270±110	5.7±2.2
CHARM II	1993	19.1	139±40(RS) 132±32(BS)	
NOMAD	2015	16.5(2.5-300)		9.865 ± 0.730

6.9 Comparison with Previous Measurements

In Table 6.89, there is a summary of experimental measurements including the result that I measured from NOMAD data. We could see that this is the first measurement of coherent π^- production after over 22 years and gives the best measurement to date.

Chapter 7

Coherent Rho and Absolute Flux Measurement

7.1 Neutrino Induced Coherent ρ^0 & ρ^+

The research on coherent ρ is very important in understanding of coherent processes, because the vector current is assumed to be dominated by the ρ meson ($J^P = 1^-$), whereas the axial current is dominated by the a_1 meson ($J^P = 1^+$). Different from the coherent ρ^+, much of information of the neutral current coherent ρ^0 events is difficult to measure directly, for example, the momentum transfer Q^2 and variables related to it. On the theoretical side, there is a certain connection between the coherent ρ^0 and coherent ρ^+ or coherent ρ^-. In Chapter 3, the cross-section of coherent $\rho^\pm$ and coherent ρ^0 have been calculated.

7.2 Photo-production of Coherent ρ^0

Beside the neutrino induced coherent ρ^+ process, photo-production of the coherent ρ^0 process can also be used to predict the information of neutrino induced coherent ρ^0, and has the following advantages compared to neutrino induced coherent ρ^+. First, the momentum transfer squared Q^2 and other related kinematic variables could be calculated; Second, different from the neutrinos, the incoming flux of electrons is easy to detect or measure as compared to neutrinos. In this section, the cross-section of photo-production of coherent ρ^0 is calculated using the Vector Dominance Model similar as the calculation of neutrino induced coherent ρ events. The process is shown in Figure 7.1 diagrammatically.

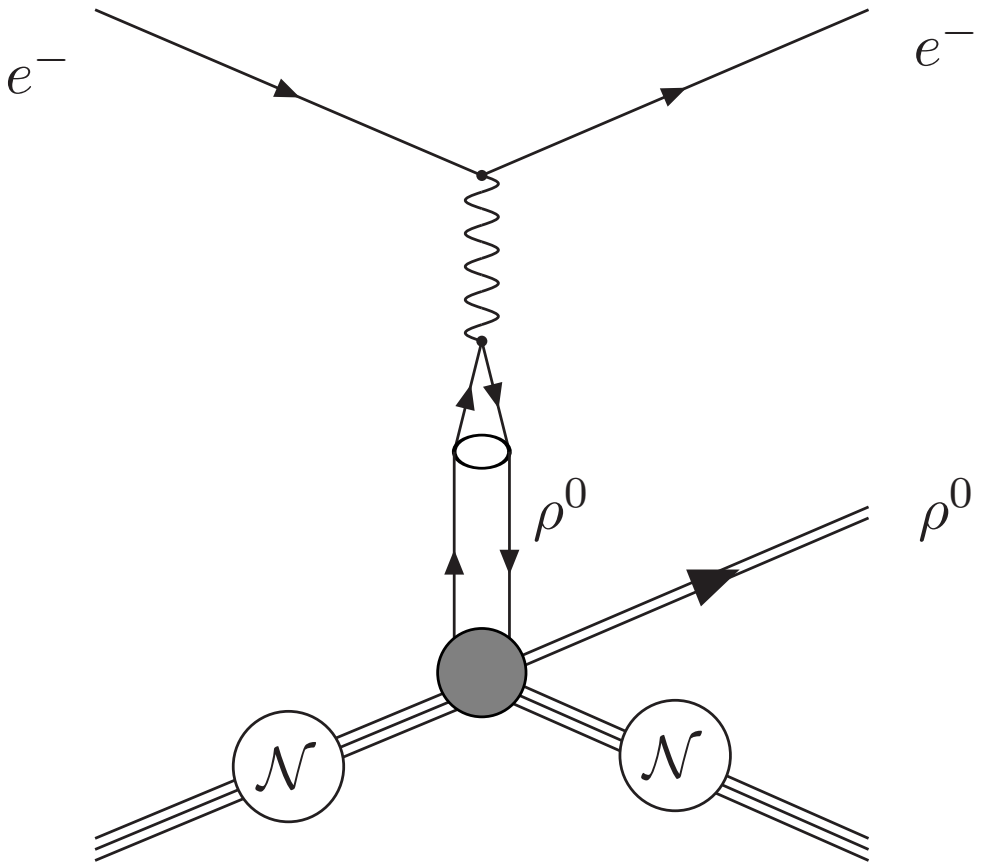

Figure 7.1: Feynman diagram of photon induced coherent ρ process.

Using Feynman Rules, we have

$$\begin{aligned}
\mathcal{M} &= -ie\bar{u}_{ef}\gamma^{\mu}u_{ei}\frac{ig_{\mu\nu}}{q^2} < 0|j^{\nu}_{em}|\rho^0_j > (-ie) \\
&\quad \mathcal{A}_j(\rho^0\alpha \to \beta) \times \frac{i}{q^2 - m^2_{\rho}} \\
&= -e^2\bar{u}_{ef}\gamma^{\mu}u_{ei}\frac{g_{\mu\nu}}{q^2} < 0|j^{\nu}_{em}|\rho^0_j > \mathcal{A}_j(\rho^0\alpha \to \beta) \times \frac{i}{q^2 - m^2_{\rho}} \\
&= e^2\bar{u}_{ef}\gamma^{\mu}u_{ei}\frac{g_{\mu\nu}}{Q^2} < 0|j^{\nu}_{em}|\rho^0_j > \mathcal{A}_j(\rho^0\alpha \to \beta) \times \frac{i}{Q^2 + m^2_{\rho}}, \qquad (7.1)
\end{aligned}$$

where j is polarization index number. For the decay constant part, we may write

$$\begin{aligned}
< 0|j^{\nu}_{em}|\rho^0_j > &= < 0|\bar{u}\gamma^{\nu}uq_u + \bar{d}\gamma^{\nu}dq_d|\frac{1}{\sqrt{2}}(u\bar{u} - d\bar{d}) > \\
&= \frac{1}{\sqrt{2}}(< 0|\bar{u}\gamma^{\nu}uq_u|u\bar{u} > - < 0|\bar{d}\gamma^{\nu}dq_d|d\bar{d} >) \\
&= \frac{1}{\sqrt{2}}f_{\rho}m_{\rho}\epsilon^{\nu}_j, \qquad (7.2)
\end{aligned}$$

where the flavor structure of ρ^0 has been used:

$$\rho^0 = \frac{1}{\sqrt{2}}(u\bar{u} - d\bar{d}). \tag{7.3}$$

$q_{u,d}$ are electrical charges of u, d quarks respectively. Eventually, we obtain

$$\begin{aligned} \mathcal{M} &= e^2 \bar{u}_{ef}\gamma^\mu u_{ei}\frac{g_{\mu\nu}}{Q^2}\frac{1}{\sqrt{2}}f_\rho m_\rho \epsilon_j^\nu \mathcal{A}_j(\rho^0\alpha \to \beta) \times \frac{i}{Q^2+m_\rho^2} \\ &= \frac{e^2}{\sqrt{2}}f_\rho m_\rho 2\bar{u}_{ef}\gamma^\mu u_{ei}\epsilon_j^\mu \mathcal{A}_j(\rho^0\alpha \to \beta) \times \frac{i}{Q^2+m_\rho^2}. \end{aligned} \tag{7.4}$$

Compare this to the scattering amplitude with the neutrino induced coherent ρ^0, we might come to the conclusion that, the differences between the two come from three parts:

• Electromagnetic interaction vertex $\frac{e^2}{\sqrt{2}} = \frac{4\pi\alpha}{\sqrt{2}}$; Weak interaction vertex $\frac{G_F}{2}(1 - 2\sin^2\theta_W)$

• Photon propagator $\sim \frac{1}{Q^2}$; Z^0 propagator $\sim \frac{1}{Q^2+m_Z^2}$ in weak interaction $m_Z^2 \gg Q^2$ then, we have $\frac{1}{Q^2+m_Z^2} \sim \frac{1}{m_Z^2}$, already included in G_F;

• The leptronic tensor:

For Electromagnetic interaction

$$\begin{aligned} Tr\{\bar{u}_{ef}\gamma^\mu u_{ei}\bar{u}_{ei}\gamma^\alpha u_{ef}\} &= Tr\{u_{ef}\bar{u}_{ef}\gamma^\mu u_{ei}\bar{u}_{ei}\gamma^\alpha\} \\ &= \frac{1}{2}Tr\{(\not{P}_f + m_e)\gamma^\mu(\not{P}_i + m_e)\gamma^\alpha\} \\ &= \frac{1}{2}Tr\{\not{P}_f\gamma^\mu\not{P}_i\gamma^\alpha + m_e^2\gamma^\mu\gamma^\alpha\}. \end{aligned} \tag{7.5}$$

Since m_e^2 is very small, after ignoring it, we obtain

$$\begin{aligned} Tr\{\bar{u}_{ef}\gamma^\mu u_{ei}\bar{u}_{ei}\gamma^\alpha u_{ef}\} &= \frac{1}{2}Tr\{\not{P}_f\gamma^\mu\not{P}_i\gamma^\alpha\} \\ &= \frac{1}{2} \times 4(P_f^\mu P_i^\alpha - P_f \cdot P_i g^{\mu\alpha} + P_f^\alpha P_i^\mu) \\ &= 2(P_f^\mu P_i^\alpha - P_f \cdot P_i g^{\mu\alpha} + P_f^\alpha P_i^\mu). \end{aligned} \tag{7.6}$$

Combine all the three terms together, we have:

$$\begin{aligned}\frac{d\sigma(e+N\to e+\rho^0+N)}{d\sigma(\nu+N\to\nu+\rho^0+N)} &= \frac{(\frac{4\pi\alpha}{\sqrt{2}})^2(\frac{1}{Q^2})^2 2^2}{\frac{G_F}{2}^2(1-2\sin^2\theta_W)^2\times 8^2} \\ &= \frac{32\pi^2\alpha^2}{Q^4\times 16\times G_F^2(1-2\sin^2\theta_W)^2} \\ &= \frac{2\pi^2\alpha^2}{G_F^2(1-2\sin^2\theta_W)^2\times Q^4}. \end{aligned} \tag{7.7}$$

7.3 Connection Between the Neutrino- & Photo-production of Coh--Rho: Absolute Flux

From the ratio of the cross-sections of photon and neutrino induced coherent ρ^0 processes, we have

$$\begin{aligned}\frac{d\sigma(e+N\to e+\rho^0+N)}{dQ^2d\nu dt} &= \frac{2\pi^2\alpha^2}{G_F^2(1-2\sin^2\theta_W)^2Q^4} \\ &\times\frac{d\sigma(\nu+N\to\nu+\rho^0+N)}{dQ^2d\nu dt}\end{aligned} \tag{7.8}$$

The factor Q^4 in the denominator implies the cross-section would be infinitely large when $Q^2\to 0$, and the integral over Q^2 would be divergent. Ignoring the lepton's mass, we would have $Q^2\simeq 4EE'\sin^2\frac{\theta}{2}$, where E and E' are incoming lepton and outgoing lepton energies. We can see that the infinity appears at $\theta=0$. This is a property of Coulomb Scattering. We could divide the integral into two parts:

$$\int_0^a\frac{d\sigma}{dQ^2d\nu dt}=\int_0^\epsilon\frac{d\sigma}{dQ^2d\nu dt}+\int_\epsilon^a\frac{d\sigma}{dQ^2d\nu dt}. \tag{7.9}$$

The first term is divergent, and the second term is finite. This means that the number of events with Q^2 between 0 and ϵ is too large compared to the events with Q^2 between ϵ and a. Practically, we could introduce a cut-off to avoid divergence.

It is easy to deduce the relation between the photon induced process and the neutrino induced coherent $\rho^\pm$ processes from Equation (3.117) and Equation (7.8):

$$\frac{d\sigma(e+N\to e+\rho^0+N)}{dQ^2d\nu dt}=\frac{\pi^2\alpha^2}{G_F^2Q^4}\frac{d\sigma(\nu+N\to\mu+\rho^+ +N)}{dQ^2d\nu dt}. \tag{7.10}$$

7.4 Simulation of Coherent ρ^+ Production

The simulation of the coherent ρ^+ events is based on the Neglib package which is used to simulate the Monte Carlo events of coherent π^+ using NOMAD flux. The procedure includes:

- **Set Input Variables:** Instead of using the NOMAD flux, LBNF flux was used as the incoming flux. Since the design of HIRESMNU is based on the experience of NOMAD detector, the target used in the simulation of Coherent ρ^+ is the same as in the Neglib package. Because the output of the StandAlone Code will be used to GENIE(Generates Events for Neutrino Interaction Experiments), all the codes are written in C++. The mass of the coherent meson (ρ^+) was generated randomly according to the distribution of relativistic breit wigner formula which is:

$$f(E) = \frac{k}{(E^2 - M^2)^2 + M^2\Gamma^2,} \tag{7.11}$$

where

$$\begin{aligned} k &= \frac{2\sqrt{2}M\Gamma\gamma}{\pi^2\sqrt{M^2+\gamma}}, \\ \gamma &= \sqrt{M^2(M^2+\Gamma^2)}. \end{aligned} \tag{7.12}$$

Xbj and Ybj are generated randomly from 0 to 1. The lepton energy(Elep) is calculated from the E_ν and Ybj (Elep=E_ν×(1-Ybj)). The |t| is also calculated from a random number, which is

$$|t| = -\frac{1}{b} \times \ln(Rand), \tag{7.13}$$

where the slope parameter b is calculated according to Equation(9) in Rein and Sehgal's paper[44]. Rand represents a random number from 0 to 1. After setting the input values of E_ν, Xbj, Ybj, mass of meson m_ρ, some other variables like ν, Q^2, W^2 could be calculated from these three variables.

- **Perform a Number of Kinematic boundaries:** After generating the four input variables, we then apply some kinematic boundary cuts to select the physical events, including, maximum of Xbj, maximum of Ybj, minimum of Ybj, maximum of t, minimum of t and so on which are consistent to the values in Neglib package.

- **Cross-Section Calculation:** the cross-section of coherent ρ^+ could be calculated from the variables generated and calculated for each event.

- **Reweight Distribution to Get Photo-production Coherent ρ^0 Events** Using the result of Equation (7.7), reweighted all the variable distributions of Coherent ρ^+, we then obtain the distributions of all the corresponding variables in photo-production coherent ρ^+ events.

To get the Q^2 distribution of $e + \mathcal{A} \to e + \mathcal{A} + \rho^0$, we just need to reweight the corresponding distribution of neutrino induced coherent ρ^+ process by factor $\frac{\pi^2\alpha^2}{G_F^2 Q^4}$. However, for other variables, we could not do this simply. What we can do is, suppose, we want to get the distribution of variable X: First, we need to create the 2-dimensional distribution of X and Q^2, then reweight each bin by this factor; Second, integrate over Q^2, then we get the distribution of variable X.

Since the ratio of the cross-section between photon induced and neutrino induced coherent processes is a function of Q^2, it is reasonable to consider Q^2 first. To avoid the condition that $Q^2 = 0$, I applied a lower cut value of Q^2, which is 0.02 GeV^2 (we could also set this cut value from experimental experience).

The analysis was done with the C++ standAlone code I wrote based on the Neglib package. Figure 7.2 is the distribution of Q^2 of neutrino induced coherent ρ^+ events vs photon induced coherent events obtained from ν-induced coherent ρ^+ events reweighted by factor $\frac{\pi^2\alpha^2}{G_F^2 Q^4}$. Similar plots for other important variables are shown from Figure 7.3 to Figure 7.7.

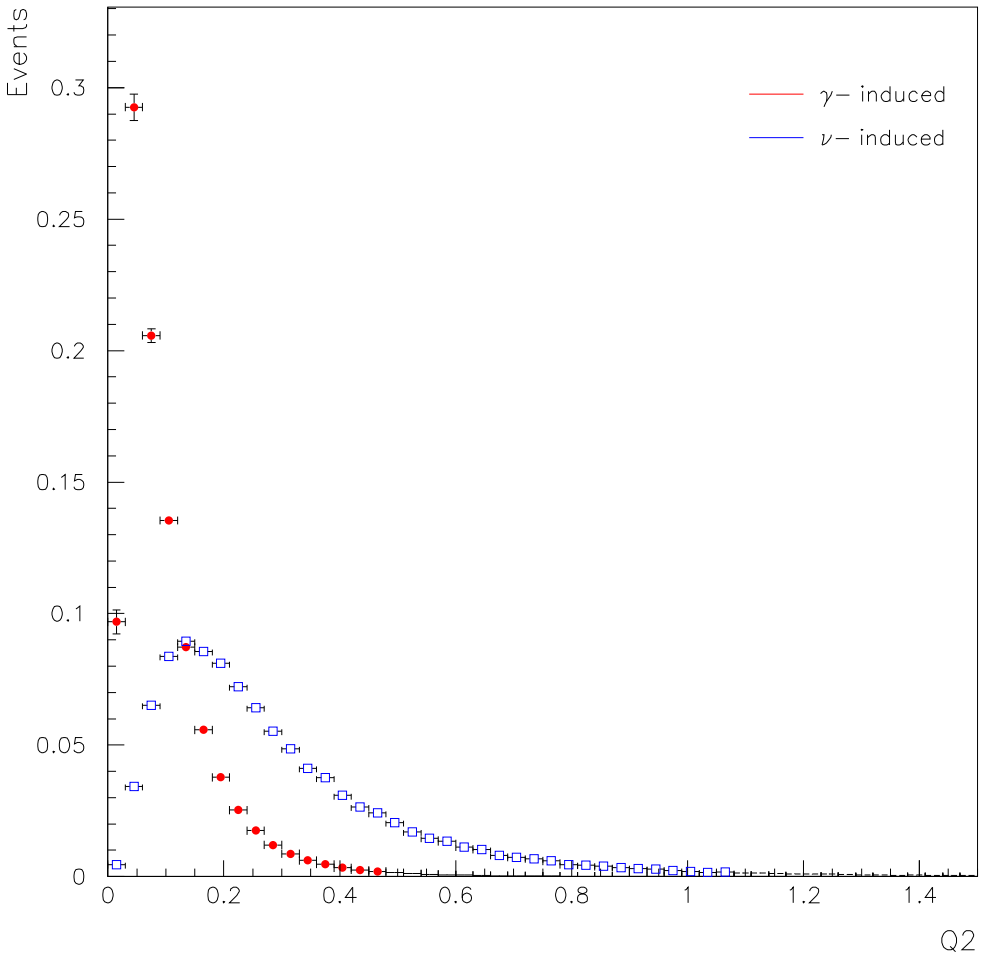

Figure 7.2: Q^2 distribution of neutrino induced coherent ρ^+ events generated from LBNE flux and photon induced coherent events obtained from ν-induced coherent ρ^+ events reweighted by factor $\frac{\pi^2\alpha^2}{G_F^2 Q^4}$.

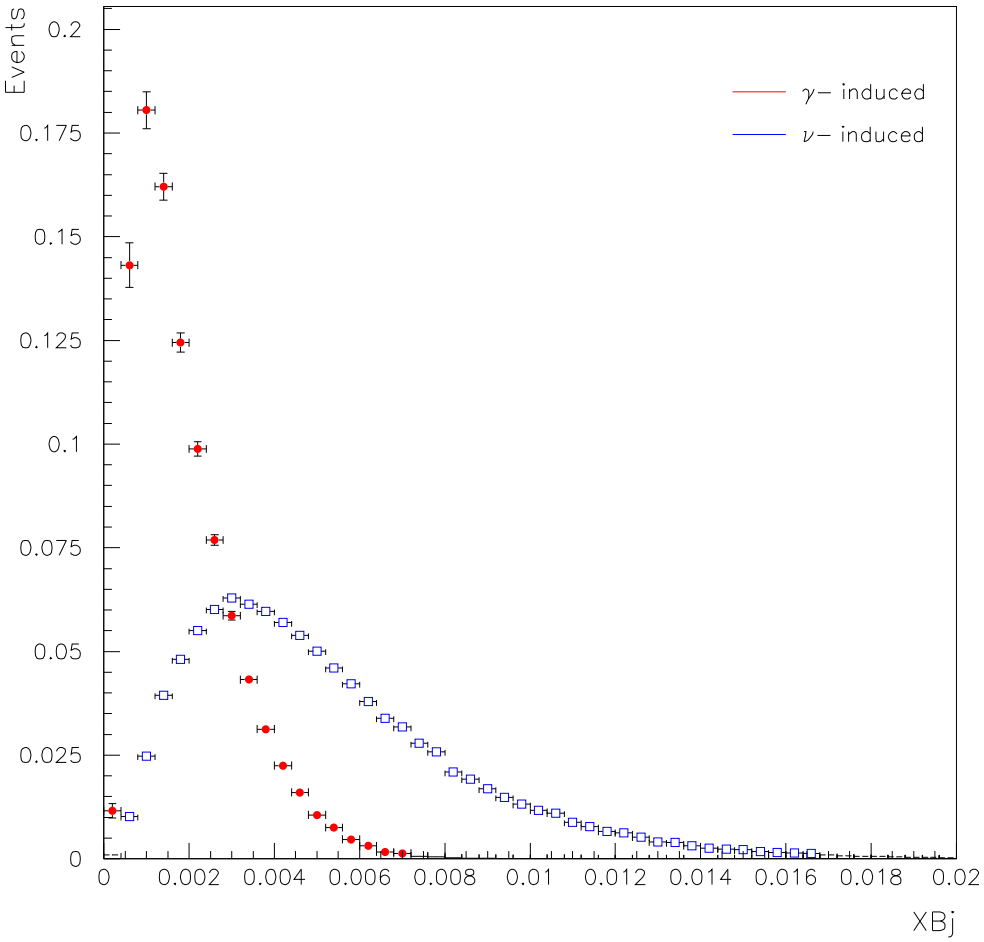

Figure 7.3: Xbj distribution of neutrino induced coherent ρ^+ events generated from LBNE flux and photon induced coherent events obtained from ν-induced coherent ρ^+ events reweighted by factor $\frac{\pi^2\alpha^2}{G_F^2 Q^4}$.

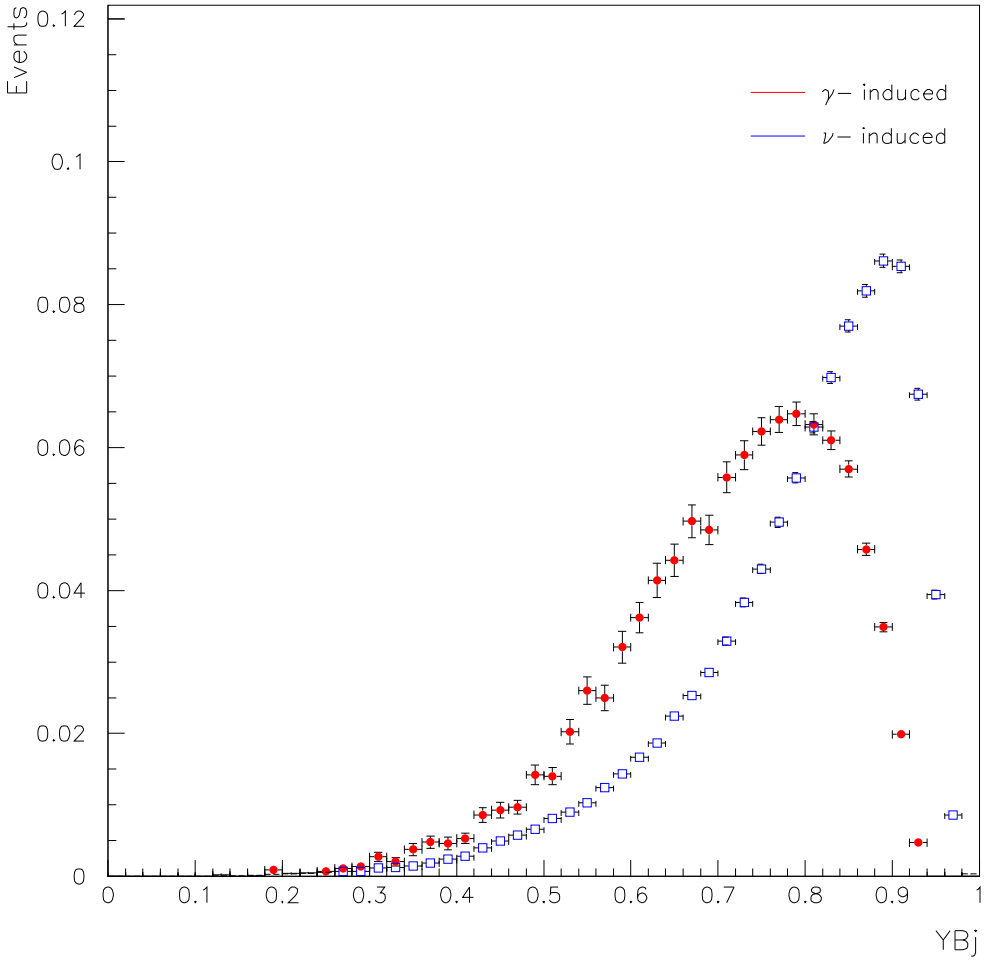

Figure 7.4: Ybj distribution of neutrino induced coherent ρ^+ events generated from LBNE flux and photon induced coherent events obtained from ν-induced coherent ρ^+ events reweighted by factor $\frac{\pi^2\alpha^2}{G_F^2 Q^4}$.

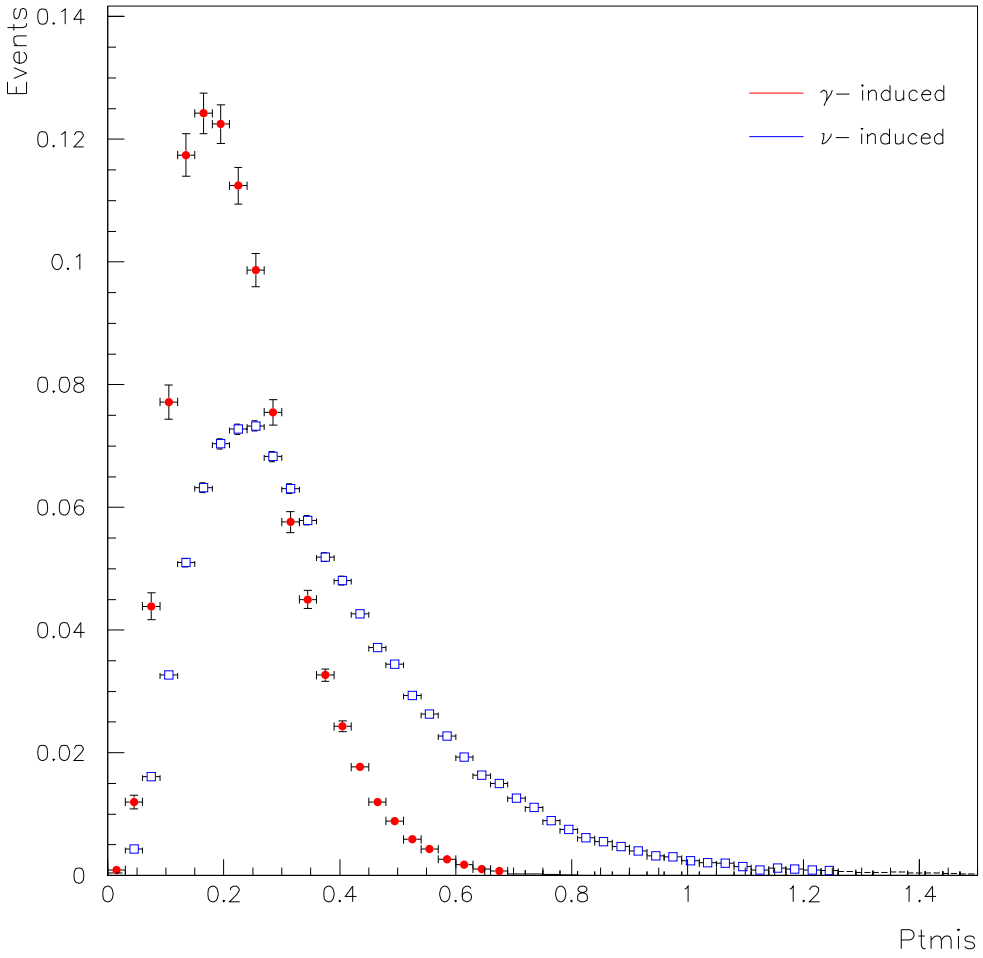

Figure 7.5: P_T^m distribution of neutrino induced coherent ρ^+ events generated from LBNE flux and photon induced coherent events obtained from ν-induced coherent ρ^+ events reweighted by factor $\frac{\pi^2\alpha^2}{G_F^2 Q^4}$.

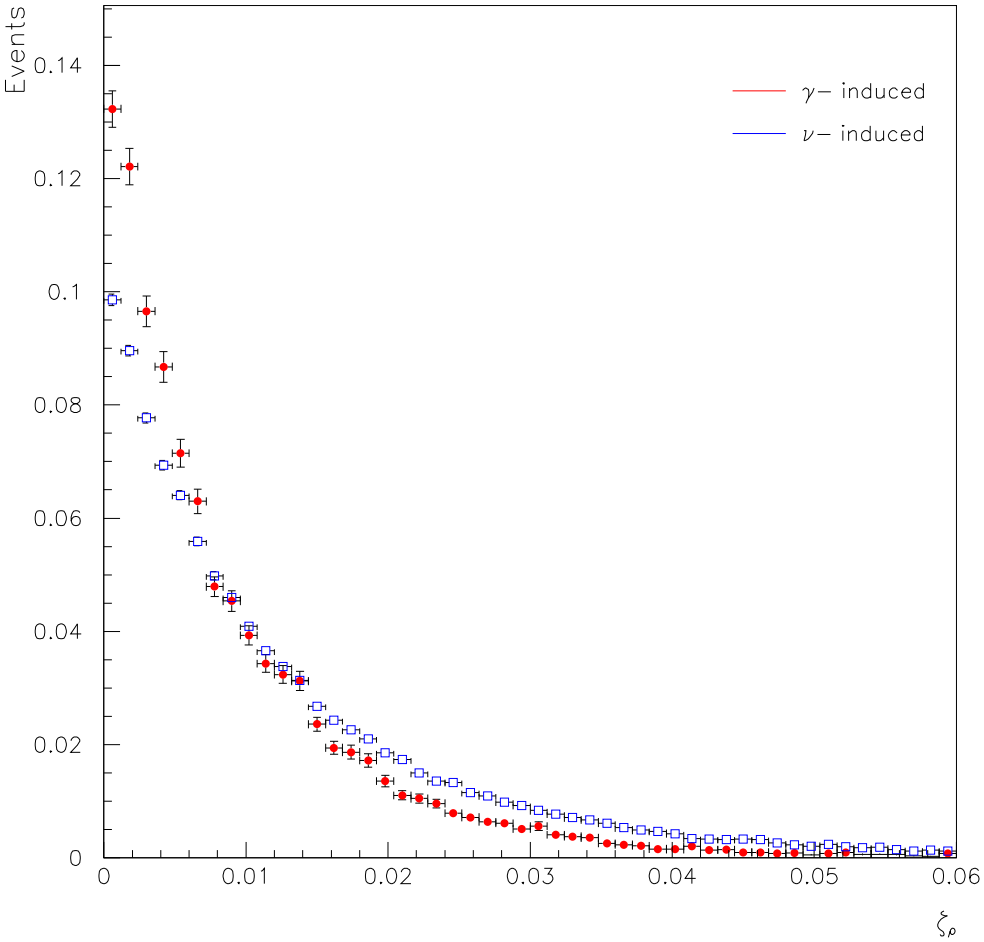

Figure 7.6: ζ_ρ distribution of neutrino induced coherent ρ^+ events generated from LBNE flux and photon induced coherent events obtained from ν-induced coherent ρ^+ events reweighted by factor $\frac{\pi^2\alpha^2}{G_F^2 Q^4}$.

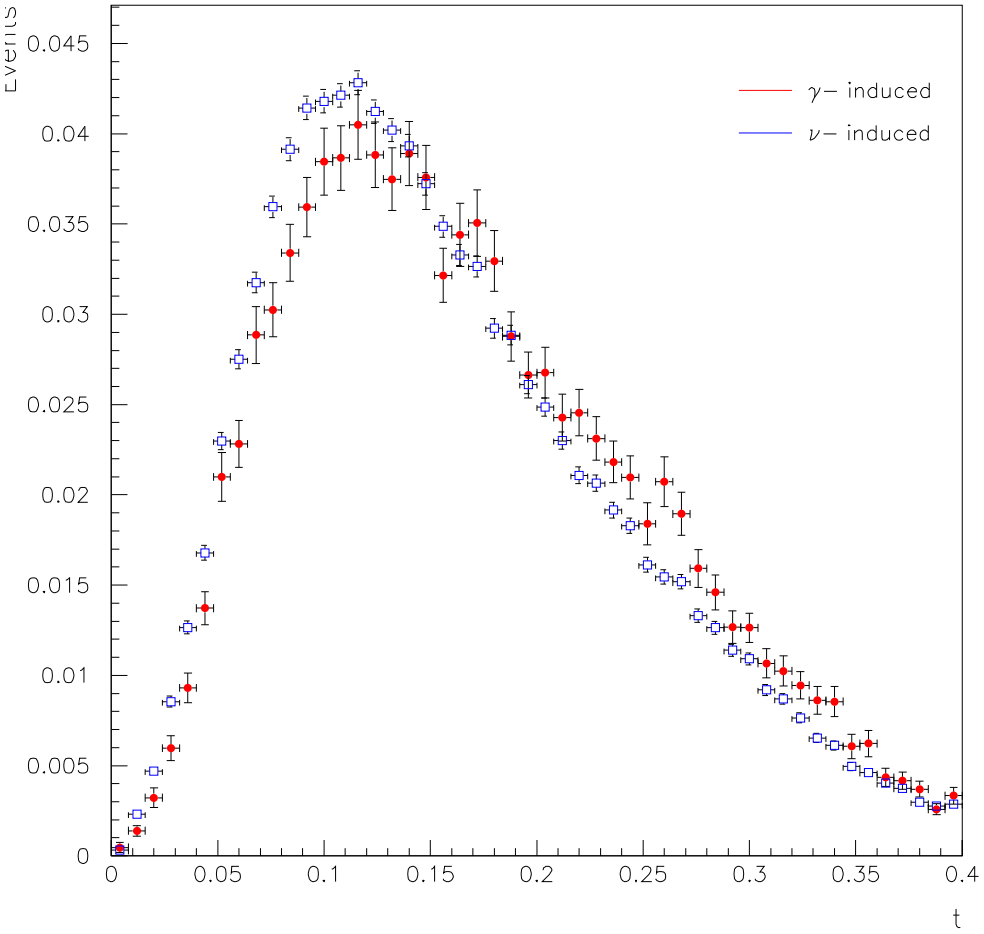

Figure 7.7: t distribution of neutrino induced coherent ρ^+ events generated from LBNE flux and photon induced coherent events obtained from ν-induced coherent ρ^+ events reweighted by factor $\frac{\pi^2\alpha^2}{G_F^2 Q^4}$.

Chapter 8

Summary and Future Work

Using the CVC, PCAC hypothesis, and Hadron Dominance Model, I calculated the the neutrino induced coherent π, and coherent ρ. I also calculated the cross-section of photon induce coherent ρ^0 process and the ratio between the photon induced coherent ρ^0 and neutrino induced coherent ρ which gives a way to get additional information to constrain the neutrino fluxes. Beside the theoretical calculations, I measured the ratio between cross-section of coherent π^- and $\bar{\nu}_\mu$ CC interactions with the NOMAD data including neutrino beam mode data and anti-neutrino beam mode data, and compared it to the measurement of coherent π^+ production. This is the best measurement of coherent π^- to date. Based upon the experience of analysis with NOMAD data, my final aim is to evaluate the sensitivity of ELBNF/DUNE project to coherent process. Then, in the second part, I used new C++ standAlone Code I wrote and simulated coherent ρ^+ interactions. After that, I reweighted the distributions of some kinematic variables with the factor (ratio between cross-section of photon induced and neutrino induced coherent ρ process). I calculated and get the corresponding distributions of photon induced coherent process.

In the future, I will integrate the C++ simulation package I wrote into the GEINE neutrino event generator which is written in C++. GENIE is a comprehensive neutrino Monte Carlo generator supported and developed by an international collaboration of scientists [6]. The GENIE model is universal. It handles all neutrinos and nuclear targets, and all processes relevant from MeV to PeV energy scales. Some experiments(including T2K, NoνA, MINERνA, MicroBooNE, LAr1-ND, ELBNF and

IceCUBE) use GENIE whose predictions is a standard reference point for the entire community.

Bibliography

[1] Corey Adams, David Adams, Tarek Akiri, Tyler Alion, Kris Anderson, Costas Andreopoulos, Mike Andrews, Ioana Anghel, João Carlos Costa dos Anjos, Maddalena Antonello, et al., *The long-baseline neutrino experiment: exploring fundamental symmetries of the universe*, arXiv preprint arXiv:1307.7335 (2013).

[2] T Akesson, F Anghinolfi, E Arik, OK Baker, E Banas, S Baron, D Benjamin, H Bertelsen, V Bondarenko, V Bytchkov, et al., *Aging effects in the atlas transition radiation tracker and gas filtration studies*, Nuclear Science Symposium Conference Record, 2005 IEEE, vol. 2, IEEE, 2005, pp. 1185–1190.

[3] T Akesson, F Anghinolfi, E Arik, OK Baker, S Baron, D Benjamin, H Bertelsen, V Bondarenko, V Bytchkov, J Callahan, et al., *Status of design and construction of the transition radiation tracker (trt) for the atlas experiment at the lhc*, Nuclear Instruments and Methods in Physics Research Section A: Accelerators, Spectrometers, Detectors and Associated Equipment **522** (2004), no. 1, 131–145.

[4] T Akesson, E Arik, K Baker, S Baron, D Benjamin, H Bertelsen, V Bondarenko, V Bytchkov, J Callahan, M Capeans, et al., *Atlas transition radiation tracker test-beam results*, Nuclear Instruments and Methods in Physics Research Section A: Accelerators, Spectrometers, Detectors and Associated Equipment **522** (2004), no. 1, 50–55.

[5] J Altegoer, M Anfreville, C Angelini, P Astier, M Authier, D Autiero, Alberto Baldisseri, M Baldo-Ceolin, G Ballocchi, M Banner, et al., *The NOMAD experiment at the CERN SPS*, Nuclear Instruments and Methods in Physics Research Section A: Accelerators, Spectrometers, Detectors and Associated Equipment **404** (1998), no. 1, 96–128.

[6] C Andreopoulos, *The genie universal, object-oriented neutrino generator*, Nuclear Physics B-Proceedings Supplements **159** (2006), 217–222.

[7] M Anfreville, P Astier, M Authier, A Baldisseri, M Banner, N Besson, J Bouchez, A Castera, O Cloue, J Dumarchez, et al., *The drift chambers of the NOMAD experiment*, Nuclear Instruments and Methods in Physics Research Section A: Accelerators, Spectrometers, Detectors and Associated Equipment **481** (2002), no. 1, 339–364.

[8] Pierre Astier, D Autiero, A Baldisseri, M Baldo-Ceolin, M Banner, G Bassompierre, K Benslama, N Besson, I Bird, B Blumenfeld, et al., *Prediction of neutrino fluxes in the NOMAD experiment*, Nuclear Instruments and Methods in Physics Research Section A: Accelerators, Spectrometers, Detectors and Associated Equipment **515** (2003), no. 3, 800–828.

[9] C Athanassopoulos, LB Auerbach, DA Bauer, RD Bolton, B Boyd, RL Burman, DO Caldwell, I Cohen, BD Dieterle, JB Donahue, et al., *Candidate events in a search for $\bar{\nu}_\mu \to \bar{\nu}_e$ oscillations*, Physical Review Letters **75** (1995), no. 14, 2650.

[10] C Athanassopoulos, LB Auerbach, RL Burman, DO Caldwell, ED Church, I Cohen, JB Donahue, A Fazely, FJ Federspiel, GT Garvey, et al., *Results on $\nu_\mu \to \nu_e$ neutrino oscillations from the LSND experiment*, Physical Review Letters **81** (1998), no. 9, 1774.

[11] C Athanassopoulos, LB Auerbach, RL Burman, I Cohen, DO Caldwell, BD Dieterle, JB Donahue, AM Eisner, A Fazely, FJ Federspiel, et al., *Evidence for neutrino oscillations from muon decay at rest*, Physical Review C **54** (1996), no. 5, 2685.

[12] Gabriel Bassompierre, S Bunyatov, T Fazio, J-M Gaillard, M Gouanere, E Manola-Poggioli, L Mossuz, J-P Mendiburu, P Nedelec, Yu Nefedov, et al., *Performance of the nomad transition radiation detector*, Nuclear Instruments and Methods in Physics Research Section A: Accelerators, Spectrometers, Detectors and Associated Equipment **411** (1998), no. 1, 63–74.

[13] TH Bauer, RD Spital, DR Yennie, and FM Pipkin, *The hadronic properties of the photon in high-energy interactions*, Reviews of Modern Physics **50** (1978), no. 2, 261.

[14] Andrew Bazarko, *Miniboone: Status of the booster neutrino experiment*, arXiv preprint hep-ex/0009056 (2000).

[15] Ch Berger and LM Sehgal, *Partially conserved axial vector current and coherent pion production by low energy neutrinos*, Physical Review D **79** (2009), no. 5, 053003.

[16] SN Biswas, Ranabir Dutt, and KC Gupta, *Subtracted dispersion relations, current algebra and momentum dependent K_{l4} decay axial vector form factors*, Annals of Physics **52** (1969), no. 2, 366–379.

[17] Chen, *CP violation and the mass hierarchy*, http://www.snolab.ca/sites/default/files/Chen5_FutureCPHierarchy.pdf, Acessed: 2015-01-23.

[18] Brajesh Choudhary, Raj Gandhi, Sanjib R. Mishra, Shekhar Mishra, and James Strait, *Proposal of indian institutions and Fermilab collaboration for participation in the long-baseline neutrino experiment at fermilab*, DOE Document (2012).

[19] E Church, I Stancu, GJ VanDalen, RA Johnson, JM Conrad, J Formaggio, T Ochs, MH Shaevitz, EG Stern, B Tamminga, et al., *A letter of intent for an experiment to measure ν_μ to ν_e oscillations and ν_μ disappearance at the fermilab booster (boone)*, arXiv preprint nucl-ex/9706011 (1997).

[20] Frank E Close, *An introduction to quarks and partons*, Academic Press, 1979.

[21] Christophe Delaere, *TMultiLayerPerceptron*, http://root.cern.ch/root/html/T--MultiLayerPerceptron.html, Accessed: 2015-04-17.

[22] C. Athanassopoulos et al., *Results on $\nu_\mu \to \nu_e$ oscillations from pion decay in flight neutrinos*, Physical Review C **58** (1998), no. 4, 2489.

[23] C. Athanassopoulos et al. (LSND collaboration), *Evidence for $\bar{\nu}_\mu \to \bar{\nu}_e$ oscillations from the lsnd experiment at the los alamos meson physics facility*, Phys. Rev. Lett **77** (1996), 3082.

[24] Gian L Fogli, E Lisi, A Marrone, D Montanino, A Palazzo, and AM Rotunno, *Global analysis of neutrino masses, mixings, and phases: Entering the era of leptonic c p violation searches*, Physical Review D **86** (2012), no. 1, 013012.

[25] Murray Gell-Mann, *Test of the nature of the vector interaction in β decay*, Physical Review **111** (1958), no. 1, 362.

[26] Murray Gell-Mann and Maurice Lévy, *The axial vector current in beta decay*, Il Nuovo Cimento **16** (1960), no. 4, 705–726.

[27] Howard Georgi, *Weak interactions and modern particle theory, revised and updated*, Dover Publications, Inc., Mineola, NY, 2009.

[28] SS Gerstein, *Yb zeldovich soviet phys*, JETP **2** (1956), 576.

[29] et al. G.Ingelman, Computer Phys. Comm. **101** (1997), 108–134.

[30] Carlo Giunti and Chung W Kim, *Fundamentals of neutrino physics and astrophysics*, Oxford university press, 2007.

[31] ML Goldberger and SB Treiman, *Form factors in β decay and μ capture*, Physical Review **111** (1958), no. 1, 354.

[32] G Grammer, Jeremiah D Sullivan, A Donnachie, and G Shaw, *Electromagnetic interactions of hadrons*, Vol. 2Plenum, New York (1978), 195.

[33] Walter Greiner, Berndt Müller, and David Allan Bromley, *Gauge theory of weak interactions*, vol. 5, Springer, 1996.

[34] David Griffiths, *Introduction to elementary particles*, John Wiley & Sons, 2008.

[35] JL Hewett, H Weerts, R Brock, JN Butler, BCK Casey, J Collar, A de Gouvea, R Essig, Y Grossman, W Haxton, et al., *Fundamental physics at the intensity frontier*, arXiv preprint arXiv:1205.2671 (2012).

[36] BZ Kopeliovich and P Marage, *Low q^2, high neutrino nu physics (cvc, pcac, hadron dominance)*, International Journal of Modern Physics A **8**, 1513.

[37] CT Kullenberg, SR Mishra, MB Seaton, JJ Kim, XC Tian, AM Scott, M Kirsanov, R Petti, S Alekhin, P Astier, et al., *A measurement of coherent neutral pion production in neutrino neutral current interactions in the nomad experiment*, Physics Letters B **682** (2009), no. 2, 177–184.

[38] K Kurek, A Korzenev, K Kowalik, A Mielech, E Rondio, and R Windmolders, *An algorithm for track reconstruction in the large angle spectrometer of the compass experiment*, Nuclear Instruments and Methods in Physics Research Section A: Accelerators, Spectrometers, Detectors and Associated Equipment **485** (2002), no. 3, 720–738.

[39] Karol Lang, *Future prospects for measurements of mass hierarchy and CP violation*, Nuclear and Particle Physics Proceedings **260** (2015), 183–187.

[40] William J Marciano and Zohreh Parsa, *Neutrino–electron scattering theory*, Journal of Physics G: Nuclear and Particle Physics **29** (2003), no. 11, 2629.

[41] Michael E Peskin and Daniel V Schroeder, *An introduction to quantum field theory*, Westview, 1995.

[42] CA Piketty and L Stodolsky, *Diffraction model of high-energy leptonic interactions*, Nuclear Physics B **15** (1970), no. 2, 571–600.

[43] Klaus Platzer, W Dunnweber, Nicolas Dedek, Martin Faessler, Reiner Geyer, Christoph Ilgner, Vladimir Peshekhonov, and Hermann Wellenstein, *Mapping the large area straw detectors of the compass experiment with x-rays*, Nuclear Science, IEEE Transactions on **52** (2005), no. 3, 793–798.

[44] Dieter Rein and Lalit M Sehgal, *Coherent π^0 production in neutrino reactions*, Nuclear Physics B **223** (1983), no. 1, 29–44.

[45] Xinchun Tian, *Neutrino induced charged-current coherent ρ production*, arXiv preprint arXiv:1310.8547 (2013).

[46] Xinchun Tian, Hongyue Duyang, and Sanjib Mishra, *Precision measurement of resonance interaction in a fine grain tracker*, Bulletin of the American Physical Society **60** (2015).

[47] T.SjÂĺostrand, Computer Phys. Comm **82** (1994), 74–90.

[48] F Vannucci, *The NOMAD experiment at CERN*, Advances in High Energy Physics **2014** (2014).

[49] D Hywel White and LSND Collaborationa, *Neutrino oscillation results from lsnd*, Nuclear Physics B-Proceedings Supplements **77** (1999), no. 1, 207–211.

[50] Stephane Willocq, *Coherent production of pions and ρ mesons in neutrino charged current interactions on neon nuclei at the fermilab tevatron*, Tech. report, Tufts Univ., Medford, MA (United States), 1992.

[51] Lyle John Winton, *Coherent diffractive pion production in charged current neutrino interactions*, Ph.D. thesis, University of Melbourne, Department of Physics, 1999.

[52] Q Wu, SR Mishra, A Godley, R Petti, S Alekhin, P Astier, D Autiero, A Baldisseri, M Baldo-Ceolin, M Banner, et al., *A precise measurement of the muon neutrino–nucleon inclusive charged current cross section off an isoscalar target in the energy range 2.5< E_ν< 40 GeV by NOMAD*, Physics Letters B **660** (2008), no. 1, 19–25.

Appendix A

CP violation

$$\nu^{CP} = \gamma^0 \mathcal{C} \bar{\nu}^T = -\mathcal{C}\nu^* \tag{A.1}$$

C: Particle$\rightleftharpoons$ Antiparticle P: Left-Handed$\rightleftharpoons$ Right-handed Neutrino fields under CP transformation is [17]:

$$\nu_{\alpha L} = \sum_k U_{\alpha k} \nu_{kL} \underrightarrow{CP} \nu^{CP}_{\alpha L} = \sum_k U^*_{\alpha k} \nu^{CP}_{kl} \tag{A.2}$$

$$|\nu_\alpha\rangle = \sum_k U^*_{\alpha k} |\nu_k\rangle \underrightarrow{CP} |\bar{\nu}_\alpha\rangle = \sum_k U_{\alpha k} |\bar{\nu}_k\rangle \tag{A.3}$$

Neutrinos $U \rightleftharpoons U*$ Antineutrinos

$$P_{\nu_\alpha \to \nu_\beta}(L,E) = \sum_k |U_{\alpha k}|^2 |U_{\beta k}|^2 + 2Re \sum_{k>j} U^*_{\alpha k} U_{\beta k} U_{\alpha j} U^*_{\beta j} \exp(-i \frac{\Delta m^2_{kj} L}{2E}) \tag{A.4}$$

$$P_{\bar{\nu}_\alpha \to \bar{\nu}_\beta}(L,E) = \sum_k |U_{\alpha k}|^2 |U_{\beta k}|^2 + 2Re \sum_{k>j} U_{\alpha k} U^*_{\beta k} U^*_{\alpha j} U_{\beta j} \exp(-i \frac{\Delta m^2_{kj} L}{2E}) \tag{A.5}$$

PMNS(Pontecorvo-Maki-Nakagawa-SaKata) Neutrino Mixing Matrix is a unitary matrix which cantains information on the mismatch of quantum states of leptons when they propagate freely and when they take part in the weak interactions. It is important in the understanding of neutrino oscillations. For three generations of

leptons, the matrix can be written as [17]:

$$
\begin{aligned}
U &= R_{23}W_{13}R_{12}D(\lambda) \\
&= \begin{pmatrix} 1 & 0 & 0 \\ 0 & c_{23} & s_{23} \\ 0 & -s_{23} & c_{23} \end{pmatrix} \begin{pmatrix} c_{13} & 0 & s_{13}e^{-i\delta_{13}} \\ 0 & 1 & 0 \\ -s_{13}e^{i\delta_{13}} & 0 & c_{13} \end{pmatrix} \begin{pmatrix} c_{12} & s_{12} & 0 \\ -s_{12} & c_{13} & 0 \\ 0 & 0 & 1 \end{pmatrix} \\
&\times \begin{pmatrix} 1 & 0 & 0 \\ 0 & e^{i\lambda_{21}} & 0 \\ 0 & 0 & e^{i\lambda_{31}} \end{pmatrix} \\
&= \begin{pmatrix} c_{12}c_{13} & s_{12}c_{13} & s_{13}e^{-i\delta_{13}} \\ -s_{12}c_{23} - c_{12}s_{23}e^{0\delta_{13}i} & c_{12}c_{23} - s_{12}s_{23}s_{13}e^{i\delta_{13}} & s_{23}c_{13} \\ s_{12}s_{23} - c_{12}c_{23}s_{13}e^{i\delta_{13}} & -c_{12}s_{23} - s_{12}c_{23}s_{13}e^{i\delta_{13}} & c_{23}c_{13} \end{pmatrix} \\
&\times \begin{pmatrix} 1 & 0 & 0 \\ 0 & e^{i\lambda_{21}} & 0 \\ 0 & 0 & e^{i\lambda_{31}} \end{pmatrix}
\end{aligned} \tag{A.6}
$$

PMNS Neutrino Mixing Matrix Then, $P_{\nu_\mu \to \nu_e} - P_{\bar{\nu}_\mu \to \bar{\nu}_e}$ could be used as a direct test of CP symmetry,

$$
\begin{aligned}
P_{\nu_\mu \to \nu_e} - P_{\bar{\nu}_\mu \to \bar{\nu}_e} &= 2Re \sum_{k>j} [U^*_{\alpha k} U_{\beta k} U_{\alpha j} U^*_{\beta j} - U_{\alpha k} U^*_{\beta k} U^*_{\alpha j} U_{\beta j}] \exp(-i \frac{\Delta m^2_{kj} L}{2E}) \\
&\quad 4Re \sum_{k>j} i\Im[U^*_{\alpha k} U_{\beta k} U_{\alpha j} U^*_{\beta j}] \exp(-i \frac{\Delta m^2_{kj} L}{2E}) \\
&= 4 \sum_{k>j} [U^*_{\alpha k} U_{\beta k} U_{\alpha j} U^*_{\beta j}] \sin(\frac{\Delta m^2_{kj} L}{2E})
\end{aligned} \tag{A.7}
$$

where $J = \Im[U^*_{\alpha k} U_{\beta k} U_{\alpha k} U^*_{\beta j}]$ is is called a Jarlskog invariant, from the quark CKM

unitary triangle

$$\begin{aligned} J &= c_{12}s_{12}c23s_{23}c_{13}^2s_{13}\sin\delta \\ &= \frac{1}{2}\sin 2\theta_{12}\sin 2\theta_{23}\sin 2\theta_{13}\cos\theta 13\sin\delta \\ &= 4\sum_{k>j}\Im[U_{\alpha k}^* U_{\beta k} U_{\alpha j} U_{\beta j}^*]\sin(\frac{\Delta m_{kj}^2 L}{2E}) \\ &= \sin\delta\sin 2\theta_{12}\sin 2\theta_{23}\sin\theta_{13}\cos^2\theta_{13}\sin(\frac{\Delta m_{31}^2 L}{2E}) \\ &\quad -\sin\delta\sin 2\theta_{12}\sin 2\theta_{23}\sin\theta_{13}\cos^2\theta_{13}\sin(\frac{\Delta m_{32}^2 L}{2E}) \\ &\quad -\sin\delta\sin 2\theta_{12}\sin 2\theta_{23}\sin\theta_{13}\cos^2\theta_{13}\sin(\frac{\Delta m_{21}^2 L}{2E}) \end{aligned} \tag{A.8}$$

From Equation (A.8) we could know, that if any angle is zero, $\Delta P = 0$; if any $\Delta m^2 = 0$, $\Delta P = 0$;

$$A_{\alpha\beta}^{CP} = 4J\sum_{k>j} s_{\alpha\beta;kj}\sin(\frac{\Delta m_{kj}^2 L}{2E}) \tag{A.9}$$

- s for 31 is -1
- s for 32 is +1
- s for 21 is +1

where, we could see that for $e \to \mu$, $\mu \to \tau$, $\tau \to e$, s is positive and the sign flips if flavors flip.

From the equation above, we could see that to determine the CP violation, first, all angles should be large; second, the detector should be placed at correct L(baseline) for neutrino beam E; third, Δm_{21}^2 is small compared to Δm_{31}^2. The normal and inverted hierarchy are

- Normal Hierarchy(NH):$\Delta m_{31}^2 = \Delta m_{21}^2 + \Delta m_{32}^2$,
- Inverted Hierarchy(IH):$|\Delta m_{31}^2| = \Delta m_{21}^2 + |\Delta m_{32}^2|$.